MULTI-SOURCE, MULTI-SENSOR APPROACHES TO DIESEL ENGINE MONITORING USING ACOUSTIC EMISSION

Pornchai Nivesrangsan

Submitted for the degree of doctor of philosophy on completion of research in the School of Engineering and Physical Sciences, Mechanical Engineering,

Heriot-Watt University

December 2004

Abstract

This thesis relates to condition monitoring of diesel engines using Acoustic Emission (AE). AE waves attenuate as they propagate through structures and this work focuses on determining the relationship between attenuation of AE wave energy and its propagation path. A number of objects such as simple plate-like structures, small diesel engine blocks and large marine diesel engine blocks were studied to develop a generic empirical approach to AE wave propagation which could be used to source locate AE events in diesel engines and reconstitute their timing and amplitude.

The attenuation of AE energy was investigated intensively in a particular model of High Speed Direct Injection (HSDI) engine using simulated sources generated by pencil lead breaks and using real sources during running at a variety of conditions of speed and load. The attenuation of AE energy was estimated using a simple absorption law (exponential decay) and time-frequency methods were used to improve data quality. The approach developed was also applied to AE energy acquired on a large power generating marine diesel engine.

Source location techniques based on attenuation factor and event timing were successfully applied to identify multiple sources from engine running signals. A generic technique for reconstituting AE signals in terms of their energy and time-of-flight was developed. The approach involves mapping the acquired AE onto events identified in the engine cycle (i.e. injectors and valves) and improving the resolution of multiple source signals (i.e. within an injector). The overall outcome is the demonstration of the potential of AE for improved identification of multiple sources for monitoring of diesel engines using AE sensor arrays, and conclusion are drawn in the generic applicability of the approach.

Acknowledgments

I would like to express my sincere gratitude to many individuals for their valuable assistance during this work. However, it is not possible for me to list all the people who encouraged and helped me during my studies and research. I apologise in advance for any omissions.

Firstly, I wish to express my thanks to my supervisors, Professor Robert L. Reuben and Dr. John A. Steel for their invaluable supervision, guidance, technical support, encouragement and friendship over the entire period of my Ph.D. and for their most useful comments in my thesis writing.

My special thanks go to Dr. J. A. Steel, Mr. R. M. Douglas, Mr. A. I. F. Robertson, and Mr. E. R. Brown, who have helped and supplied me with various invaluable data acquired at KOS power station, Greece and some useful perspectives and discussions on the diesel engines. I would also like to thank the mechanical and electronic technicians who have helped me to manufacture and advised me on the test rigs especially Dave, Richard, Mark and Andy. Thanks must also go to Mr. J. D. Gill for his technical support on the diesel engine.

I would also like to take this opportunity to express my appreciation to Mrs. M. Thomson, Mrs. A. Blyth, Dr. T. Lim, Jimmy, Virgil, Ying, Mohamed, Tae, Michal, Carmen and all those friends and colleagues who made these years very memorable and extremely enjoyable. Thanks to Thai friends, Jeep, Ton, Dao, Big, Pae, Gong, Preaw, Pui to name a few who have been wandering around Edinburgh, keeping me company during my hard time.

Specially and most importantly, I would like to thank my grandmother, parents, brothers, sisters, aunt Ms. Sunisa Nivesrangsan and Ms. Amornsiri Arunsuwannakorn for their love, patience and unlimited support during my time in Scotland, UK. Without them I would never have made it this far. I would like to express my special thank to Dr. L. Vongsarnpigoon, Dr. W. Nerdnoi, Dr. S. Wongrassamee, Dr. V. Meeyoo, and Dr. T. Huyanan for their encouragements, supports and suggestions over the entire period of my Ph.D.

Finally, I am extremely grateful to Mahanakorn University of Technology, Thailand for the financial support.

Table of Contents

Lists of Tables

Lists of Figures

Nomenclature

α	Attenuation coefficient (dB/m)
β	Angle (deg)
γ	Angle (deg)
$\gamma(t)$	Window function
λ	Wavelength (m)
$\theta, \theta_1, \theta_2, \theta_3$	Angles (deg)
ν	Poisson's ratio
$\xi(k)$	The frequency transfer characteristic of medium
ρ	Density (kg/m^3)
σ	Standard deviation
τ	Time duration of the signal (s)
ψ	Angle (degrees)
ω	Angular frequency (rad/s)
A_i, A_{1i}, A_{2i}	Amplitude of AE signal (dB or V)
A_r	Relative amplitude (dB)
c, c_i	Wave speed (m/s)
c_e, c_f	Extensional and flexural wave speeds (m/s)
c_{HF}, c_{LF}	Wave speed of each component (m/s)
C_k	Coefficients of expansion
C_k^*	Coefficients
c_r	Raleigh wave (or surface wave) speed (m/s)
c_1	Dilatational wave speed (m/s)
c_2	Distortional wave speed (m/s)
d_1, d_2	Distance from source (m)
D, D_1, D_2	Distance between sensors (m)
E	Energy content (V^2.s)
$E(x)$	Energy at distance, x (V^2.s)
$E_{d\theta_i}$	Energy content of a small crank angle
E_o	Energy of the source (V^2.s)
$Erms_{1i}, Erms_{2i}$	RMS energy at each window
E_s, E_l	Energy content at distance, x_s and x_l
E_t, E_r	Percentage of transmission and reflection energy
E_w	Mean energy of noise signal in a specific window
E_y	Young's modulus of elasticity (N/m^2)
f	Frequency (Hz)
$f(t)$	Fourier series
k	Attenuation factor or Attenuation coefficient (m^{-1})
K_i	Wave number
Kurt	Kurtosis
P1-P12	Sensor positions
Q1-Q9	Sensor positions

r	Propagation distance (m)
r_1, r_2, r_3, R	Distance from source (m)
s	Distance (m)
$s(t)$	Spectral coefficients
Skew	Skewness
S0, S1, S2, S3	Sensor positions
t	Time (s)
t_1, t_2, t_3	Arrival time at each sensor (s)
$\Delta t_1, \Delta t_2, \Delta t_3$	Arrival time difference (s)
$v(t)$	Amplitude of signal (V)
Var	Variance
V_i, V_1, V_2, V_3	Wave velocity (m/s)
x	Distance (m)
x_s, x_l	Direct and circumferential transmission paths (m)
$\bar{x}, x_{\max}, x_{\min}$	Mean, maximum and minimum values
z_1, z_2	Distance (m)
Z_1, Z_2	Acoustic impedances (kg/m^2.s)

Abbreviations

ADC	Analogue to digital converter
AE	Acoustic emission
ANN(s)	Artificial neural network(s)
BDC	Bottom dead centre
CWD	Choi-Williams Distribution
CWT	Continuous wavelet transform
EV(s)	Exhaust valve(s)
EVC	Exhaust valve closing
EVO	Exhaust valve opening
FFT	Fast Fourier Transform
HSDI	High speed direct injection
ICA	Independent component analysis
ICAV	Instantaneous crankshaft angular velocity
INJ(s)	Injector(s)
IV(s)	Inlet valve(s)
IVC	Inlet valve closing
IVO	Inlet valve opening
MLP(s)	Multilayer perceptron(s)
PCA	Principal component analysis
PSD	Power spectrum density
REP	Reconstitution error percentage
RMS, rms	Root mean square
SNR	Signal to noise ratio
SOM	Self-organising mapping
STFT	Short Time Fourier Transform
TDC	Top dead centre
UGM	Unsupervised Gaussian Mixture
WT	Wavelet transform
WVD	Wigner-Ville Distribution

Chapter 1 Introduction

1.1 Background to condition monitoring of diesel engines

International Standards [1] provide a useful general definition of condition monitoring as: *"Detection and collection of information and data that indicate the state of a machine"*. The condition monitoring of diesel engines has a long development history from the earliest methods based on the experience and background knowledge of operators/technicians to modern methods using intrusive or non-intrusive sensors with diagnostic strategies, all of which have the common aim of improving or maintaining economic performance through increased availability and reduced component replacement costs.

Perhaps the most common traditional condition monitoring method for diesel engines is oil analysis. The major stated benefit of this method is that it can detect the cause of a problem [2], although it might be added that this is only provided that the problem manifests itself in either a change in the lubricant and/or the introduction of debris into the lubricant. Furthermore, oil analysis has no means of locating a fault, for example to a specific cylinder or bearing. Finally, the necessary analysis is normally performed at a laboratory in batches and requires specific equipment rendering it not particularly amenable to continuous or on-line monitoring. Many continuous condition monitoring methods rely on combinations of various intrusive sensors such as those for pressure, fuel flow and temperature. These methods are often indirect and non-specific (for example, a rise in temperature at a particular location could be caused by a multitude of possible faults) and they may necessitate modification of the engine for installation, and this is of particular concern, for example, in the use of in-cylinder pressure sensors.

Amongst the non-intrusive methods, vibration analysis is possibly the most common one used in machinery and diesel engines [3]. Measurement of airborne sound radiation has also shown a potential of monitoring diesel engines [4, 5]. Both vibration and sound have benefits in inspection-based condition monitoring applications because the installation of sensors is simple and the hardware requirement is of low to medium specification. However, both vibration and airborne sound signals are sensitive to low frequency environmental noise such as from machine resonances or ancillary

equipment. Finally, both methods are indirect, but do not have the potential benefit of source location, which would help to overcome this, and the problem of noise rejection.

Acoustic emission (AE) has been used successfully for condition monitoring of machinery and has proven to be a useful tool for monitoring a number of diesel engine conditions, for example combustion [6], head gasket leakage [7], exhaust valve leakage [8], injector faults [9] and liner scuffing [10]. AE is carried by a high frequency stress wave that propagates in materials and can be detected directly using sensors mounted externally on a surface of an engine. As such, it is insensitive to airborne noise and whole body vibration and the filters used in most preamplifiers select a frequency band of around 0.1 to 1 MHz. This means that all recorded information (even at lower frequencies) is confined to that carried within the stress wave, hence constituting a genuine source of AE. Because of the carrier frequency, AE offers extremely high temporal resolution in the signal and its propagative nature offers the additional facility to locate the source of the signal emission. It is to these benefits of AE monitoring that this thesis particularly relates.

The condition of diesel engines is typically identified by monitoring the change of features such as statistical and waveform parameters that can be extracted from the AE signal, itself obtained from a sensor placed close to the source. The use of such features with advanced methods such as pattern recognition would help to improve the accuracy of classification of the engine state, but this approach requires a training target, which implies information related to each fault or engine condition. Such data are expensive to acquire and, to be practicable, probably need to be developed by "on the job" learning. Here, we take a different approach, which is to try to locate as accurately as possible in both time and space, the "normal" AE signatures of the events in a complex machine such as a diesel engine. Since such a location also incorporates a knowledge of the mechanical function of the machine, deviations from "normal" behaviour offer immediate diagnosis without the need to train to specific faults.

AE has already proven to be capable of locating various types of sources such as crack extension, material deformation, mechanical impact and fluid flow activity. Successful applications of AE to locate sources include pipe leakage and structure integrity monitoring [11] and it has been observed by Steel and Reuben [12] that the localised fluid flow and impact events occurring in an engine essentially constitute a multi-source

problem to which a multi-sensor solution is appropriate. In order to achieve this, the propagation of AE in the object of interest needs to be carefully quantified. In general, AE wave propagation in a real structure is affected by reflection, refraction, mode conversion and attenuation [13, 14], which can distort the AE signal in its passage from source to AE sensor. As mentioned above, typical AE signals detected on diesel engines derive from multiple sources (such as those coming from exhaust valves, injectors, combustion, bearings and ancillary equipment) some of which overlap in time and/or space, and most of which are made up of combinations of localised fluid flow, sliding contact and impact. To locate and diagnose each source event more clearly, a sensor can be placed close to the source so that a high AE signal amplitude can be obtained and this, combined with time windowing, has been reported to be successful in both small [6] and large [8] diesel engines. Clearly, the ability to enhance signal resolution by locating sources in space as well as time will considerably enhance diagnostic outcomes.

1.2 Research objectives

A full 3-dimensional analysis of stress wave propagation phenomena in such a 3D complex asymmetric geometry (plate/shell-like structure) as an engine block with variations of thickness and boundaries is a complex mathematical problem with too many unknown parameters to be of value solving. This is even more the case when the effects of reflection, refraction and mode conversion, the unknown nature of the source disturbance, and the imperfect nature of transduction are taken into account. This research will therefore mainly concentrate on using effective wave attenuation and effective velocities in order to obtain a tie-in between experimental measurements and signal analysis, a pragmatic and semi-empirical approach.

The research objectives were therefore:

1. To develop a simple model for wave propagation based on identifying group velocities and attenuation coefficients for simple cast iron shapes and more complex geometries such as cylinder heads and cylinder blocks.
2. Based on the velocities and attenuation coefficients, to develop a means of segmenting the signals from running engines in the time and space domains in

order to improve the resolution of multi-source signals, called "spatial reconstitution"

1.3 Research methodology

So far, AE wave propagation on diesel engines has not been studied, neither for attenuation nor for time of flight. In this study, experimental data were collected from various simple cast iron shapes and from more complex objects by introducing simulated sources (pencil lead breaks) at various locations on the objects and recording the result simultaneously in an array of sensors at various distances from the source. Particular attention was paid to the time-of-flight and attenuation mapping on a small high speed direct injection (HSDI) engine for later use on a sister engine whilst running. In order to examine scaling effects, some limited studies were also carried out on a very large two-stroke marine diesel engine. Various methods of signal processing in the time and frequency domain were carried out on the acquired signals in order to obtain a small set of wave speeds and attenuation factors for spatial reconstitution.

1.4 Thesis outline

This thesis is organised in 8 chapters, the contents of which are summarised as follows.

Chapter 1: Introduction

This chapter introduces the general background of condition monitoring of diesel engines and the place of AE monitoring in this context. The objectives of the research and the claimed contribution to knowledge are also identified.

Chapter 2: Literature review

This chapter reviews critically the published literature on condition monitoring of diesel engines and other machinery using AE and other types of sensor, as appropriate. The various simple and advanced diagnostic methods used for fault monitoring of diesel engines are also reviewed, as are the techniques of AE source location. The chapter concludes with an identification of the thesis topic in the light of current knowledge of AE monitoring of machines.

Chapter 3: Acoustic emission wave propagation

This chapter describes the general physics of AE wave propagation including wave types, wave propagation speed, effects of AE wave attenuation, and application of source location using AE. A review of published work specifically on AE wave propagation is provided in this chapter. Particular attention is paid to studies of attenuation of AE wave energy, and methods of determining attenuation factors.

Chapter 4: Experimental apparatus and procedures

This chapter describes the experimental apparatus, data acquisition methods, experimental set-up and experimental procedure for the laboratory and industrial tests on various cast iron blocks and diesel engines using simulated sources and engine running sources along with the relevant data handling and acquisition strategies.

Chapter 5: AE transmission tests

This chapter presents the experimental results and analysis applied to determine attenuation factors, transmission paths and wave speeds for the various test objects and diesel engines. Results obtained using simulated sources are also compared and discussed.

Chapter 6: Engine running tests

This chapter presents and discusses the experimental results and analysis techniques applied to determine attenuation factors for engine running sources with a view to determining the simplest useful array and propagation description consistent with achieving time and space segmentation on running engines.

Chapter 7: Application of source location and signal reconstitution in diesel engines

The development of source location using energy-based techniques is discussed in this chapter. Results of the traditional velocity-based techniques and the proposed technique will be compared using the experimental data obtained from the tests using simulated and engine running sources on the cylinder head of the small diesel engine, with particular emphasis on injectors and exhaust valves. The signal reconstitution is also demonstrated showing improved resolution of multiple-source signals on the small and large diesel engines.

Chapter 8: Discussion, conclusions and future work

A brief summary of the work, the results presented in the thesis, the main findings and achievements of this research are given, along with recommendations for possible future studies.

Contribution to knowledge:

As far as the author is aware, detailed attenuation and time-of-flight mapping for AE wave transmission on such complex objects as engine blocks has not previously been attempted. Furthermore, the location of multiple sources in a semi-continuous signal, where the potential sources are only known generally in time and space, is, to the author's knowledge, a significant contribution. The overall outcome of improved diagnosis based on segmentation of the signal in time and space is therefore the specific area in which a contribution to knowledge is claimed.

Bibliography (publications by the author relating to the work contained in this thesis)

1. Nivesrangsan, P., Cochrane, C., Steel, J. A., and Reuben, R. L., "AE mapping of engines for spatially located time series," *The 25th European Conference on Acoustic Emission Testing, EWGAE 2002*, Vol. 2, 2002, pp. 51-58.
2. Nivesrangsan, P., Steel, J. A., and Reuben, R. L., "AE mapping of engines for spatially located time series, Part I: Preliminary studies," *Mechanical Systems and Signal Processing* (In Press, 2005, Ref. YMSSP:1747).
3. Nivesrangsan, P., Steel, J. A., and Reuben, R. L., "AE mapping of engines for spatially located time series, Part II: Spatial reconstitution," (Submitted to *Mechanical Systems and Signal Processing*).
4. Nivesrangsan, P., Steel, J. A., and Reuben, R. L., "AE mapping of engines for spatially located time series, Part III: Source location," (In preparation).
5. Douglas, R. M., Nivesrangsan, P., Robertson, A. I. F., Brown, E. R., Steel, J. A., Reuben, R. L., and Fog, T. L., "Acoustic emission as a tool to reveal diesel diesel injector performance," *Proceeding of the 17th International Conference on Condition Monitoring and Diagnostic Engineering Management, COMADEM, Cambridge, UK,* 2004, pp. 315-324.

6. Robertson, A. I. F., Douglas, R. M., Nivesrangsan, P., Brown, E. R., Steel, J. A., and Reuben, R. L., "Source identification using acoustic emission on large bore cylinder liners," *Proceeding of the 26th European Conference on Acoustic Emission Testing, EWGAE, Berlin, Germany*, 2004, pp. 637-643.

7. Lim, T., Nivesrangsan, P., Corney, J. R., Steel, J. A., and Reuben, R. L., "Predicting AE attenuation within solids by Geometric Analysis," *International Conference on Shape Modeling and Applications SMI-05, MIT, USA*, 13-17 June 2005 (Submitted).

Chapter 2 Literature review

2.1 Introduction

In general, condition monitoring relies on selecting a measurable parameter which will change when the condition of a machine deteriorates [15], an extremely wide definition covering sensor selection and signal processing and interpretation. Fault detection is one of the main reasons for condition monitoring of diesel engines although it is sometimes of interest to detect running conditions. The most common diagnostic techniques are based on vibration analysis [3] and lubrication analysis [16]. However, recently, there has been some effort in developing AE-based diagnostics because of its relatively high signal to noise ratio, where "noise" can be defined as any part of the signal (such as whole body, low frequency movement) which is not of immediate relevance to the condition being monitored. This chapter first reviews the use of AE monitoring of diesel engines and other machinery for various fault conditions in order to establish the state of knowledge against which this current work is set. Next, the processing techniques that are used to extract information from the AE signal, such as statistical features and waveform features are discussed, along with how these are used to arrive at an assessment of machine condition. The final section summarises the state of knowledge and then identifies the research target.

2.2 Condition monitoring of diesel engines and machinery

This section is concerned with identifying the state of knowledge of AE monitoring of diesel engines and machinery. The first part is concerned mainly with AE monitoring for various common engine fault conditions such as valve leakage and abnormalities in combustion or injection processes, although other monitoring techniques using various types of sensors to diagnose faults in diesel engine are also described and their relative advantages and disadvantages discussed. Finally, examples of AE monitoring of machinery, and associated fault diagnosis are discussed, including pumps, seals, gears, bearings and turbines.

2.2.1 AE monitoring of diesel engines

Condition monitoring of diesel engines using AE has been introduced over the past ten years benefiting from the high signal to noise ratio and limited low frequency background noise associated with its high frequency carrier wave (0.1-1 MHz) [17]. AE has been used for fault detection in both small and large marine engines, being sensitive, for example, to combustion faults [6], head gasket leaks [7], exhaust valve leaks [8], injector faults [9] and liner scuffing [10].

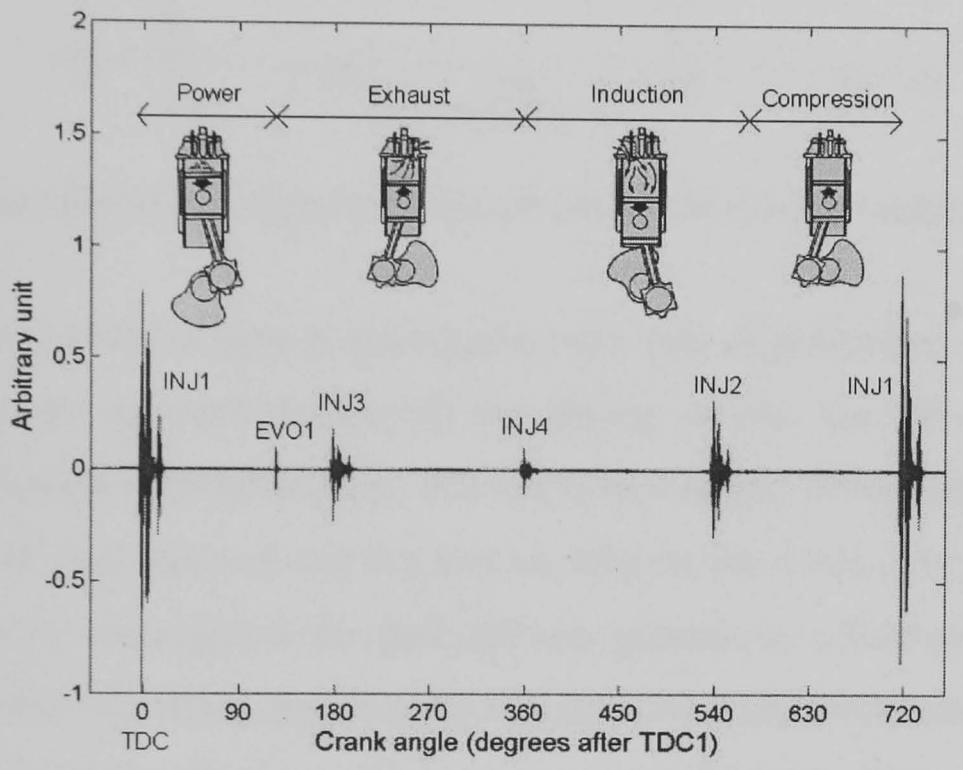

Figure 2.1: Example of AE signal and related processes recorded at cylinder no.1 of a four-stroke diesel engine.

In the four-stroke diesel engine cycle, each stroke (induction, compression, power and exhaust) consists of a series of processes, which are related to mechanical movement and fluid flow activities in the engine, i.e. those coming from the injectors, the exhaust valves, the inlet valves and other ancillary equipment. Figure 2.1 shows a typical raw AE signal obtained from the cylinder head of a small four-stroke, four-cylinder, diesel engine. The INJ, EVO and TDC represent injector event, exhaust valve opening event and top dead centre, respectively. In the two-stroke diesel engine cycle, the strokes involve compression and expansion (power). Each stroke consists of a series of mechanical and fluid flow processes. The induction and exhaust processes are not separate from each other and interact in the scavenging process which occurs around bottom dead centre (BDC). Examples of AE events related to mechanical and fluid flow processes of the two-stroke cycle can be seen in Figure 2.2 and here events on a single cylinder, INJ, EVO and EVC (exhaust valve closing) are visible.

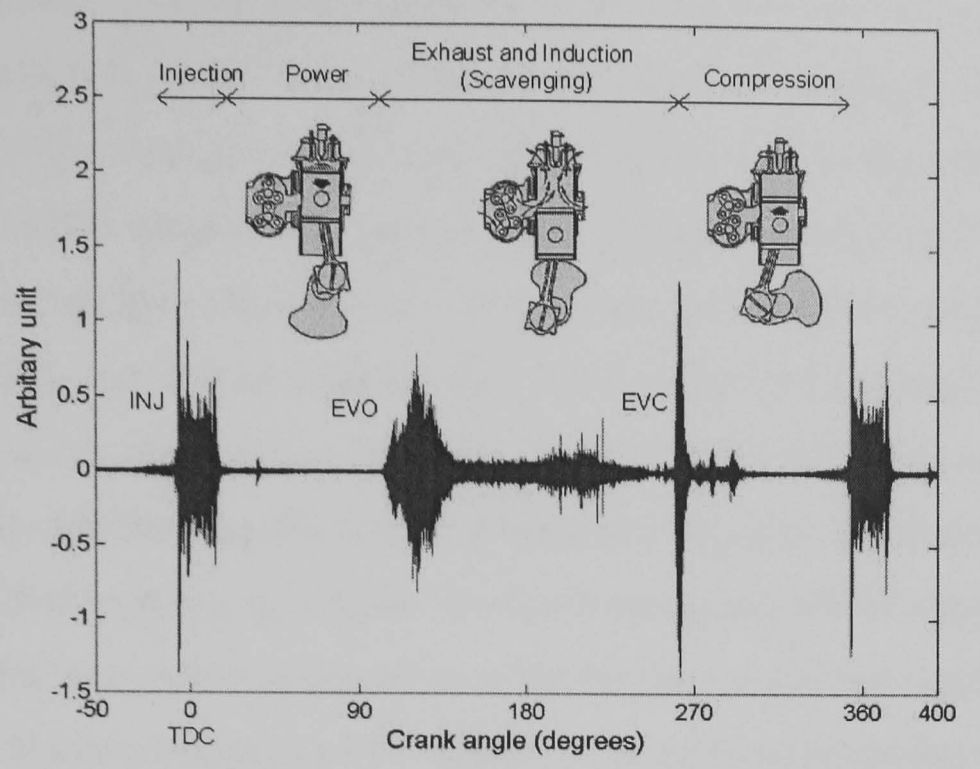

Figure 2.2: Example of AE signal and related processes in a two-stroke diesel engine.

The power output of the engine is governed by the sum of the power stroke intensities and is an indicator of performance. In the power stroke, the two main processes involved are injection and combustion, and the power output of the engine is controlled by the amount of fuel injected and the precise time in the cycle over which it occurs. Gill *et al* [6] have investigated the fuel delivery process in a four-stroke, high speed direct injection (HSDI) diesel engine with two induced fault conditions; fuel starvation in one cylinder and reduced injector discharge pressure, both of which affect directly the power output of the engine. In that work, data were acquired from an AE sensor placed at various positions with a sampling frequency of 50 kHz along with an engine timing signal. It was found that a sensor positioned on the camshaft side of the engine, as close to the point of combustion as possible, could be used to examine the valve mechanism movement and fuel combustion characteristics. However, sensors placed on other parts of the engine had more complex signals which may be associated with other engine-driven components. Gill *et al* [6] reported that the signal associated with the normal running condition showed clearly the "combustion" event for each cylinder along with the associated valve actions over the entire engine cycle. They also noted that attenuation of the signal increased as the distance from the source increased but did not investigate this quantitatively. They suggested splitting the entire signal into four time bands relating to the combustion events, then calculating the energy content of each band and averaging over ten cycles. However, they did not mention the duration of the time bands used in their calculation. They noted that the signal energy was found to be remarkably consistent between cycles, but they did not give more detailed analysis of

this result. However, Frances *et al* [18] have found that the variability of AE energy of each cylinder within the combustion period, which was calculated from rms AE signals (crank angle window size around 200 degrees from 300 to 500 degrees) acquired from a medium speed, turbocharged, four-stroke, eight-cylinder marine diesel engine using an AE sensor placed on the cylinder head exhaust port, was small but could vary between the cylinders. Gill *et al* [6] also reported that, for the case without combustion, i.e. when the fuel supply to the cylinder was disconnected, the part of the signal in the combustion window for that cylinder was eliminated completely. Equally, a reduction in the setting for injector discharge pressure affected the combustion part of the signal and the initial point of injection was earlier in the cycle as the fuel pump did not require as much time to build up the lower pressure, and the reduction in combustion energy was found to be roughly proportional to the reduction in fuel discharge pressure. They concluded that calculating the cylinder energy with careful time-windowing provided an indication of the condition of the combustion process on a per cylinder basis.

The power output of engines has also been investigated by Douglas *et al* [19] who found a relationship between AE energy and the variation of the Instantaneous Crankshaft Angular Velocity (ICAV) waveform [19]. In that work, experiments were carried out on two large, low-speed, two-stroke, marine diesel engines of similar design; engine no. 1 was a 10 MW, 7-cylinder, 600 mm bore, 1740 mm stroke engine used for 50 Hz electrical power generation operated at a single speed; engine no. 2 was a 7.5 MW, four-cylinder, 500 mm bore, 2220 mm stroke marine diesel engine loaded by a water-brake dynamometer operated at various speeds. Rms AE signals were acquired simultaneously with a sampling frequency of 20 kHz over a range of engine operating conditions from an AE sensor placed on the cylinder cover, at a position close to the injectors, the exhaust valve housing and the combustion chamber. A shaft encoder gave a top dead centre (TDC) marker with reference to cylinder no. 1 and also gave 1024 and 2048 pulses per revolution on engines nos. 1 and 2, respectively. The ICAV waveform was obtained from the shaft encoder signal, which exhibited cyclic variation about the mean engine speed. A decrease in angular velocity indicated the compression stroke of each cylinder whereas an increase in angular velocity indicated the expansion stroke (combustion). For engine no. 1, peaks in the frequency spectra of the ICAV waveform were at 4, 7 and 66 times that of the crankshaft speed. The peak at 66 times running speed was associated with a generator consisting of 22 pairs of poles for 3-phase electricity production. It was found that the number of peaks in the ICAV waveform

was associated with the number of cylinders in the engines. They showed that the standard deviation calculated from the ICAV waveform of each cycle for both engines increased with load. Rms signals in the time domain were mapped onto the crank angle domain so that the AE events associated with the entire engine process could be identified. They noted that there were various types of AE source associated with the fuel injection/combustion event; diesel fuel pressure build up prior to injection, the opening/closing impacts associated with the injector spindles, high-pressure discharge of fuel into the chamber, and fuel ignition and combustion. They also found that the timing of the beginning and end of the injection event changed with load (Figure 2.3) and that AE energy in the injection event could be used as an indication of power output. The rms signal acquired during the injection/combustion event, over a crank angle window from -10 to $+30$ degrees (40 degrees) relative to TDC of each cylinder was used to calculate the rms AE energy, which increased with load (power output). They concluded that both the rms AE energy and standard deviation of the ICAV waveform could be used as power output indicators.

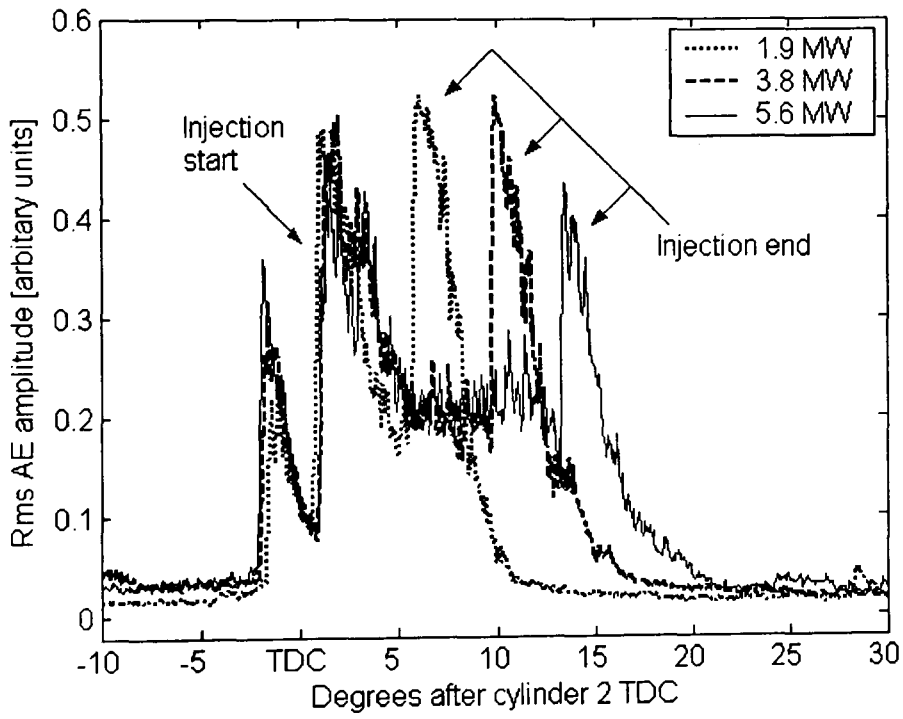

Figure 2.3: Example of injector event measured from various load conditions on a large two-stroke diesel engine using rms AE signal (After Douglas *et al* [19]).

Both the injection and the combustion process have been examined in more detail with regard to mechanical and fluid flow phenomena by Gill *et al* [9]. They studied fuel injection equipment faults of a small HSDI diesel engine using AE. Faults were diagnosed using data acquired from an AE sensor, a needle lift sensor, an in-cylinder pressure sensor and a shaft encoder (reference signal). Two different fault conditions were examined on a 76 kW, four-cylinder, Perkins T1004-4 HSDI diesel engine with

Bosch KD fuel injectors operated by a Bosch EPVE rotary fuel pump in which the injector discharge pressure was reduced from 258 bar to 165 bar in all cylinders and the injector discharge pressure reduced to 100 bar in cylinder 4 (the instrumented cylinder). The engine speed was varied from 1000-2500 rpm. By comparing the mean and standard deviation of the rms energy of all tests, it was found that the timing of the increase of fuel line pressure and the time at which the injector needle becomes fully open could be detected using AE and these times advanced while injector discharge pressure reduced.

Gas leakages from the head gasket or exhaust/inlet valves during the compression and power strokes are important because they reduce the cylinder pressure so that the engine is unable to produce its maximum power output. The example of a head gasket leakage has been studied by El-Ghamry *et al* [7] on a 76 kW, four-cylinder, four-stroke HSDI diesel engine using a variety of sensor positions. The AE signal detected from a sensor placed on the cylinder head was found to be the most complicated consisting of a number of different peaks associated with valve actions and combustion. They also observed that sensors placed on the cylinder block recorded the combustion events as being of higher amplitude than the valve events. For the head gasket leak, it was found that the peak AE at the combustion event of the leaking cylinder was considerably higher and broader. From this, they concluded that AE is sensitive not only to mechanical impacts and the shock loading associated with the combustion process, but also to high-speed gas flow, and that the combustion signal modulates the high-frequency leakage signal.

Detailed AE analysis has also been applied to large two-stroke marine diesel engines for example to investigate a gas flow leakage from an exhaust valve (Fog *et al* [8]). The causes of exhaust valve leakage may be accretion of deposits (combustion particles) on the valve sealing face or material damage from knocking of the exhaust valve. An rms AE signal was acquired from a sensor placed on the valve housing with various sized grooves cut in the face of the exhaust valve. For normal valve actions, the pattern of the events in the signal relating to valve opening/closing remained unchanged with engine speed but some events seemed to change with engine load (Figure 2.4(a)). In addition, Fog *et al* [8] observed that the rms AE signal associated with valve leakage showed abnormalities on either side of the combustion event (Figure 2.4 (b)) and that the AE

energy associated with the leakage process increased as the cross-sectional area of the groove increased.

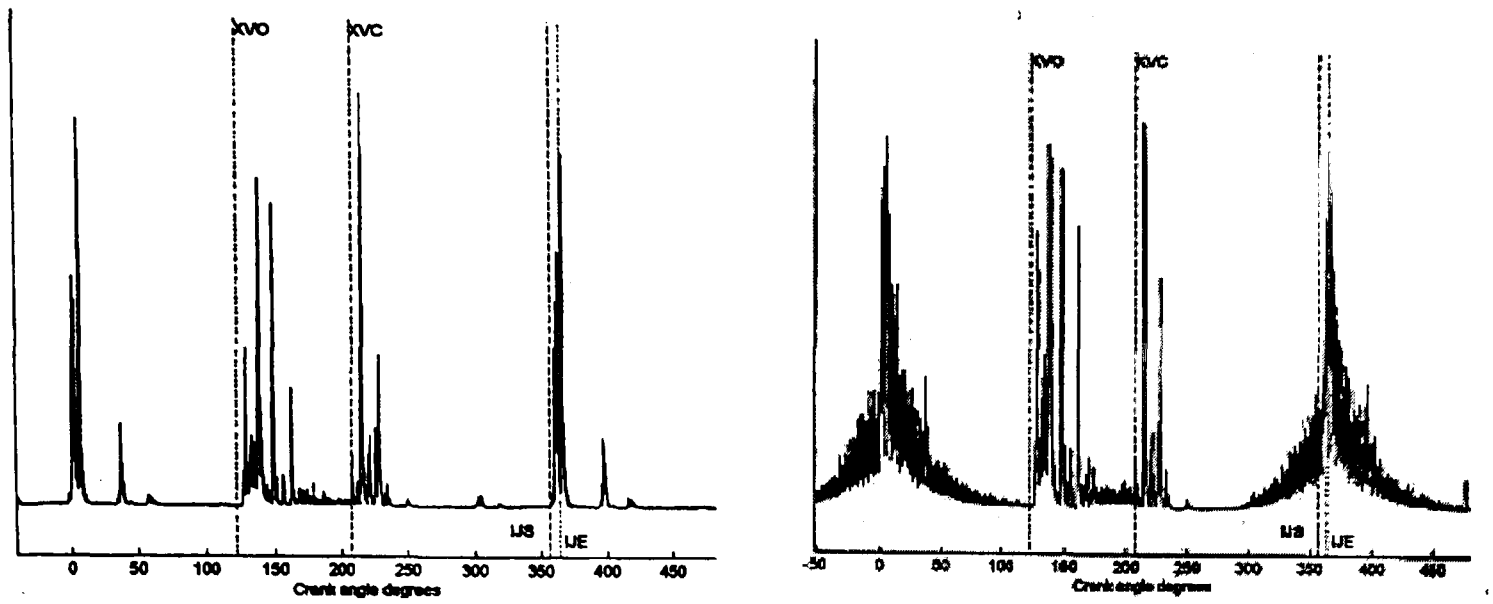

(a) Normal condition

(b) Exhaust valve leak

Figure 2.4: Rms AE signal under 25% of full load with normal and exhaust valve leak conditions and associated events in a two-stroke diesel engine cycle (From Fog *et al* [8]).

The attenuation of AE is a natural phenomenon where amplitude decreases inversely with source-sensor distance [11], and will be discussed in more detail in the next chapter. In all of the above mentioned work, it has been noted that attenuation of some events can be seen relative to others in the AE signals and that higher signal amplitudes are obtained from a sensor placed closer to the source and this offers the possibility of source location. As yet, no systematic studies of this attenuation have been made on engines, but it is the subject of part of the work carried out here.

Piston ring/cylinder liner interaction is another area where diagnostically significant AE might be generated. Liner scuffing, which can affect large-bore engines, can reduce the engine compression ratio and the power output because of the increase of piston ring blow-by. The scuffing phenomenon is associated with the transfer of cylinder liner particles to piston ring surfaces due to inadequate lubrication and high temperature at top dead centre (TDC). Pontoppidan *et al* [20] have investigated lubrication condition changes in the cylinder liner of a large two-stroke marine diesel engine using AE under various operating conditions. Rms AE signals were acquired from two AE sensors placed on the cylinder liner and cover. It was shown that the AE changes when the lubrication condition is changed. Shuster *et al* [10] carried out an experimental study of piston-ring/cylinder-liner scuffing phenomena using AE. In this study, segments of

piston ring and cylinder bore were used to reproduce scuffing phenomena in a standard sliding wear rig. By using AE, it was possible to produce results relating to the original source, which may be caused by, for example, asperity contact, micro-crack initiation and growth and plastic deformation and flow. The wear phenomena may be reproduced by an experiment, but, since there is no cylinder pressure, the potential signal from blow-by is missing. The overall results indicated that the detected rms AE signal provided more information about the scuffing phenomenon dividing it into three different levels; scuffing initiation, irreversible scuffing and severe scuffing. In particular, the rms AE signal was sensitive to scuffing initiation through its sensitivity to friction coefficient and it was shown that the first peak of spikes in the rms AE signal was associated with the initial iron particles transferring from cylinder liner to piston ring surfaces which was confirmed using scanning electron microscopy (SEM).

Douglas *et al* [21] have investigated piston ring/cylinder liner interaction on a large two-stroke, slow speed, marine diesel engine under normal operation using AE. Raw AE signals were acquired at a sampling frequency of 2.5 MHz from two AE sensors placed on the exposed area of the upper (position G) and lower (position H) part of the cylinder liner as seen in Figure 2.5. They showed that it was possible to detect sliding contact between the piston rings and the cylinder liner and related blow-by or exhaust valve leakage during the compression and expansion strokes. They observed peaks at fuel injection start and end with mechanical impacts during the injection period, attributed to the piston ring/cylinder liner contact. The scavenging process ends with closure of the exhaust valve, and peaks during the scavenging period were seen at both sensor positions. It was observed that, during the compression stroke, when the piston ring-pack was moving toward TDC, and the in-cylinder pressure and the sealing forces exerted on the piston rings were increasing, the AE increased accordingly. During the expansion stroke, the combustion of the fuel increases the in-cylinder pressure resulting in a higher contact force between rings and liner again leading to increased AE. In this engine, an oil groove located on the inner surface around the lower part of the exposed area of the cylinder liner was used to aid the circumferential spread of injected lubricating oil. When the ring-pack passed over the groove (around 55 degrees after TDC), the resulting fluid and mechanical activities gave rise to increased AE, and this was seen at both sensor positions. This event could be seen clearly from the signal detected at position H and could be seen somewhat attenuated in the signal detected at position G.

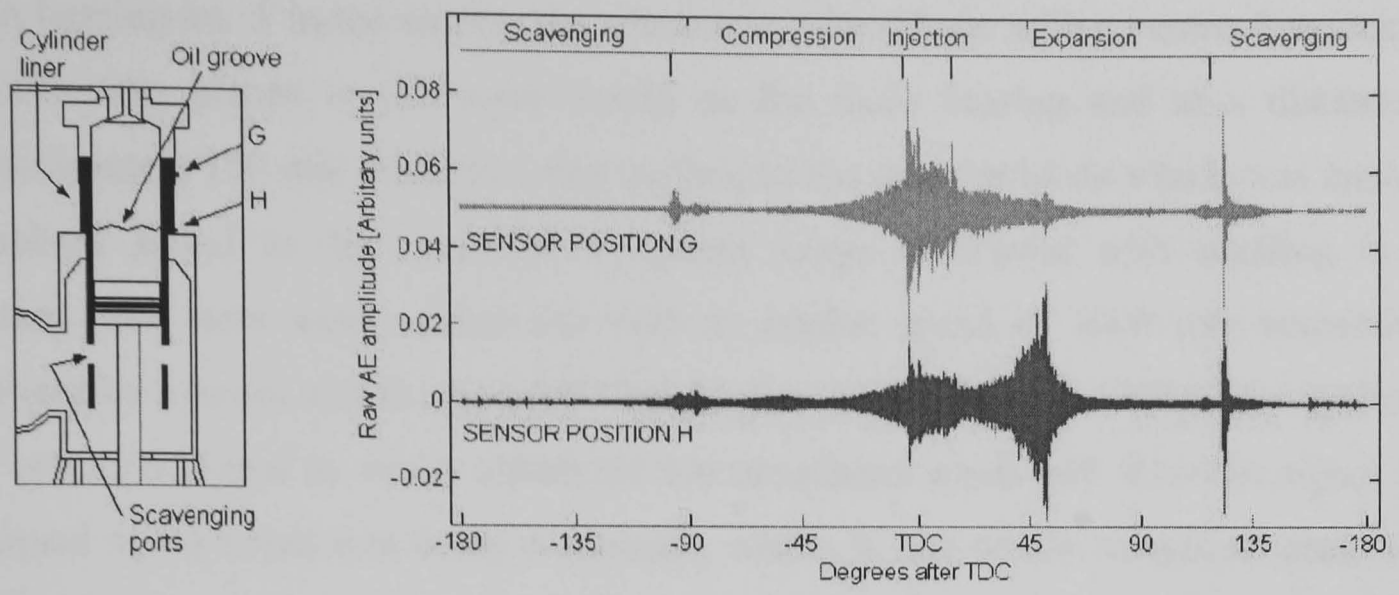

Figure 2.5: Raw AE signals measured from the upper (Position G) and lower (Position H) part of a large two-stroke diesel engine (From Douglas *et al* [21]).

The pressure waveform during the combustion process is a valuable parameter for monitoring the performance of diesel engines. The obvious direct method involves using a through-cylinder-head pressure sensor to measure directly in the combustion chamber. In practice, this method is inconvenient because it requires one pressure sensor per cylinder, requires modification of the engine, and the sensors themselves are expensive and of limited life. Reconstruction of cylinder pressure has been achieved using the vibration response measured from externally mounted sensors on diesel engines [22] and the technique has been extended to use AE by El-Ghamry *et al* [23]. They used a smoothed, enveloped AE signal, in which the raw signal was divided into two sections; a compression part and an expansion part. The compression part of the pressure signal was reconstructed directly by using a polynomial fit. For the expansion part, an ARX model was applied to the smoothed, enveloped AE signal and mapped to the pressure signal with a stable model. However, this method required a separate model for each engine speed and load condition. More generic success was achieved using the rms AE signal and a complex cepstrum model to accurately reconstruct the cylinder pressure directly.

Abnormal wear of rotating components such as bearings is also an important fault, which can affect engine performance, and early detection, for example of abnormal lubrication, can prevent severe damage. Koike *et al* [24] have used the term "acoustic emission" in a somewhat literal sense, to describe the use of an ultrasonic microphone to detect abnormal wear of the main engine bearings. In their study, a four-cylinder, in-line, double overhead camshaft (DOHC) engine was used in laboratory test and a solenoid valve was installed into the main oil gallery and used to stop oil delivery to

main bearing no. 5 in the engine. An ultrasonic microphone with a centre frequency of 80 kHz was placed at the same height as the main bearing and at a distance of approximately 150 mm from the outer surface of the cylinder block which was intended to record sound in the ultrasonic frequency range associated with scuffing in the bearing. The tests were carried out with an engine speed of 6000 rpm respectively powered by a motor and firing at full load. High-pass filtering (>50 kHz) was applied to the recorded signal to avoid effects of low-frequency noise and then the signal was analysed using count rate every 5 seconds, which is one of the waveform parameters traditionally used in AE analysis. At the end of the test, scuffing marks were noted on the surfaces of the relevant bearing, and it was concluded that ultrasonic sensors were able to detect the onset of abnormal wear using count rate as an indicator.

Apart from AE, other techniques for fault detection and diagnosis include vibration, acoustic microphones, temperature, speed, torque and cylinder pressure measurement. An example of fault detection in diesel engines using vibration signals has been demonstrated by Long and Boutin [3]. They pointed out that there were three types of sources that gave rise to vibration signals; mechanical impacts which produced sharp vibration patterns; gas leaks which occurred over a longer period of time and had a lower amplitude; and roughness or friction which was described by a noisy low amplitude pattern. Vibration signals in the study were mapped from the time domain onto the crank angle domain so that the events associated with processes in the engine cycle could be compared. The condition of the diesel engine was identified by comparing the detected vibration pattern with the normal vibration pattern or baseline vibration pattern (Figure 2.6(a)) to check the presence of expected events and the absence of any other events (Figure 2.6(b)). This study showed the detection of various potential faults from vibration patterns, for example piston slap, liner scuffing, excessive wrist pin clearances, worn or improperly loaded rings, collapsed exhaust lifter, improper tappet setting, valve bouncing, damaged seat or lifter, exhaust valve not seating properly and leaking and faulty fuel injection, although, it was not made clear where the accelerometer should be placed on the engines to acquire vibration signal associated with above-mentioned faults. Long and Boutin [3] also mentioned that a Severity Index (SEV) could be used to indicate the engine condition, determined by a ratio between measured vibration and a product of baseline vibration and threshold factor in each crank window associated with the processes of the engine, the higher the SEV (>1) the more severe the problem. A smaller value of SEV (<1) suggested that an

expected event was missing. An example of a diagnostic report was shown where the SEV based on energy or peak values in a specific crank window, around 300-430 degrees after TDC, could be used to identify possible faults such as upper liner scoring and excess pin clearance, but it did not show any detailed analysis of the SEV. Most of the faults in the study could be identified clearly for an impact source i.e. piston slap (Figure 2.6(b)). However, Fog *et al* [25] and Gill *et al* [26] have also noted that the vibration signal is normally sensitive to the mechanical activity of the machine component involved but have found AE to be at least as reliable, and often more so.

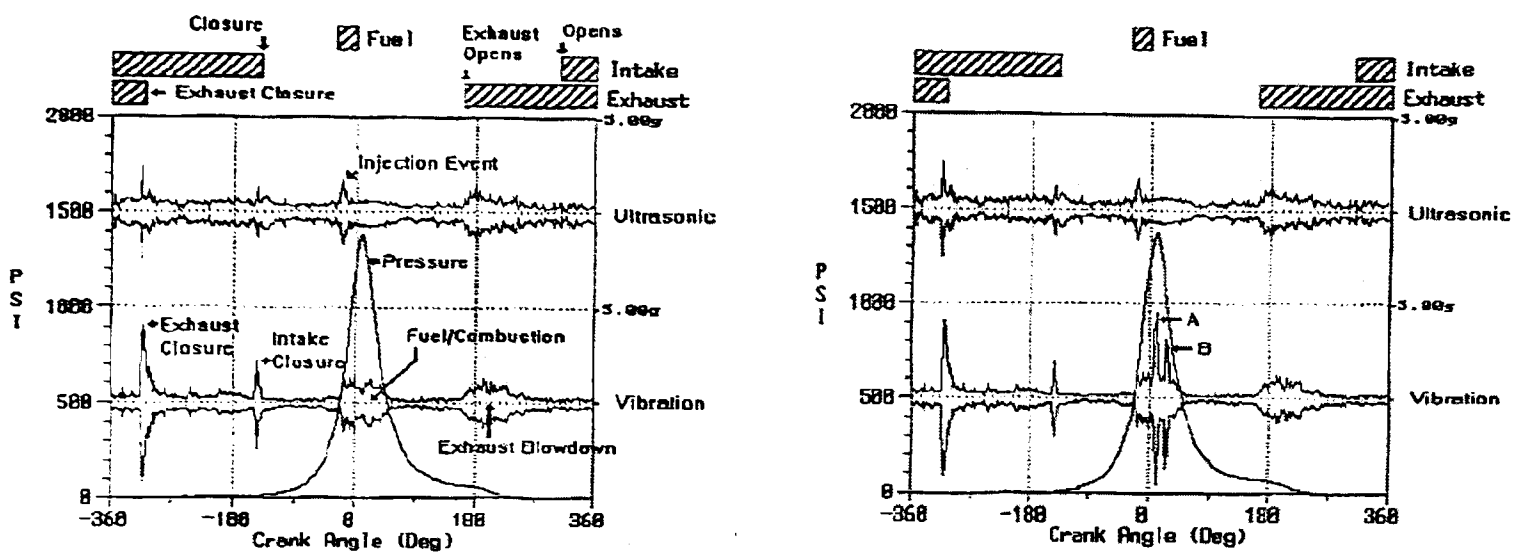

(a) Normal condition

(b) Piston slap (A & B events)

Figure 2.6: Example of vibration signals under normal and fault conditions (From Long and Boutin [3]).

The condition monitoring of diesel engines has also been achieved using airborne sound to detect such faults as compression ratio reduction, injector opening pressure reduction and internal fuel leakage [4, 5], all of which affect the combustion process directly. Gu *et al* [4, 5] have carried out experiments in a laboratory on a 50 kW four-stroke, four-cylinder, direct injection diesel engine using a microphone to record sound (Figure 2.7) and a hall effect probe placed on the engine flywheel to record the TDC position of cylinder no. 1. By determining an average rms value and a variance of the rms of the multi-cycle signal, they could detect faults and also estimate the severity of each fault type, although neither feature could be used to locate faulty cylinders. Also, this airborne sound technique was ineffective at the lower frequency audio band (below 10 kHz) due to the effect of room resonance that distorted the signal, but, for higher frequency bands (between 10-50 kHz), this technique was relatively successful.

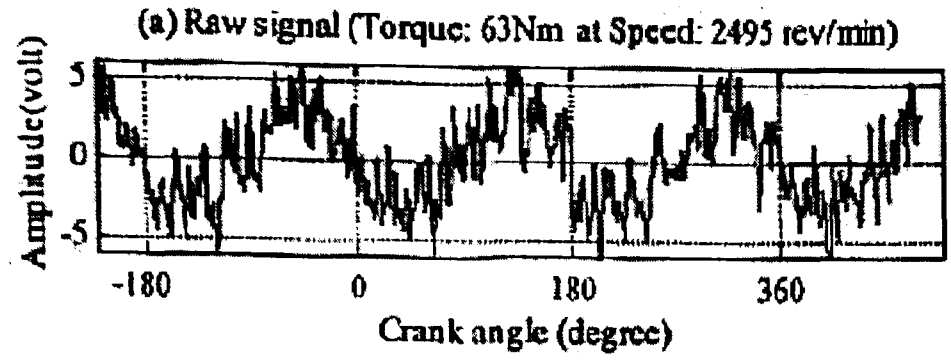

Figure 2.7: Example of an airborne sound signal (From Gu *et al* [4]).

Other examples of fault monitoring on diesel engines include the use of some of the traditional sensors, such as fuel flow meters, air flow meters, pressure sensors, TDC position sensors and crank angle position sensors to examine the engine performance. For example, Twiddle and Jones [27] have investigated injector faults and inlet valve faults using conventional sensors and have diagnosed faults based on load estimates calculated from frequency analysis of the speed signal and from the air-fuel ratio. Faults in diesel engine cooling systems have also been investigated by Twiddle and Jones [28] including such conditions as thermostatic valve failures (in the closed or open position), radiator faults and low coolant flow rate, all identified by measuring coolant flow rate and temperatures in the cooling system. However, both of these techniques required modification of engines for sensor installation and necessitated more detailed background models (for example, a thermomechanical mode of the cooling system) of the engine cycle than those cases using AE and vibration, which might inhibit their generic application.

This section has shown that AE, like a number of other vibration-based techniques (such as the use of accelerometer or microphone) is sensitive to the essential processes of sliding contact, gas flow in confined spaces and impact which make up the operation of a diesel engine whether or not it is abnormal (Figures 2.1-2.5). Furthermore, a wide range of specific faults have been successfully detected using AE. Whereas the physics of propagation of AE suggest that its structure-borne nature and high frequency carrier would make it less susceptible to noise than acceleration or airborne sound, there are relatively few studies where a direct comparison has been made. One advantage of AE, namely its ability to locate sources, has yet to be exploited in the condition monitoring of engines.

2.2.2 AE monitoring of machinery

AE monitoring has a future not only in the diesel engine application but also on other machinery because of its sensitivity and its capability to reveal more details than many other measurands of mechanical and fluid flow phenomena as well as the physical processes such as friction, impacts and wear which typically occur in machines and increase with deterioration of the machine condition. AE monitoring has been used in quite a number of machinery applications, currently focused on fault detection. In this section, examples of AE monitoring will be given in order to help to illuminate how mechanical and fluid mechanical processes in pumps, compressors, turbines, bearings and gears give rise to AE and how such signals can be used in a deterministic way to assist condition monitoring.

The development of detection of incipient cavitation in pumps is one such example, being a phenomenon which can cause damage to internal surfaces of fluid carrying components and can lead to reduction in bearing life and failure of seals. Neill *et al* [29] investigated cavitation in both laboratory scale and industrial scale centrifugal pumps and concluded that the rms AE signal could be used to examine cavitation with the degree of cavitation being identifiable from the detected signal using frequency analysis. They also pointed out that the further the sensor was from the cavitation site, the weaker the detected signal was, although there were further complications according to whether the AE was structure or fluid-borne.

Miettinen and Siekkinen [30] used AE to monitor sliding contact behaviour in the double-acting mechanical face seals of a 15 kW centrifugal pump. The mechanical face seal works normally in the boundary lubrication region, and, typically, the failure of these seals may be caused by the disappearance of cooling water in a contact and cavitation in the lubrication region due to the resulting high temperature. Because of the potentially high attenuation, AE sensors had to be placed close to the sliding contact in order to obtain a strong enough signal. It was shown that, using rms AE energy, it was possible to detect a leaking seal, vaporisation, dry running and cavitation in the face sliding contact, although no analytical analysis was presented to distinguish between the different cases. Miettinen and Siekkinen [30] mentioned that the value of rms AE energy characteristic of a leaking seal fault was smaller than for the normal running condition by approximately 25%. For the case of vaporisation, it was observed that the

rms AE energy increased with temperature and this was related to increased vaporisation. For the case of dry running, AE energy increased substantially when the seal face contact temperature exceeds 200°C. Ferguson *et al* [31] have also studied failure of mechanical seals in pumps using AE. In this work, a laboratory test rig for mechanical seal failure was developed, consisting of a 43 mm unbalanced mechanical seal, housed in a stuffing box and driven by an electric motor. Two configurations were investigated with various test conditions; a hard/soft combination of sintered silicon carbide/antimony loaded carbon which was used to detect the increased face contact associated with increasing pressure and a hard/hard combination of two sintered silicon carbide faces which was used to detect fluid film breakdown as the temperature was increased. Rms AE and raw AE signals were acquired from an AE sensor placed on the seal housing. The mean and variance of the amplitude of the rms AE signals under normal conditions were calculated for both configurations and were set as a datum value. It was shown that the mean and variance could be used to monitor both test conditions. In the case of the increase of face contact, both features increased with increasing pressure. In the case of increasing temperature, both features dropped initially and then slowly increased with temperature, and it was suggested that the initial drop might be due to the reducing solubilities of oxygen and nitrogen in water as temperature increased, whereas the subsequent increase could be due to increased vaporization within the seal gap. Frequency analysis was also applied to the rms signal and it was observed that frequency analysis could be used to detect pressure increase, but not the temperature increase.

The failure of compressor valves due to spring failure, valve face damage or valve seat damage can cause reduction in compressor efficiency. Gill *et al* [26] demonstrated the diagnosis of plate valve failure on a small, two-cylinder, reciprocating compressor using rms AE signals which were obtained from an AE sensor placed on the cylinder head studs using an aluminium clamp along with a shaft encoder signal and an accelerometer (fitted in the same axis as the piston). It was shown that AE monitoring was capable of detecting various plate valve fault conditions by determining the change in timing of valve operation when compared with the normal condition (no fault), such as a leaking discharge valve seat, unseated discharge valve plate, fatigued inlet valve spring and valve flutter. It was also observed that the vibration data could be used to detect mechanical events in the cycle such as the valve opening time, but not, the fluid flow noise generated by the leaking of gas into the cylinder. The ability of AE to detect

abnormal gas flow within the compressor has proven to be transportable to much larger industrial compressors [32]. For example, valve failure and failure of the packing in the stuffing box on a two-stage, chemical process, gas hyper-compressor of output pressure 3200 bar has been investigated by El-Ghamry *et al* [7] using AE. In that study, a rms AE signal was acquired from an AE sensor placed on the cylinder end face along with a TDC signal. It was shown that AE could be used to detect automatically both faults. Typical valve opening events under normal conditions could be identified in the recorded signal by using the TDC signal, and two major peaks were observed; the higher peak represented the opening of the delivery valve and the lower peak represented the opening of the suction valve. In the case of valve failure, the pattern of the rms AE signal was similar to the normal condition but it could be seen that there was a higher amplitude and more variable energy content of both valve events. For packing failure, two major peaks (normal) were combined into one wider peak (fault). To diagnose fault conditions, they divided the rms signal into five segments; the opening of the delivery valve, the high-pressure part of the compression stroke, from the end of the compression stroke until the opening of the suction valve and the suction stroke. By calculating mean and variance of rms AE for each segment of the signal, it was found that the mean value could be used to indicate the range of fault conditions and variance was useful for detecting the faults in some cases.

For gear fault diagnosis, the most popular technique, used by McFadden and Smith [33], Staszewski *et al* [34] and Dellomo [35], is based on vibration monitoring. Gear monitoring techniques have been extended to use AE by Al-Balushi and Samanta [36] because of its high sensitivity and reduced interference from low frequency noise. They applied AE to early fault detection on standard spur gears made of EN32 steel without hardening. An experimental test rig for spur gears powered by a variable speed motor was used in this work. The raw AE signal was acquired at 1 MHz along with other signals such as speed and reference gear tooth position. During the experiments, the load was gradually increased in order to accelerate the gear teeth failure. It was shown that energy-based features, extracted from the time domain signal, such as energy index (which was defined as the square of the ratio of the rms value for a segment of the signal to the overall rms value of the entire signal), the square root of the energy index, the cumulative energy index and the cumulative square root of the energy index, had a superior capability to detect the early stages of gear failure than other conventional detection techniques. Al-Balushi and Samanta [36] also applied their approach to the

work of (Hardman *et al*, [37]) an helicopter gearbox vibration based on measurements from two accelerometers placed on the gearbox casing. The time domain data were averaged over twenty cycles and the frequency spectrum of the averaged signal was determined. The presence of low-frequency, was observed, so a high pass filter was applied to the signal to eliminate it. They claimed that the energy index approach was equally applicable to vibration signals as to AE signals.

Defects in rolling bearings are a classic problem in a number of different types of machinery, and one in which the use of vibration monitoring is relatively mature. A number of investigators have recently turned to applying AE techniques to detect defects on rolling bearings, on the basis that this will give a "clearer" signal, uncontaminated by structural and environmental noise. Neill *et al* [38] investigated rolling bearings in both laboratory scale tests and on an industrial pump, and compared AE-based diagnosis with acceleration monitoring. Both raw AE and rms AE signals were analysed using energy analysis and spectral analysis and were successful in detecting rolling bearing defects, for example outer/inner race, ball and cage defects. The effect of different sizes of simulated defects on the inner race and a radially loaded cylindrical roller bearing has been investigated by Choudhury and Tandon [39]. An AE sensor was mounted on the top of the test bearing housing, and the defects from both the inner race and roller of the bearings were detected using a ringdown count method. A threshold level of 1 V (automatic) was selected for determining ringdown count for every 10 seconds up to 60 seconds in to all measurements. It was noted that the ringdown count increased rapidly with defect size up to 0.5 mm in the case of inner race defects and 1 mm in the case of roller defects and, beyond those defect sizes, it tended to a constant up to the 2 mm defect, which was the maximum defect size considered in the study. In addition, it was shown that the bearing bore and applied load was not affected by the ringdown counts for test conditions with and without defects although the ringdown counts increased with speed. The distributions of events using ringdown counts and peak amplitudes were also good indicators of the intensity of the bearing defect. Aside from monitoring rolling bearing defects, AE has also been used to observe rolling contact fatigue failure by Yoshioka [40] who applied axial loads to rolling element thrust bearings. In this study, an AE sensor was placed on the bearing housing and a ball position sensor was used to detect passage of a marker on the outside surface of a retainer for so that the time elapsed from the ball passing to AE generation could be determined. The AE event rate per minute was used to detect defects on bearings with a

threshold level of 1V. It was shown that the AE event rate increased rapidly due to an occurrence of spalling before the experiment was stopped. It was also reported that, by using AE event rate and elapsed time, the location of spalling could be determined during a rolling contact fatigue test.

Zuluago-Giralda *et al* [41] have observed AE activity during the run-up and run-down of a 550 MW low speed steam turbine, in order to investigate shaft-seal rub. The sources of AE activity during the operational period were identified as being associated with steam flow, oil flow, turbulence at blades and bearing friction. Three parameters, load, speed and rms AE, were used to monitor the turbine, the last using two AE sensors mounted on the two journal bearing casings connected to a commercial AE system. The AE signals were acquired with time intervals of 100 ms and the rms AE energy calculated simultaneously and stored for later analysis. They noted that, using rms AE, it was possible to detect the cyclic machine phenomena during the run-up period, passing through its critical speed, but not during the run-down period. The cyclic rate was around 0.033 Hz or 1 cycle every 30 seconds, although no further detailed information on these phenomena was presented.

In this section, the successful detection of mechanical and fluid flow activities related to processes in machinery i.e. fluid flow, sliding contact and impact, which are typical phenomena in diesel engines, using AE has been discussed. Although vibration data can be used to detect some machinery conditions, it is normally only sensitive to mechanical activities of machine parts [25, 26] and not activities involving of fluid flow [26], and can be affected by low-frequency interference [36]. A number of faults or abnormal conditions in machinery have been identified using AE and, to diagnose fault conditions, knowledge of physical phenomena of machinery operation under normal and fault conditions has been so that patterns or features related to machinery conditions can be extracted from the signals. The methods used for interpreting AE signals are described in more detail in the next section.

2.3 Diagnostic methods

This section concentrates on diagnostic methods used to classify fault symptoms and severity based on sensor inputs. There are two basic approaches to classification, which

will be referred to here as "deterministic" and "statistical". "Deterministic" methods are based on an understanding and, in some cases, a simulation of the physical process, which lead to the sensor signal. Diagnosis thus becomes a matter of comparing the mechanical signal with that expected for each possible fault condition. "Statistical" methods are those which regard the sensor signal in the abstract, and aim to correlate it with the machine condition by a process of supervised or unsupervised learning. It is argued in this work that statistical methods are generally rather expensive since they necessitate a considerable amount of experimentation to establish the effects of faults (which are often difficult to simulate) in the measured signal. Irrespective of whether the approach is deterministic or statistical, there is often a stage of higher level processing which might involve pattern recognition and/or some type of rule-based or knowledge-based system.

2.3.1 Deterministic methods

Deterministic methods use more or less sophisticated mathematical simulation models based on physical processes to predict the behaviour of machinery for both healthy and faulty conditions and then use more or less direct measurements to assess condition. To develop a monitoring system based on these methods, it is necessary to encode some level of knowledge of the machinery and the processes into the diagnostic system. One example of this approach is given by Grimmelius *et al* [42] who proposed a mathematical model, based on a rotor system, of a medium size, five-cylinder, two-stroke marine diesel engine to determine cylinder pressure. This was a lumped mass model and could also be used to calculate the vibrations of the rotor system during one firing sequence, so that it could be used for reverse calculation to obtain the cylinder pressure by using a measured torsional vibration signal. The cylinder pressure evolution was split into two parts, the first part being caused by compression and expansion and the second by combustion, the latter part being scaleable and dependent on the engine load. By using this method, it was sufficient to calculate all cylinder pressures using a best fit procedure for the measured and calculated vibrations and it was possible to calculate each cylinder power using a single torsional vibration signal to an accuracy of 10%.

Another example is the approach proposed by Hountalas and Kouremenos [43] to monitor a large two-stroke slow speed marine diesel engine. They developed an

advanced automatic troubleshooting method based on thermodynamics to monitor engine condition and to detect the actual cause of an engine fault. However, to develop this monitoring method, more detailed knowledge of processes in the engine cycle is needed. In the diagnostic process, experiments were used to determine the model's constants at a given current engine state and these constants were compared with the constant values at the reference engine state so that the current engine condition could be predicted. Thus, the required adjustments and modifications to the engine could be made in order to gain the optimum engine performance. They suggested that the simulation model proposed in their study was capable of describing the behaviour of the engine and its sub systems at both the reference and the current engine state, characterising the cylinder system, the inlet and exhaust systems, the fuel injection system, the turbocharger, the air coolers and the exhaust duct. The experiment was carried out under actual operating conditions at sea when the engine suffered high cylinder exhaust gas temperatures and low power output. The measured in-cylinder pressure from the cylinders and fuel injection system were the main parameters used in the diagnostic method. However, to cover the full proposed monitoring approach, other measurements were needed such as inlet and outlet temperatures and pressures of the turbine and scavenging air inlet/outlet temperatures. By using these measurements, various parameters could be determined, such as the injection delay, the ignition point, the indicated cylinder power, the heat release rate and the duration of combustion, which could be used to predict engine condition as well as any fault condition. It was suggested that, by using the measured parameters, faults in the engine such as a wear of the cylinder-piston assembly, improper injection timing of various cylinders and clogging of the turbine inlet nozzle and exhaust gas duct could be monitored. They also noted that, after a major repair and adjustment was performed on the engine, it was not possible to repeat the measurements or compare the new engine condition with the previous engine condition because the model constants at the reference state had changed.

A fuzzy model-based system has been used to detect fault conditions in a diesel engine cooling system by Twiddle and Jones [28]. Typically, heat in the engine is generated from the combustion process and the cooling system is used to maintain the engine at a proper working temperature and is controlled by a thermostatic valve. Heat generated from the combustion process is transferred to the engine block and from the engine block into the coolant. A part of the heat is also convected and radiated from the engine

block to ambient air. Heat is transferred from coolant to ambient air by forced convection from the radiator. The fuzzy model of the cooling system was developed using heat transfer assumptions so that fault conditions could be detected. The fuzzy models consist of three sub-models; thermostatic valve model, radiator coolant flow rate model and coolant temperature differences across the engine block and radiator model. Experiments were carried out in the laboratory to obtain coolant flow rate between the thermostatic valve and the radiator and temperature measured from cooling system of a 65 kW turbo-charged diesel engine with various fault conditions such as a thermostatic valve held in the closed and opened positions, a radiator fault, and low coolant flow rate. In the fuzzy system, faults were detected using residual vectors which were calculated from the difference between measured variables and output variables from the model such as coolant flow rate, and temperature difference between the block and radiator. Then the residual vectors were classified with respect to normal condition so that the fault condition of the thermostatic valve could be identified. However, to detect other faults, background knowledge of the faults is needed in order to develop the mathematical model and knowledge base in the fuzzy model-based system.

Gu *et al* [44, 45] have developed a dynamic model to estimate injection parameters including fuel injection pressure, fuelling rate and timing. They used a two-mass, vibro-impact model to describe characteristics of a single-stage, hole-type, direct injection, diesel fuel injector. This model was based on needle motion during an injection period and consisted of four effects; compression or relaxation of the needle seat, the retraction and advance of the needle seat, the impact of the needle with its back stop, and spring seat and needle separation. They suggested that the use of this model permitted analysis of both the needle impact behaviour and the general dynamics of the fuel injection process. The model was validated by measuring the needle lift from the injector of a diesel engine in a laboratory test. They noted that some parameters used in the model were unable to be obtained directly from the injector, such as the contact stiffnesses and the damping ratios. Thus, a trial and error approach was used to estimate these parameters until the predicted needle lift from the model was close to the measured needle lift. The motion of the injector needle was controlled by the flow of high-pressure fuel within the injector so that the models of fuel flow, injection rate and pressure in the nozzle chamber were defined. Gu et al [44, 45] concluded that the peak amplitude of the first needle opening impact from the model could be used to estimate the initial pressure and initial fuel delivery. Furthermore, the experimental study using a

vibration signal confirmed that the peak amplitude of the vibration signal had a linear relationship with fuel supply line pressure which was similar to the results obtained from the model.

As mentioned previously, Douglas *et al* [19] have studied the relationship between Instantaneous Crankshaft Angular Velocity (ICAV) waveform and output power on large two-stroke, marine diesel engines. The ICAV waveform represented cyclic variations about the mean engine speed due to the compression and expansion strokes associated with each cylinder and was measured from a shaft encoder mounted on the end face of the flywheel of the engines. They suggested that the in-cylinder pressure and the resulting indicated torque was a major factor that affected the ICAV fluctuations. The relationship of the ICAV waveform and output power was related to the torque balance equation of the engine which was defined using the inertia of the system, the angular position of the crankshaft, the indicated torque, the inertial torque due to the reciprocating mass and the piston motion, and the external load torque. They noted that when the in-cylinder pressure increased, the indicated torque in the torque balance equation increased, resulting in increased power output, and then the amplitude of the indicated torque waveform increased. Thus, the magnitude of the crankshaft acceleration fluctuations increased with increasing power and the magnitude of the fluctuations in the ICAV amplitude increased. The power output could be directly related to the ICAV amplitude. They showed that the experimental results of the ICAV waveform were in a good agreement with the assumption mentioned above. In addition, the standard deviation calculated from the ICAV waveform could be used to indicate power output of the engines.

2.3.2 Statistical methods

Irrespective of whether a statistical or deterministic approach is being taken, it is usually necessary to reduce measured data time series to a manageable number of features. Generally, AE waveforms are very complex and difficult to use directly to determine the condition of the system. Because of this, it is better to use statistical parameters and waveform parameters to study characteristics of the signals or to extract information from them. In general, AE signals are discrete time-series, some properties of which vary over time. Typical statistical properties are well-known [46-49], and some of the

ones used to describe characteristics of time series data from random, stationary, ergodic and continuous processes can be seen in Table 2.1.

Descriptions	Details
Maximum value (x_{max})	- Indicate the maximum value of discrete time series data
Minimum value (x_{min})	- Indicate the minimum value of discrete time series data
Mean value ($\bar{x}$) or the first moment of amplitude distribution function $\bar{x} = \frac{1}{N}\sum_{i=1}^{N} x_i$ (2.1) where N is the number of data points; and x_i is the data at each discrete point in time.	- Measure the central distribution of discrete time series data.
Root mean square (RMS) value $rms = \sqrt{\frac{\sum_{i=1}^{N} x_i^2}{N}}$ (2.2)	- Measure square root of mean square in discrete time series data. - Indicate energy contained in continuous AE data.
Variance (Var) or the second moment of the amplitude distribution function. $Var = \sigma^2 = \frac{1}{N}\sum_{i=1}^{N}[x_i - \bar{x}]^2$ (2.3)	- Indicate the spread or dispersion or distribution of discrete time series data.
Standard deviation (σ) $\sigma = \sqrt{\frac{1}{N}\sum_{i=1}^{N}[x_i - \bar{x}]^2}$ (2.4)	- Indicate the spread or dispersion or distribution of discrete time series data.
Skewness ($Skew$) or the third moment of amplitude distribution function $Skew = \frac{1}{N}\sum_{i=1}^{N}\left[\frac{x_i - \bar{x}}{\sigma}\right]^3$ (2.5)	- Measure the lack of symmetry of distribution of discrete time series data. - $Skew = 0$ represents normal distribution - For, $Skew < 0$ the left tail of distribution is heavier than the right tail and opposite for. $Skew > 0$
Kurtosis ($Kurt$) or the fourth moment of amplitude distribution function. $Kurt = \frac{1}{N}\sum_{i=1}^{N}\left[\frac{x_i - \bar{x}}{\sigma}\right]^4 - 3$ (2.6)	- Measure the degree of peakedness of distribution of discrete time series data. - $Kurt > 0$ represents a peaked distribution. - $Kurt < 0$ represents a flat distribution. - $Kurt = 0$ represents normal distribution.

Table 2.1: Summary of typical statistical parameters

Other specific parameters have been developed to describe non-continuous AE (Figure 2.8), and normally, the waveform parameters shown are used to describe individual time-series burst signals, where the amplitude usually rises rapidly to a maximum value and decays nearly exponentially to the background noise level. The methods used to obtain the waveform parameters shown in Figure 2.8 are well-documented [11, 50, 51] and each parameter is defined as follows.

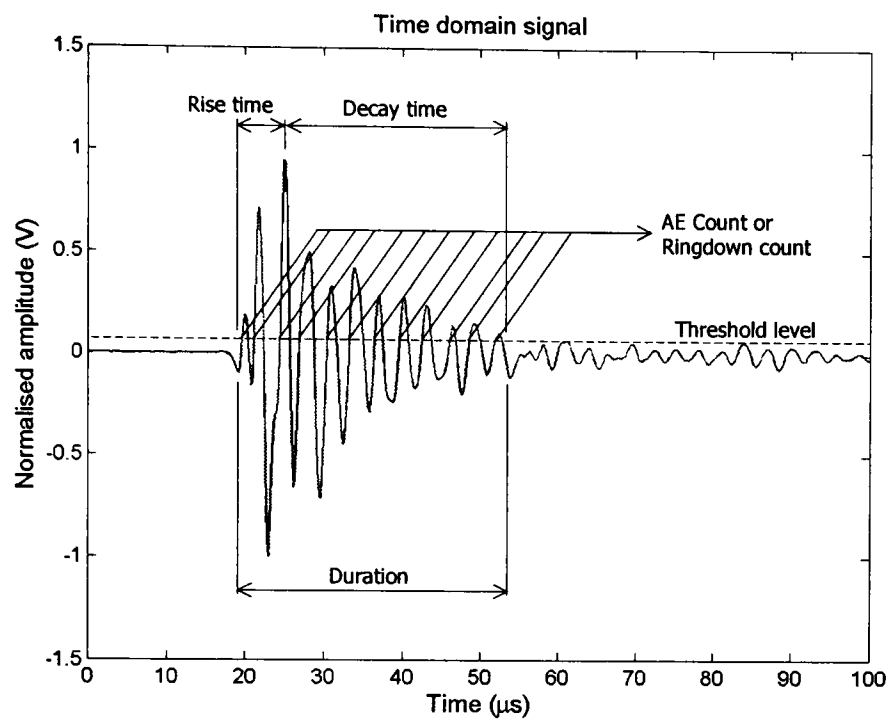

Figure 2.8: AE event and AE waveform parameters

- AE event count is the number of times that the burst signal crosses a preset threshold and AE event rate is the time rate at which AE event counts occur.
- AE count or ringdown count is the number of times the burst signal amplitude exceeds the preset threshold and count rate is AE count per unit time.
- Rise time is the time interval between the first threshold crossing and the maximum amplitude of the burst signal.
- Decay time is the time interval between the maximum amplitude and the last time that the burst signal exceeds the preset threshold.
- Signal duration is the time interval between the first and the last threshold crossing of the burst signal.
- AE energy is the measurement of the relative energy of an AE signal, which is calculated from the area under the envelope of the square of the signal.
- RMS AE is the energy rate or the root mean square of voltage, which is generally an indicator of average AE energy over each averaging time.

The above waveform parameters were mostly used in the early studies of material properties, material deformation and crack propagation using AE [11, 52-56]. However, AE energy and rms AE energy are capable of describing phenomena in diesel engines and other machinery as mentioned before. For applications on diesel engines, rms AE energy has been widely used to investigate behaviour of various faulty conditions, for example faults in the combustion process [6], fuel injection equipment [9], head gasket leakage [7], exhaust valve leakage [8] and cylinder liner scuffing [10]. It might, however, be noted that AE signatures of engine cycles have some of the attributes of burst-type signals and so threshold and rise time parameters can also be of use.

Although time domain analysis is commonly used in AE applications, frequency domain analysis can add a dimension to the nature of the AE signature. Normally, frequency domain analysis is limited to comparative studies if the different spectra to establish qualitative relationships between frequency content of AE and the physical processes which cause it [55], for example cracking, leakage, impact and friction which are associated with mechanical and fluid flow processes in machinery. The Fast Fourier Transform (FFT) is one of the most powerful tools for converting the discrete time domain (data) into the frequency domain. The advantages of FFT techniques are the reduction of the computation time and the reduction of round-off errors associated with this computation [57]. Power spectral density (PSD) estimation is another useful tool that uses the advantages of the FFT to indicate how the signal energy is distributed in the frequency domain [58]. The Welch method is an improved PSD estimator [59] and it is implemented in the well-known commercial MATLAB software [60]. This method calculates PSD by dividing the time series data into segments (possibly overlapping), calculating a modified periodogram of each segment using an FFT and then averaging these periodograms. The averaging of modified periodograms tends to reduce the variance of the PSD estimate. Both FFT and PSD are general tools used in many applications including diesel engines and other machinery. For an example of diesel engine application, El-Ghamry [23] used the PSD to describe the combustion signal obtained from a 76 kW small HSDI diesel engine. He pointed out that the frequency contents of five stages of the combustion signal were almost the same as the frequency content of raw AE signals calculated from four complete cycles.

Typically, both FFT and PSD are adequate to describe stationary signals but, for non-stationary signals, They cannot indicate how the frequency spectrum changes in time

[61]. A number of time-frequency analysis techniques are readily available such as the Short Time Fourier Transform (STFT), Wigner-Ville Distribution (WVD), Smoothed WVD and Wavelet Transform (WT). The STFT is a simple technique which describes the energy distribution of the signal as a time-varying spectrum. The drawback of STFT is that it provides constant resolution for all frequencies because it uses the same window size (Figure 2.9(a)) for the analysis of the entire signal [58] and there is therefore a trade-off between time resolution and frequency resolution as seen in Figure 2.10, which depicts the transform of a linear chirp signal. The left plot in Figure 2.10 used a short time duration window (good time resolution but poor frequency resolution) whereas the longer time duration shown in the right plot (poor time resolution but better frequency resolution) is better.

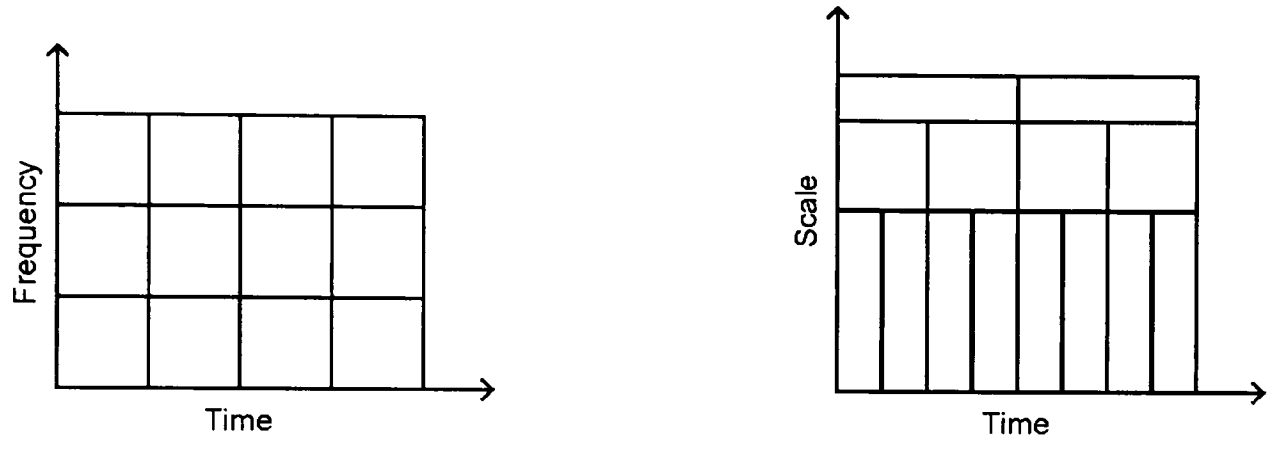

(a) (b)

Figure 2.9: Resolution in the STFT (a) and the WT (b).

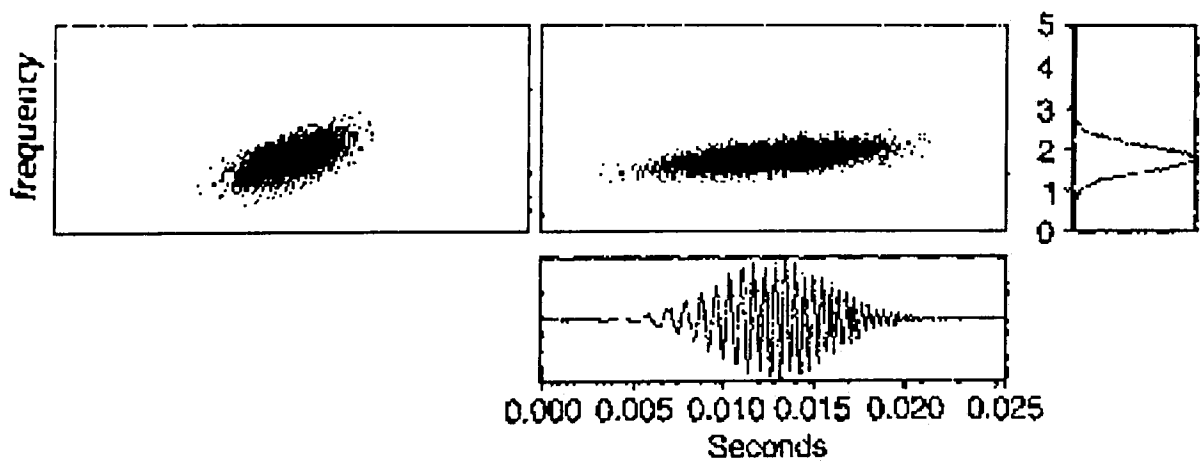

Figure 2.10: The STFT of a linear chirp signal (From Qian and Chen [62])

The WVD can be thought of as a distribution of signal energy in a time-frequency domain, which provides a better time-frequency resolution (Figure 2.11) than the STFT. However, the drawback of the WVD is known as "cross-term" interference (Figure 2.12) which can mislead signal analysis.

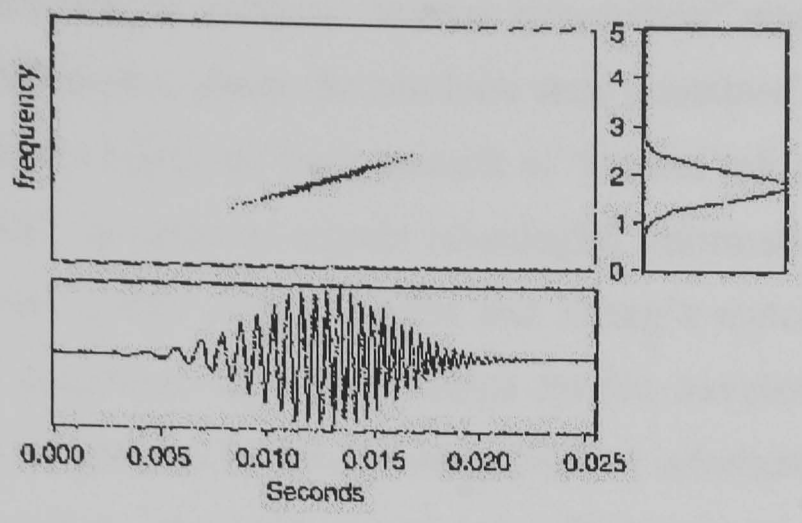

Figure 2.11: The WVD of a linear chirp signal (From Qian and Chen [62])

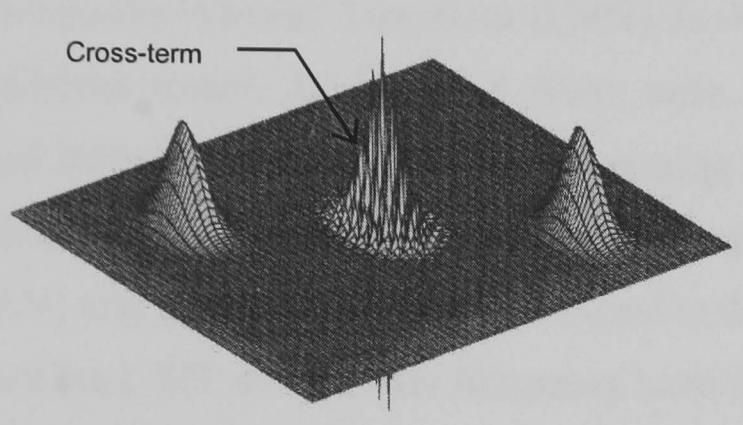

Figure 2.12: The WVD for sum of two signals (From Qian and Chen [58]).

To ameliorate this cross-term interference in Figure 2.12, the smoothed WVD and Choi-Williams Distribution (CWD) can be used [63], although other useful information may be lost. The WT is a powerful method that analyses the signal using multi-scaling where the resolution of time and frequency vary in the time-frequency plane (Figure 2.9(b)). Longer time intervals give more precise low frequency information and shorter time intervals give high frequency information. Therefore, a high resolution of time-frequency representation can be obtained [64]. A number of investigators have used time-frequency analysis to describe the nature of physical processes in machinery, for example; Staszewski *et al* [34] who used the WVD and pattern recognition method to detect tooth faults in spur gears using the vibration signal, Baydar *et al* [65] who applied a smoothed pseudo WVD method to describe vibration and airborne acoustic signals detected from various gear failure conditions such as broken tooth, gear crack and tooth wear; and Li and Ma [66] who used a WT to detect defects in bearings such as outer-race defects and single roller defects. In applications to diesel engine monitoring, Liu and Ling [67] used a WT with a neural network to identify faults such as injection timing advance and piston ring wear on a four-stroke, four-cylinder diesel engine (Isuzu, model C240) using the vibration signal. In the diagnostic process, the vibration signal was decomposed using the Daubechies WT and then WT coefficients in a

wavelet directory were used to compute "mutual information" which could be regarded as the quantity of information about the machine state contained in the wavelets. The wavelets that contained a relatively large amount of "mutual information" were termed "informative wavelets". In order to extract meaningful information of machine states from redundant wavelets, they applied Mallat and Zhang's matching pursuit concept, which used the best matching criterion to search for the wavelets that represented an individual signal, to develop an approach using "mutual information" as a criterion to search for wavelets which contained significant information on machine state. They suggested that the proposed approach could be used to identify faults in the engine. Gu *et al* [4, 5] used a Continuous Wavelet Transform (CWT) to diagnose induced diesel engine faults using airborne sound. The induced faults were directly related to the combustion process and included fuel leakage, injector opening pressure reduction and compression ratio reduction. To detect and locate a faulty cylinder, the continuous wavelet transform (CWT) was applied to the recorded signal to describe the combustion process. They noted that the CWT of the lower frequency band (below 10 kHz) did not provide much detail of the change in the frequency spectrum (Figure 2.13(a)). However, the use of a contour at 10% of the peak CWT amplitude of the higher frequency band (10-50 kHz), as seen in Figure 2.13(b), was able to describe faults in the combustion process. They compared the shape of the contour plot of the CWT shown in Figure 2.13(b) at each test condition with a normal condition, then the faults were identified. However, they presented no analytical results to show the comparison of contour shape in this work.

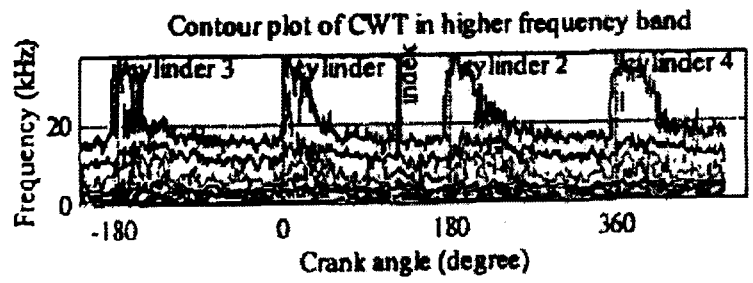

(a) An example of typical contour plot of CWT

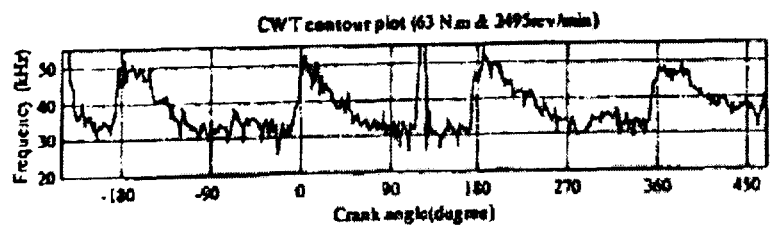

(b) An example plot of contour at 10% of the peak amplitude

Figure 2.13: Two different contour plots of the CWT in the higher frequency band (10-50 kHz) used by Gu *et al* [4, 5].

Time-frequency analysis plays an important role in describing physical processes occurring in the non-stationary signals obtained from diesel engines and other machinery using vibration and airborne acoustic signals. For AE applications, the WT method has been used to study source identification by Hamstad *et al* [68] who investigated the relationship between AE source type and a ratio of the CWT coefficients of the fundamental anti-symmetric mode to the fundamental symmetric mode. For source location applications, Jeong and Jang [69] used the CWT applied to the detected signals from a triangular sensor array and then determined arrival time difference between sensors at a specific frequency so that location of the source could be determined. More detailed information of both of these studies will be discussed in the next chapter. Both applications were mostly from a single source and, no work has yet been published on the WT method applied to multiple-source AE signals as obtained from diesel engines.

2.3.3 Pattern recognition methods

"Pattern recognition" is a term used to describe the process of classifying data into a number of categories or classes based on prior knowledge using statistical parameters extracted from the data. This method is widely used in many practical applications such as speech recognition, medical diagnosis, robotics, automatic vision and fault detection in machinery [70, 71]. In general, both pattern recognition and feature extraction are used together, feature extraction being used to isolate features of interest from the raw signal while pattern recognition is used to match the features to the condition of interest. The classification is achieved by matching the signal with a set of reference signals, in which the signal is classified as a member of the class that corresponds to the best matching reference signal. This technique requires a mathematical description of "match", for instance the linear discriminant function classifier or a lookup table for each feature that corresponds with a fault, which can be performed over a wide range of operating conditions [11, 42].

El-Ghamry *et al* [7] used a statistical pattern recognition method to diagnose faults from various types of reciprocating machinery including a 0.5 MW gas engine, a gas hyper-compressor and a 76 kW, small HSDI diesel engine using various statistical features such as variance, standard deviation, energy content and event location (in time or crank angle domain from a known reference). The diagnostic algorithm for this work can be

described in three parts. First, a generic pattern recognition technique was applied to window each separate event in the cycle from the acquired rms AE signal in the time domain. Then, a numerical signal processing strategy was used to extract statistical features from each signal. Lastly, abnormal characteristic and fault identification could be achieved from extracted features of each windowed event separately. For the simplest case of the small HSDI diesel engine, the rms AE signal detected from the engine with head gasket leakage had a higher peak representing the combustion process. Thus, it was possible to construct an input class with a single member to represent the combustion event. The mean value of the signal segment, which represented the energy content of that part of the signal, was adequate to identify the fault as the head gasket leak.

Principal component analysis (PCA) is a useful tool for analysing complex data. Fog *et al* [8] investigated exhaust valve leakage on a two-stroke large marine diesel engine, using PCA to extract indicative features from the synchronised rms AE data. First the time-series was resampled from rms AE signals with 2048 samples per cycle (related to crankshaft angle position) and then organized into synchronized data vectors from all the engine and valve conditions involved yielding a matrix of dimension 2048×476, each column representing one piston cycle. By selecting the 40 largest eigenvalues from eigendecomposition of the covariance matrix, 40 features of the signal were obtained. Using the 40 features with a feed forward neural classifier (4 hidden neurons, 10 networks and 2 output neurons), the three valve leakage conditions could be discriminated. By applying Optimal Brain Damage pruning (OBD), which was used to remove redundant weights from a trained network in order to obtain the best network, the number of parameters for a fully connected network was reduced from 174 to 64 and thus the optimum network was obtained for detection of valve faults.

Independent component analysis (ICA) is a statistical and computational technique for finding a set of hidden factors or independent components from multivariate statistical data [72]. Pontoppidan and Larsen [73] have introduced unsupervised learning for detection of significant changes in measured rms AE signals, modelled as probability density functions using noise-free independent component analysis (ICA), noisy ICA, principal component analysis (PCA) and Unsupervised Gaussian Mixture (UGM) models. The rms AE data were acquired from a sensor placed on the cylinder liner of a large two-stroke marine diesel engine with sampling rate at 2.5 MHz using an rms time

constant of 50 μs. The AE signals were recorded while the engine load was changed from 25% to 75%. During the tests, the cylinder lubrication was shut off in the middle of the 25% of engine load period and turned on in the middle of the 75% of engine load period. The rms AE signals were resampled into crank angle domain and AE features were extracted with 2048 vectors for each cycle. They noted that the noisy ICA model using mean-field Bayesian learning showed the best performance to detect condition change.

Another application of ICA to identify the sources in airborne sound signals radiating from an engine has been proposed by Li *et al* [74]. In this study, the main sources considered were combustion, valve operation, and piston slap generated from a four-stroke diesel engine. A microphone was used to measure sound at various speeds (1000-2500 rpm) and loads (0-60 Nm) in a laboratory. One requirement of the source signals for ICA is that the signals are non-Gaussian, and kurtosis (Eq. (2.6)) was used to assess this. If kurtosis is greater than zero, the signal is classified as super-Gaussian and if kurtosis is less than zero, the signal is classified as sub-Gaussian. For kurtosis close to zero, the signal is classified as Gaussian (normal distribution). It was shown that all airborne sound sources were of sub-Gaussian distribution so that ICA could be applied. The ICA could separate individual sources based on their statistical independence, and, in this way, all sources were identified including combustion, piston slap, fuel injection, inlet valve opening and exhaust valve opening and the results of the ICA contained at least one component corresponding to one of the physical sources. To display the results, they applied the continuous wavelet transform (CWT) to each independent component signal so that each source could be displayed in the time-frequency plane.

Artificial neural networks (ANNs) are also used in machinery diagnosis for recognising and classifying complex fault patterns [42]. Sharkey *et al* [75] used a multi-net system with in-cylinder pressure data to classify engine conditions into 3 known classes; normal, leaky exhaust valve and leaky fuel injector. The cylinder pressure data were acquired from a 10.4 kW, four-stroke, two-cylinder, air cooled diesel engine using an in-cylinder pressure sensor under operating conditions ranging from 1800 rpm at no load to 2800 rpm at full load. A water cooled eddy current dynamometer was used to control the load on the engine. The multi-net system used feedforward multilayer perceptrons (MLPs) which comprised 4 modules such as NEF, NE, NF and EF (where N, E and F represent normal, exhaust fault and fuel fault, respectively), and was made

up of two levels. The first level contained the NEF module, which had the capability to classify data in terms of three classes and the second level contained the rest of the modules which were able to classify data into one of the two classes. It was observed that the classification performance of the multi-net system was 86.2% in comparison with the classification performance of the NEF module alone at 78.7%. This work has been extended to diagnose faults using AE, vibration and cylinder pressure data collected from the same diesel engine under five conditions; normal, leaking exhaust valve, leaking air inlet valve, blocked fuel injector and poor fuel atomisation conditions [76]. During training, input data from each sensor, for example power spectral density of the AE signal, maximum variance calculated from wavelet coefficients of the vibration signal and cylinder pressure data corresponding to combustion period, were used. It was found that the results obtained from a NN trained on AE data gave a better performance than from a NN trained on other sensors. Combining NNs trained on data obtained from all sensors in the manner mentioned above, it gave the best classification performance at around 99.5%. Failure of each sensor was also simulated using a multi-net system and the performance of the network remained at around 85-95%.

Li, *et al* [77] have used a self-organising map (SOM) neural network to analyse airborne sound signals collected from a four-cylinder four-stroke diesel engine connected to a hydraulic dynamometer. Faults in the exhaust and inlet valve clearances were simulated at cylinder no. 1 and the engine was tested at speeds of 1000, 1500, 2000 and 2500 rpm with five load conditions of 0, 15, 30, 45 and 60 Nm. An unsupervised SOM was used to perform feature extraction and classification. It was shown that, using network synaptic weights or the spectral analysis of network synaptic weights, SOM networks were able to extract significant information from the measured airborne sound signal. By calculating the standard deviation of both network synaptic weights methods, it could identify the difference between the normal or faulty conditions in the engine. In this study, they noted that the airborne sound signal could be distorted by the room acoustics so that it was difficult to detect faults using traditional signal processing methods. The proposed SOM network was able to extract information from the airborne sound signal and identify valve clearance faults, although it could not identify exactly which valve was faulty.

Expert systems are knowledge based programmes which make or evaluate decisions based on rules established within the software, and, when used for fault diagnosis, can

be regarded as a deterministic approach. Autar [78] has used an expert system to characterise the internal condition of a Caterpillar 3208T marine engine using physical evidence and behaviour symptoms together with knowledge based diagnosis rules. For diagnosis, all raw data acquired from the different engine-mounted sensors were analysed and stored in databases and then compared against the rules in the expert system, so that any abnormalities could be reported and remedial action recommended. The valve operations, combustion process, injection process, and other ancillary components were measured using various types of sensors such as accelerometers, pressure transducers, thermocouples, exhaust gas analysers, microphones, engine speed encoder, and engine cycle reference encoder. The fault-source information of this system was derived from vibration, oil temperature and pressure, crankcase pressure, exhaust gas temperature and pressure, exhaust emissions, manifold noise levels, inlet manifold pressure, fuel delivery pressure and instantaneous engine speed applied to the fault conditions such as combustion faults, valve seating and valve tappet clearance problems, piston slap, valve mechanical faults, oil cooler problems, faults in cooling system, piston ring and liner faults, and injector faults. Autar [78] was able to show that the above faults could be diagnosed unambiguously in the laboratory.

Also on the deterministic side, the Dempster-Shafer Theory (also known as Theory of Evidence or Theory of Belief Functions) has been applied to condition monitoring of diesel engines by Parikh *et al* [79]. They demonstrated the detection of thermostatic valve faults in the cooling system of a four-litre, four-cylinder, turbo-charged diesel engine. The faults induced in the thermostatic valve were caused by the reduction of the maximum coolant flow rate to 30%, 50%, 65% and 80% of the normal value, and the engine was operated under load at 60 kW and at a speed of 1500 rpm over all tests. Several sensors were used to measure engine speed, ambient temperature, radiator inlet temperature and engine inlet temperature. Using the primary classifiers, for example the multilayer perceptron (MLP), radial basis function (RBF) neural networks and k-nearest neighbour (k-NN), they were unable to classify all engine conditions to a sufficiently accurate level. The use of Dempster-Shafer Theory was combined with the primary classifiers, which is an example of fusion classifiers, in order to improve the overall classification performance. To combine output of the primary classifiers, the recognition-substitution-rejection (RSR) and predictive rate were used for computing beliefs for individual decisions from the primary classifiers. The use of Dempster-Shafer Theory based on RSR rates with a combination of the primary classifiers

recognised only 79.5% of fault conditions. They noted that the best classifer used a combination of Dempster-Shafer Theory based on predictive rate with the primary classifiers which had a successful prediction level of fault condition of about 95%.

Fuzzy logic has also been applied to fault detection in diesel engines for example by Zhang *et al* [80] who used the measures of fuzzy nearness and fuzzy cluster and vibration characteristic parameters obtained from vibration features such as power spectral density, total power, average PSD value, maximum amplitude and rms amplitude to identify wear conditions of a 8.31 kW, single cylinder diesel engine running at 1550 rpm. Three different wear conditions were induced by varying gaps between the piston skirt and the cylinder wall; normal (0.13 mm), wear (0.4 mm) and extreme wear (0.48 mm) were successfully identified. Twiddle and Jones [27] also used a Fuzzy model-based system to identify combustion faults in a small diesel engine based on the load estimations and the residuals obtained from the reference model. The load estimations were obtained from the air-fuel ratio and the power spectrum of the speed signal. The reference model was the predictive model for engine speed and was implemented by predicting speed fluctuations with respect to crank angle. It was shown that, by measuring the five input signals, speed, TDC, fuel flow rate, air inlet flow rate and air inlet manifold pressure, fault conditions on the fuel injector and air inlet could be identified.

2.3.4 Source location methods

Source location is widely applied in AE monitoring of structural integrity, material deformation or pipe leaks [11, 13, 69, 81-87] and normally deals with one type of source. However, AE has been used to determine location of sources on machinery in a few cases. For example, AE has been used to determine a rubbing location on the rotor of a laboratory test rig by Wang and Chu [88]. They used a WT based on Daubechies method to decompose the detected AE envelope signals from two AE sensors placed on the bearing housing. The use of a cross-correlation technique enabled determination of the maximum normalised cross-correlation coefficients from the decomposed signals and hence the time delay from which the rubbing location can be determined using wave velocities calculated from wave propagation equations (i.e. transverse wave and longitudinal wave) and material properties.

In the case of diesel engines, there are multiple AE sources associated with mechanical impact, sliding contact and fluid flow processes including injection, combustion and valve opening/closing operations as well as the functioning of ancillary equipment. The typical detected AE signal is very complex and can be further confused by reflection, mode conversion and attenuation of waves. Whereas there are no published instances of spatial location of these sources, it is commonplace to locate sources in the engine cycle, using crank angle and/or TDC pulses as reference signals. Typically, event maps are used to study faults by monitoring feature changes at each event such as injector events [6], exhaust valve events [8] and combustion events [7], and this can be regarded as a deterministic approach.

This mapping technique is also generally used in conventional vibration monitoring [3]. For example, Gu *et al* [44, 45] who developed a dynamic model for the needle motion of a common hole-type, single stage diesel fuel injector. They then compared the model with the experiment using a vibration signal detected at the injector body, the fuel line pressure and the needle lift. The dynamic behaviour of an injector during the injection process was described by three components; fluid excitation commencing prior to needle opening impact, needle opening impact and needle closing impact, offering a deterministic means of monitoring injector performance using vibration analysis. The model does not account for fluid flow in the injector, nor is the acceleration signal sensitive to it [9].

A detailed study of mechanical and fluid flow phenomena during the injection process has also been carried out using AE (Gill *et al* [9]). This work used an AE sensor, an accelerometer, a needle lift sensor, an injector pressure sensor and a shaft encoder to examine injector phenomena on a small HSDI diesel engine. It was found that the AE activity preceded the injection start and this was associated with the build up of fuel pressure in the fuel delivery pipe. It was noted that there was no sign of initial fluid excitation immediately preceding the lifting of the injector needle in the acceleration signal, although the AE measure was sensitive to fuel flow through the injector.

2.4 Summary of state of knowledge and thesis identification

AE plays an important role in condition monitoring and diagnostics not only in structural integrity but also, increasingly, in rotating and reciprocating machinery. AE has been applied to condition monitoring of diesel engines for the last ten years and has been used successfully to identify various conditions such as combustion, head gasket leakage, exhaust valve leakage, injector faults and liner scuffing. The fault conditions have been identified by monitoring the change of statistical or waveform features extracted from the AE signal. In addition, pattern recognition methods have been applied to improve fault identification, including PCA, ICA and neural networks, Whereas AE sources have been located in single-source applications, spatial location has not yet been demonstrated in multi-source systems such as diesel engines. It is expected that time- and space-location will provide additional diagnostic advantages for AE.

The attenuation of AE has been mentioned by a number of authors, noting that high amplitude AE signals can be seen with sensors placed close to the source. Typically, AE that propagates through a diesel engine even from a single, simple source is very complex because the reflection, refraction, mode conversion and attenuation of waves, which is inherent in the nature of AE wave propagation, and can distort the AE signal along a propagation path. It is likely, therefore, that spatial source location using AE in diesel engines will be difficult and will be further complicated because of overlap of multiple sources, which emanate from various processes. Most of the published work uses crank angle and TDC signals to map the AE events from the time domain onto the crank angle domain so that each known mechanical process in the engine cycle can be compared to the events in the AE signal.

In the light of this, the current research attempts to find a way to gain more understanding of AE wave propagation in diesel engines in order to obtain more detailed information from the detected signal. In addition, the effects of AE attenuation will be studied to find a way to determine the relationship between attenuation of AE energy and distance from the source and to overcome the problems associated with multiple sources.

With this in mind, the work in this thesis aims to make a contribution to condition monitoring where multiple sensors are involved and a sensor array is used to segment time series in time (or crank angle) and space. The main challenges are:

- To develop a simple attenuation/time of flight model for simple, simulated sources in a diesel engine.
- To develop means of isolating different sources within an event and different event locations with a view to enhancing the level of determinism in AE analysis and a consequent sharpening of diagnosis.

Chapter 3 Acoustic emission wave propagation

3.1 Introduction

Engelbrecht [89] has stated that *"Nonlinear wave motion means complexities and complexities mean the hard work to grasp essentials."* Acoustic Emission (AE) is a type of nonlinear wave and natural phenomena of AE wave propagation are very complex. This chapter describes the ways in which AE wave propagation in media are described and the effects of wave attenuation along the propagation path. Various wave types exist depending on the type of confinement, the most common being dilatational (compression) waves, distortional (shear) waves, surface waves and Lamb waves (or plate waves). In real structures, AE wave types cannot be controlled and the different wave types travel with different speeds, which are theoretically dependent on material properties. As well as the source being made up of an unknown collection of modes, reflection, refraction and mode conversion occur when the wave impinges on a boundary so that distortion of the AE signal may occur. In addition, the amplitude of the wave decreases with distance propagated and different modes may suffer different degrees of attenuation. Finally, piezoelectric sensors respond only to the passage of waves and it is difficult to tell which type of wave has stimulated them. In this chapter, we concentrate on attenuation and group velocity effects in AE wave propagation and we examine the extent to which the extremely complex wave propagation phenomena can be dealt with using such simple considerations.

3.2 Acoustic emission wave propagation

3.2.1 Acoustic emission

Acoustic emission (AE) has been used in many applications to monitor mechanical phenomena, processes or faults. AE is defined in ASTM1316-99a [50] as:

"the class of phenomena whereby transient elastic waves are generated by rapid release of energy from localized sources within a material"

As well as being used to monitor processes, structures and machinery, AE is also used in inspection where it differs from other test methods because the detected energy is released from mechanisms within a medium rather than being generated by external sources. Sources of AE can be divided into two types. The first includes fundamental materials sources of AE such as crack growth, plastic deformation or phase transformation [11] where the "rapid releases of energy" are associated with collective atomic movements, such as fatigue damage, dislocation movement or martensitic (shear) transformations. The secondary sources, sometimes called "pseudo sources", are phenomena which give rise to the fundamental sources, such as leaks [90], cavitation [29], faults in machinery [7], and wear and friction [91]. In general, an AE source radiates energy in all directions, and a sensor located near to the source will detect a signal which is generally a complex transient disturbance. The complexity of the signal depends on transmission paths, geometries and structural features, such as edges, corners, and cavities. In addition, when a wave propagates, it loses energy in a number of ways such as during reflection, refraction, scattering and mode conversion [11, 17], some of which result in secondary waves which may themselves be detected by the sensor.

AE signals are a sensor's response to elastic waves propagating in a solid medium, and are therefore subject to the fidelity of transduction and signal conditioning. The waves themselves are complex because the solid medium is able to resist shear forces. In the simplest case of an infinite medium (no boundaries) only two types of plane waves exist. Dilatational waves (also called longitudinal waves) are those where the particles of the medium move parallel to the direction of wave propagation as seen in Figure 3.1(a) and distortional waves (also known as shear waves) are those in which the particles of the medium move perpendicular to the direction of wave propagation (Figure 3.1(b)). The speed of both waves can be determined from basic material properties; Young's modulus of elasticity (E_y), density (ρ) and Poisson's ratio (ν). The speed of a dilatational wave, c_1, is given by:

$$c_1 = \frac{E_y(1-\nu)}{\rho(1+\nu)(1-2\nu)} \tag{3.1}$$

and that of a distortional wave, c_2, is given by:

$$c_2 = \frac{E_y}{2\rho(1+\nu)} \tag{3.2}$$

The speeds of dilatational waves and distortional waves are independent of frequency. In the simple case, both can propagate as a simple harmonic wave where the wave speed (c_i) is a function of frequency (f) and wavelength (λ).

$$c_i = f\lambda \tag{3.3}$$

Simple harmonic waves are often described by wave number (K_i), which is defined as the ratio between the circular frequency ($\omega = 2\pi f$) and wave speed (c_i).

$$K_i = \frac{\omega}{c_i} \tag{3.4}$$

These simple properties of compression and shear waves are widely exploited in ultrasonic NDT, where the type of wave injected can be controlled by the type of transducer. In practical AE applications, however, one has no control of (or implicit knowledge of) the types of waves being generated or recorded.

In a semi-infinite medium, Rayleigh waves, or surface waves, can exist [11, 89, 92, 93], where the particles move in an elliptical orbit, rather like water waves. The particle motion is in the plane perpendicular to the free surface and parallel to the direction of propagation as shown in Figure 3.1(c). The amplitude of the surface waves decreases exponentially with the depth, and they propagate with a lower speed than shear waves. The approximate surface wave speed (c_r) is given by the expression [94]:

$$c_r \approx 0.9 \cdot c_2 \tag{3.5}$$

Examples of wave speeds for longitudinal waves, shear waves and surface waves in metallic media can be seen in Table 3.1.

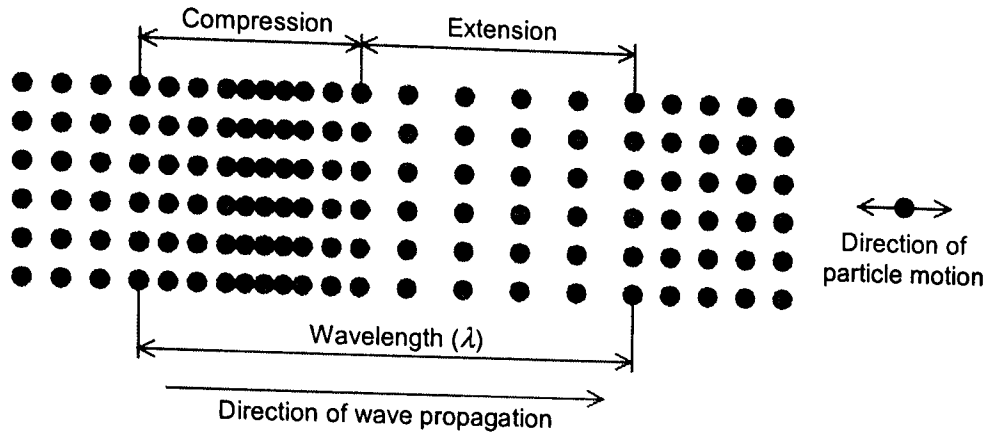

(a) Dilatational wave (Longitudinal wave)

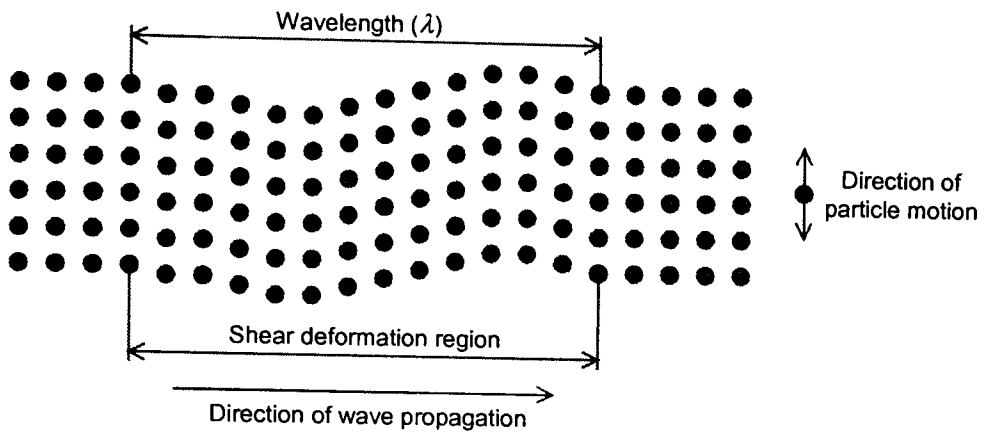

(b) Distortional wave (Shear wave)

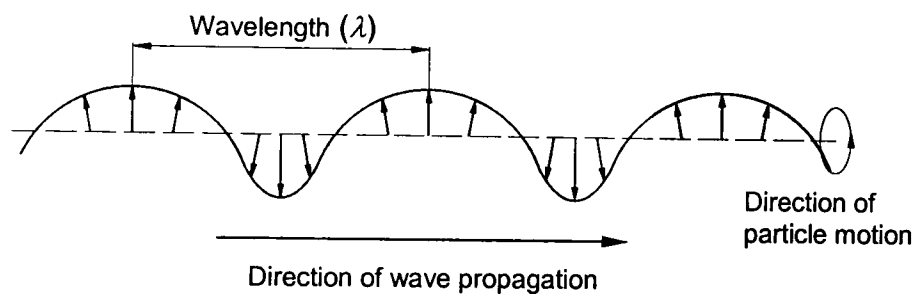

(c) Rayleigh wave or surface wave

Figure 3.1: The main wave types: dilatational wave, distortional wave and Rayleigh wave (or surface wave).

Materials	Wave speed (m/s)		
	Longitudinal wave	**Shear wave**	**Surface wave**
Aluminium	6300	3100	2900
Cast Iron	5000	3000	2700
Steel	5900	3200	3000

Source: Non-Destructive Testing Handbook Vol. 5 - Acoustic Emission, Society of Non-Destructive Testing, 1987 [11]

Table 3.1: AE wave speeds for various materials

Lamb waves are a collection of individual solutions to the wave equation for plane wavefronts in an infinite plate. The propagation of Lamb waves (or plate waves) has been studied by numerous authors [13, 81, 85, 93, 95]. In the infinite plate, a solid bounded by two parallel planes, wave propagation is more complicated than the infinite

and semi-infinite cases because the multiple reflections from boundaries are unavoidable. For cases where the wavelength is small compared with the plate thickness, the wave propagates as a Rayleigh wave, but, when wavelength is large with respect to the plate thickness, plate waves propagate with two possible types of mode, i.e. the symmetric (s) modes (or often called extensional waves) and the asymmetric (a) mode (often called flexural waves) as illustrated in Figure 3.2. Both wave modes propagate at various speeds, which are dependent on both frequency and plate thickness. Extensional (c_e) and flexural (c_f) wave speeds are given by:

$$c_e = \left[\frac{E_y}{\rho\left(1-\nu^2\right)}\right]^{\frac{1}{2}} \tag{3.6}$$

and

$$c_f = \left[\frac{D}{\rho h}\right]^{1/4} \omega^{1/2} \tag{3.7}$$

where D is related to the bending stiffness (Nm) given, for rectangular plates, by

$$D = \frac{E_y h^3}{12\left(1-\nu^2\right)};$$

h is the plate thickness (m);

E_y is the Young's modulus of the material (Pa or N/m^2);

ρ is the material density (kg/m^3);

and ω is the angular frequency, $\omega = 2\pi f$ (rad/s);

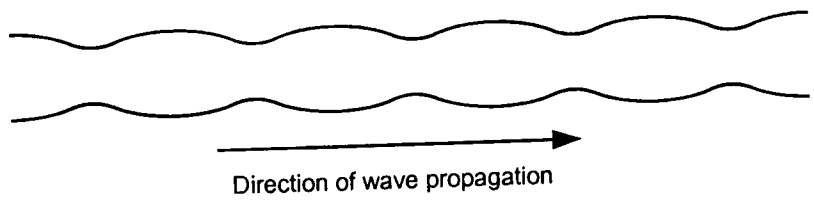

(a) Symmetric mode (or extensional mode)

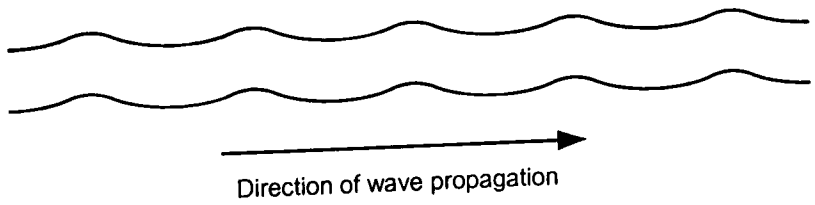

(b) Asymmetric mode (or flexural mode)

Figure 3.2: Two different modes of Lamb wave (or plate wave).

In practice, the structures of machines such as diesel engine blocks may be composed of some plate-like components. Each plate may be of small dimensions with variable thickness and features such as webs and surfaces may be in contact with liquids such as water and oil. AE wave propagation will therefore be much more complex than simpler plate- and block-like structures.

Reflection, refraction and mode conversion can occur when waves encounter boundaries. When waves propagate through a solid medium and impinge on a boundary between two media, they may be reflected and/or transmitted [13, 14]. The reflection and refraction of waves depends on the angle of incidence and a material property known as the acoustic impedance (Z), defined as [96]:

$$Z = \rho \cdot c \tag{3.8}$$

where ρ is the material density (kg/m^3)

c is the wave speed (m/s)

In certain cases, and for some wave types, the impedance is complex with real and imaginary components [97]. The acoustic impedance can be used to determine the percentage of energy transmitted and reflected between two media. For two materials of different acoustic impedance, Z_1 and Z_2, the percentage of energy transmitted, E_t can be given by:

$$E_t = \frac{4Z_1Z_2}{(Z_1+Z_2)^2} \times 100 \tag{3.9}$$

and the percentage of energy reflected, E_r is given by

$$E_r = \left(\frac{Z_1 - Z_2}{Z_1 + Z_2}\right)^2 \times 100 \tag{3.10}$$

The acoustic impedance of typical materials can be seen in Table 3.2. When the acoustic impedance of two media is well-matched ($Z_1 \approx Z_2$ or $Z_2 \approx Z_1$), the incident wave is largely transmitted to the other medium (Figure 3.3(a)). On the other hand, when the

acoustic impedances are dissimilar ($Z_1 >> Z_2$), the incident wave is mostly reflected (Figure 3.3(b)). Both longitudinal waves and shear waves are reflected or refracted when they impinge on a boundary. The angles of reflection and refraction can be determined using Snell's Law (Equation (3.11)) and are dependent on wave velocities in the material in question.

$$\frac{\sin\theta}{V_1} = \frac{\sin\beta}{V_2} = \frac{\sin\gamma}{V_3} \tag{3.11}$$

where θ, β and γ are various angles (degs), as shown in Figure 3.3

and V_1, V_2 and V_3 are wave velocities (m/s)

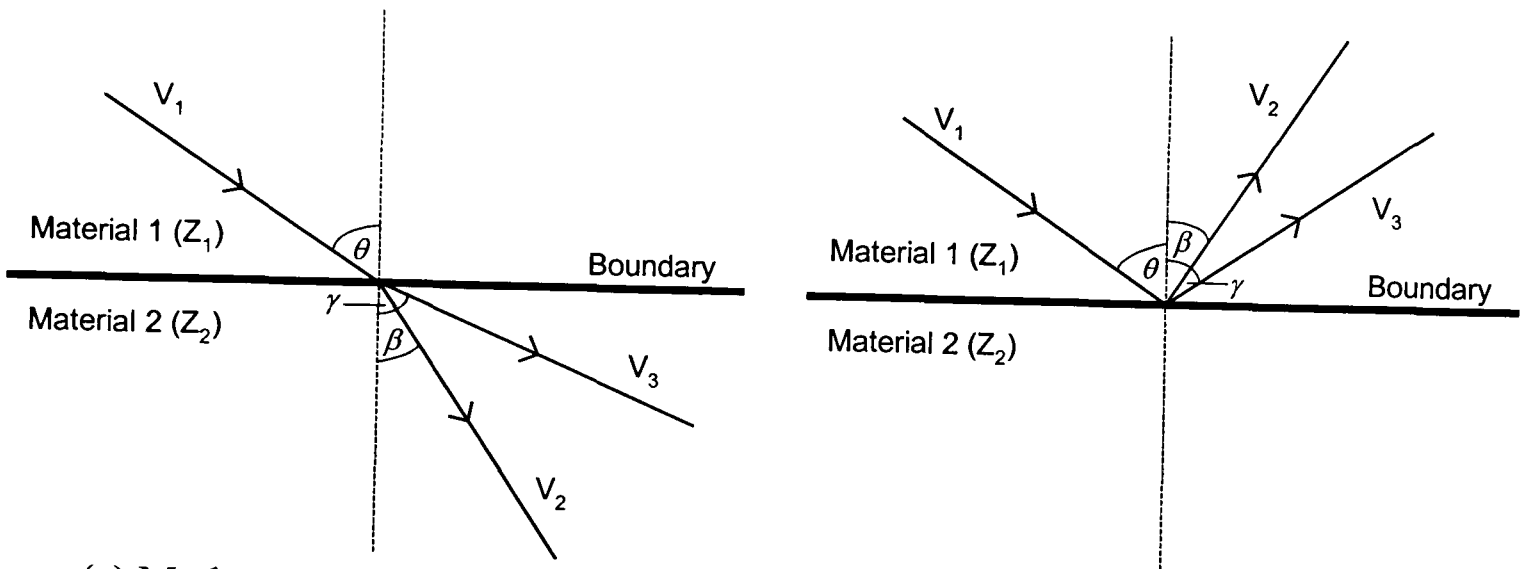

(a) Mode conversion in refraction (b) Mode conversion in reflection

Figure 3.3: Reflection, refraction and mode conversion of wave

Mode conversion can also occur on a boundary when the acoustic impedance of the two media are different and angle of incidence is not normal to the interface, leading, for example to longitudinal waves transforming to shear waves or shear waves transforming to Rayleigh waves [92, 98]. The angle of incidence of each wave can be determined using Equation (3.11) and the relevant wave velocity.

Materials	**Acoustic impedance, Z (kg/m^2s)**
Aluminium	17.10×10^6
Steel	45.63×10^6
Cast iron	37.44×10^6
Water	1.483×10^6
Air	4.3×10^2

Table 3.2: Acoustic impedance of materials [99, 100].

3.2.2 Attenuation

Attenuation is a term used to describe the reduction of wave amplitude as it travels along a propagation path. The effects of wave attenuation have been suggested by Miller and McIntire [11], Pollock [13] and Kolsky [14], and four mechanisms have been identified; geometric attenuation, internal friction, attenuation from scattering and diffraction, and attenuation from dispersion. When an AE wave is generated by a localised source in an infinite medium, it spreads as a spherical surface in all directions from its source. Geometric attenuation arises from the law of conservation of energy, where the energy of the wavefront would remain constant along the propagation path, and so the amplitude of the wave (A) will decrease inversely with propagation distance, r, ($A \propto 1/r$). In plates, wave propagation can be considered to be two-dimensional, expanding as a cylindrical wavefront. In this case, the wave amplitude (A) decreases inversely as the square root of the propagation distance, r, ($A \propto 1/\sqrt{r}$) in order to maintain a constant energy at the wavefront. This approach does not, of course, consider any of the possible effects of reflection.

Wave propagation in real media is not usually conservative. Some of the mechanical energy associated with particle motion can be converted to thermal energy, a process normally referred to as internal friction. Here, the amplitude of the wave attenuates exponentially with distance, an effect seen, for example in wave propagation in viscoelastic materials and composite materials.

Scattering and diffraction occur when AE waves propagate through media with complex boundaries and discontinuities such as slots, holes, cavities, inclusions and cracks. Scattering occurs when waves propagate through a finite void or inclusion while diffraction occurs when waves propagate and encounter a sharp edge such as a crack. These effects can generally cause a decrease in the amplitudes of waves with distance, although there may be local focusing or constructive/destructive interference effects.

Dispersion is a phenomenon of wave propagation where different frequency components travel through media at different speeds. The effect of this attenuation causes a decrease in amplitude although the total energy may remain constant, and it is commonly found in Lamb waves.

Pollock [13] has suggested that steep attenuation is typical for all kinds of structures in the near field which is dominated by geometry spreading. However, in the far field, internal friction dominates and leads to an exponential relationship of attenuation with distance. In plates and shells, the transition distance at which internal friction starts to dominate geometry spreading is given by $4.34/\alpha$, where α is a (measured) attenuation factor (dB/m).

AE wave attenuation in real structures has been studied empirically by various authors, essentially by acquiring AE signals at various positions relative to a source [11, 101]. The peak amplitude is a parameter generally used to calculate attenuation [13, 85, 101-103], normally using a logarithmic scale (decibel), in which case it is called relative amplitude (A_r) and is given by:

$$A_r = 20 \cdot \log(\frac{A_i}{A_o}) \tag{3.12}$$

where A_i is maximum signal amplitude (V) at a receiver sensor at distance, x from the source, and;

A_o is maximum signal amplitude (V) at the source position

and the amplitudes can be measured in volts provided that the amplifiers are consistently calibrated.

Then, wave attenuation can be determined from a plot of the relative amplitude versus distance and can be expressed as decibels per unit distance [11], determined by:

$$\alpha = \frac{20}{x} \cdot \log(\frac{A_2}{A_1}) = \frac{A_r}{x} \tag{3.13}$$

where α is attenuation coefficient (dB/m)

A_1 is amplitude of signal at P1 (V)

A_2 is amplitude of signal at P2 (V) and;

x is distance between P1 and P2 (m)

Graham and Alers [101] have measured attenuation of AE waves on various structures, using a white noise generator (WNG) as an AE source. The WNG consisted of a steel plate with a depression on one face arranged so that fine particles of silicon carbide were fractured continuously under the rotating action of a fused silica rod. The AE signals were acquired at various distances from the source, and frequency spectra were calculated. Using Equation (3.12), the loss in amplitude as a function of distance was obtained as a function of frequency. One example in their study was a gas pressure vessel on which AE was measured from the outside surface. This example, also reported in [11] permitted the general conclusion for plate-like structures in the near-field zone, that the attenuation follows the expected form for geometrical spreading and varies with $1/\sqrt{r}$. For the far-field zone, the attenuation of the signal is caused by absorption (mechanical energy is converted to thermal energy) with a limited amount of dispersion.

The attenuation of Lamb waves propagating on a 12m long structural steel I-beam has been studied in the laboratory by Holford and Carter [85], who identified an extensional and flexural component. The attenuation was measured using the peak amplitude of the highpass filtered (HF) extensional part of the signal generated by an Hsu-Nielsen source measured at various source-sensor distances. The peak amplitude at the source position was not included in the calculation because it was not possible to separate the extensional mode from the rest of the signal at the short distances. The attenuation of waves was sharpest in the near-field zone at around 10 dB over 0.5 m (20 dB/m) for the first measurement point and lower for longer source-sensor distances (1 dB/m). They noted that, for the near-field zone, the higher attenuation was attributed to geometric spreading and, for the far-field zone, the attenuation was caused by absorption or conversion of AE wave energy into heat.

Working with graphite/epoxy composite plate of dimension $990\times990\times1.2$ mm (for 8-ply) and $990\times990\times3.7$ mm (for 24-ply), Prosser [102] has measured separately attenuation of extensional and flexural wave modes using peak amplitude. He also calculated the peak frequency of each peak amplitude of the waves and found that, for the 8-ply plate, the attenuation rate was 42 and 83 dB/m with peak frequency of 410 and 85 kHz for the extensional and flexural modes, respectively. For the 24-ply plate, the attenuation rate was 35 and 51 dB/m with peak frequency of 230 and 90 kHz for the extensional and flexural mode, respectively. He suggested that the larger effect on the flexural wave was caused by dispersion.

Another example of AE wave attenuation has been measured on large-scale turbine rotors by Mba and Hall [86] using peak amplitude and the energy content of the entire signal. They used a pencil lead break technique to simulate positions of seal and blade rubbing and used an AE sensor mounted in the region where the turbine was supported by its bearing. Both peak amplitude and energy content were calculated with reference to the first position of the simulated source on the turbine and then plotted against source position. However, the AE attenuation in dB/m was not determined in this study. They suggested that AE could detect rubbing in the turbine at sensor positions up to 2 m from the source and AE may be detectable on the bearing housing.

A simpler practical example is given in [11] for the attenuation of AE on gas trailer tubes which are used to transport gases (i.e. hydrogen) along a highway. One example was a steel tube of 560 mm diameter, 10.4 m length and 10.5 mm minimum wall thickness. The relative amplitude was calculated using Equation (3.12) from various source-sensor pairs where a source was generated using a pencil lead break technique, and the attenuation coefficient (α) was determined to be about 0.178 from a power law curve, $A = A_o \cdot x^{\alpha}$ where A is the signal amplitude at distance, x and A_o is the initial amplitude of the source. In addition, Finlayson *et al* [103] have studied attenuation on cylindrical graphite epoxy motor cases (GEM), assuming a simple absorption law that has the amplitude of the peaks (A) decaying exponentially with distance (x), $A = A_o \cdot e^{-k\alpha}$ where A_o is the reference amplitude of the source and k is the attenuation coefficient in unit of m^{-1}. The experiment was carried out using a pencil lead break technique and impacts of different energy levels (0.5, 1, 3, 5, and 7 ft-lb) to generate the AE source. Both sources were detected at various distances from 0.5 to 5.5 m (0.5 m intervals) on the GEMs, although the actual dimension and analysis of attenuation was not given in detail in their study. The main use of the attenuation function here was only to determine the maximum sensor separation in order to effect source location in the GEMs.

Most of the experimental studies of attenuation mentioned above were used simply to find the maximum distance at which a sensor can detect a signal. Table 3.3 summarises attenuation factors from published work including materials, geometries, wave types and transmission paths where they are available. Because, the attenuation of signals increases as source-sensor distance increases. It is possible to determine source location

using signal amplitude, the highest signal amplitude being detected at the sensor placed closest to the source (Figure 3.4(a)). This method is most often used to identify coarse source location or zone location, and can be improved using the highest and second highest signal amplitude (Figure 3.4(b)). One application of this method involved location of a continuous source in a pipe [11]. However, in the case of severe wave attenuation and more complicated structures, this method will not be practical.

Materials	Wave type	Transmission path /Attenuation
Steel tube (3T) of dimension 560 mm dia., 10.4 m length and 10.5 mm wall thickness (From Miller & McIntire, p. 163 [11])	N/A	Sources and sensors were on the same surface where path lengths (straight line from source) were varied up to 10 m Power law, $A = -15.88x^{0.178}$ α = 0.178 dB/m
Steel I beam of dimension 12 m long (From Holford and Carter [85])	Lamb wave	Sources were generated at the end of the beam. An array of 7 sensors was used where the first sensor was placed 266 mm from the end of the beam on the centre line of the web and the other 6 sensors were placed at various distances (straight line) up to 11.7 m. For extensional mode, For near field, α = 20 dB/m For far field, α = 1 dB/m
Graphite/epoxy composite plate of dimension For 8-ply, 990×990×1.2 mm For 24-ply, 990×990×3.7 mm (From Prosser [102])	Lamb wave	Sources and sensors were on the same surface. The source was generated 127 mm from the plate edge and an array of 5 sensors was placed as a straight line from the source with step of 101.6 mm. For 8-ply, Extensional mode: 42 dB/m at 410 kHz Flexural mode: 83 dB/m at 85 kHz For 24-ply, Extensional mode: 35 dB/m at 230 kHz Flexural mode: 51 dB/m at 90 kHz
Steel pipe, 150 mm diameter (From Miller and McIntire, p. 139 [11])	N/A	No detailed information for transmission path For near field, α = 8.1 dB/m For far field, α = 1.9 dB/m
Fiber-reinforced composite material (From Pollock [13])	N/A	No detailed information for transmission path α = 10-30 dB/m (at 140 kHz)

Remark: N/A indicates that no information was provided in the source document

Table 3.3: Summary of attenuation factor for various materials

In this work, it is considered that a more general description of attenuation is desirable to cover situations of more complex objects and more realistic sources, which may be semi-continuous or continuous. In addition, because wave propagation can be affected also by attenuation, reflection, refraction and mode conversion, the effects of geometric features, as opposed to source-sensor distance need to be taken into account including the number of interfaces crossed by the wave. The use of AE energy can help to overcome the above limitations and allow the energy loss factors to be lumped so that a

general attenuation factor can be obtained. Furthermore, studying the phenomena of AE wave propagation and AE source location using energy might help to understand in more detail propagation behaviour in more complex structures such as diesel engine blocks.

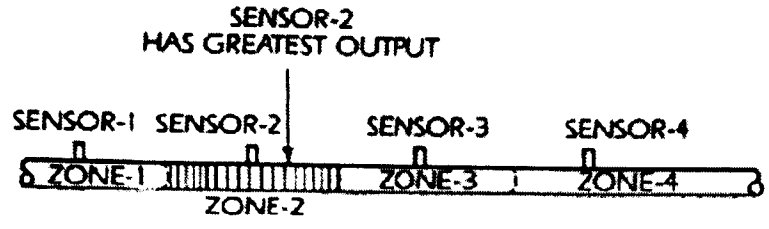

(a) Using the highest amplitude

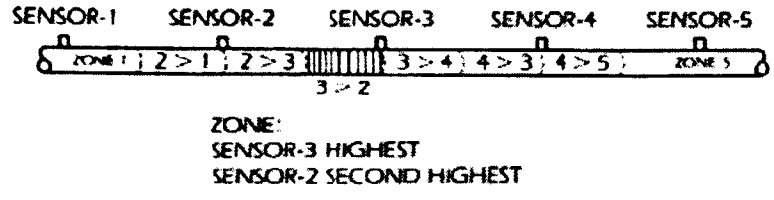

(b) Using the highest and second highest signal amplitude

Figure 3.4: Schematic diagram of zone location method (From Miller and McIntire [11])

3.3 Acoustic emission energy

The energy contained in a raw recorded AE signal can be estimated simply by taking a square value over a time, t, as follows:

$$E = \int_0^t v^2(t)dt \tag{3.14}$$

where $v(t)$ is amplitude of the AE waveform in volts (V);

t is time in seconds (s);

and E is acoustic emission energy in $V^2.s$

In a semi-infinite medium, the acoustic emission energy can be considered to be lost as the wave travels according to a simple absorption law:

$$E(x) = E_o e^{-kx} \tag{3.15}$$

where $E(x)$ is acoustic emission energy at distance x from the source ($V^2.s$);

E_o is the energy of the source ($V^2.s$);

k is an attenuation factor (m^{-1});

and x is the source-sensor distance (m)

The AE energy at each source-sensor distance can be rewritten as a linear equation by applying natural logarithms. Thus, Equation (3.15) becomes:

$$\ln E(x) = \ln(E_o e^{-kx}) = \ln(E_o) + \ln(e^{-kx})$$

$$\ln E(x) = \ln(E_o) - kx \tag{3.16}$$

which is not phenomenologically different to Equation (3.13). In the case, where the amplitude is determined by smoothing the raw signal (rms), the energy is simply the square of the amplitude and so amplitude based attenuation factors can, to a first approximation, be compared with those based on energy by using a simple factor of 2. The attenuation factor can be determined directly using an exponential fit according to Equation (3.15) or using a linear fit according to Equation (3.16).

In a simple case of wave propagation in plate-like structures, there is generally one dominant transmission path from source to sensor, and so attenuation can be determined using Equations (3.14)-(3.16). However, for circumferential wave propagation in a cylindrical structure, for example, the initial detected signal has two main components due to transmission paths travelling in opposite directions round the circumference as illustrated in Figure 3.5. (For convenience of argument, these paths are shown as arcs although in practice they will involve multiple reflections)

Defining the short transmission path of the AE wave as distance x_s and the longer one as x_l, the AE energy of a wave of source energy E_o at a specific distance (x) is given by,

$$E(x) = E_s + E_l = E_o e^{-kx_s} + E_o e^{-kx_l} \tag{3.17}$$

where E_s is an energy content at x_s ($V^2.s$)

E_l is an energy content at x_l ($V^2.s$)

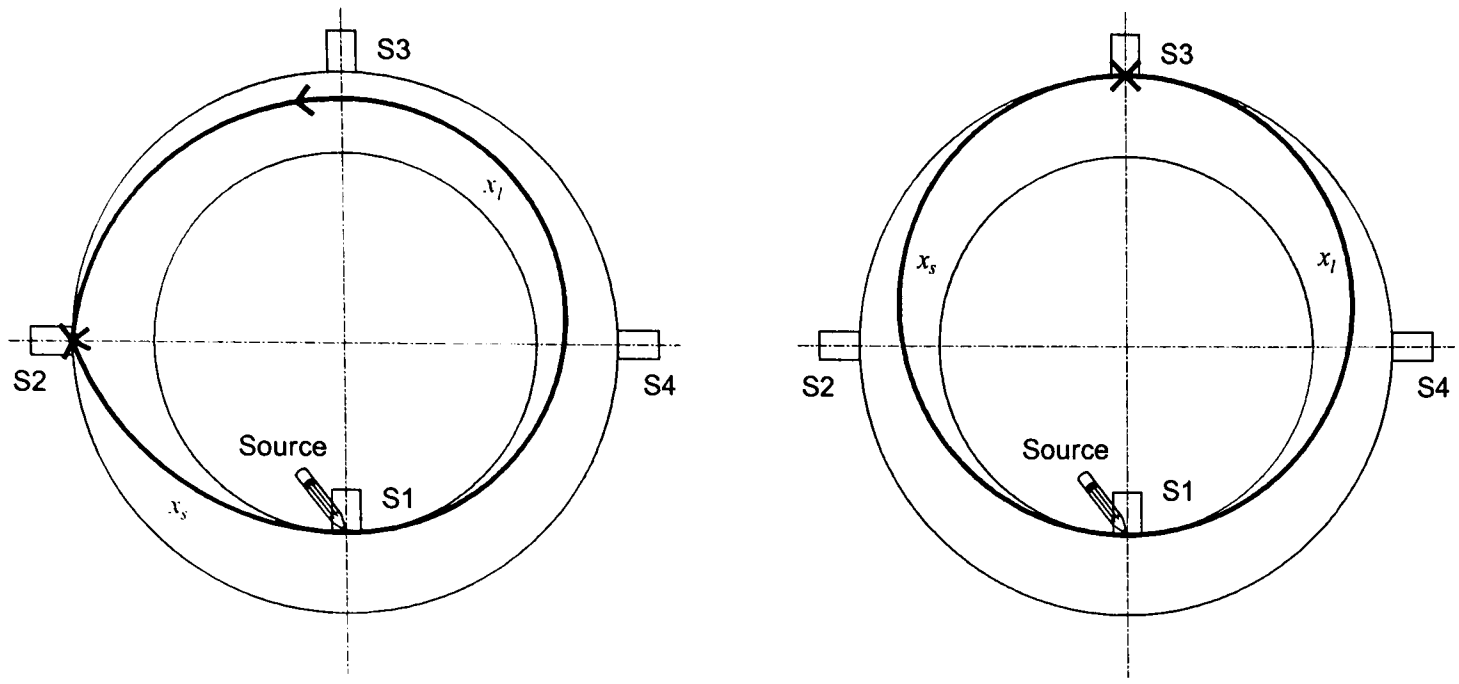

(a) $x_s < x_l$ (b) $x_s = x_l$

Figure 3.5: Two direct transmission paths of AE propagating on cylinder liner with different sensor positions. (Where x_s and x_l are the shorter and the longer circumferential transmission path length, respectively).

Equation (3.17) can be rewritten

$$E(x) = E_o e^{-kx_s}\left(1 + e^{-k(x_l - x_s)}\right)$$

and, acknowledging that there is, in the general case, some relationship between x_s and x_l which, for a cylinder is:

$$x_s + x_l = C \tag{3.18}$$

$$x_l = C - x_s$$

so

$$E(x) = E_o \cdot e^{-kx_s}\left[1 + e^{-k(C-2x_s)}\right]$$

$$E(x) = E_o \cdot e^{-kx_s}\left[1 + e^{-kC} \cdot e^{-2kx_s}\right] \tag{3.19}$$

This relationship is used later to analyse results of attenuation tests on a large cylinder liner.

3.4 Source location

Source location is central to AE-based inspection, such as proof testing of metallic and composite vessels, and other monitoring applications include pipe leakage and bridge monitoring [11]. Real applications of source location are mostly on less complicated structures such as pipes and plates. The time of arrival of the AE wave propagating from source to sensor is the main feature that is extracted from the detected signal, and, by measuring this arrival time at various sensors in an array, the position of the source can be determined. The following sections review the types of geometric algorithms that are used to determine source position given arrival times at the sensors.

3.4.1 Source location in one dimension

The simplest case is when two sensors are mounted on the surface of a linear structure such as a pipe, beam or bar, and an AE event occurs somewhere between the two sensors and travels with constant wave speed (c), as seen in Figure 3.6(a). Using two arrival times (t_1 and t_2) at both sensors S1 and S2, the source location can be calculated from:

$$d_1 = \frac{1}{2}\left[D - c \cdot (t_2 - t_1)\right] = \frac{1}{2}\left[D - c \cdot \Delta t\right] \tag{3.20}$$

where d_1 is distance from source to first sensor (S1);

D is distance between two sensors;

t_1 is arrival time of signal at first sensor (S1);

t_2 is arrival time of signal at second sensor (S2); and

Δt is arrival time difference between two sensors.

From Equation (3.20), if the arrival times at S1 and S2 are equal, the source location is midway between the sensors. However, if the source occurs outside the sensor array (Either beyond S1 or S2) as seen in Figure 3.6(b), the time difference measurement is constant and corresponds to the time of flight between the sensors, and the source can only be located according to which sensor it is beyond.

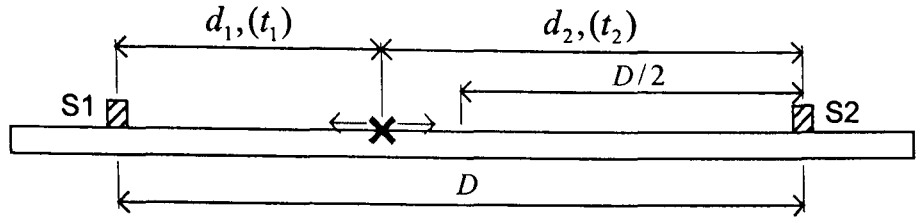

(a) Source occurs inside sensor array

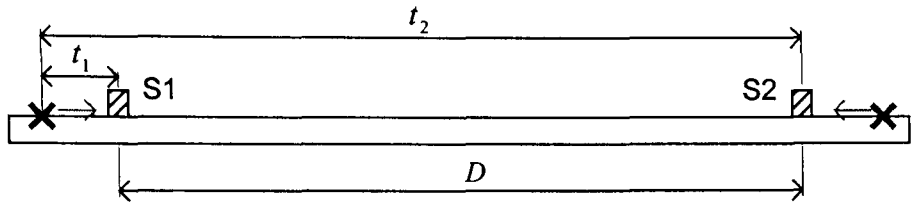

(b) Source occurs outside sensor array

Figure 3.6: Schematic diagram of 1D source location technique.

3.4.2 Source location in two dimensions

The general case is where an AE wave is generated from a source at P1 (x_s, y_s) on an infinite plane and propagates with a constant wave speed (c) in all directions. When the sequence of arrival at two sensors is sensor, S1 and then S2 as shown in Figure 3.7, the location of the source is given by the equation of a hyperbola:

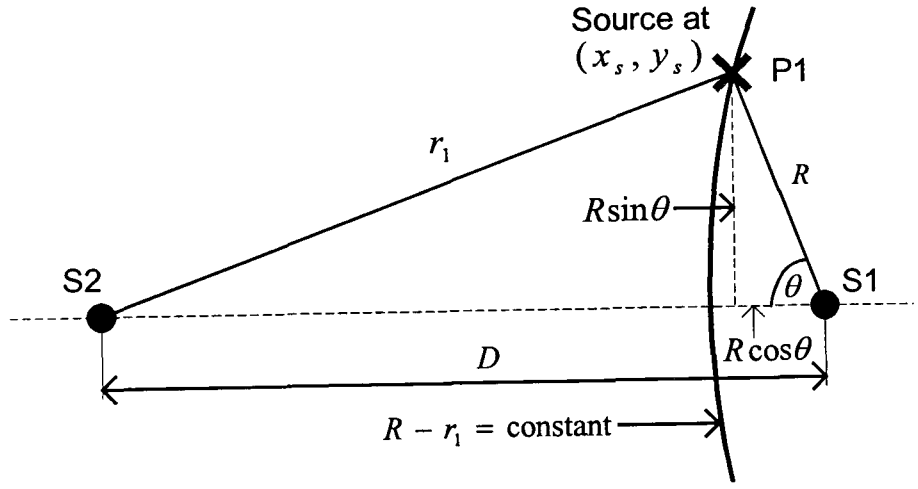

Figure 3.7: Schematic diagram of 2D source location technique.

$$r_1 - R = (t_2 - t_1)\cdot c = \Delta t \cdot c \tag{3.21}$$

and

$$R = \frac{1}{2}\left(\frac{D^2 - \Delta t^2 \cdot c^2}{\Delta t \cdot c + D\cos\theta}\right) \tag{3.22}$$

where R and r_1 are the distance from the source to the sensors, S1 and S2, respectively. The derivation of equation (3.22) can be seen in [11].

Equation (3.22) is insufficient for most cases of 2D source location because any point on the hyperbola satisfies the input data, wave arrival sequence and arrival time difference. The situation can be improved by mounting three sensors on the plane in a triangular configuration. An array forming an equilateral triangle is economical and can be combined to form hexagonal arrays to monitor a large area or structure [55]. In this configuration as seen in Figure 3.8, the sequence of arrival at the sensors is S1-S2-S3. There are three signals and two arrival time differences (Δt_1 and Δt_2), each of which is used to define a hyperbola, whose intersection gives the source location. Thus, the source location can be given using the solution of the two hyperbolas, as follows [11]:

$$r_1 - R = (t_2 - t_1)\cdot c = \Delta t_1 \cdot c \tag{3.23}$$

$$r_2 - R = (t_3 - t_1)\cdot c = \Delta t_2 \cdot c \tag{3.24}$$

$$R = \frac{1}{2}\left(\frac{D_1^2 - \Delta t_1^2 \cdot c^2}{\Delta t_1 \cdot c + D_1 \cos(\theta - \theta_1)}\right) \tag{3.25}$$

$$R = \frac{1}{2}\left(\frac{D_2^2 - \Delta t_2^2 \cdot c^2}{\Delta t_2 \cdot c + D_2 \cos(\theta_3 - \theta)}\right) \tag{3.26}$$

Planar source location can be determined by solving simultaneously Equations (3.25) and (3.26) for θ and R to obtain the location of the source with reference to S1.

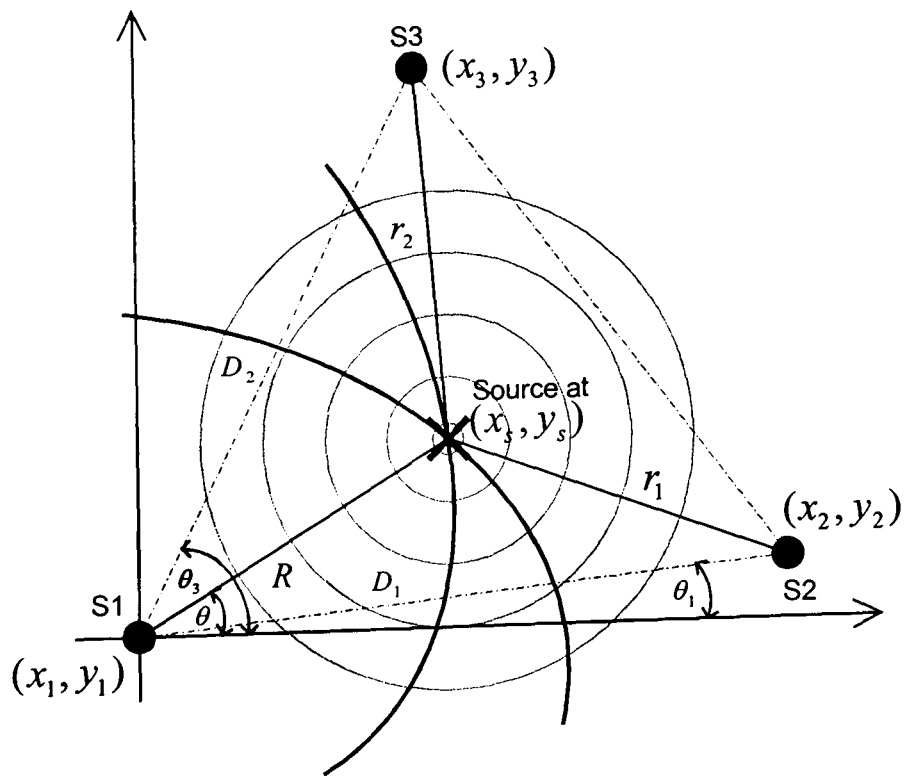

Figure 3.8: Source location using an equilateral triangular array.

Source location using three asymmetrically placed sensors can be calculated using three intersecting circles, where each sensor represents the centre of a circle. Ziola and Gorman [83] have used an approach proposed by Tobias [87], in which the radii of the circles were determined using arrival time difference from the source to the respective receiver sensors. Three sensors, S0, S1 and S2, shown in Figure 3.9 are located at (0,0), (x_1, y_1) and (x_2, y_2), respectively. The source location is defined using polar co-ordinates r and θ.

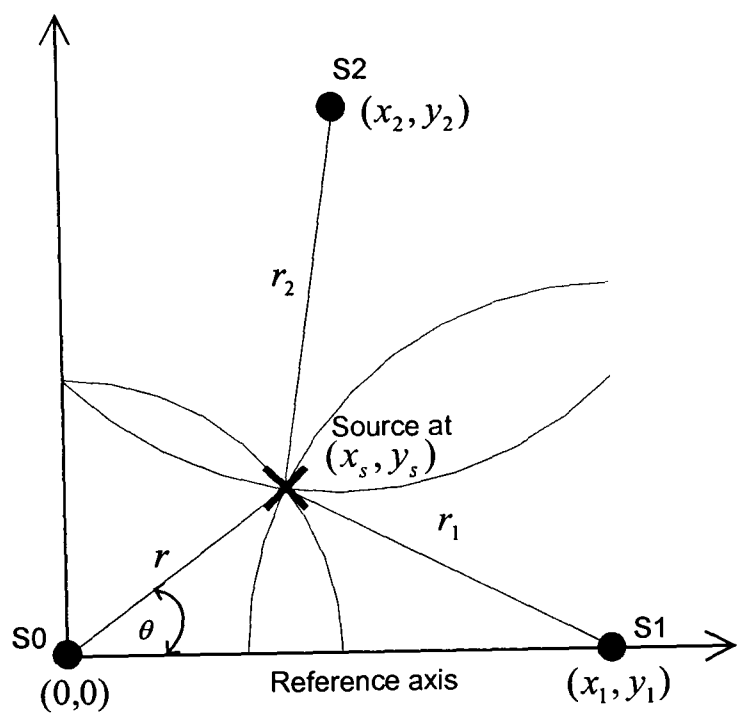

Figure 3.9: Source location using intersection of circles.

The location of the source is therefore determined from [87]:

For this distance, r:

$$r = \frac{A_1}{2(x_1 \cos\theta + y_1 \sin\theta + \delta_1)} \tag{3.27}$$

$$r = \frac{A_2}{2(x_2 \cos\theta + y_2 \sin\theta + \delta_2)} \tag{3.28}$$

where $A_1 = x_1^2 + y_1^2 - \delta_1^2$;

$A_2 = x_2^2 + y_2^2 - \delta_2^2$;

$\delta_1 = t_1 \cdot c$;

$\delta_2 = t_2 \cdot c$;

c is the wave speed (m/s);

and t_1 and t_2 are the time differences (s) between sensors S0-S1 and S0-S2, respectively.

For the angle, θ:

$$\cos(\theta - \psi) = K \tag{3.29}$$

where $K = [(A_2\delta_1 - A_1\delta_2)/B]$;

$$B = \left[(A_1x_2 - A_2x_1)^2 + (A_1y_2 - A_2y_1)^2\right]^{\frac{1}{2}};$$

and $\tan\psi = (A_1y_2 - A_2y_1)/(A_1x_2 - A_2x_1)$

For planar source location, a special four-sensor array configuration has been proposed by Ying *et al* [11, 104] using a four array. The four array positions can be defined as at $(X,0)$, $(-X,0)$, $(0,Y)$ and $(0,-Y)$, and the technique was used to determine the intersection of two hyperbolas, the arrival time differences being determined between the pair of X sensors and the pair of Y sensors. Thus, the location of the source (x_s, y_s) is governed by:

$$x_s = aB\sqrt{\frac{b^2 + A^2}{b^2B^2 - a^2A^2}} \tag{3.30}$$

$$y_s = Ab\sqrt{\frac{a^2 + B^2}{b^2B^2 - a^2A^2}} \tag{3.31}$$

where $a = (1/2)\Delta t_x \cdot c$;

$A = (1/2)\Delta t_y \cdot c$;

$b = (X^2 - a^2)^{1/2}$;

$B = (Y^2 - a^2)^{1/2}$;

and c is wave speed (m/s).

Both triangular source location methods have some common difficulties. If there is double intersection of the hyperbolae or circles (processing or measurement error), then two possible solutions are found. This difficulty is found in the areas around sensor positions as seen in Figure 3.10. To improve accuracy of source location, an additional

sensor (the fourth sensor) is used to determine extra time differences and generate a third hyperbola which should give a single point of intersection [11]. The input data of both methods are arrival time difference between sensors and wave speed. The difference between the methods is that the method based on intersection of hyperbolas needs to iterate θ and R until they satisfy an input condition, whereas the method based on intersection of circles should give an exact-solution. However, if there is only one solution of source location, the accuracy of both source location techniques depends on wave speed and time difference measurement.

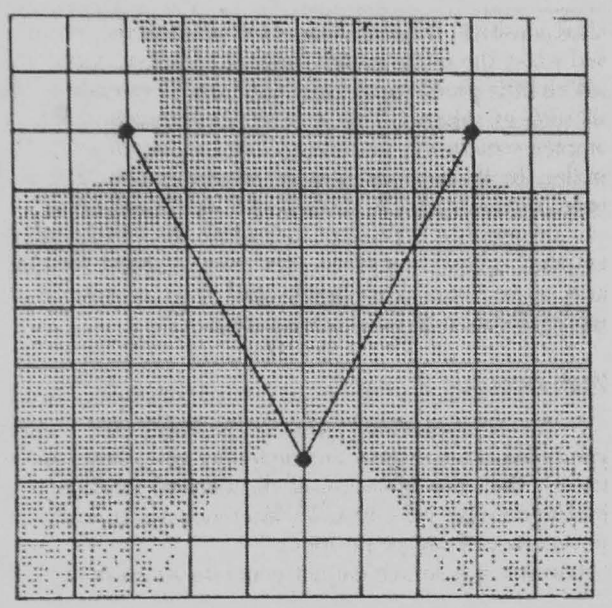

Figure 3.10: Area where source location is possible, shown shaded. (From Miller and McIntire [11], p. 150)

In the case of the array of four sensors, only one solution will be found, however the accuracy of all source location techniques will be affected by changes in signals caused by wave attenuation, reflection, refraction and mode conversion.

3.4.3 Source location in three dimensions

The source location techniques mentioned above are applicable to plate- and shell-like structures. However, source location in three dimensions may be necessary when a structure acts as a thick plate and when the location of the source lies within the body of the material. The application of 3D source location has been demonstrated in [11] for an intermediate (thick walled) cylindrical vessel using a four-sensor array. The details of sensor configurations and the derivation of the source location equation can be seen in [11].

3.4.4 Source location using Lamb wave

For linear source location, the traditional technique requires two sensors as described in Section 3.4.1. For Lamb waves, it is possible to achieve linear location using only one sensor, because their dispersive nature means that they travel through media with different wave speeds. For the case of simultaneous propagation of extensional and flexural wave modes with different frequency spectra and wave speeds, Maji *et al* [81] and Holford and Carter [85] have demonstrated this method of source location on structures in the far field. By applying high-pass (HF) and low-pass (LF) filters with an appropriate cut-off frequency at ω_c, two wave components propagating at speeds at c_{HF} and c_{LF} can be identified and time differences (Δt) between their arrival can be measured. Thus, the source position (d) can be located on a one dimensional object using a single sensor as follows:

$$d = \Delta t\left(\frac{c_{HF} \cdot c_{LF}}{c_{HF} - c_{LF}}\right) \tag{3.32}$$

This linear source location technique has been used successfully on a large structure such as an I-beam up to 12 m [85] long. However, for short distances, or small structures, this technique may not be effective because extensional and flexural waves are not sufficiently separated from each other (depending on the difference in the wave speeds).

3.5 Time difference measurement

For source location, the wave speed is assumed to be known and constant and, in general, it is recommended that a measured wave speed is used rather than a published value which depends upon how arrival time is determined [11]. Then, the error in source location depends on any errors in measured arrival time differences. In the case of complex structures, attenuation, reflection, refraction, mode conversion and interference can all distort the shape of the wave as it propagates. Also, for some waves and media, dispersion effects can cause time of arrival to be triggered at different phase points of the signal. The sensor sensitivity to the component frequencies of the wave can also contribute to variations in arrival time.

The traditional techniques for time difference and arrival time measurement in source location applications are those based on threshold crossing and cross-correlation. Each technique may use a combination of time, frequency and time-frequency methods to improve the accuracy of the measurement. Threshold crossing techniques involve determining the time at which a signal crosses a set threshold level and is automated in a number of commercial systems [11]. Threshold crossing can be used to measure the arrival time of the envelope of the AE signal or may simply be applied to the raw signal amplitude. The threshold can be set just above noise level or can be a proportion of the maximum signal amplitude, sometimes the maximum itself. Filtering can be applied to the signal so that a specific frequency band is used, and this is particularly used for waves propagating in dispersive media such as in thin plates (Lamb waves) or in composite materials because the waves travel with a speed which is a function of frequency, applied, for example, by Maji *et al* [81] and Holford and Carter [85].

One time frequency method which has been used to determine arrival times for each frequency component is the wavelet transform (WT). Jeong and Jang [69] have used a Gabor WT (continuous WT) to identify the arrival time of signals from the tests on a large plate of graphite/epoxy laminate using the maximum magnitude in time and frequency space. Also, Ding *et al* [105] have used a Gabor WT to identify arrival time from a test on a smaller plate of similar material, observing that the first peak of the WT magnitude gave better results than using the maximum of the WT magnitude because reflections on small objects can distort the shape of the waveform.

Cross-correlation techniques give the arrival time difference between two signals directly, and are very effective for non-dispersive geometrically simple systems when the wave propagates from source to sensor without reflection, as reported by White [106] and Holmes [107]. For dispersive media, Holmes [108] has used a controlled source which had a single frequency component to study flexural wave propagation for multiple paths on a bar. It was shown that time differences of multiple paths could be determined using a cross-correlation technique between controlled source and received signal. However, for AE, it is not possible to control the source and so the cross correlation technique may not be successful in determining time difference. Ziola and Gorman [83] have studied source location on a thin aluminium plate using flexural wave modes. They noted that, when using threshold crossing techniques to measure a time difference, the same phase point of the waveforms was not reliably identified.

They proposed a phase point detection method to isolate single frequency components from a received signal. Here, the received signal at each sensor was cross-correlated with a single-frequency cosine wave modulated by a Gaussian pulse, and thus a frequency component in the received signal was isolated allowing the time difference between sensors to be measured and used for source location analysis. However, Ding *et al* [105] have reported that, for Carbon Fibre Reinforced Plastic (CFRP) composite materials, arrival time difference measurement from a filtered signal (bandpass filtering around 0.3125–0.4688 MHz) using a cross-correlation technique was very poor when compared with threshold crossing and WT-based techniques.

Generally, arrival time difference measurement between sensors using cross-correlation is effective when the signal is dominated by a single frequency and a single wave speed. Both threshold crossing and cross-correlation techniques can be used to measure arrival time difference but the characteristics of AE waves propagation through the medium need to be known. Then, both techniques in conjunction with other signal processing techniques can be used to sharpen the measurement of arrival time difference and help improve the accuracy of source location.

3.6 Source reconstruction

As mentioned before, AE wave amplitude attenuates as propagation distance increases. Furthermore, the effects of reflection, refraction and mode conversion are typical phenomena in real structures, and AE waves in a real structure may have one source or a combination of different sources. The latter case is a more complicated problem and can be found in diesel engines and machinery. Polesskaya and Vangeli [109] have presented a procedure for reconstructing the original form of an AE signal at its source when the form of the signal is known at the receiver sensor, distorted because of effects of reflection from boundaries and attenuation as it propagates from the source. The transfer function of the receiving system was assumed to be known and was normalised to equal unity. The original form of the source was described in terms of a mathematical model and the assumption of the model was that the AE source generates only a spherically symmetrical wavefront which had no sharply delineated inhomogeneities. In this work, the simple case of a solid waveguide with reflection of the spherical wave was considered. The model considered only the effect of attenuation of the wave and a

single reflection of the wave from a boundary. The pulse at the source of the AE was modelled in the form of the Fourier series [109]:

$$f(t) = \sum_{k=-N}^{N} C_k \exp(i\frac{2\pi}{\tau}kt) \tag{3.33}$$

and

$$C_k = \frac{C_k^*}{\xi(k)} \tag{3.34}$$

where N is number of terms

τ is time duration of the signal

t is time

C_k^* are coefficients

and C_k are coefficients of expansion

However, the values of C_k^* were calculated on the basis of a known displacement pulse at the receiver and the quantity $\xi(k)$ is the frequency transfer characteristic of the medium. However, for more complex cases such as multiple sources in a running engine, it is not possible to reconstruct the original signal using this method because wave propagation in real structures from real sources is more complicated and difficult to predict.

The question of source identification has been tackled by Hamstad *et al* [68], who have modelled a range of source types in order to extract meaningful source identification features using the Continuous Wavelet Transform (CWT). Effects of wave propagation over distance, AE source type, and the depth of the AE source below a plate surface were considered. In this study, Lamb wave AE signals were created from databases using three-dimensional Finite Element Modelling (FEM) for point sources on a plate with dimension of $1000\times1000\times4.7$ mm and source-sensor distances at 60, 120 and 180 mm. They noted that the use of a source model was better than experimental signals because key information could be controlled which may not have been available in the experimental data, such as point source location in three dimensions; source rise time; magnitude and orientation of source dipoles; absolute out-of-plane displacement of a perfect wideband point sensor at an exact location; known filtering of the AE signal; signals both with specimen edge reflections and without such reflections; and signals

that are largely free of noise. Three types of buried point sources were considered, an in-plane dipole (aligned with the propagation direction to the sensors), an out-of-plane dipole, and crack initiation with the largest dipole aligned with the propagation direction to the sensors. They noted that by using the CWT to analyse the signal, the signal energy distribution could be shown in frequency, time and mode. By determining the ratio of the maximum magnitude of the Asymmetric (Ao) (at 50 kHz) and Symmetric (So) (at 522 kHz) Modes, Ao/So, it was found that, for all sources which were centred at the same depth below the plate surface and with the same source-sensor distance, this ratio could be used to distinguish different source types. In addition, the Ao/So ratio was related to source depth. For example, at the same depth, the microcrack initiation source had the highest ratio and the out-of-plane dipole gave the lowest ratio. However, for sources at different depths below the plate, it was not possible to uniquely identify the source type. However, in the case of real sources such as in engines and other machinery, multiple sources can potentially overlap and the effects of reflection, refraction and mode conversion of AE waves will be important. Therefore, the Ao/So ratio cannot be used simply to classify the source type in structures such as engines because the wave types and wave propagation paths are potentially very complicated.

3.7 Signal mapping

AE signal mapping has been used to improve diagnostic capabilities in time and space on engines so that the mechanical and fluid flow processes can be monitored. El-Ghamry *et al* [7] suggested that a signal could be mapped using the strongest event in the cycle to identify each cycle and then map AE events to the mechanical operation of particular components or processes in the engine. It was possible to focus data handling and analysis on changes in the nature of the signals associated with each of these events using an "event map". In addition, a time reference such as top dead centre (TDC) and/or angle encoder signals have been used to map the events in acquired signals [8, 9]. Once the events are mapped, detailed analysis of the timing (or angle) at which events occur give detailed information relating to engine operation. Information about component condition can be extracted as well. Example of mapping of signals are given by Gill *et al* [9], El-Ghamry *et al* [7], and Fog *et al* [8].

3.8 Summary of the relevant aspects

For real applications in diesel engines, there are multiple sources (i.e. impact, fluid flow activities and sliding contact) generated in each cylinder of the engine over each cycle. Furthermore, AE wave propagation in diesel engines is very complicated because geometries of engine blocks are complex including variation of wall thicknesses and boundaries. Wave types (i.e. longitudinal, shear, Lamb and surface) propagating in diesel engines are unpredictable and uncontrollable. The effects of wave attenuation, reflection, refraction and mode conversion can potentially occur for each wave type, attenuation being perhaps one of the major effects. Most published work has used maximum amplitude [85, 86, 102] to determine attenuation of AE through structures, but in the case of diesel engines, AE attenuation is more complicated because cast iron, the typical material used in diesel engines, has a higher damping factor which can distort the AE wave further. In this work, it is recognised that the AE wave is extremely complicated, and mathematically intractable so the application of a simplified model of attenuation is therefore investigated where the attenuation factor, k, for the energy in the acquired signals is assumed to decay exponentially due to whatever of the effects discussed here might be involved. Wave speeds are also measured on an engine block and are used to estimate transmission path length from source to sensor so that the relationship between attenuation of AE energy and propagating distance in diesel engines will be obtained. A simple model of attenuation of AE energy would help to locate source position or zone and to gain more understanding of the problems associated with multiple sources. In addition, source location using an arrangement of a triangular sensor array will be studied to find a way to locate multiple sources in diesel engines. Furthermore, source reconstruction, or "spatial reconstitution", will be attempted in this study, where attenuation of AE energy and time-of-flight are the main factors used to reconstitute the signal. This will help to improve resolution of multiple source signals.

Chapter 4 Experimental apparatus and procedures

4.1 Introduction

This chapter describes the experimental apparatus and procedures that were used for the various experiments in the laboratory and at industrial sites. The first part describes some requirements, features and specification of apparatus, where necessary. The second part presents the detail of each experiment of which there were two different series in this research. The first series was a study of AE wave transmission through various simple and complicated cast iron (the most common material used in diesel engines) blocks using a standard Hsu-Nielsen source (pencil lead break). The various blocks in this study were a plate-like engine base, a surface table, a strip, a flat panel forming part of the cylinder block on a large marine diesel engine, the cylinder head and the cylinder block of a small diesel engine and the cylinder head, the cylinder liner and the cylinder block of a large marine diesel engine. The second series was to carry out some running engine tests on a 76 kW (102 Hp) small four-stroke, high speed direct injection (HSDI) diesel engine and a 10 MW large marine diesel engine. The AE signals, which consist of multiple sources from injectors, valves and other mechanical parts, were acquired from the engines and used to study AE wave propagation through engine structures with different loads and speeds.

4.2 Apparatus

A typical AE acquisition system and experimental set-up are shown schematically in Figure 4.1. The system generally comprised a test object, an array of AE sensors with their preamplifiers, a data acquisition card, and a computer with software for controlling the acquisition and storage of data. Two different AE acquisition systems were used and each had its associated software to record the AE signal into a file for later analysis. In addition, other related apparatus was designed and built to suit the experimental needs.

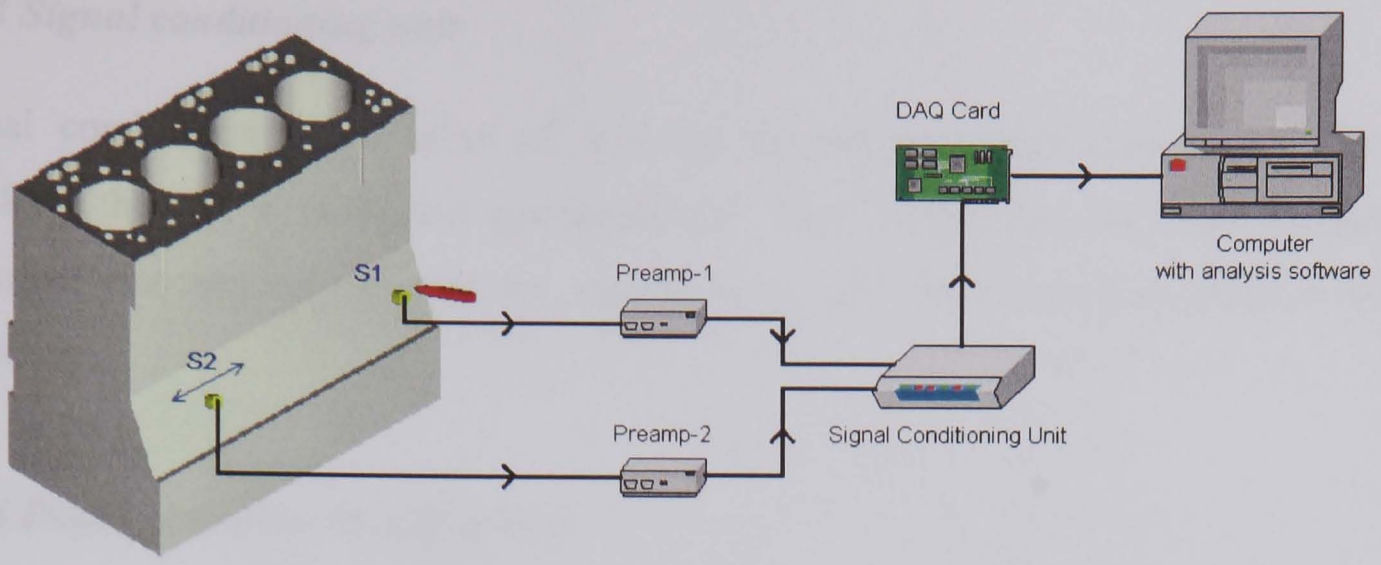

Figure 4.1: Test block and AE acquisition system.

4.2.1 AE sensors and coupling

Commercial broadband AE sensors of type Physical Acoustics (PAC), Micro-80D, based on lead zirconate titanate (PZT), were used to detect AE signals in this research. The AE sensor converts detected waves propagating through the material under examination into a time varying voltage signal. This AE sensor is omnidirectional and produces a relatively flat frequency response from 175 – 1000 kHz, over an operating temperature range from -65 to $+177\ ^{\circ}C$ The sensors are 10 mm in diameter and 12 mm high and were held onto the test object surface using in-house designed magnetic clamps. In order to obtain good transmission of the AE signal, the surface was kept smooth and clean and silicone grease was used as couplant to fill any gaps caused by surface roughness and eliminate air gaps which might otherwise impair AE transmission. The sensitivity of sensor at each position was checked by breaking a pencil close to it [11] and amplitude of signal at each position should be at the same level for example around 4-5 volts.

4.2.2 Preamplifiers

Preamplifiers of type PAC 1220A were used to amplify the AE signal to a level that can be comfortably transmitted and converted by an Analogue to Digital Converter (ADC). They had a switchable 40/60 dB gain and internal bandpass filters from 0.1-1 MHz. The preamplifier was powered by a $+28$ V power supply and used a single BNC connection for both power and signal.

4.2.3 Signal conditioning unit

Signal conditioning units were of in-house construction and were used to power (+28 V) the AE sensors and pre-amplifiers. They could also be used to perform analogue rms processing with the capability of amplification or attenuation where necessary.

4.2.4 Data acquisition (DAQ) system

Most of the experiments in this research were concentrated on acquiring raw AE signals and also required high performance systems and machines, of which two were used. The first was based on an in-house assembled industrial PC with a 12 bit, Compuscope CS512 board. This board occupied one ISA slot and was capable of recording two channels of data at a sampling rate up to 5M samples/s with buffer memory depth of 2 MB. The input range was bi-polar varying from ±100 mV to ±5 V, controlled by the software. This board also had over-voltage protection at ±15 V. The software provided with the DAQ card was DOS based and was used to control some DAQ parameters such as sampling frequency, sample size, input range, pre-trigger data and trigger channel.

The second system was based on an in-house built desktop PC with a 12 bit, National Instruments (NI), PCI-6115 board as seen in Figure 4.2. This board can be used to acquire simultaneously the raw AE signal for 10M samples/s for up to four channels and uses a full length PCI slot in a PC, which has a better transfer rate of data than the older ISA slot. This board is a multifunction analogue, digital and timing device without on-board switches or jumpers so that it can be configured and calibrated by software. The software-programmable gain can be set to 0.2, 0.5, 1, 2, 5, 10 or 50 and covers an input range from ±200 mV to ±42 V. The data can be sampled from 20k samples/s up to 10M samples/s at each channel with a total on board memory of 32 MB. This board supports only differential input configuration and has an over-voltage protection at ±42 V. For source location applications, this board can be used to record raw AE signals (sampled at 5M samples/s) over up to four channels and for a running diesel engine, it can record raw AE at 2.5M – 5M samples/s of an entire engine cycle. LabVIEW software from National Instruments was used to develop a programme to control and to obtain the maximum performance from the PCI-6115 board. This programme could be used to control sampling frequency, number of acquired data per channel, number of records, input range, pre-trigger data, trigger channel and trigger

level. The front panel and the main block diagram of the programme are shown in Figures 4.3 and 4.4. The signals shown in Figure 4.3 were acquired from four AE sensors at different positions for a pencil lead break source.

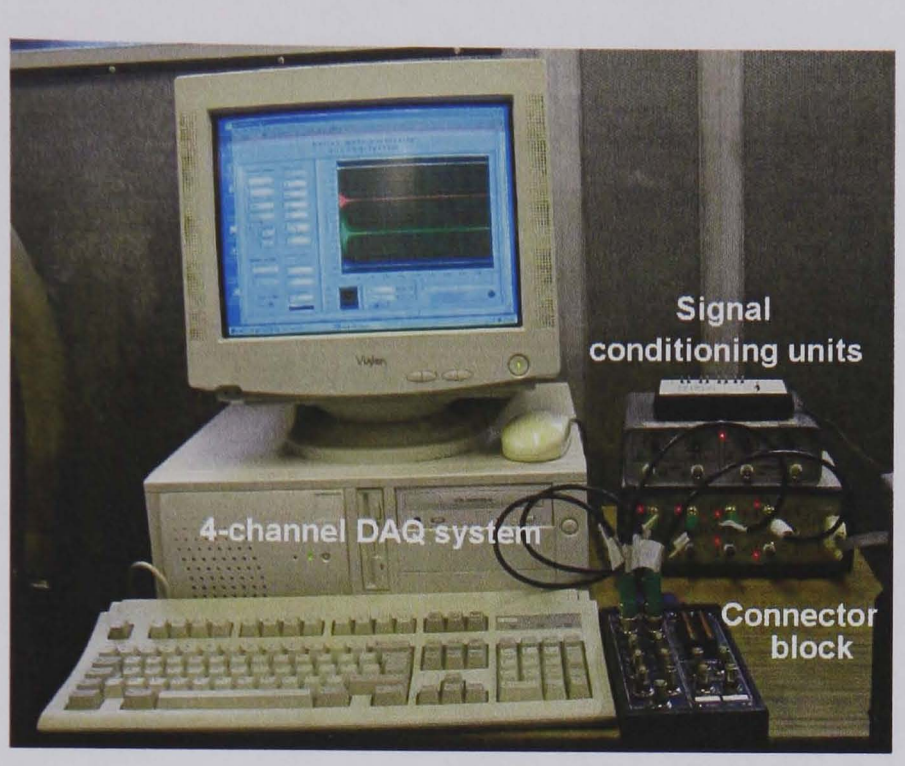

Figure 4.2: 4-Channel DAQ system with connector block and signal condition units.

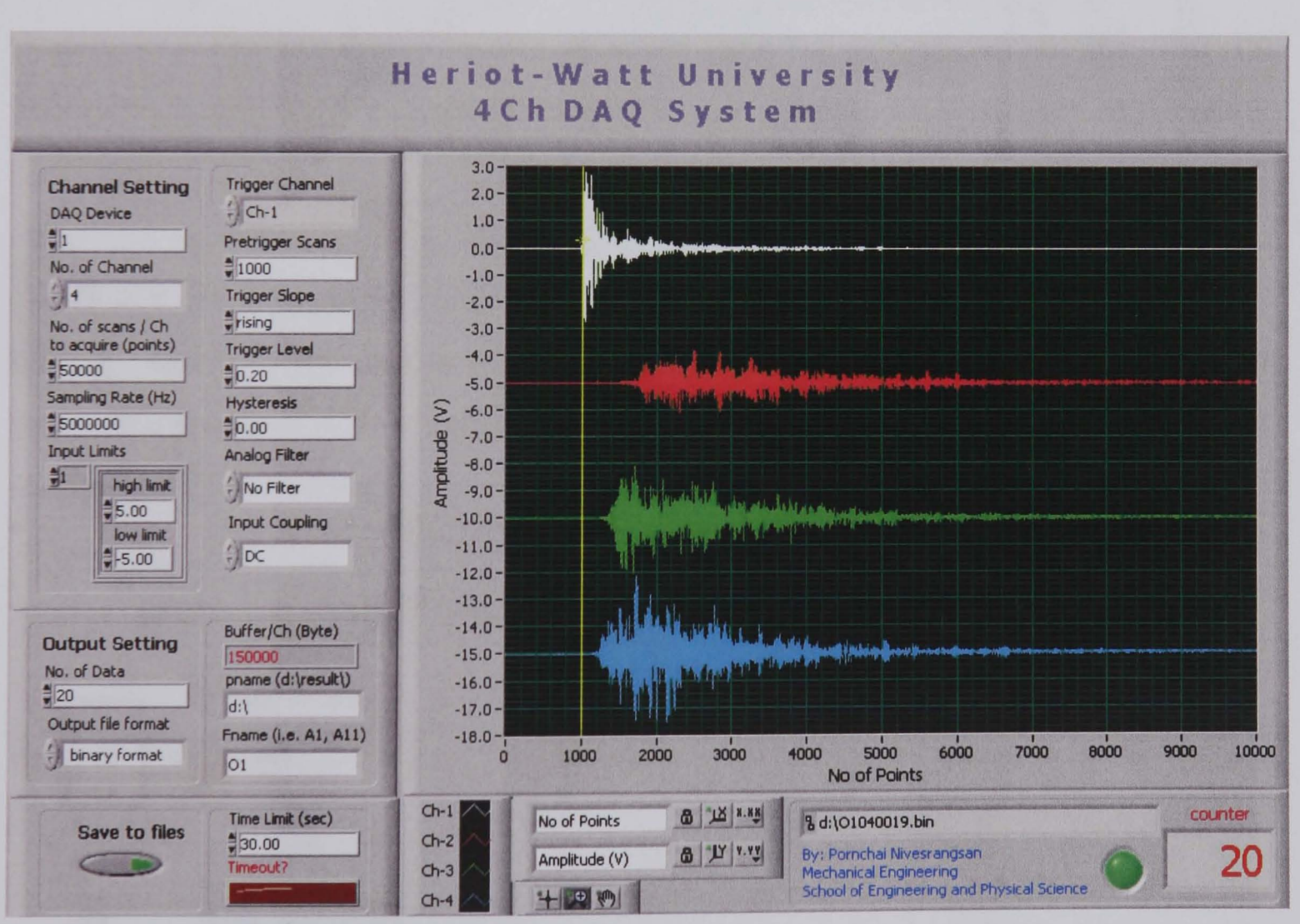

Figure 4.3: Front panel of LabVIEW programme for 4-channel DAQ system.

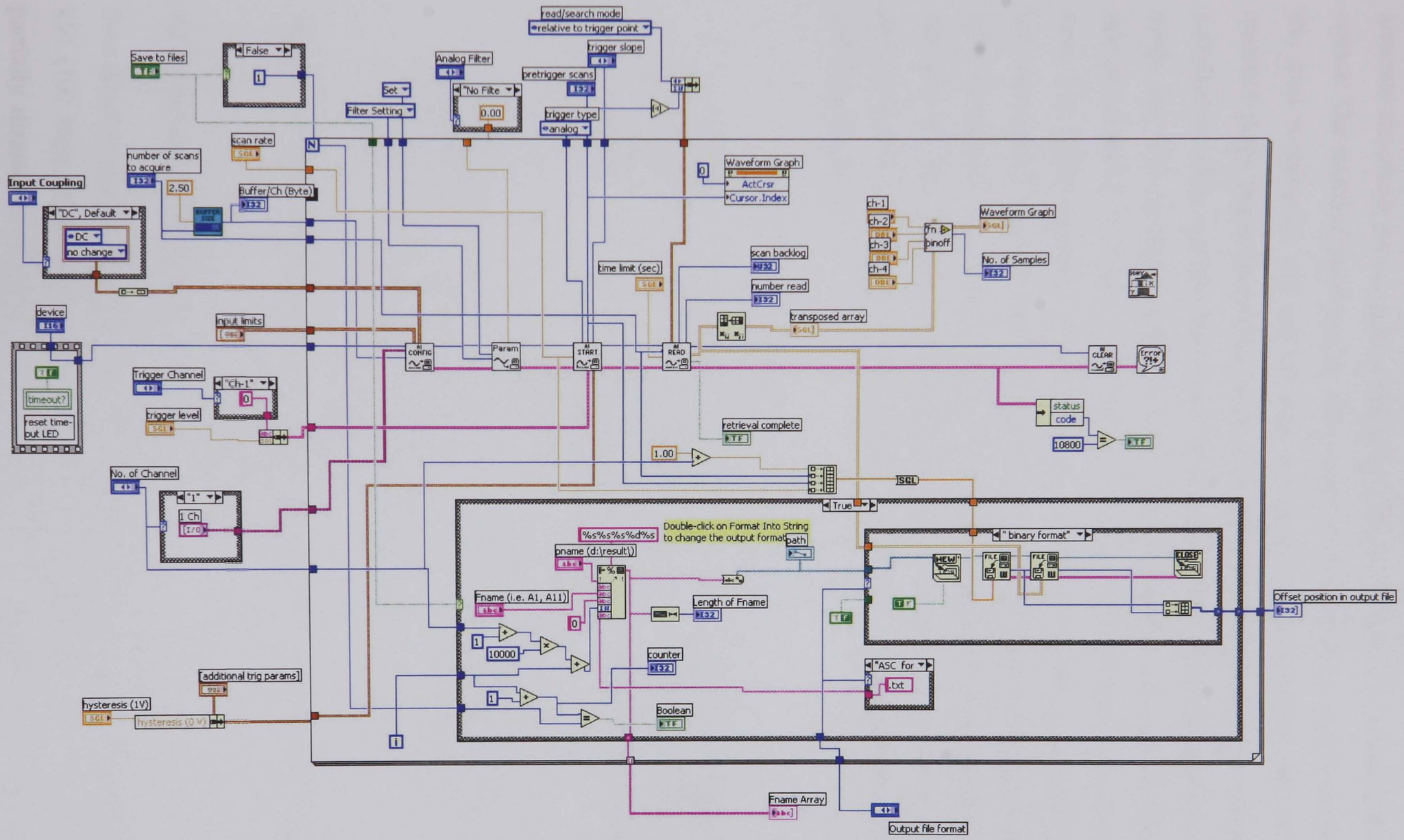

Figure 4.4: Block diagram of LabVIEW programme for 4-channel DAQ system.

4.2.5 Mechanical pencil and guide ring

A commercial mechanical pencil and an in-house machined guide ring were used to generate simulated AE sources by breaking a 2H pencil lead, the so-called Hsu-Nielsen source. The standard guide ring (Nielsen shoe [110]) is normally used to aid in breaking the load consistently and can be seen in Figure 4.5(a). However, the collar of the standard guide ring deforms very easily when pencil lead is breaking and also becomes mis-sharpen when used for many tests. Higo and Inaba [111] have suggested a modified guide ring with increased stiffness of the collar to improve the reproducibility of AE, and this is shown in Figure 4.5(b) and it was such a modified guide ring that was used here. The ASTM standard, E976–99 [110] recommends that the pencil lead should be the same type (0.3 or 0.5 mm diameter, HB or 2H pencil lead) with a length of 2-3 mm and, accordingly this research used a 2H, 0.5 mm diameter lead to generate simulated AE sources. The lead was broken under the same conditions, for example, at the same position on the test surface, using the same angle and the same orientation of the pencil for all repeat tests.

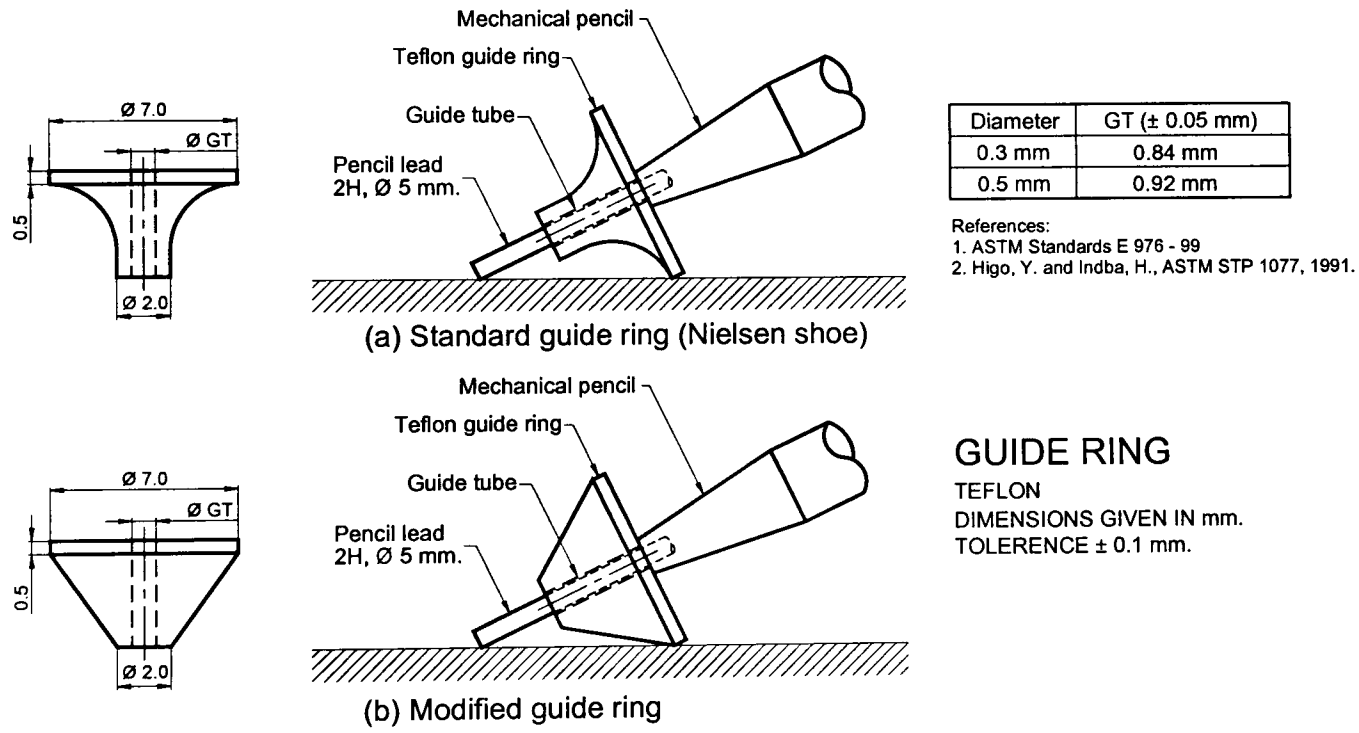

Figure 4.5: Drawing and dimensions of standard (a) and modified (b) guide rings [110, 111].

4.2.6 Four-stroke 76 kW diesel engine

Two diesel engines of this type were used in this research, both Perkins, four-stroke, 76 kW (102 bhp), high speed direct injection (HSDI) diesel engines. The first was the partially disassembled engine shown in Figure 4.6(a), and was used to investigate transmission in the cylinder block, the cylinder head, the cylinders, the injectors and the

valves. Essentially, the standard source (pencil lead break) was used to simulate transmission from various source positions on the cylinder head and cylinder block. The second was a running engine connected to a dynamometer as shown in Figure 4.6(b), in which load could be altered to provide a range of test conditions.

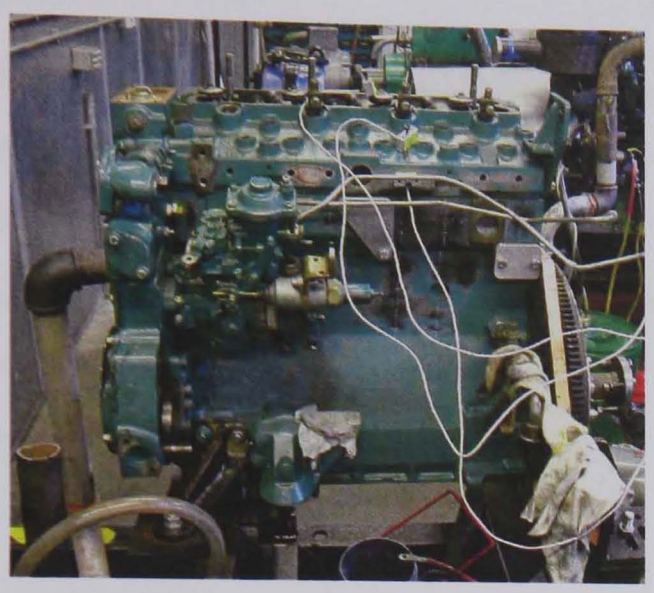

(a) Partially disassembled engine

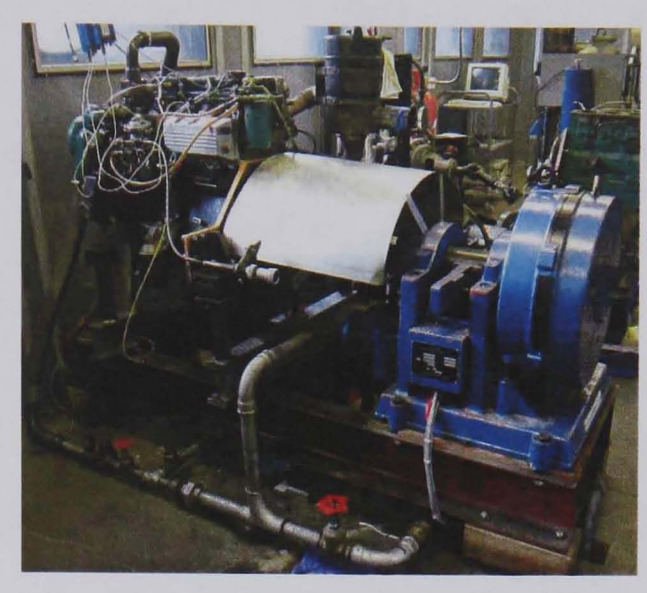

(b) Assembled engine (running engine)

Figure 4.6: Disassembled and running four-stroke, small HSDI diesel engines

4.2.7 Shaft encoder

Shaft encoders are widely used to transform shaft rotation angular position into electrical signals. A commercial incremental shaft encoder, Omron E6C2 – CWZ6C, was used as a timing signal on the running diesel engine so that top dead centre (TDC) position (normally set at TDC of cylinder no. 1) and crank angle positions could be recorded synchronously with the AE signals. The encoder generated 360 pulses per revolution and so had a resolution of around 1 degree. The encoder shown in Figure 4.7 was connected directly to the injector pump shaft by a flexible coupling so that the timing signal could be obtained for the entire engine cycle.

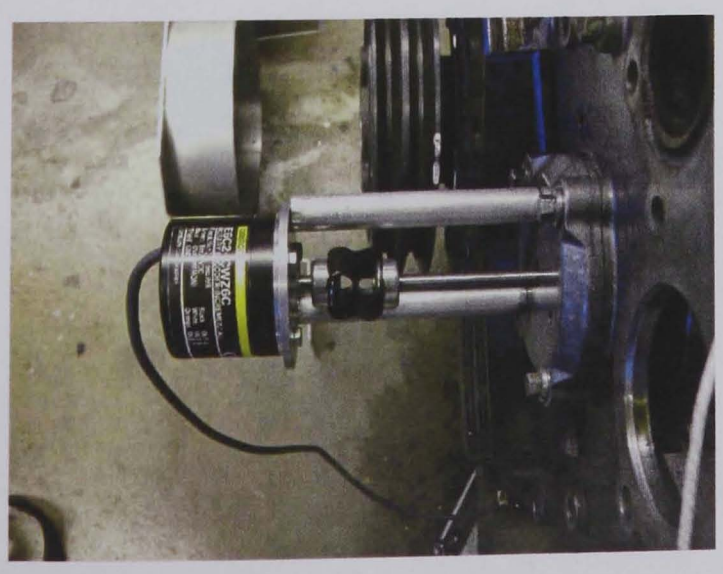

Figure 4.7: Location of shaft encoder on a diesel engine.

4.3 Transmission tests on various cast iron blocks

The objective of these experiments was to study the characteristics of AE wave propagation through various geometries of cast iron, which is used widely in various diesel engine structures as this has not been studied in detail before. Because of its high volumetric content of graphite (typically 25%), cast iron is expected to show much higher damping than, say, steel. Cast iron blocks were selected with a range of geometries and features from simple to more complicated blocks, and included an engine base, a surface table, a strip, a cylinder block and a cylinder head from the small HSDI engine, and a flat panel on a large marine diesel engine. Attenuation of AE wave propagation was determined from the signals acquired by a sensor array. Various AE signal features were also derived such as energy content, frequency content, wave speed and transmission path length. The series of experiments are described in the following sub-sections.

4.3.1 Transmission tests on simple geometric blocks

A variety of simple geometry cast iron blocks (objects) were chosen, including a roughly slab shaped engine base plate of approximate dimensions $965 \times 1370 \times 120$ mm (Figure 4.8(a)), a surface table (Figure 4.8(c)) of approximate dimensions $1220 \times 1860 \times 25$ mm, a strip (Figure 4.8(d)) of approximate dimensions $58 \times 483 \times 5$ mm cut from cylinder head of scrap diesel engine, and a flat panel forming part of one cylinder block of a large marine diesel engine (Figure 4.8(e)) of approximate dimensions $1476 \times 1950 \times 36$ mm. More detailed dimensions and source and sensor positions for each cast iron block can be seen in Appendix A. The objective of these experiments was to determine certain aspects of AE wave propagation on simple geometric blocks which have known dimensions (length, width and thickness). A severe constraint in the simplicity of the experiment was that cast iron is rarely used to make artefacts of constant cross section.

The experiments consisted of acquiring the raw AE from a standard Hsu-Nielsen source acquired at different source-sensor distances (along a straight line) on each of the test blocks as shown in Figure 4.8 assuming that the cross-section was constant between source and sensor. In the experiments, two Physical Acoustics (PAC), micro-80D broadband AE sensors with the output band-pass filtered between 0.1 and 1 MHz were mounted on the surface. The first sensor, S1, was fixed near the source and used as a

trigger to start the acquisition sensor, S2, which was moved to different test positions so that data were acquired for a range of source-sensor distances. The computer with the 4-channel NI acquisition system was used to acquire data with sampling frequency of 5 MHz, except for the strip, where the 2-channel data acquisition system was used to record data with the same sampling frequency. For all tests, five pencil lead breaks gave raw AE records at each position. Almost all tests were carried out in the laboratory except for the flat panel test on the large marine diesel engine, which was performed at an industrial site.

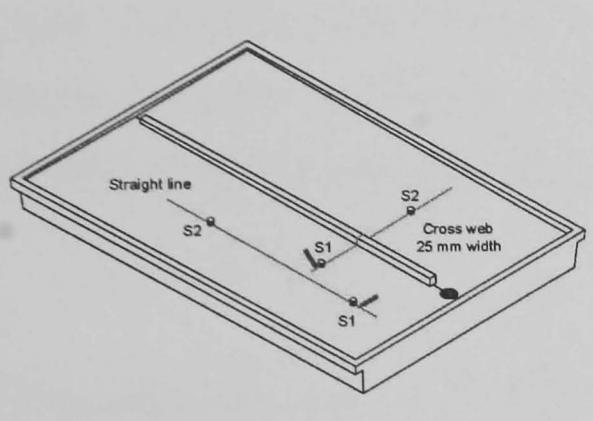

(a) Engine base

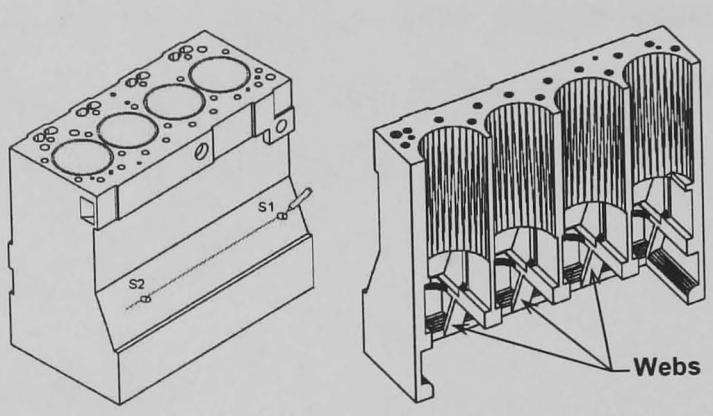

(b) Cylinder block

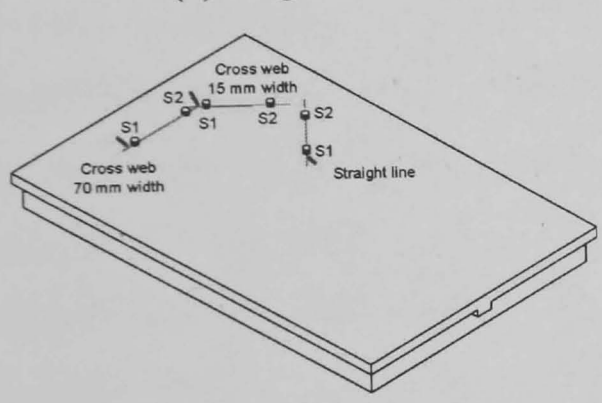

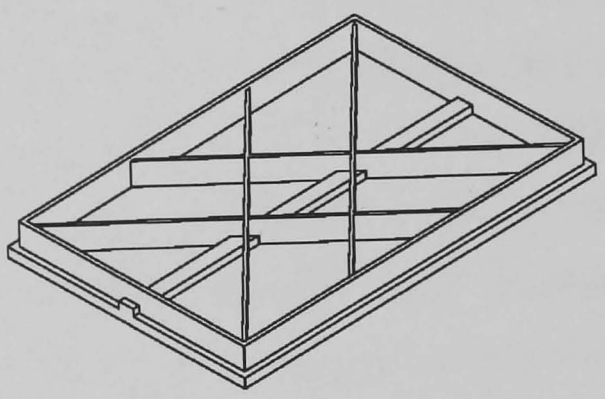

(c) Surface table

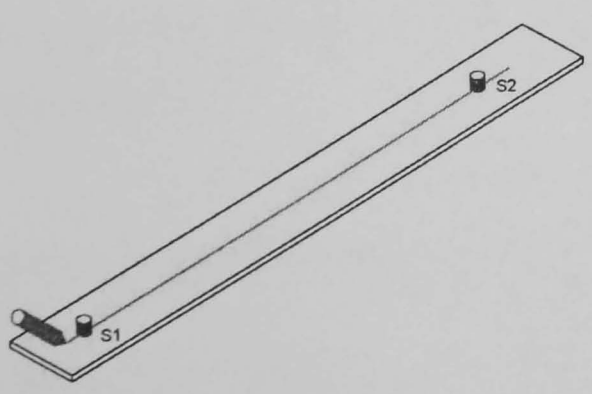

(d) Strip

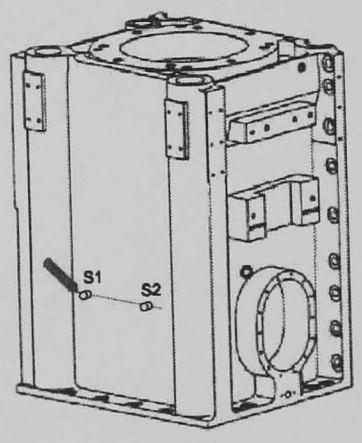

(e) Engine panel

Figure 4.8: Test objects and their various geometries and features.

4.3.2 Transmission tests on complex geometric blocks

The objective of this series of experiments was to determine the effect of AE attenuation on blocks of more complex geometry, where the transmission path involves material of non-uniform cross-section including the effects of reinforcing webs. Here, the varying geometrical complexity was achieved by having source and sensor in opposite sides of the webs on the engine base plate and the surface table and by choosing various paths on the cylinder block of the small diesel engine. The engine base plate had a single fin on its upper surface whereas the surface table and the cylinder block had a web structure on their underside. More detailed information of dimensions and source-sensor positions on these test objects can be seen in Figure 4.8 and Appendix A. The experiments were otherwise identical to those described in Section 4.3.1.

4.4 Transmission tests on small HSDI diesel engine

AE wave transmission in three dimensions (such as in the cylinder head and the cylinder block of an engine) is more complicated than on simple geometries and even than in complex geometries where the source and sensor are on the same surface. Sources inside the engine can reflect, refract and suffer mode conversion before being detected by surface mounted sensors, which may affect the detected signals. In general, AE signals from a running diesel engine are a combination of multiple sources coming from injectors, valves, combustion and ancillary equipment and so these tests used a Hsu-Nielsen to simulate events at the relevant locations and to detect the response at horizontal and vertical sensor arrays on the cylinder block and cylinder head, as described below.

4.4.1 Transmission test on cylinder head of small HSDI diesel engine

The main AE events that occur around the cylinder head of the engine are expected to come from the injectors (INJ), the inlet valves (IV) and the exhaust valves (EV). Therefore, it was decided to examine the effect of AE wave attenuation from those source positions to a horizontal sensor array on the cylinder head. One AE sensor was positioned close to the simulated source and was used as a trigger to start acquiring data where the source signal was generated by breaking a pencil lead on the injector bodies, the tops of IV stems, and the surfaces of EV spring seats on each cylinder. The

remaining three sensors were positioned sequentially in groups of three around the cylinder head to cover all the positions from P1 to P9 as shown in Figure 4.9. The 4-channel DAQ card (National Instruments, PCI-6115) was used to acquire data with sampling frequency of 5 MHz, and five raw AE records were acquired for each combination of source and sensor positions.

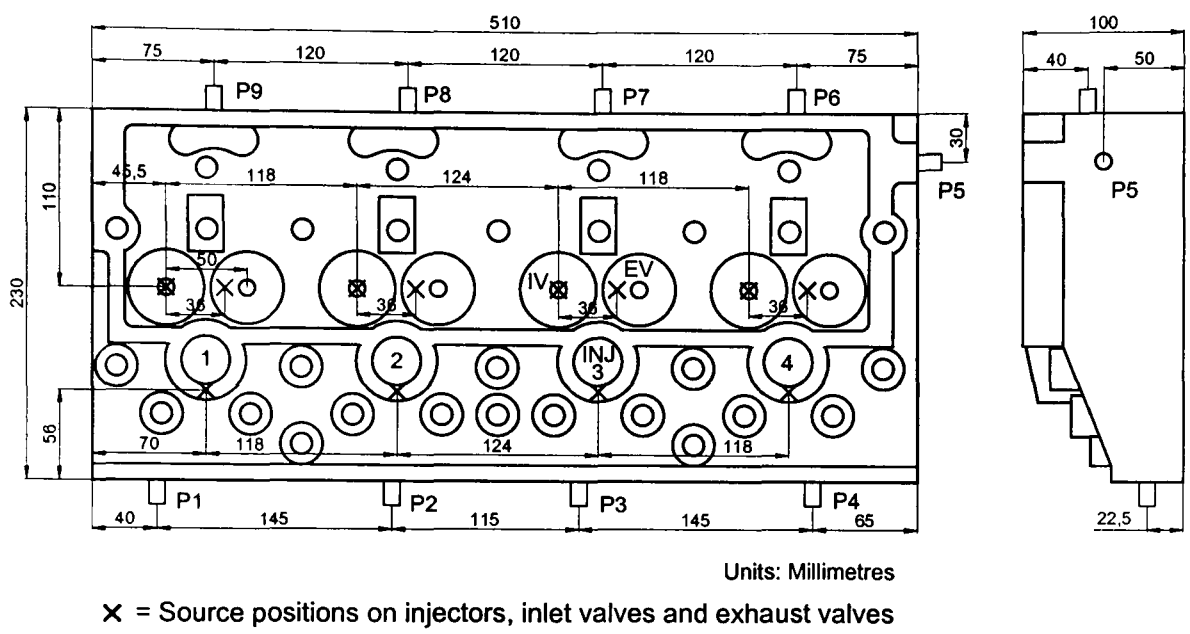

Figure 4.9: Drawings and dimensions of cylinder head of four-stroke HSDI diesel engine showing sensor positions (P1 – P9) and various source positions on injectors, top of IV stems and surface of EV spring bases.

4.4.2 Transmission test across head gasket for horizontal sensor array on cylinder block

Sources can potentially be adjacent to the cylinder head or the cylinder block, or bolts, and so it is worth knowing the attenuation rate of AE energy when a wave propagates across boundaries such as the head gasket. Transmission tests across the cylinder head were carried out using a simulated source in the same positions as in Section 4.4.1. As before, the first sensor was positioned close to the source as a trigger and the remaining three sensors were placed at various horizontal sensor positions on the cylinder block. Two horizontal sensor arrays were selected at 30 mm and 120 mm below the top surface of the cylinder block as shown in Figure 4.10. A number of sensor positions on both sensor array levels were selected which it would be possible to use on both the disassembled block and a running engine block, with 12 positions (P1-P12) for the array at level 1 and 9 positions (Q1-Q9) for the array at level 2. As before, the 4–channel, National Instruments PCI-6115 card was used with a sampling frequency of 5 MHz, and five raw AE records were acquired for each source-sensor combination.

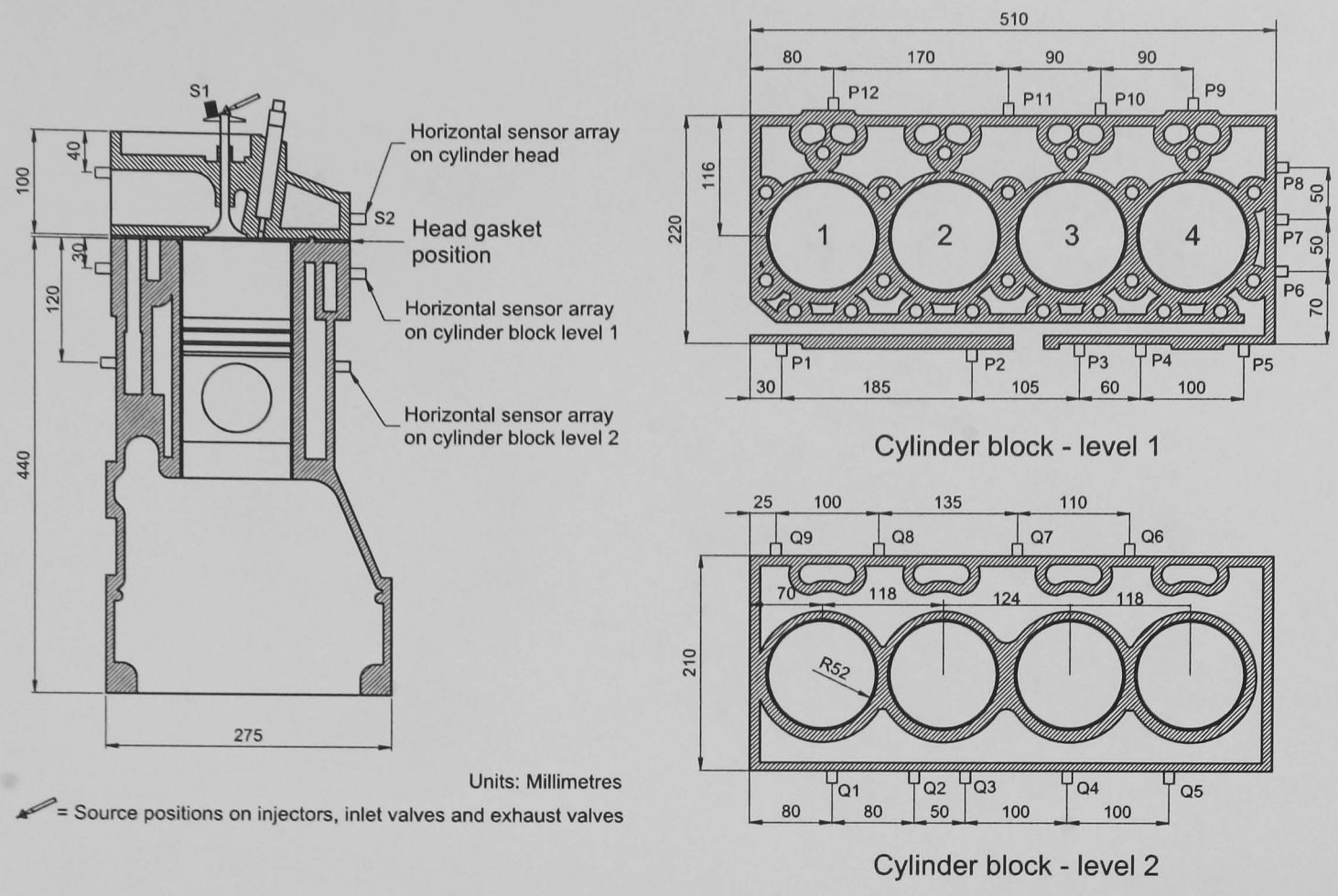

Figure 4.10: Section drawings of cylinder head and block of four-stroke HSDI small diesel engine showing two horizontal sensor arrays on the cylinder block (P1 – P9 for level 1 and Q1 – Q9 for level 2). The source was generated using a pencil lead break on injectors, IV stems and EV spring bases as shown in Figure 4.9.

4.4.3 Transmission tests on cylinder block of small HSDI diesel engine

The combustion process is the main mechanical event in the engine although it is not clear how much AE is generated during combustion. The experiment was set up to determine attenuation of sources propagating from each cylinder to sensor arrays around the cylinder block. Two horizontal arrays were selected 30 mm and 120 mm below the top surface of the cylinder block as shown in Figure 4.11, and each piston was placed at around 75 mm below the top surface of the cylinder block. Pencil lead breaks were used to generate AE at positions A1 and A3 on the internal surface of each cylinder liner around 30 mm below the top surface of the cylinder block. Experiments were carried out with and without water inside the gallery in the cylinder block. The tests without water inside the gallery involved signals from sources at A1 and A3 on cylinders 1-4, but, for the tests with water filling, only sources generated at A1 and A3 for cylinder no. 1 were used. As before, four AE sensors were used, one being fixed close to the source position as trigger, with the remaining three being mounted around the cylinder block and moved to cover all the test positions (P1-P12) and (Q1-Q9). The data acquisition strategy was as for Sections 4.4.1 and 4.4.2.

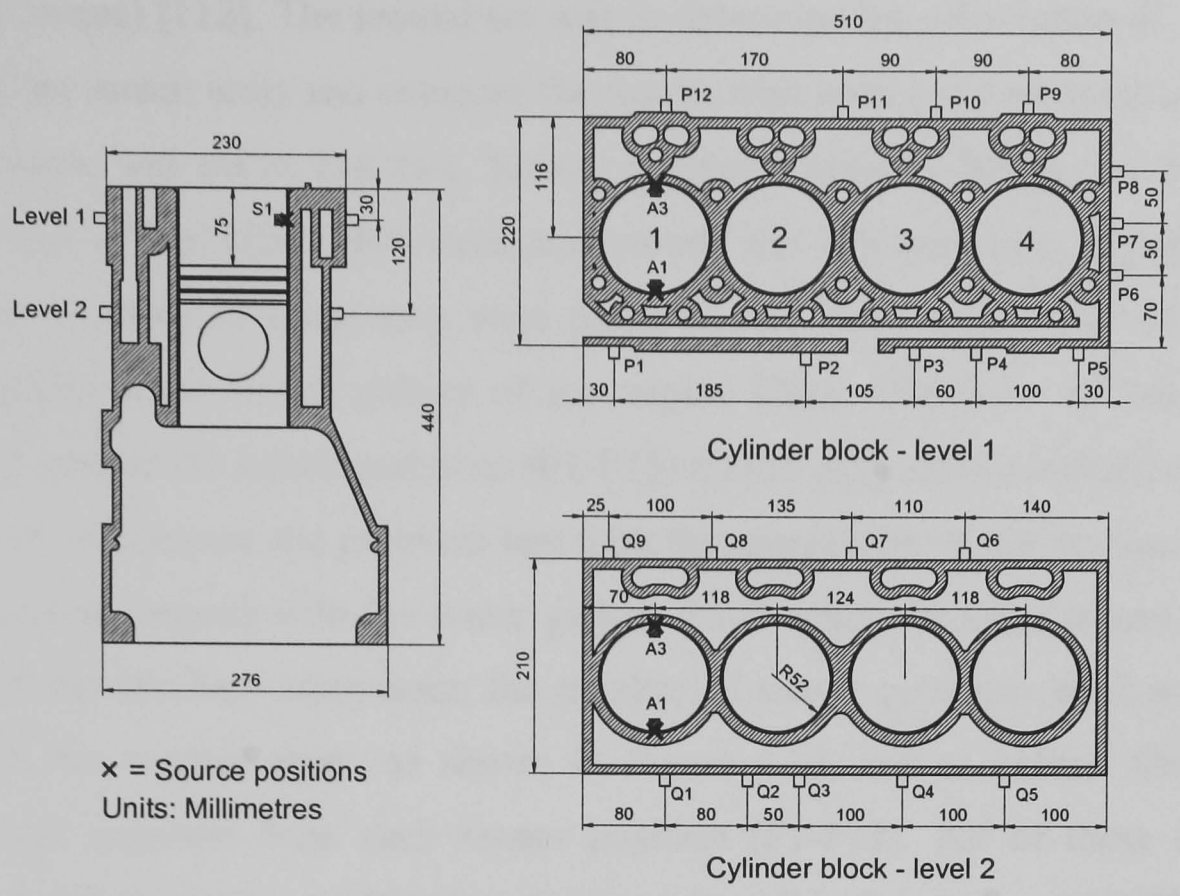

Figure 4.11: Section drawings and dimensions of cylinder block of Perkins, four-stroke HSDI diesel engine showing; two levels of sensor arrays at 3 cm (P1 – P12) and 12 cm (Q1 – Q9) from top surface of cylinder block; and various source positions on the surface of each cylinder (A1&A3, 3 cm from top surface of cylinder block).

4.4.4 Transmission test across head gasket for vertical sensor array

The tests in Sections 4.4.1 and 4.4.3 used horizontal sensor arrays either on the cylinder head or the cylinder block to detect signals where source and sensor were on the same block. In Section 4.4.2, a horizontal sensor array on the cylinder block was used to interrogate AE sources generated at various positions on the cylinder head. A final set of experiments was set up to investigate specifically vertical wave propagation by using vertical sensor arrays as shown in Figure 4.12 (vertical straight line on front elevation running from injector no. 3 to cylinder block) and also to compare the attenuation of AE energy with the results from horizontal sensor arrays. The tests were carried out using a Hsu-Nielsen source applied at various positions around cylinder no. 3; on the injector body, the top of the IV stem, and the surface of EV spring base. As before, the first AE sensor was positioned close to the source as a trigger and the remainder (three AE sensors) were positioned in the vertical array.

Three sets of experiments were performed, the first of which was to investigate if AE propagates through the bolts from the cylinder head to the cylinder block. In this test, the source was applied to the top of IV no. 3 stem with the head gasket bolts loose, finger tight, and at torques of 45, 80 and 110 Nm (the last being the recommended

tightening torque) [112]. The second set was to determine the attenuation of AE energy in the vertical sensor array and compare the results with horizontal sensor arrays, and so the bolt torque was set at 110 Nm. Source positions were, as before, on the injector body, the top of the inlet valve stem and around the exhaust valve spring bases on cylinder no. 3. Both of these tests were performed on the disassembled HSDI diesel engine without water in the gallery of the engine block. Five raw AE records were acquired at each of the sensor positions (P1-P15) on the array shown in Figure 4.12. The last test was to compare the previous test with the attenuation of AE on the assembled engine (running engine) with the water gallery filled using the same source positions. Because of the ancillary equipment, the number of sensor positions used was slightly reduced on the vertical array, as shown in Figure 4.13, and as before, five raw AE records were acquired from each sensor position (P1-P12). All of these tests were carried out with the 4–channel DAQ card using a sampling frequency of 5 MHz.

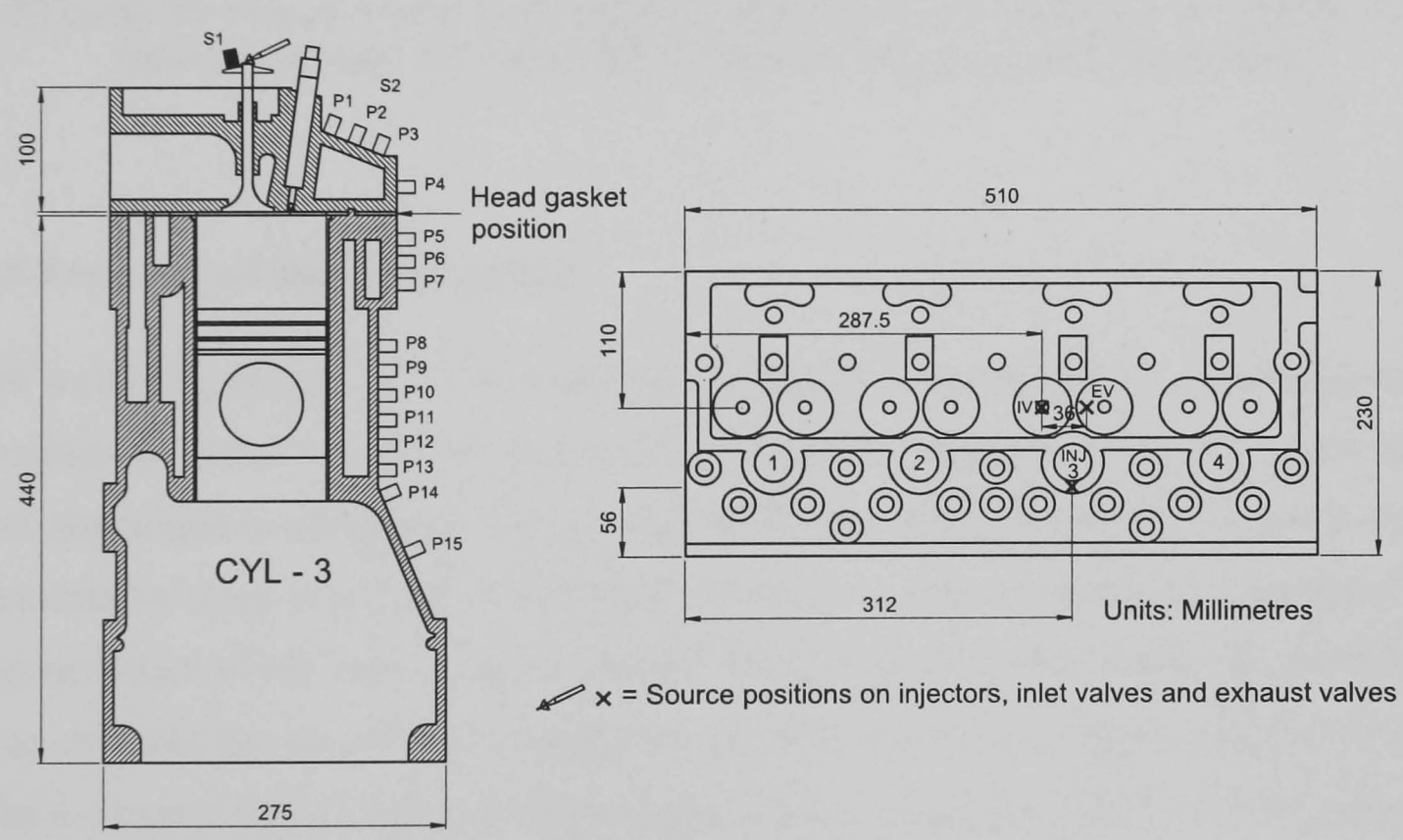

Figure 4.12: Drawings, sections and dimensions of the cylinder head and the cylinder block of four-stroke HSDI diesel engine (disassembled engine) showing sensor positions (P1 – P15) on the vertical sensor array around injector no. 3 and various source positions on the injector body, the top of the IV stem and around the EV spring base.

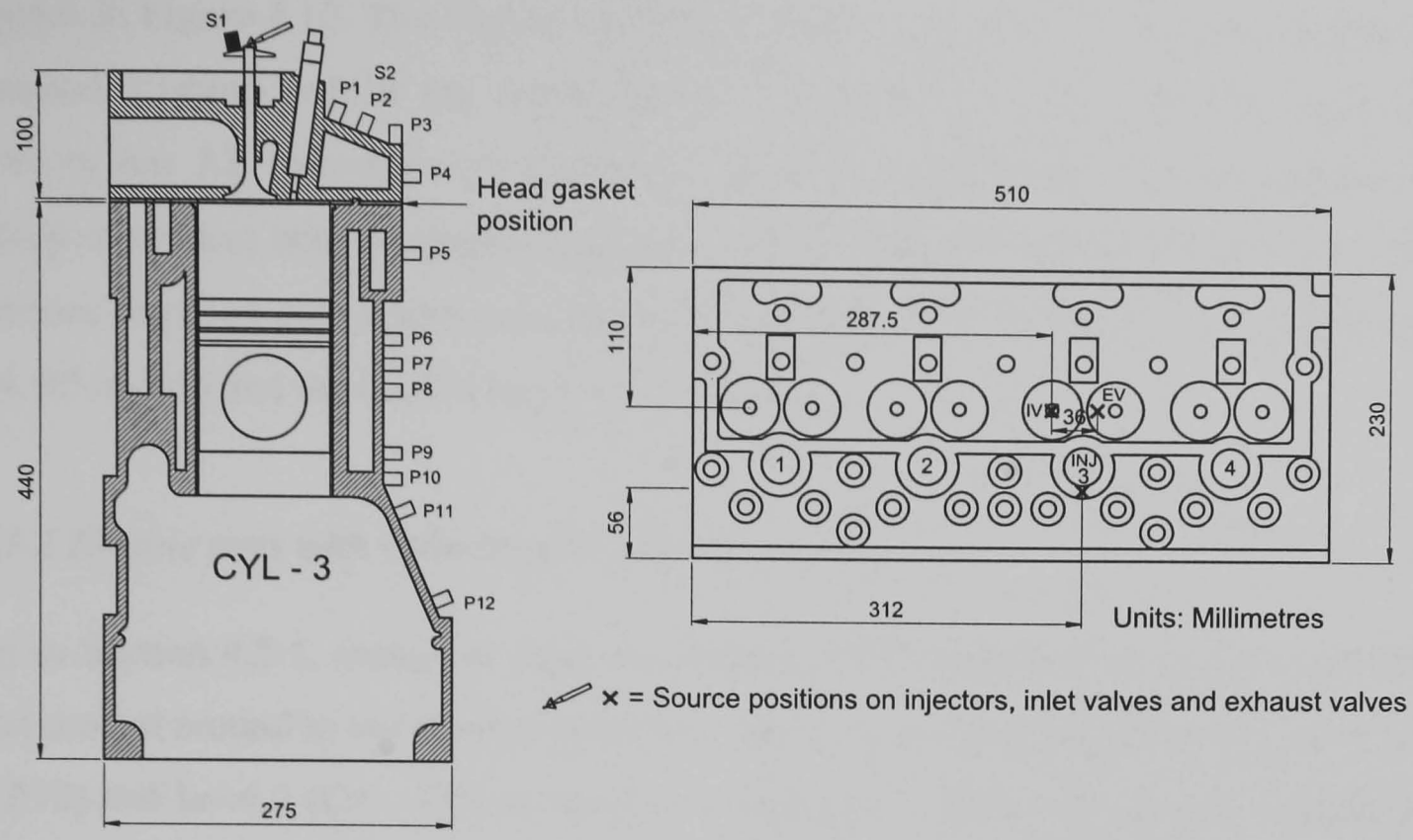

Figure 4.13: Drawings, sections and dimensions of the cylinder head and the cylinder block of four-stroke HSDI diesel engine (running engine) showing sensor positions (P1 – P12) on the vertical sensor array around injector no. 3 and various source positions on the injector body, the top of the IV stem and around the EV spring base.

4.5 Tests on running HSDI engine

For a running engine, it is expected that the acquired signal will be a combination of mechanical impacts and fluid excitation coming from injectors, IVs, EVs, combustion and also ancillary equipment. The purpose of these tests was to exploit the results of the transmission tests described in Section 4.4 on real sources to examine the potential for reconstitution of the various source signals. The test rig described earlier (Figure 4.6(b)) was used and the engine was connected to the dynamometer so that it could be loaded. The 4–channel DAQ (National Instruments, PCI-6115) system with LabVIEW program was used to acquire data for all running tests. Three AE sensors were used to obtain raw AE signals, the last channel being required to record the shaft encoder signal, which was a combination of TDC and timing signals. The shaft encoder signal was used as a trigger to start acquiring data from the AE sensors. The various tests for the running engine are described in the following section.

4.5.1 Engine tests with cylinder head array

Groups of three AE sensors were positioned on the cylinder head, and moved around to cover all positions on the horizontal sensor array on the cylinder head (P1 – P9) as

shown in Figure 4.10. The engine was run normally with no load and with a small load (around 30 Nm), whilst the engine speed was adjusted to 800 rpm and 1200 rpm. Twenty raw AE records ($\approx$1.5 cycles per record) were acquired at each condition and group of sensors with a sampling frequency of 2.5 MHz. Note that only groups of three sensors acquired data simultaneously the first being P1, P2, and P3, the second being P4, P5 and P6 and the third being P7, P8 and P9.

4.5.2 Engine tests with cylinder block array

As in Section 4.5.1, groups of three AE sensors were positioned on the cylinder block, and moved around to cover all positions on the two horizontal sensor arrays, level 1 (P1 – P12) and level 2 (Q1 – Q9) as shown in Figure 4.11. Again, the engine was run with no load and with a small amount of load with the engine speed at 800 rpm and 1200 rpm, and twenty raw AE records ($\approx$1.5 cycles per record) acquired at each condition and set of positions.

4.5.3 Engine tests with vertical array

These tests were identical to those described in Sections 4.5.1 and 4.5.2, except that the vertical array around injector no. 3 (Figure 4.13) was used to acquire data.

4.5.4 Engine tests for source location and signal reconstitution

These tests were identical to the engine tests in Section 4.5.1, except that the shaft encoder and TDC signals were not acquired in this case. The purpose was to demonstrate applications of source location and signal reconstitution for multiple-source signals. With this in mind groups of four AE signals were acquired simultaneously always with reference to P4 using the cylinder head array as seen in Figure 4.9, in the following groups; P1-2-3-4, P5-6-7-4, P-6-8-9-4, and P1-4-7-8. Five raw AE signals were acquired ($\approx$1.5 cycles per each signal) for each test with a sampling rate of 2.5 MHz. The engine was run with no load at the engine speed of 800 rpm

4.6 Transmission tests on 10 MW large marine diesel engine

Transmission tests were carried out on various parts of a large 10MW marine diesel engine including sources at injector, valve housing, cylinder liner, and cylinder block. The purpose of the tests was to study propagation of AE in a larger scale diesel engine in order that some generic conclusions might be drawn. The engine was in use for power generation on the Greek Island of Kos. The Hsu-Nielsen source was impractical for longer transmission paths because the signal energy is too weak for AE wave propagation over such large distances (over 1m) and across boundaries and features. In this case, the source signal was generated using a spring-loaded centre-punch, which has a larger amount of energy than a pencil lead although is not as controllable or as reproducible. Three AE sensors were used with the 4 – channel DAQ card operating at a sampling frequency of 5 MHz. The transmission tests carried out on the large marine diesel engine are described in the following sections.

4.6.1 Transmission tests from injector to valve housing, cylinder liner and cylinder block on 10 MW engine

Figure 4.14 shows schematically the construction of the cylinder head and block of the engine, which essentially consists of a set of cylinder liners embedded in an engine block above the crank-case. The upper parts of the liners are exposed and each has its own cover with valve housing and injector gear. Three AE sensors were used to acquire AE generated by the automatic centre-punch at the injector head (P1a) of cylinder no. 3. The first AE sensor was fixed close to the source at the injector head (P1a) and was used as a trigger, and the remaining sensors were mounted on the valve housing (P1b), and on the upper part of the exposed cylinder liner (P2). The two sensors were then moved to cover the rest of the positions on the lower part of exposed cylinder liner (P3), the flat surface of the cylinder frame (P4a and P5a) and the surface of the web on the cylinder frame (P4b and P5b) as shown in Figure 4.14. Ten records of raw AE signals were acquired for each test.

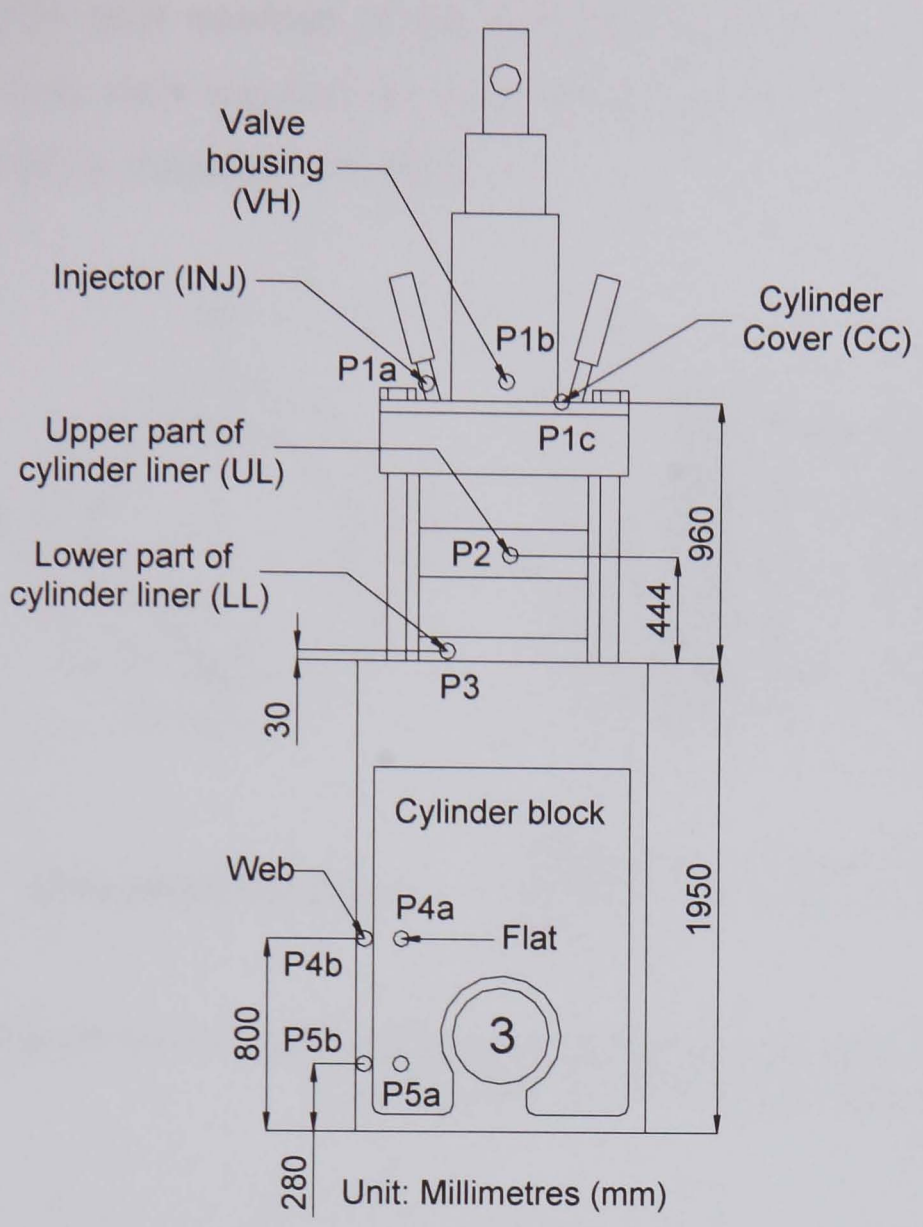

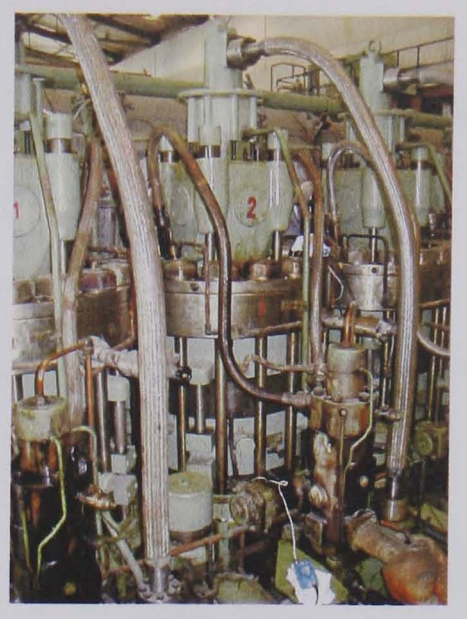

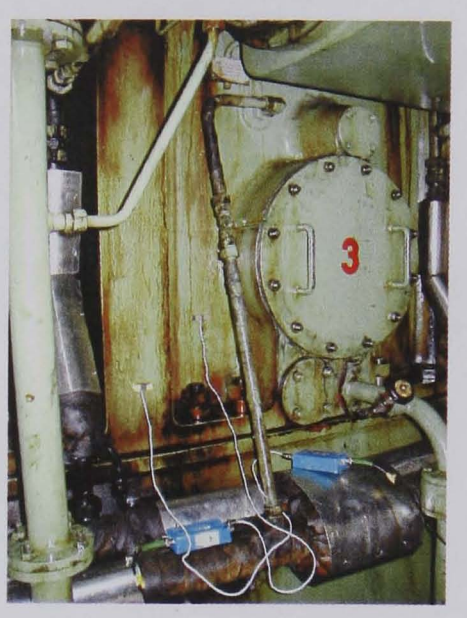

Figure 4.14: Schematic diagram of large marine diesel engine showing sensor positions on valve housing, injector body, liner, and cylinder block.

4.6.2 Transmission tests on cylinder liner

The cylinder liner forms one of the main structural components of a large marine diesel engine, and is connected to the valve housing, cylinder cover and cylinder block. The liner has two exposed areas on which a sensor can be applied as shown in Figure 4.14, and a variety of mechanical sources are possible associated with the piston moving inside the liner. The geometry of the liner is quite complex because of lubrication and cooling channels and also features associated with cylinder-liner interaction such as scavenge ports. AE propagation in the liner was studied because it is potentially possible to isolate signals associated with piston ring/liner interaction at one end or the other, even using the two positions, P2 and P3 (Figure 4.14) relatively near the top.

Four AE sensors were used to record raw AE signals from a source, generated by breaking a 2H pencil lead. One sensor (S1) was used as a trigger and was moved down the internal surface of the liner along with the source. Three other AE sensors were placed on the outside surface of the upper part of the liner at fixed positions S2, S3 and

S4 (at each quadrant of the cylinder liner), as shown in Figure 4.15. Five raw AE records were acquired for each source position, using the NI 6115 DAQ card with a sampling frequency of 5 MHz.

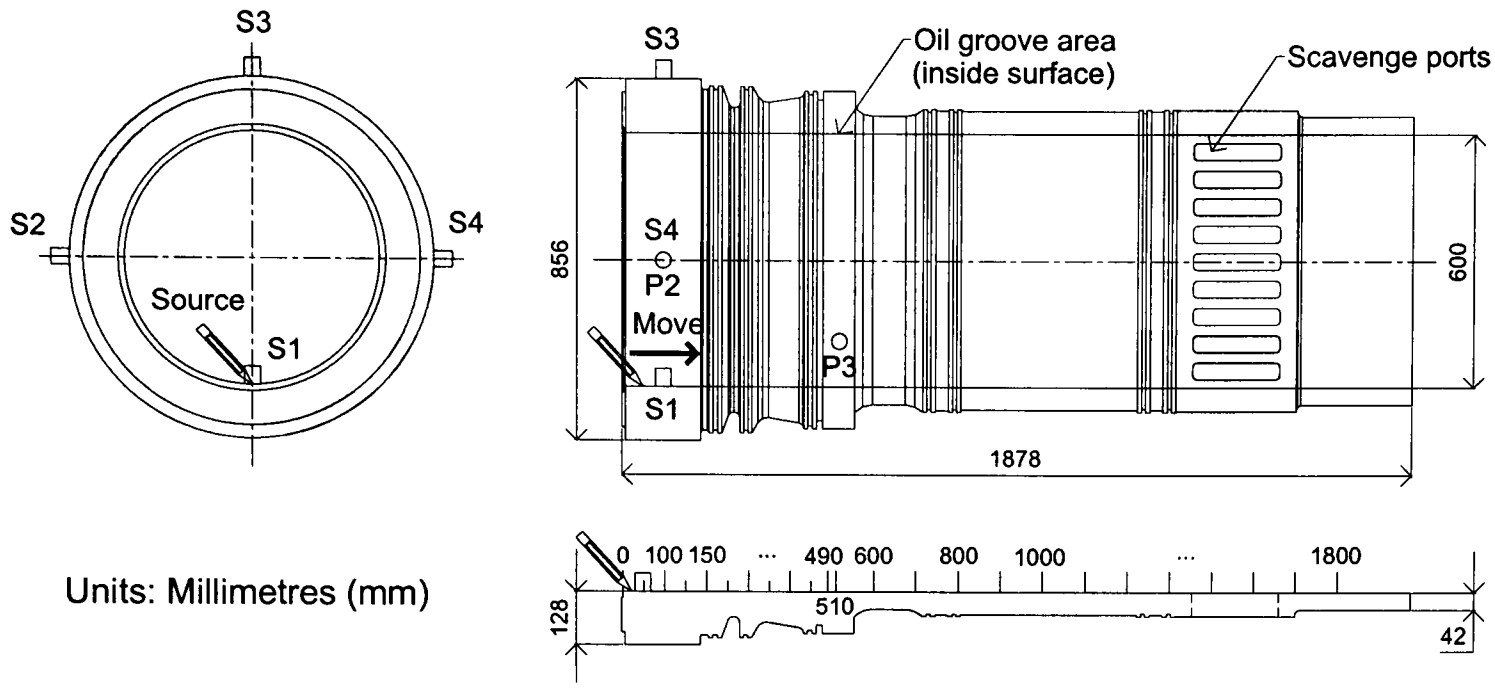

Figure 4.15: Overall dimensions, geometric features, source and sensor positions on cylinder liner of 10 MW marine diesel engine.

4.7 Running Tests on 10 MW marine diesel engine

For a large scale running engine, it is expected that the acquired signal will be a combination of mechanical and fluid excitation coming from injectors, combustion, scavenging, EV and also ancillary equipment. Furthermore, it was expected that the long distances and relative structural isolation of the cylinder would mean that only sources from the local cylinder would be detectible at any given sensor position. The purpose of these tests was to use the analysis method of AE attenuation using a real source from the small HSDI engine applied to examine a single cylinder of the large marine diesel engine and then compare with the results of the transmission tests described in Section 4.6. Raw AE signals were acquired from various positions such as the injector (P1a), the valve housing (P1b), the upper liner (P2) and the lower liner (P3) of cylinder no. 2 on a large marine diesel engine as shown in Figure 4.14. The engine was connected to an electric generator and was operated at constant speed and approximately 9 MW load. The 4–channel DAQ (National Instruments, PCI-6115) system with LabVIEW program was used to acquire data from all running tests. Two AE sensors were used to obtain raw AE signals, the other two channels being required to record the shaft encoder signal and TDC (referenced to cylinder no. 1) signals. The

TDC signal was used as a trigger to start acquiring data from the AE sensors and the timing signal. Three raw AE records (≈2.5 cycles per record) were acquired from each set of positions with a sampling frequency of 2.5 MHz. It might be noted that the results given here for this engine only concern a small part of a more extensive study carried of the monitoring and management of this type of engine using AE [113].

4.8 Summary of experiments

Table 4.1 summarises all tests carried out on various cast iron shapes (Figure 4.8), the small HSDI diesel engine block (Figures 4.9-4.13), and also the 10 MW engine and liners (Figures 4.14-4.15). The test conditions (or sources), array positions, and total records and data size are also shown in the table. The analysis of these results is discussed in the following two chapters for transmission tests and running engine tests, respectively.

No	Experimental details	Source types	No. of tests	No. of sensor positions	No. of records per position	Total records	Data sizes (MB)
1	Transmission tests on various cast iron blocks (see Section 4.3)						
	1.1 Engine base	Pencil	1	21	5	210	16
	1.2 Surface table	Pencil	1	21	5	210	40
	1.3 Flat panel of a 10 MW large marine diesel engine	Pencil	1	8	5	80	31
	1.4 Strip (cut from scrap diesel engine)	Pencil	1	19	5	190	190
	1.5 Cylinder block of a small diesel engine	Pencil	1	19	5	190	190
	1.6 Engine base with web 25 mm width	Pencil	1	18	5	180	14
	1.7 Surface table with web 15 mm width	Pencil	1	12	5	120	120
	1.8 Surface table with web 70 mm width	Pencil	1	11	5	110	110
2	Transmission tests on a 3D small diesel engine block (see Section 4.4)						
	2.1 From injectors, IV and EV to sensor array on cylinder head	Pencil	12	9	5	1080	205
	2.2 From injectors, IV and EV to sensor array on cylinder block level 1	Pencil	12	12	5	1440	274
	2.3 From injectors, IV and EV to sensor array on cylinder block level 2	Pencil	12	9	5	1080	205
	2.4 From cylinder liner to sensor array on cylinder block level 1 (dry)	Pencil	8	12	5	960	106
	2.5 From cylinder liner to sensor array on cylinder block level 2 (dry)	Pencil	8	9	5	720	100
	2.6 From cylinder liner to sensor array on cylinder block level 1 (wet)	Pencil	2	12	5	240	19
	2.7 From cylinder liner to sensor array on cylinder block level 2 (wet)	Pencil	2	9	5	180	14
	2.8 From IV3 to vertical sensor array (dry) with various set screw forces	Pencil	5	15	5	750	153
	2.9 From INJ3, IV3 & EV3 to vertical sensor array (dry)	Pencil	3	15	5	450	86
	2.10 From INJ3, IV3 & EV3 to vertical sensor array (wet)	Pencil	3	12	5	360	69
3	Tests on a running HSDI engine (see Section 4.5)						
	3.1 Engine tests with cylinder head array	Real sources	4	9	20	720	1200
	3.2 Engine tests with cylinder head block array (level 1)	Real sources	4	12	20	960	1600
	3.3 Engine tests with cylinder head block array (level 2)	Real sources	4	9	20	720	1550
	3.4 Engine tests with vertical array	Real sources	2	12	20	480	1272
	3.5 Engine tests for source location and signal reconstitution	Real sources	1	12	5	20	180
4	Transmission tests on 10 MW large marine diesel engine (see Section 4.6)						
	4.1 From injector to valve housing, cylinder liner and cylinder block	Centre-punch	1	7	10	140	73
	4.2 Transmission tests on cylinder liner	Pencil	37	3	5	1110	423
5	Tests on a running large marine diesel engine (see Section 4.7)	Real sources	1	4	6	12	293
	Total		**128**			**12712**	**8533**

Remark: Source types, Pencil – Pencil lead break; Centre-punch – Automatic centre-punch; and Real – running engine sources.

Table 4.1: Summary of experiments carried out on various test objects in Sections 4.3-4.7.

Chapter 5 AE transmission tests

5.1 Introduction

This chapter describes and discusses the results of the various tests using simulated sources for transmission on various cast iron blocks, on engine blocks of the small HSDI diesel engines and on the 10 MW diesel engine, all described in Chapter 4. The analysis techniques used in this chapter, which are described first, are based mostly on relatively simple statistical signal processing techniques. The focus is on AE wave propagation, in particular the effects of wave attenuation and time-of-flight through simple and more complex structures. The techniques are used to observe features of the detected AE signals, which are derived from analysis in the time domain, the frequency domain, and a combination of time and frequency domain. The approach is to examine the effects of scaling from small four-stroke to very large two-stroke engines and from simple to more complex geometry in order to develop a more generic methodology.

5.2 Analysis techniques

The main objective of the analysis was to develop signal processing techniques to describe the nature of AE waves propagating through objects where the geometry varies from simple to very complex. In almost all cases, the material is cast iron which shows relatively high internal damping for a metal. For the most part, the source is that resulting from a pencil lead break (Hsu-Nielsen source), which results in a step-unload of the surface, generating a single impulse at a single point.

For all the transmission tests on the various objects, raw AE signals were acquired at a sampling rate of 5 MHz for a fixed period of 10 ms (50000 points), and energy content, attenuation factor, frequency content, wave speed and transmission path length were determined using time domain, frequency domain, and a combination of time and frequency domain processing.

5.2.1 Time domain analysis

A typical raw AE signal obtained from transmission tests on a relatively simple structure such as one of the cast iron blocks can be seen in Figure 5.1(a) where source and sensor are on the same surface. One general observation of the signal is that a lower energy, faster wave (which may be made up of one or a number of modes) precedes the main signal, which carries the peak amplitude of the signal. On the other hand, Figure 5.1(b) shows an example of raw AE signal obtained from a more complicated structure such as the cylinder head of the small diesel engine where source and sensor are on different surfaces. It can be seen that here it is difficult to separate the waves from each other because the effects of wave attenuation, reflection, refraction and mode conversion distort the AE wave.

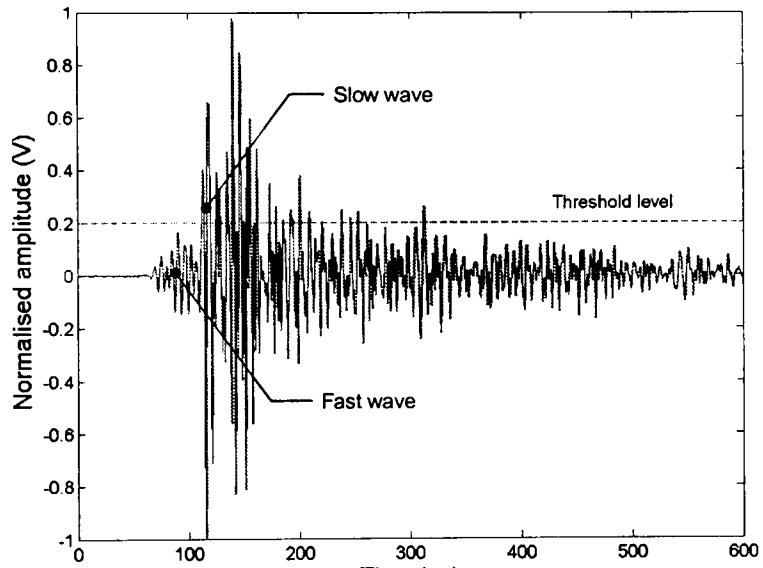

(a) A raw AE signal from one of the cast iron blocks

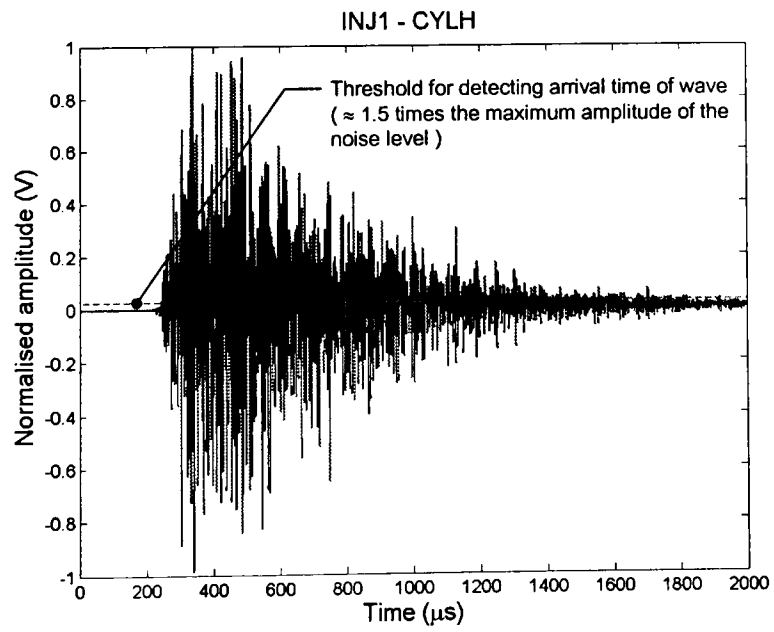

(b) Raw AE signal acquired from a cylinder head source

Figure 5.1: Example of raw AE signals showing fast wave, slow wave and threshold level.

Energy content is one of the main features used here, determined from the signals by using Equation (3.14). For the transmission tests on cast iron blocks (Section 4.3), the energy content was calculated between the arrival time of the slow wave and the end of the entire signal for each source-sensor pair. The arrival time for the slow wave for the tests on the simpler structures was determined by eye as shown in Figure 5.1(a) as it had to be distinguished from the fast wave arrival. For the more complex geometries described in Sections 4.4 and 4.6, the energy content was calculated from the arrival time of the wave to the end of the signal for each source-sensor pair. In this case, it is difficult to identify the arrival of fast wave and slow wave because the signal attenuated below detectable level so that the threshold level for determining the arrival time was set at around 1.5 times the maximum amplitude of the noise signal (within the first 200 μs) as illustrated in Figure 5.1(b). Except for the tests on the large diesel engine in Section 4.6.1, the threshold level was set by eye because of the low signal to noise ratio for signals detected at longer distances. Table 5.1 summarises the simulated source type, threshold setting technique, arrival time and data length used for energy analysis for each transmission test.

Experiments	Source	Threshold	Data points (μs)
Cast iron blocks (Section 4.3)	Pencil lead break	By eye	5000 (1000)
HSDI diesel engine, CYLH sources to CYLH array (Section 4.4.1)	Pencil lead break	1.5 times max. noise level	10000 (2000)
HSDI diesel engine, CYLH sources to CYLB L1&L2 array (Sections 4.4.2)	Pencil lead break	1.5 times max. noise level	10000 (2000)
HSDI diesel engine, CYLB sources to CYLB L1 & L2 array (Section 4.4.3)	Pencil lead break	1.5 times max. noise level	10000 (2000)
HSDI diesel engine, CYLH sources to CYLB vertical array (Section 4.4.4)	Pencil lead break	1.5 times max. noise level	10000 (2000)
Large marine diesel engine, INJ to CYLB (Section 4.6.1)	Automatic centre-punch	By eye	10000 (2000)
Large marine diesel engine, Cylinder liner (Section 4.6.2)	Pencil lead break	1.5 times max. noise level	10000 (2000)

Table 5.1: Summary of source type, threshold setting, starting point, and data length for energy analysis of each transmission test.

Once the energy has been obtained for a range of source-sensor distances, the attenuation factor for AE propagation through the various blocks can be determined using two different methods as illustrated schematically in Figure 5.2. A best-fit exponential decay curve (Equation (3.15)) was used for the transmission tests in Section 4.3 and the best-fit straight line (Equation (3.16)) was mostly used for transmission tests on small and large diesel engine blocks (complex 3D structures). Although both

techniques are mathematically equivalent, the exponential fit was found to be unsuitable for cases where it was not practicable to obtain many points close to the source position, where poor fits resulted because the decay constant was reliant on two or three points only.

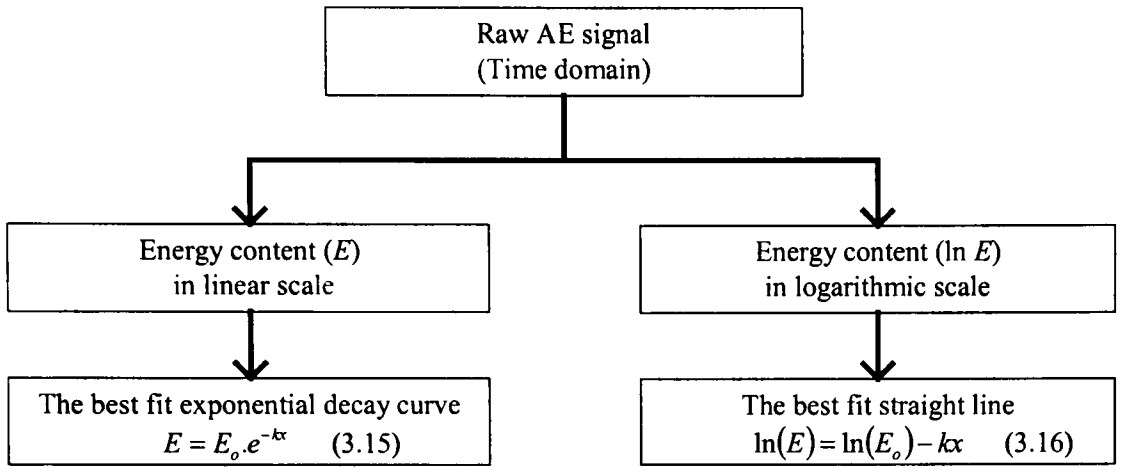

Figure 5.2: Diagram of methods for determining attenuation factors

Of the two coefficients E_o and k in Equations (3.15) and (3.16), k is the more meaningful, E_o being a (virtual) source energy whose value may depend on details of sensor positioning such as surface finish and coupling of the sensors. To minimize this effect, Equation (3.15) can be modified to use a relative energy or energy ratio so that Equation (3.15) becomes

$$\frac{E}{E_o} = e^{-kx} \tag{5.1}$$

5.2.2 Frequency domain analysis

The frequency content of the AE signals was between 0.1-1 MHz because the detected signal was analogue bandpass filtered in the pre-amplifier. Furthermore, the sensors themselves have a sensitivity which varies with frequency across this range. Nevertheless, changes in frequency content were detectable in some signals rendering some analysis worthwhile, and the frequency content was therefore calculated in terms of power spectral density using Welsh's method [59]. In addition, when considering only specific frequency bands, a Butterworth filter, which gives a flat amplitude response in the passband [114], was applied in some cases.

5.2.3 Combination of time and frequency domain analysis

Using a sliding time window with frequency analysis is one time-frequency technique that can be used to describe complex signals and can be useful for scanning. This technique was applied to the data from transmission tests on the cast iron blocks in order to show the frequency spectra and help to distinguish the arrival time of the fast and slow waves in the signal. In this process, the frequency spectrum was calculated from the raw AE signal using the sliding time window illustrated in Figure 5.3 starting from the arrival time of the fast wave, which was determined by eye. The time window was extended through 5 μs increments from the arrival of the fast wave until the frequency spectrum for the whole signal with the maximum time window width of around 500 μs was obtained. The amplitude of the frequency spectrum for each time window was normalized as a proportion of the maximum amplitude in the window in order to avoid distortion by the varying total energy considered. Then 3D waterfall plots of time, frequency and amplitude were used to scan the results in order to detect potential patterns in time-frequency space.

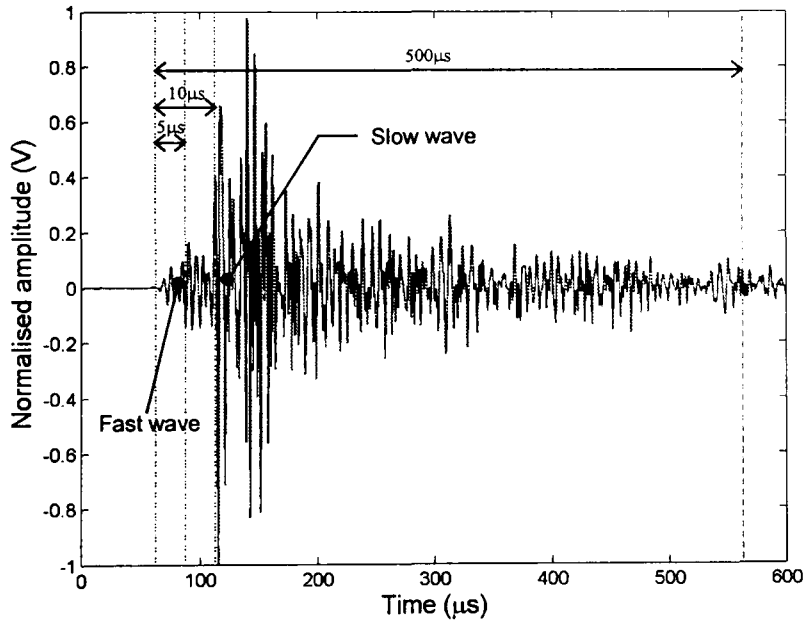

Figure 5.3: Typical plot of raw AE signal showing separation of fast wave and slow wave and the sliding time window technique for frequency analysis.

A more general view of AE wave frequency domain phenomena can be obtained by using energy ratios. Two main frequency bands were normally identifiable for cast iron blocks at approximately 100-200 kHz and 300-350 kHz. A typical example is shown in Figure 5.4 which was calculated from the signal shown in Figure 5.3. The frequency bands were isolated from each other by digital low-pass filtering at 200 kHz and high-

pass filtering at 300 kHz so that the proportion of energy in each of the low-pass and high-pass components could be determined using Equation (3.14).

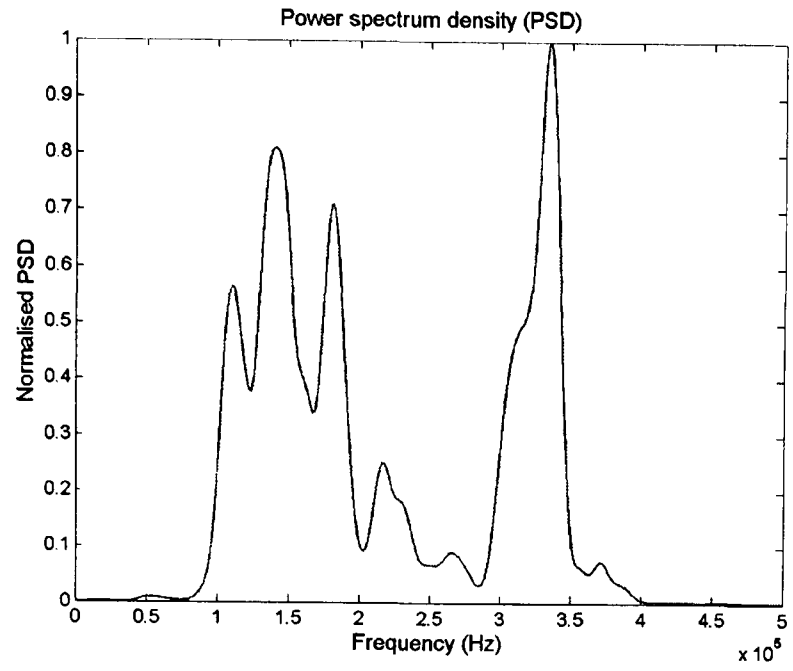

Figure 5.4: Plot of power spectral density (PSD) versus frequency (Hz) of signal shown in Figure 5.3.

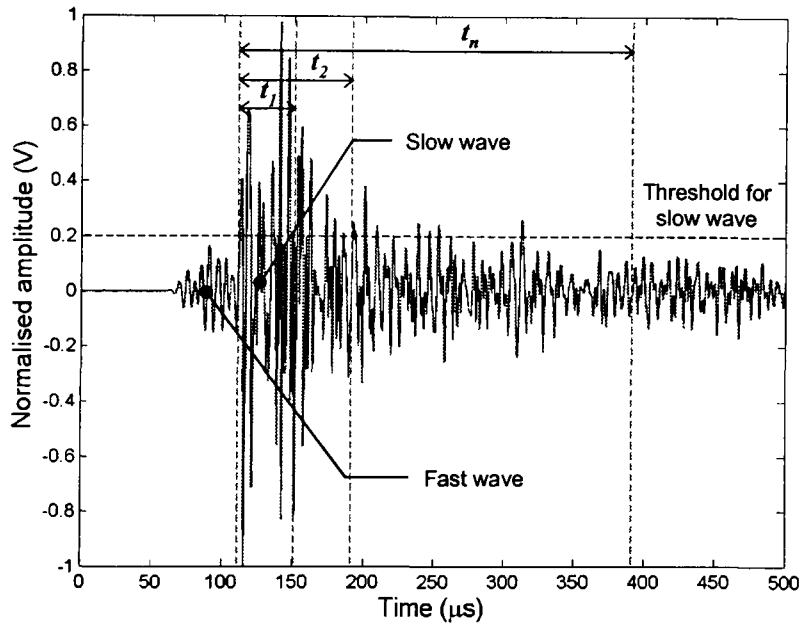

Figure 5.5: Plot of raw AE signal and the sliding time window durations, t_n, used for energy analysis.

Sliding time window and frequency filtering analysis, as illustrated in Figure 5.5, can be used to examine the effect of time window size and frequency on attenuation factor. Here, the sliding time window process was started from the arrival of the slow wave and moved over the entire signal, because the slow wave carried a good proportion of the AE energy, and so is largely responsible for the attenuation factor. It was normally possible to determine the arrival time reliably by eye. The energy content of each time window for a range of sensor positions was re-calculated using Equation (3.14) and then the attenuation factor was determined assuming a best-fit exponential decay according

to Equation (3.15). The energy and attenuation factors were determined for the unfiltered time series signal and also the filtered signal using the low-pass (<200 kHz) and high-pass (>300 kHz) bands. The purpose of all this analysis was to examine the extent to which apparent attenuation was influenced by reflections which would be absent from the earlier part of the time window.

5.2.4 Wave speed determination

In principle, the wave speed of AE propagation in cast iron can be calculated from the equations of classical wave theory shown in Section 3.2. In practice, it is normally recommended [11] that the wave speed used should be measured on the actual object rather than using the calculated values shown in Table 3.1. One reason for this is that the theoretical speeds only apply for pure modes of propagation, implying simple sources and structures. Furthermore, the theoretical approach considers the material to be a homogeneous elastic continuum, which may not be applicable to cast iron whose microstructure can contain a significant amount (around 25% by volume) of graphite. The wave speed (V) can be determined from AE signals for a single source, recorded by sensors positioned on the surface of a block at a known separation (s) [83]. The arrival time difference between the signals (Δt) can be determined using a threshold crossing techniques as shown in Figure 5.6. Then, the wave speed is given by

$$V = \frac{s}{\Delta t} \tag{5.2}$$

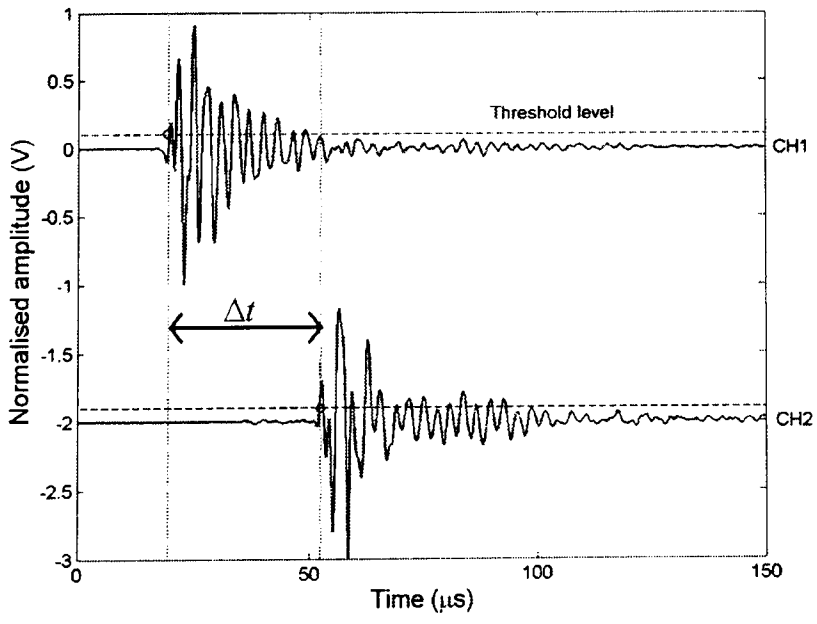

Figure 5.6: Plot of two AE signals at source (CH1) and receiver sensor (CH2) positions and show time difference (Δt) of both signals using threshold crossing technique.

Wave propagation in diesel engines is complicated and it is difficult to know which wave types propagate because the effects of wave reflection, refraction and mode conversion are unpredictable, and wall thicknesses, boundaries and geometries of the engine blocks vary. In the work with simulated sources, the threshold crossing method with a threshold value at 0.2 of maximum amplitude was used to automatically determine the time difference between arrival times of the slow wave so that wave speed can be obtained automatically. However, for the fast wave, a threshold value was set by eye because of low signal to noise ratio of the signals.

5.2.5 Source – sensor distance determination

Source-sensor distance is a key variable for determining attenuation factors from transmission tests. For the transmission tests on the cast iron blocks where the source and sensor are both on the external surface, the source-sensor distance can simply be measured directly. However, the source-sensor paths in a running engine rarely represent transmission across the surface of the block and there are, in general, various possible transmission paths involving the crossing of interfaces, mode conversions and various structural thicknesses. Thus, the transmission paths are very complicated and impractical to measure directly. However, an empirical method can be used to measure effective transmission path length from source to sensor by measuring the time difference between two AE signals acquired at source and receiver sensor positions using the threshold crossing technique shown in Figure 5.6, then multiplying by the wave speed measured in a simple structure (see Figure 5.14) to yield the effective source-sensor distance. This technique was used to estimate the effective transmission path length for all tests on the cylinder head and cylinder block of the small diesel engine. It must, of course, be recognised that path lengths so determined assume that the propagating signal can be represented by a single group velocity and that the velocity is the same as for surface propagation. The implications of this are discussed later.

5.3 Results and discussion of surface transmission tests on various cast iron blocks

The transmission tests on various simple and complex cast iron blocks were used as a preliminary study of AE wave propagation and the effects of wave attenuation and principally involved source and sensor on the same surface. The main parameters determined were the attenuation factor that indicated the decay of AE energy along a clearly-defined transmission path, and the effective wave speed. Figures 5.7-5.24 and Tables 5.2-5.3 show the results of transmission tests on the various blocks, using the analysis techniques described in Sections 5.2.1-5.2.5.

Figures 5.7 and 5.9 show the decay of AE energy against source-sensor distance on simple shapes (the engine base, the surface table, the flat panel and the strip), which are less complicated and do not involve transmission across any feature such as a web. Figures 5.8 and 5.10 show the decay of AE energy from more complex objects, which involve variable thickness structures.

The results in Figures 5.7 and 5.8 use the best-fit exponential decay curve using Equation (3.15), and two observations can be made immediately from these curves. The first is that the variability in signal total energy becomes much greater at sensor positions very close to the source, a fact which can be understood in terms of the sensor being within a zone where more complicated near-field waves may be important, where multiply reflected waves will show lower attenuation, and where waves travelling at different speeds will have had less opportunity to separate from each other [85, 115, 116]. The second is that the block geometry has a profound effect on apparent attenuation with smaller blocks (such as the strip, Figure 5.7(d)) having a reduced apparent attenuation (probably due to reflections), and blocks with leakage paths (at webs on the engine base and surface table as seen in Figures 5.7(a) and 5.7(b), respectively) showing greater attenuation. The cylinder block is the most complex of all the objects examined, and probably has contributions from both of the factors (reflection and leakage) suggested above. For example, the relative discontinuities shown as dotted lines in Figure 5.8(a) can be associated with the spacing of the webs inside the cylinder block identified in Figure 4.8(b).

The results in Figures 5.9 and 5.10 use a straight line fit according to Equation (3.16). As can be seen, this method puts less reliance on the first few points for determining the

value of k and results in rather different values. For the more complex blocks in Figure 5.10, the discontinuities at web positions (dashed lines) tend to be clearer than in the results expressed as a best fit exponential decay in Figure 5.8. This observation is consistent with Kline [117] who suggested that the energy measured can be related to geometric features such as curves and joints at webs and is also sensitive to wave mode conversions.

Tables 5.2 and 5.3 summarise all of the results from the best fit exponential decay curves and the best fit straight lines shown in Figures 5.7-5.10, as the apparent attenuation factor (k), apparent source energy (E_o) and coefficient of determination (R^2). As can be seen, the attenuation factors are different for the two fits although the order of results is generally the same. The attenuation factors for simple blocks are in the region $k \approx$ 10-13 for exponential fits and 5-10 for straight line fits. For the more complex blocks, the attenuation factors are in the region $k \approx$ 12-29 and 7-8 for exponential fits and straight line fits, respectively. The coefficients of determination from both sets of results are in good agreement, with confidence levels over 75% except for the strip. Here, the attenuation factors using both methods are around 2 and the correlations are very poor with coefficients of determination below 22 %.

Whilst acknowledging that attenuation factors in exponential and straight-line fits are different, due to the way in which a least-square algorithm works [118], the exponential decays will be used in later discussion in this section.

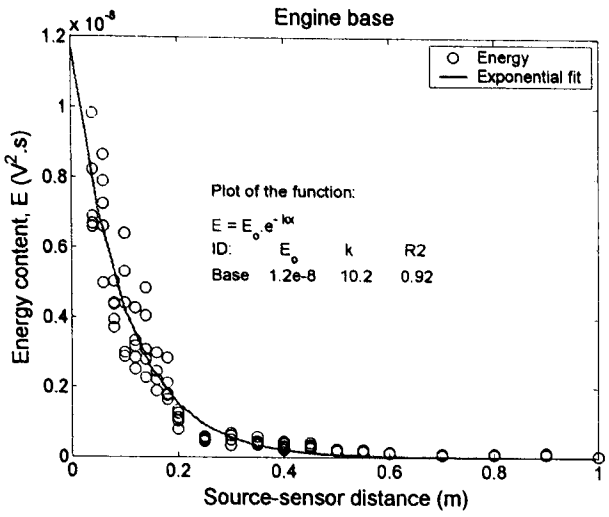

(a) Engine base

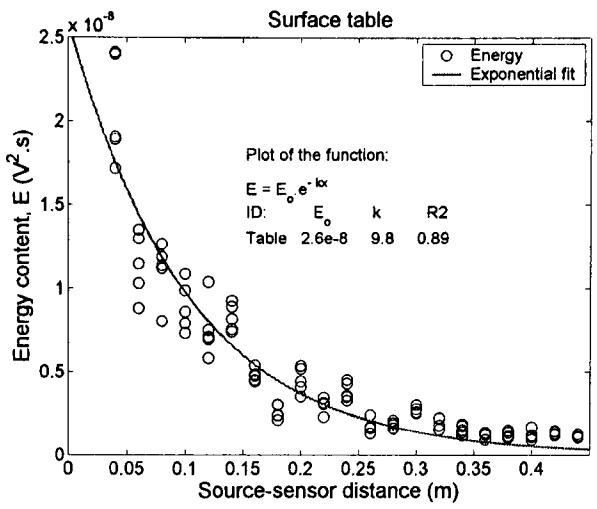

(b) Surface table

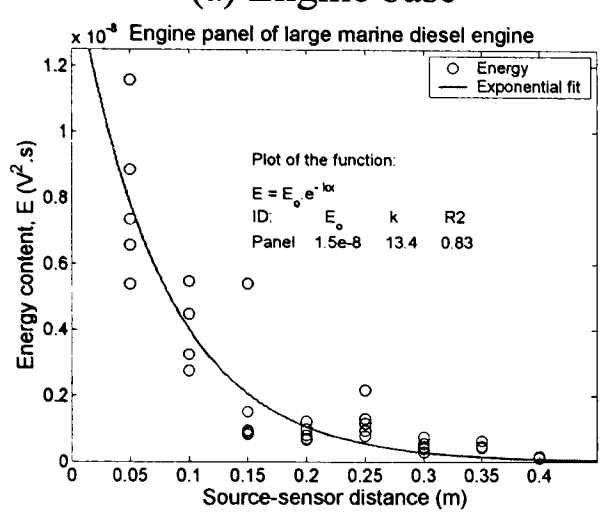

(c) Engine panel

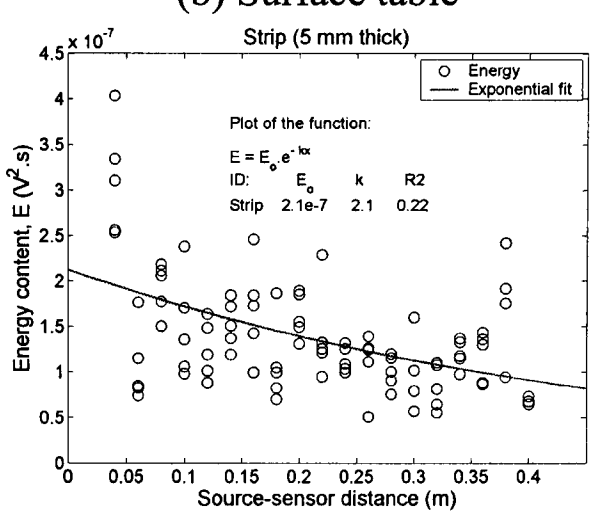

(d) Strip (5 mm thick)

Figure 5.7: AE energy versus source-sensor distance (best-fit exponential decay curve) from four simple objects.

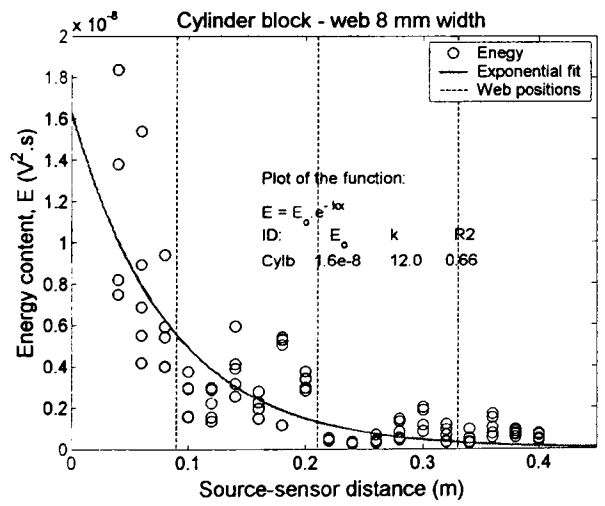

(a) Cylinder block – web 8 mm width

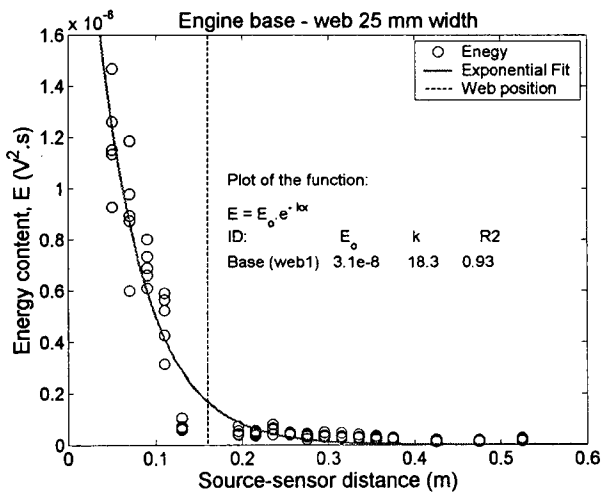

(b) Engine base – web 25 mm width

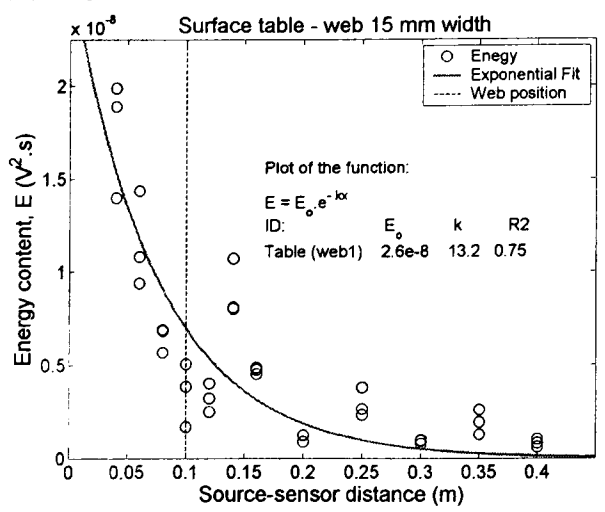

(c) Surface table – web 15 mm width

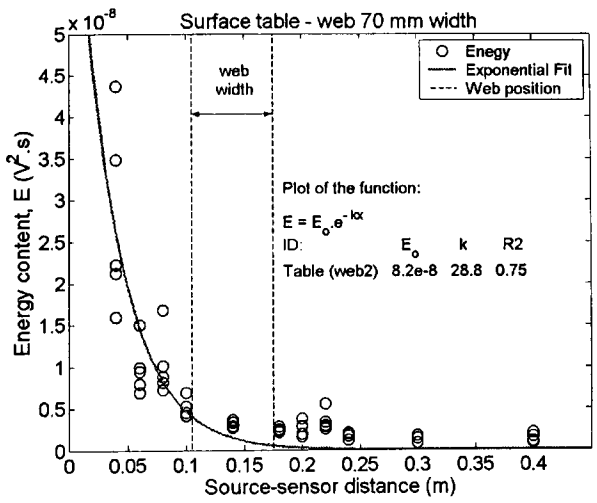

(d) Surface table – web 70 mm width

Figure 5.8: AE energy versus source-sensor distance (best-fit exponential decay curve) from four complex objects. (Dashed lines indicate web positions)

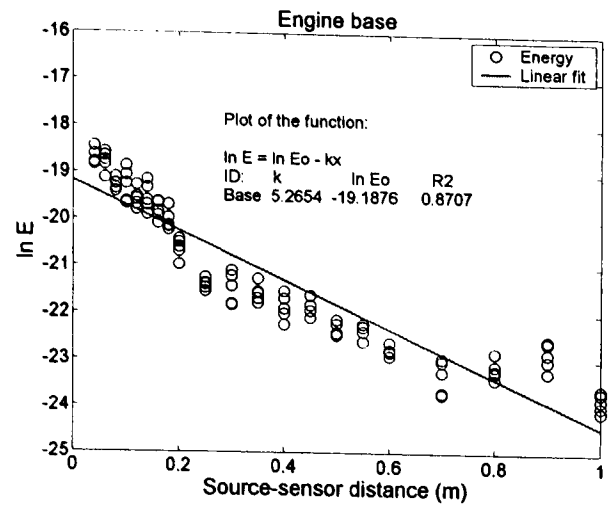

(a) Engine base

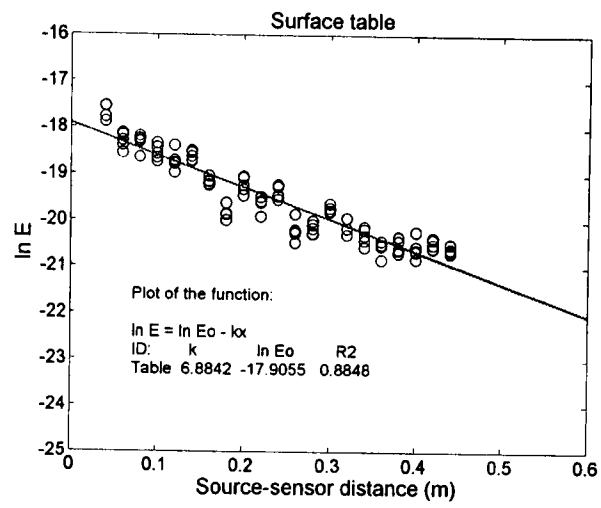

(b) Surface table

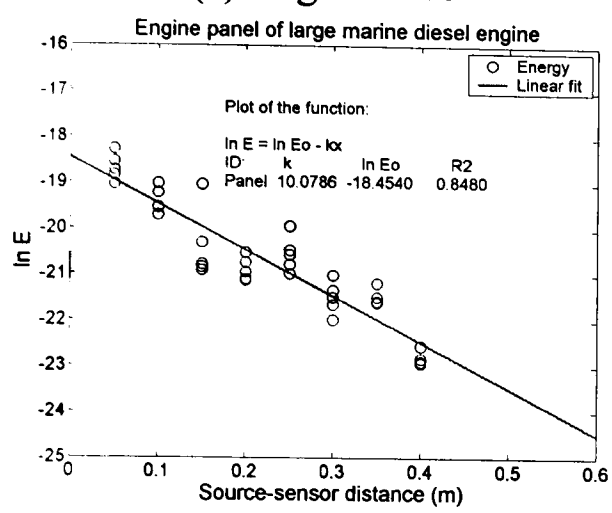

(c) Engine panel

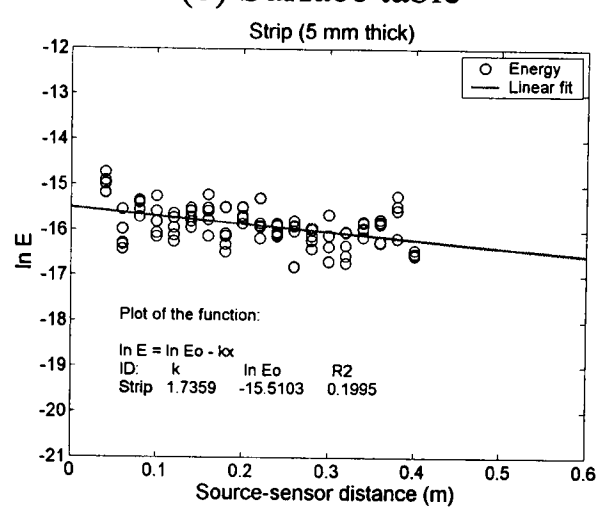

(d) Strip (5 mm thick)

Figure 5.9: AE energy versus source-sensor distance (best-fit straight line) from four simple objects.

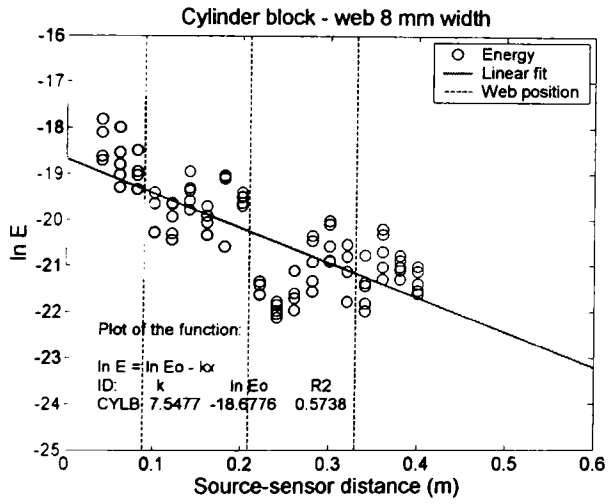

(a) Cylinder block – web 8 mm width

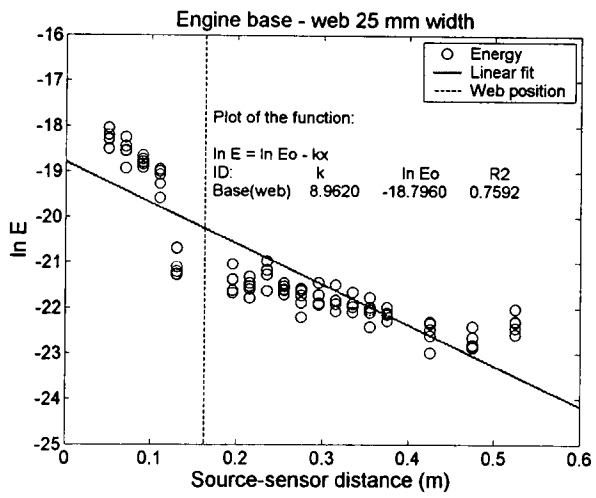

(b) Engine base – web 25 mm width

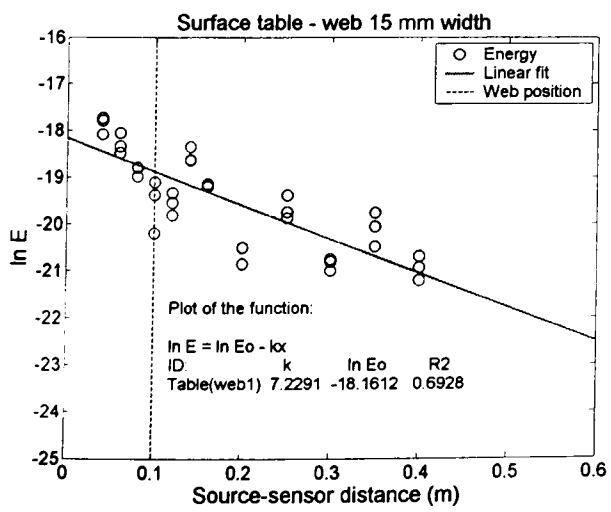

(c) Surface table – web 15 mm width

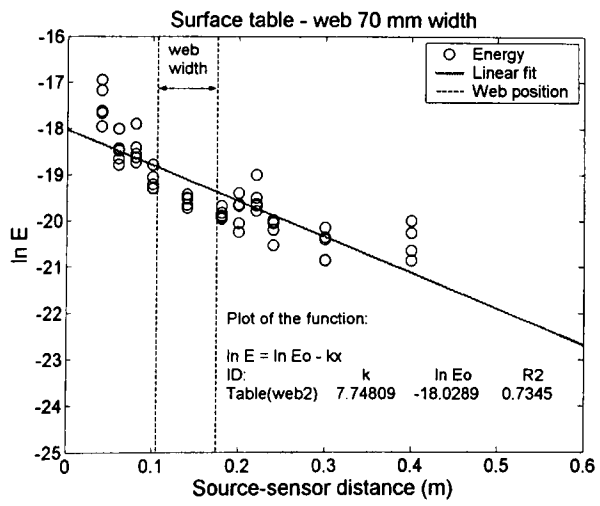

(d) Surface table – web 70 mm width

Figure 5.10: AE energy versus source-sensor distance (best-fit straight line) from four complex objects (dashed lines indicate web positions).

No	Test blocks	Thickness mm	Coefficients		
			E_o	k	R^2
1	Engine base	≈ 85–100	1.2e-8	10.1774	0.9218
2	Surface table	≈ 25	2.6e-8	9.7936	0.8928
3	Flat panel of large marine diesel engine	≈ 36	1.5e-8	13.3856	0.8270
4	Strip (cut from cylinder head of diesel engine)	≈ 5	2.1e-7	2.1129	0.2236
5	Cylinder block of small diesel engine	≈ 8	1.6e-8	12.0008	0.6583
6	Engine Base (cross web-1, 25 mm width)	≈ 85–90	3.1e-8	18.3365	0.9314
7	Surface Table (cross web-1, 15 mm width)	≈ 25	2.6e-8	12.1839	0.7455
8	Surface Table (cross web-2, 70 mm width)	≈ 25	8.3e-8	28.7564	0.7452

Table 5.2: Summary of effective attenuation factor (k), apparent source energy (E_o) and coefficient of determination (R^2) for different simple and complex objects and paths using the best-fit exponential decay curve ($E = E_o.e^{-kx}$).

No	Test blocks	Thickness mm	Coefficients		
			k	$\ln E_o$	R^2
1	Engine base	≈ 85–100	5.2654	-19.1876	0.8707
2	Surface table	≈25	6.8842	-17.9055	0.8848
3	Flat panel of large marine diesel engine	≈36	10.0786	-18.4540	0.8480
4	Strip (cut from cylinder head of diesel engine)	≈5	1.7359	-15.5103	0.1996
5	Cylinder block of small diesel engine	≈8	7.5478	-18.6776	0.5739
6	Engine base (cross web – 1, 25 mm width)	≈85–90	8.9620	-18.7960	0.7592
7	Surface table (cross web – 1, 15 mm width)	≈25	7.2291	-18.1612	0.6928
8	Surface table (cross web – 2, 70 mm width)	≈25	7.7481	-18.0289	0.7345

Table 5.3: Summary of effective attenuation factor (k), apparent source energy in logarithmic scale ($\ln E_o$) and coefficient of determination (R^2) for various simple and complex objects and paths using the best-fit straight line ($\ln(E) = \ln(E_o) - kx$).

Figure 5.11 collects all of the transmission test results (Table 5.2) for surface sources using a normalised energy or energy ratio (E/E_o) versus source-sensor distance. The lines, numbered 1-8, represent the best-fit exponential decay curves using Equation (5.1). Expressed in this way, the effect of geometry of the block can be seen in a more generic way, generally showing greater decay rates the more complex the geometry. This presentation highlights the exceptional nature of the results for the thin narrow strip, most probably due to the multiplicity of paths affected by reflections where the path is not much longer than the direct one. Curves 1-3, for relatively featureless slabs (the engine base, the surface table, and the engine panel), are almost coincident. One might also expect the attenuation to increase with slab thickness, which it does for all but the engine base, which had a projecting fin on the test surface. Similarly, the attenuation rate for more complex paths and objects (best fit curves 5-8) increases directly with web thickness, the larger web width giving the steepest attenuation.

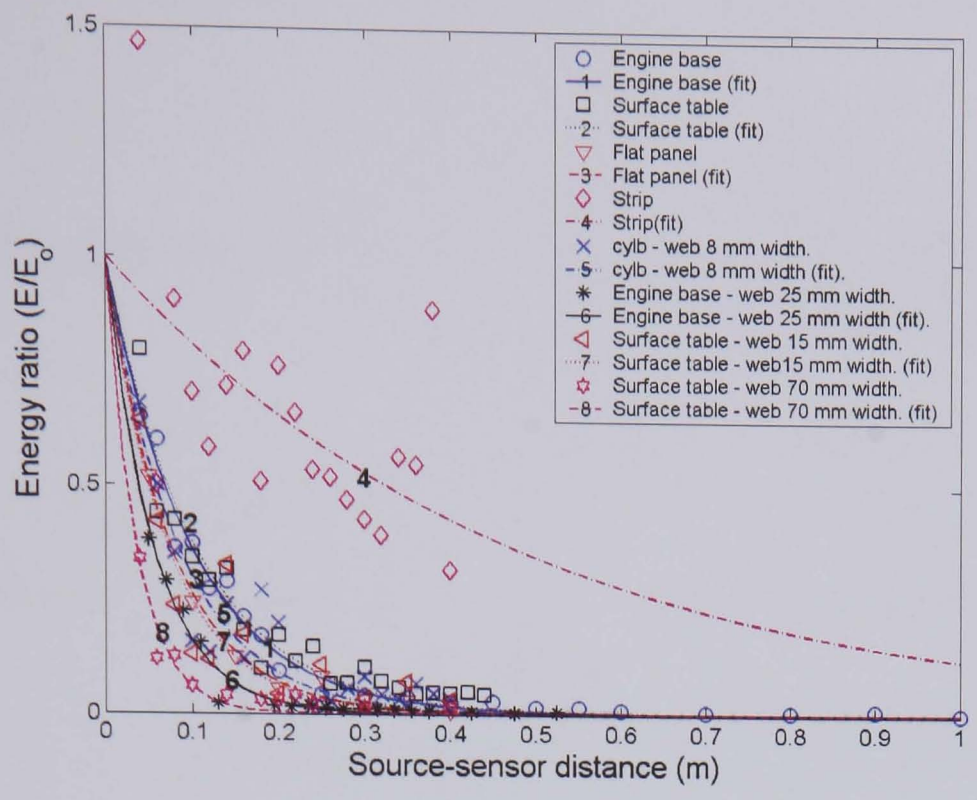

Figure 5.11: AE energy ratio (E/E_o) versus source-sensor distance for all objects with surface transmission.

Some authors e.g. Maji *et al* [81] and Holford and Carter [85] have isolated specific acoustic emission wave modes from a broadband source and have identified wave speeds which can be used to improve source location. Figure 5.12 shows typical measured raw AE signals against time acquired on the cylinder block at the source position (trigger sensor) and at receiver sensors with measured distances of 0.14 m and 0.4 m from the source, respectively. In the second case, there will be multiple wave modes, but there will also be reflections in the observed signals. In Figure 5.12, it is clear that a lower energy, faster wave (which may itself be made up of one or a number of modes) precedes the main signal, which carries the peak amplitude of the signal and travels with slower speed (slow wave). These observations are similar to those reported, for example by Holford and Carter [85] and also by Shehadeh *et al* [119]. The times t_1 and t_2 represent the arrivals of the two different wavefronts, so a time difference $(t_2 - t_1)$ can be identified in each of Figures 5.12(b) and 5.12(c). This time difference was determined using the threshold crossing technique having set the threshold level for both waves by eye. The results for all the surface transmission tests (Figure 5.13) show the arrival time difference to be directly proportional to source-sensor distance, at least up to a distance of 0.7 m. The time difference at distances beyond 0.7 m (only possible on the engine base) was difficult to estimate due to the low signal to noise ratio and effects of wave reflection from the boundaries so the curvature may be due to noise contamination or contamination by reflections rather than any real effect.

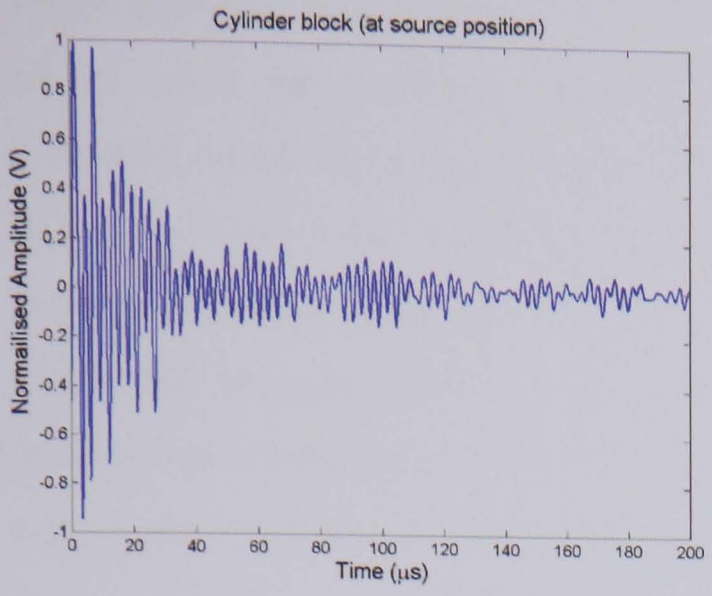

(a) Raw signal at source position

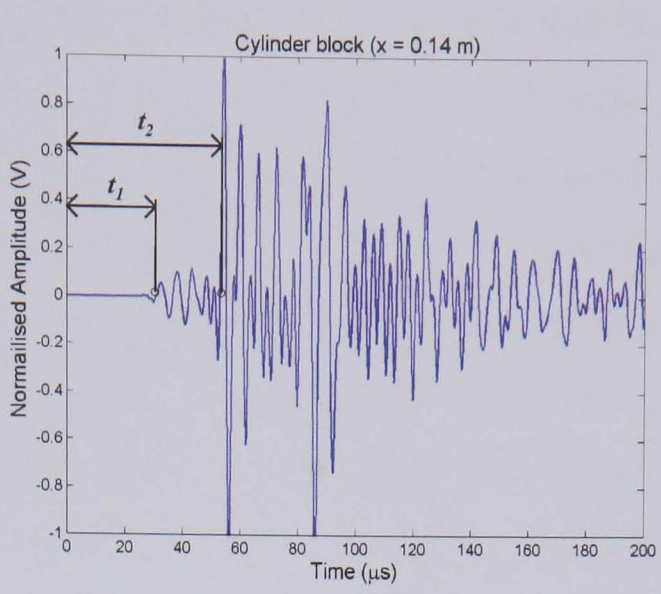

(b) Raw signal at $x = 0.14$ m

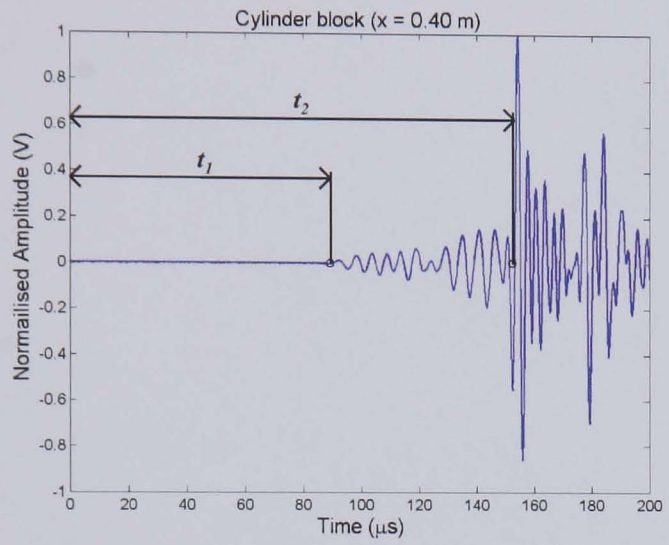

(c) Raw signal at $x = 0.40$ m

Figure 5.12: Measured raw AE signal against time, acquired on cylinder block; (a) raw signal at trigger sensor, (b) and (c) raw AE signal at 0.14 and 0.40 m from the source position, respectively.

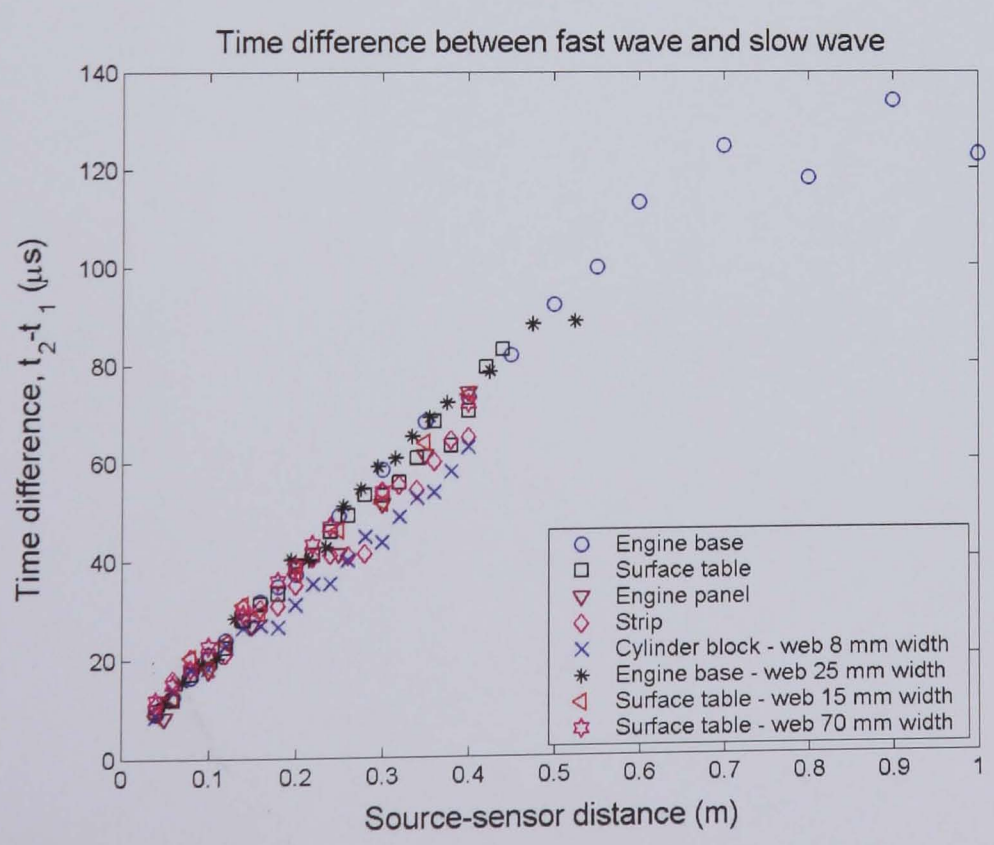

Figure 5.13: Time difference between fast wave and slow wave arrivals $(t_2 - t_1)$ against source-sensor distance.

It was therefore possible to estimate the speed of both wavefronts in the cylinder block of the small diesel engine using the method described in Section 5.2.4, with the threshold levels being set by eye. The fast and slow wave speeds so estimated are shown in Figure 5.14, and it can be seen that the values for both wave speeds are highly variable at distances of up to 0.12 m, probably because the wavefronts are difficult to distinguish at short distances. Using the data beyond 0.12 m, the fast and slow wave speeds were established to be 4500 ± 64 m/s and 2650 ± 41 m/s, respectively and these wave speeds will be used in the next section.

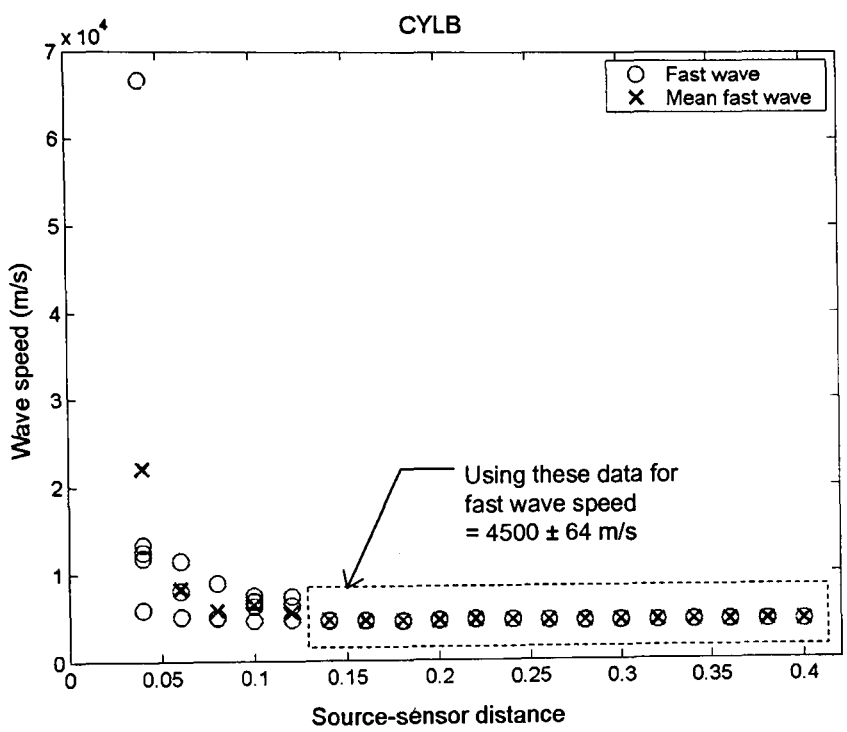

(a) Fast wave speed

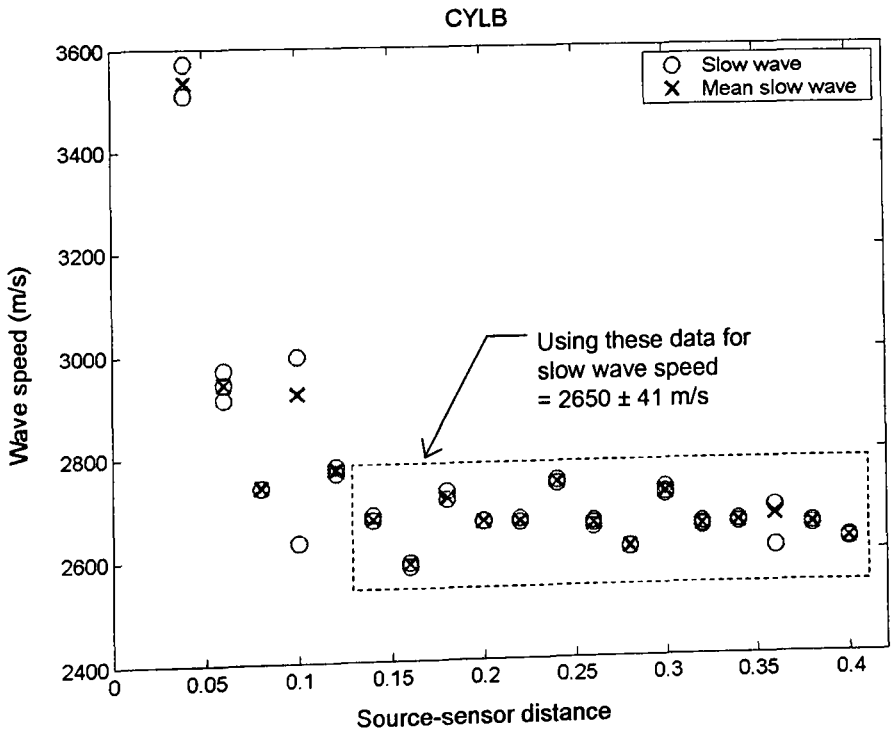

(b) Slow wave speed

Figure 5.14: Estimated fast and slow wave speed from the cylinder block.

The frequency content of a signal recorded at a point on the surface of a block might be affected by a number of factors, including the nature of the source [120], the response of the sensor, wave mode conversion at joints or discontinuities and wave velocity dispersion. To investigate these effects for a fixed source type and surface-surface transmission, time-frequency plots were calculated using the sliding time window techniques described in Section 5.2.3 and the results were averaged from five records. Figure 5.15 to 5.17 show some typical examples of the results as 3D time-frequency graphs with time in μs, frequency in kHz and amplitude, normalised to the peak value in the spectrum to avoid distortion resulting from the varying energy in the window as time increases. As can be seen, two main frequency bands are present in the signals at around 100-200 kHz (low frequency) and around 300-350 kHz (high frequency), with a rather different frequency content in the early part of the signals associated with the fast wave. Figure 5.15 shows plots for the tests on the four simple configurations (the engine base, the surface table, the engine panel and the strip) for two selected receiver sensor positions at 0.04m (0.05 m for the engine panel) and 0.3m from the source. For the engine base, for example, the early part of the wave (the fast wave) is observed for around 20 μs at 0.04 m from the source and this extends to around 70 μs at 0.3 m from the source. The early parts of the waves arriving have complicated frequency content, which varies between samples although part of this may be due to the short record lengths. As the time window is extended, the energy of the signals is concentrated in the two bands mentioned above and, as the source-sensor distance and sliding time window increase, the frequency content becomes increasingly contained in these bands.

The results for the engine base, the surface table and the flat panel show similar trends. However, for the thin, narrow strip, the frequency content of the main body of the signal is much more variable, in that, at some sensor positions, the energy content can be concentrated around one or other of the 100-200 kHz or 300-350 kHz bands. This is thought to be due to an interference pattern on this object brought about by reflections from the edge of the strip.

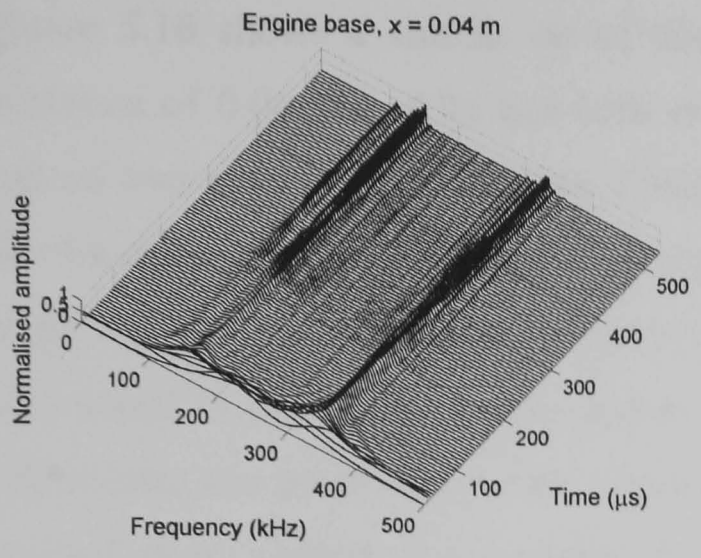

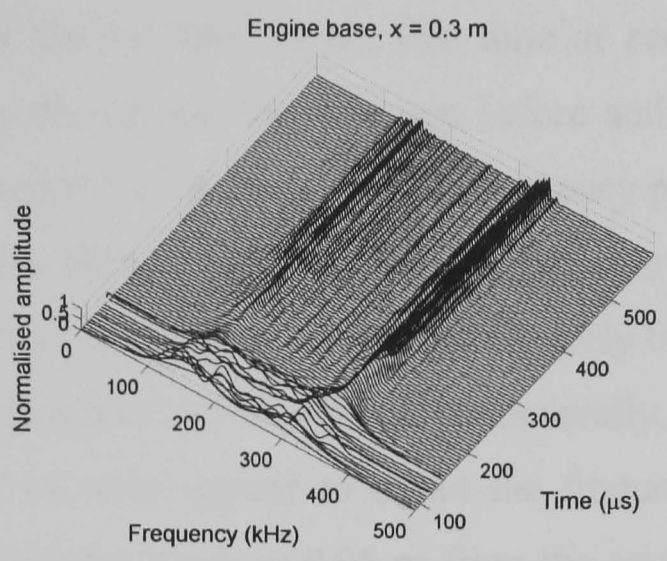

(a) Engine base

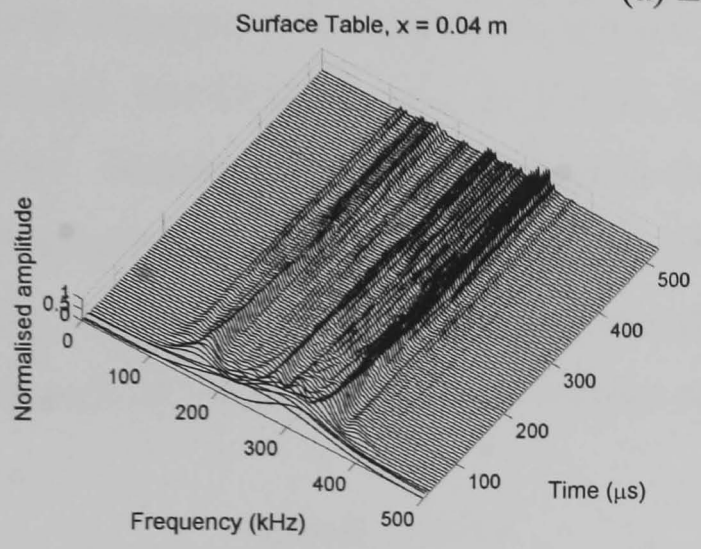

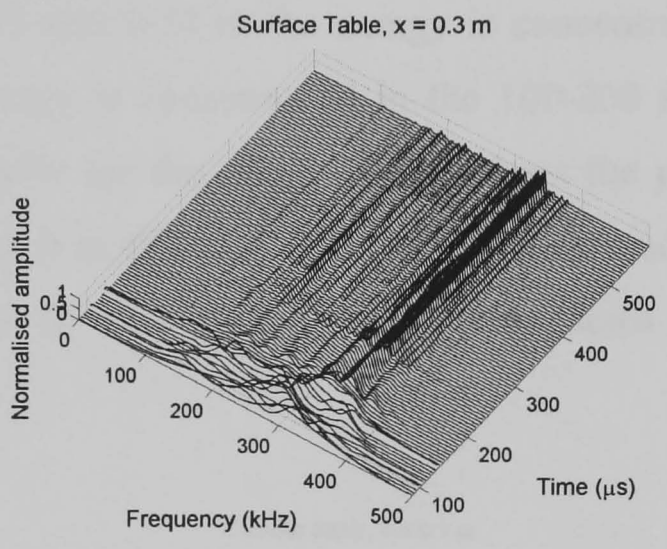

(b) Surface table

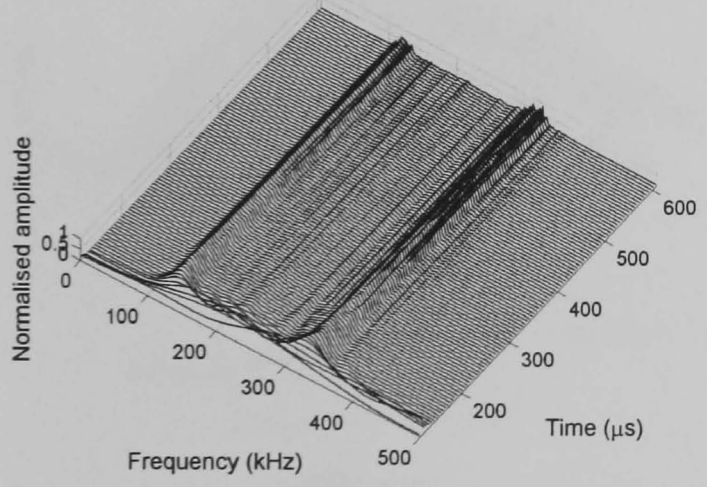

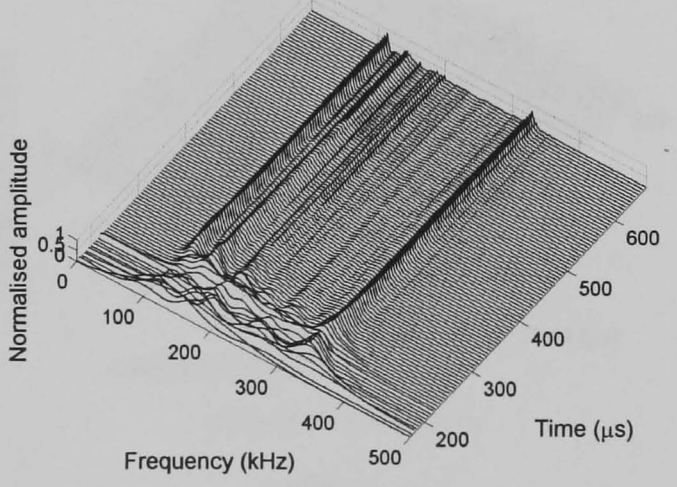

(c) Engine panel

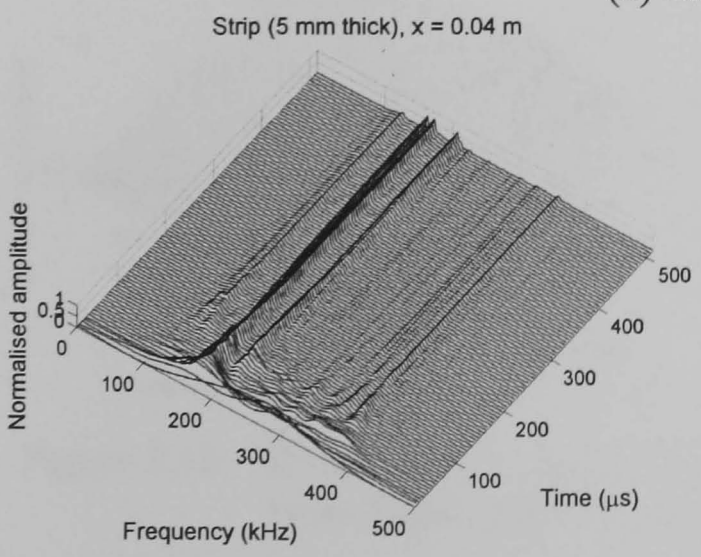

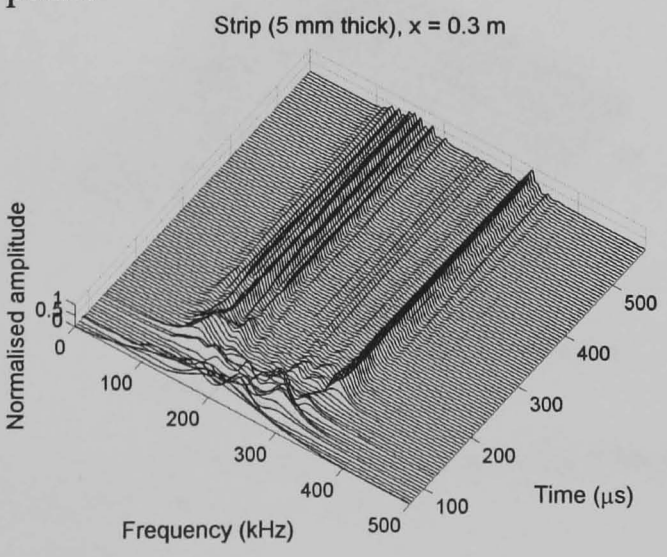

(d) Strip (5 mm thick)

Figure 5.15: 3D magnitude, time, frequency plots of AE signal from four simple objects at various distances from the source.

Figure 5.16 shows a similar set of plots for the cylinder block, this time at sensor positions of 0.06, 0.1, 0.24 and 0.26 m from the source, the first two before and the second two after the web position. Finally, Figure 5.17 shows 3D time-frequency plots for the other complex blocks, the selected plots being at positions before and after the webs. For the cylinder block (Figure 5.16), webs are positioned at approximately 0.09, 0.21 and 0.33 m from the source and so four positions are shown for S2. Generally, the reflections and associated mode conversions at webs appear to affect the frequency content of the signals. For example, for the cylinder block at 0.06 m from the source, both frequency components are present, at 0.1 and 0.24 m the energy is concentrated around 300-350 kHz and, at 0.26 m, the energy is concentrated in the 100-200 kHz band. Similar trends are observed in the results for the other objects where the path followed crosses a geometric feature. Although it is difficult, with the data presented so far, to arrive at a systematic explanation it is clear that different frequencies are attenuated differently in more complex shapes.

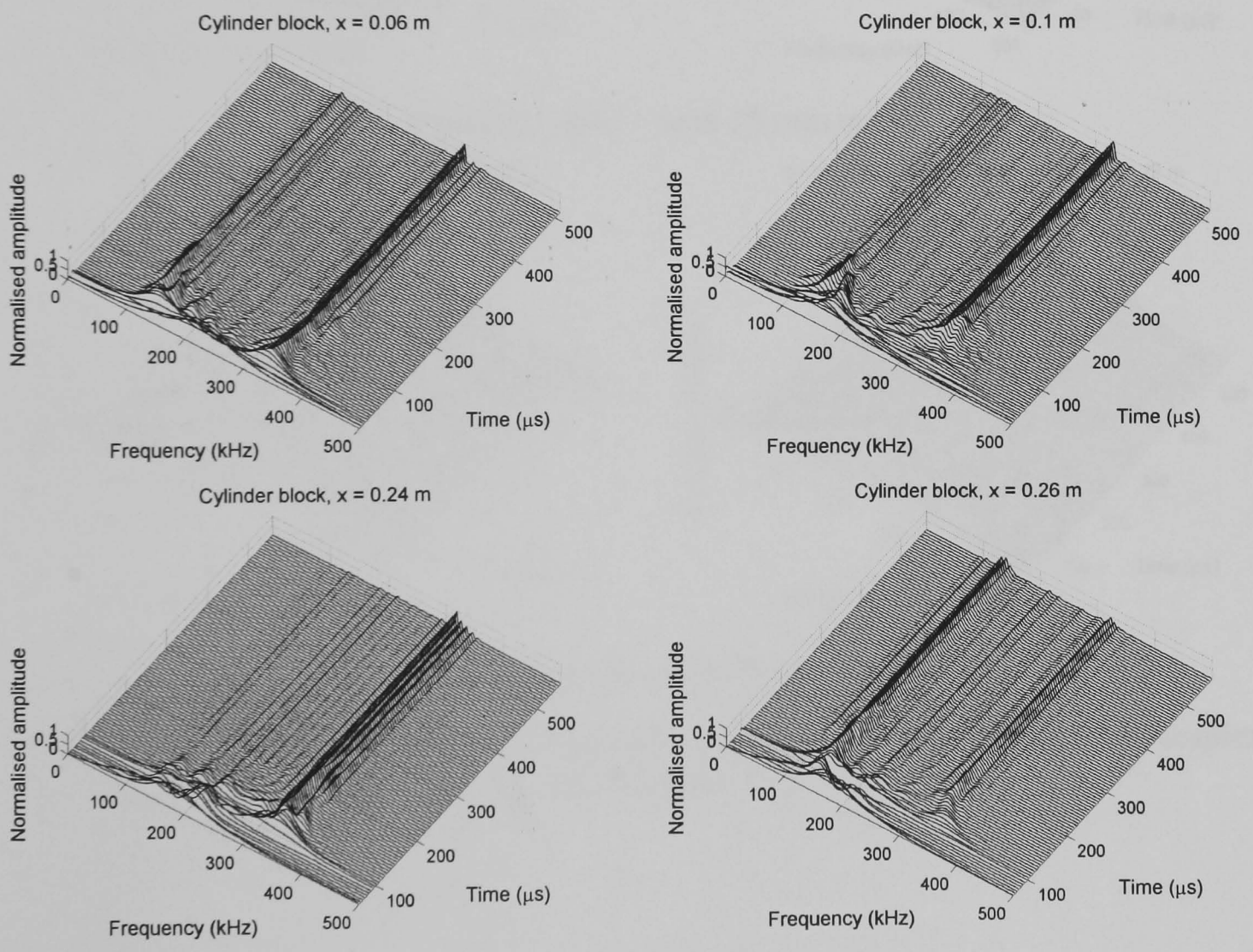

Figure 5.16: 3D magnitude, time, frequency plots of AE signals from cylinder block (web 8 mm width) at various distances from the source.

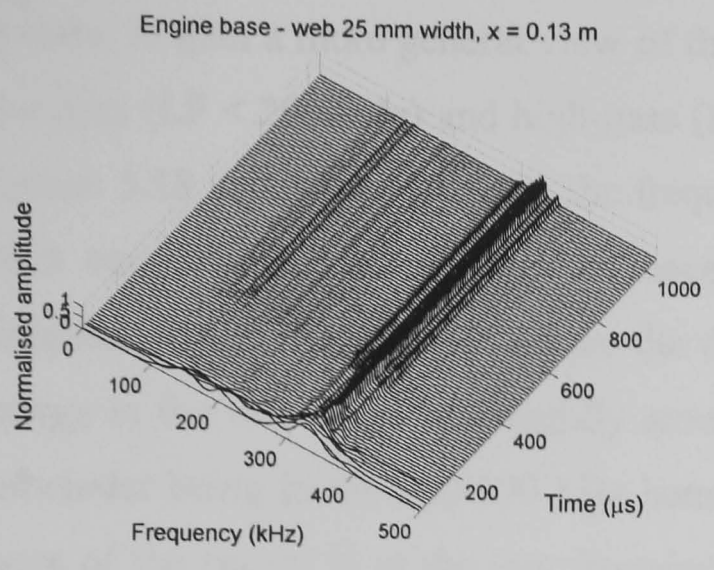

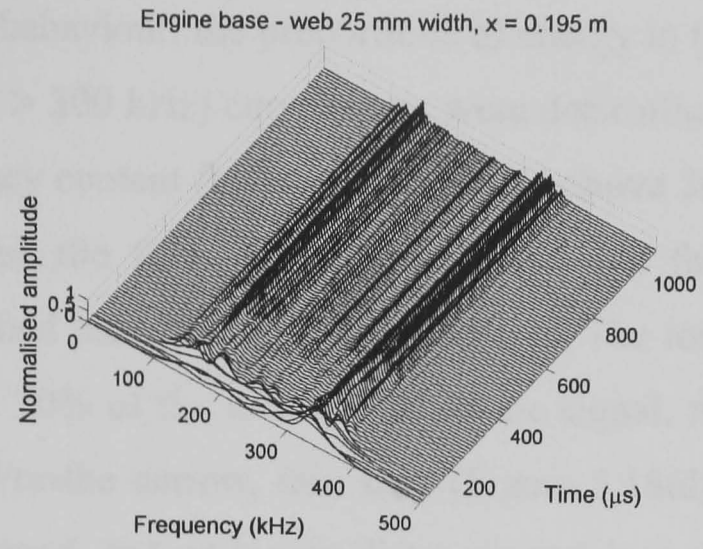

(a) Engine base – web 25 mm width

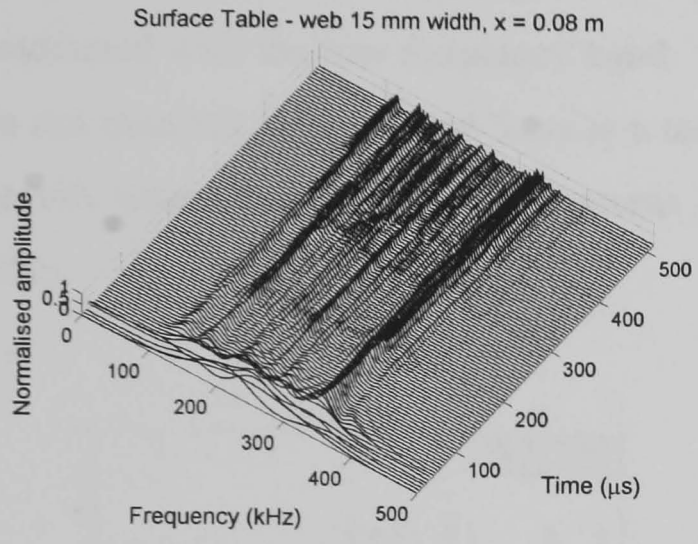

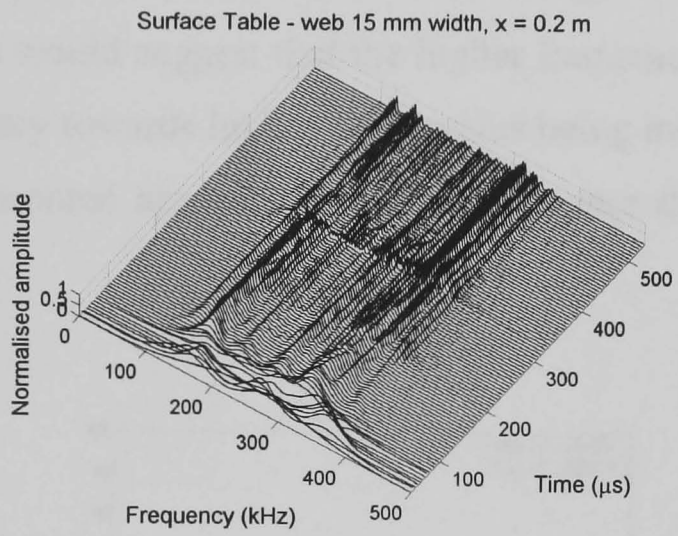

(b) Surface table – web 15 mm width

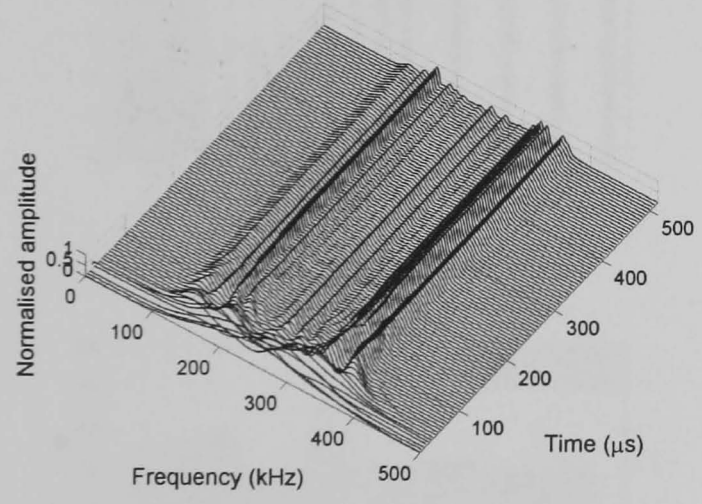

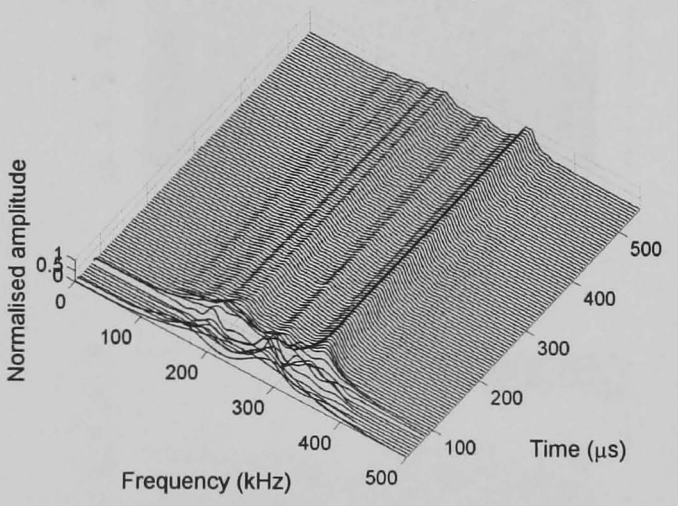

(c) Surface table – web 70 mm width

Figure 5.17: 3D magnitude, time, frequency plots of AE signals from three complex objects at various distances from the source.

In order to gain a more general view of this behaviour, the proportions of energy in the low-pass (LF < 200 kHz) and high-pass (HF > 300 kHz) components were determined. Figures 5.18 and 5.19 show how the frequency content (below 200 kHz and above 300 kHz) varies with source-sensor distance for the four simple objects and the four complex objects respectively, where the dashed lines indicate web positions. The total energy in the two bands is generally around 70% of the total energy in the signal, the remainder being in the 200-300 kHz band. For the narrow, thin strip (Figure 5.18(d)), more of the energy is in the low frequency band, and, at longer distances and in more complex objects, the tendency is for an increased proportion of the energy to be associated with the low frequency band. This would suggest that the higher frequencies do not transmit as easily and there is a tendency towards higher frequencies being more heavily attenuated, but this only seems to become apparent at distances greater than 0.5m.

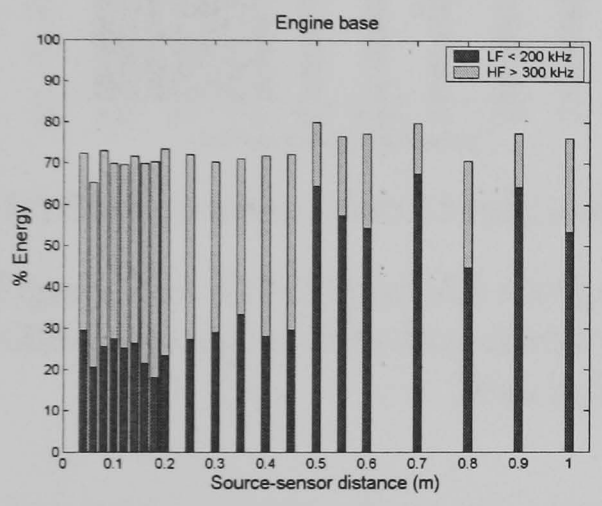

(a) Engine base

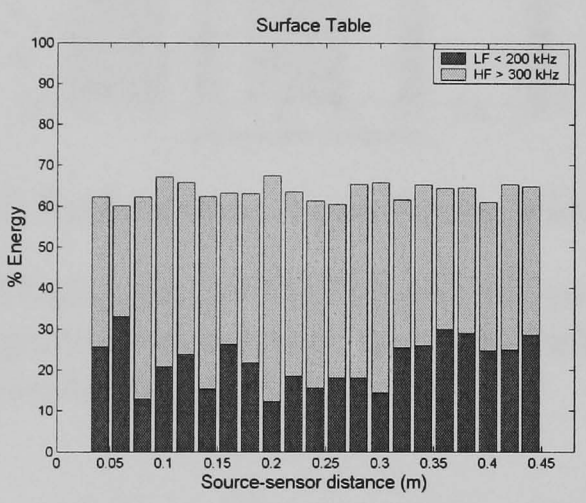

(b) Surface table

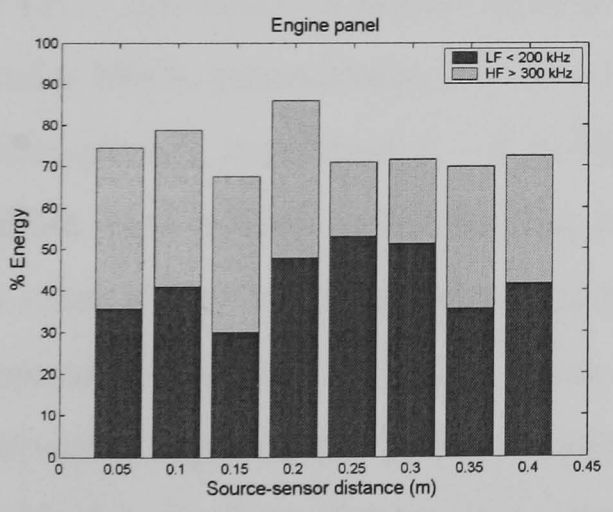

(c) Engine panel

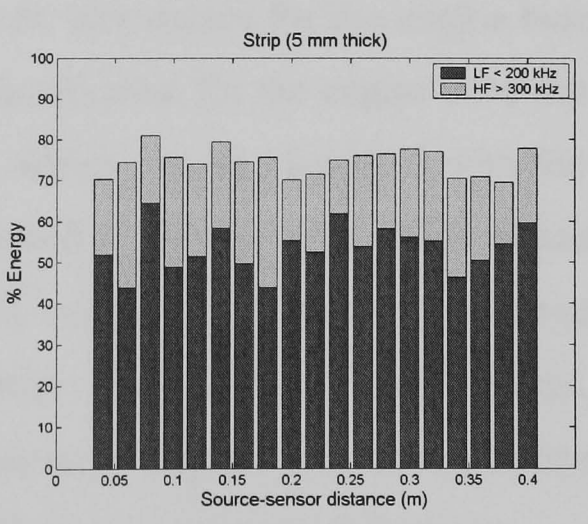

(d) Strip (5 mm thick)

Figure 5.18: Bar chart of AE energy content of high-pass (>300 kHz) and low-pass (<200 kHz) signal from four simple objects against source-sensor distance.

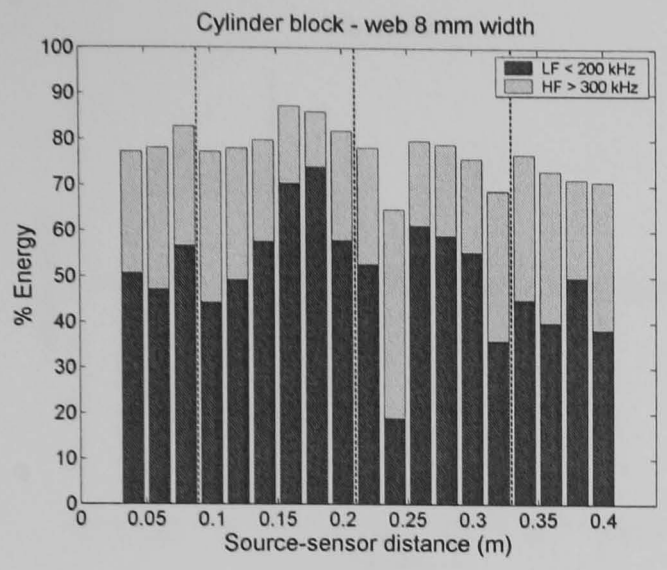

(a) Cylinder block – web 8 mm width

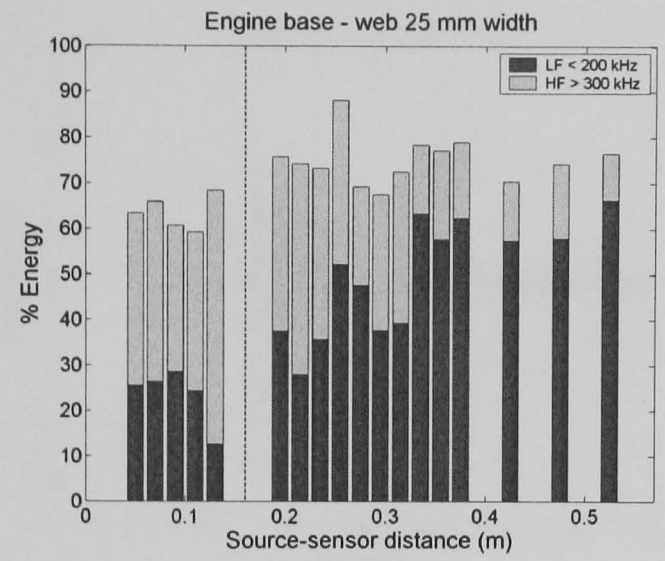

(b) Engine base – web 25 mm width

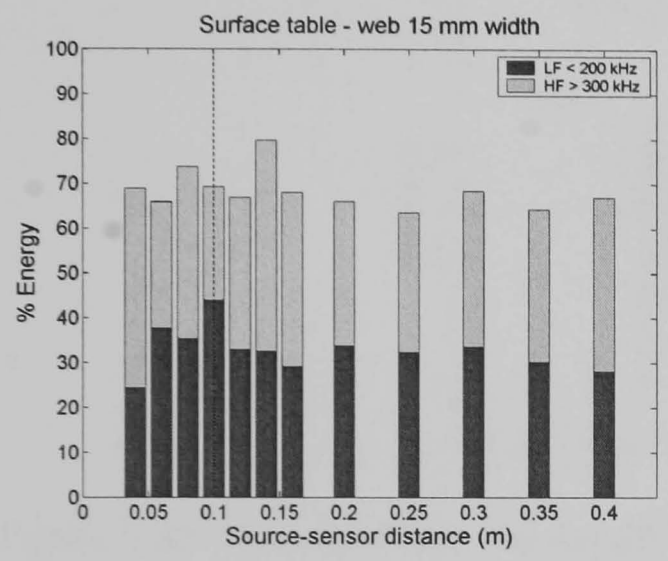

(c) Surface table – web 15 mm width

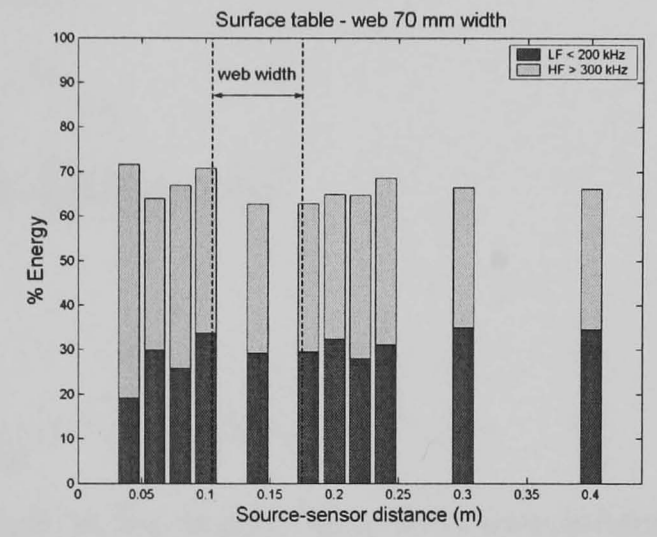

(d) Surface table – web 70 mm width

Figure 5.19: Bar chart of AE energy content of high-pass (>300 kHz) and low-pass (<200 kHz) signal from four complex objects against source-sensor distance (dashed lines indicate web positions).

Figures 5.20 and 5.21 show the effect of high- and low-pass filtering (HF > 300 kHz and LF < 200 kHz) on typical examples of the raw time-series for the engine base and cylinder block, respectively. The low frequency component for the engine base shows 4 distinct phases, numbered 1 – 4 in Figure 5.20, which can be identified with the four possible transmission and reflection paths illustrated in Figure 5.22. These phases are less clear in the high frequency component and neither the high nor low frequency components for the cylinder block permit such segmentation. Nevertheless, the observation supports the notion that the low frequency component is more persistent in the signal in the four of geometric objects where there may be many reflections.

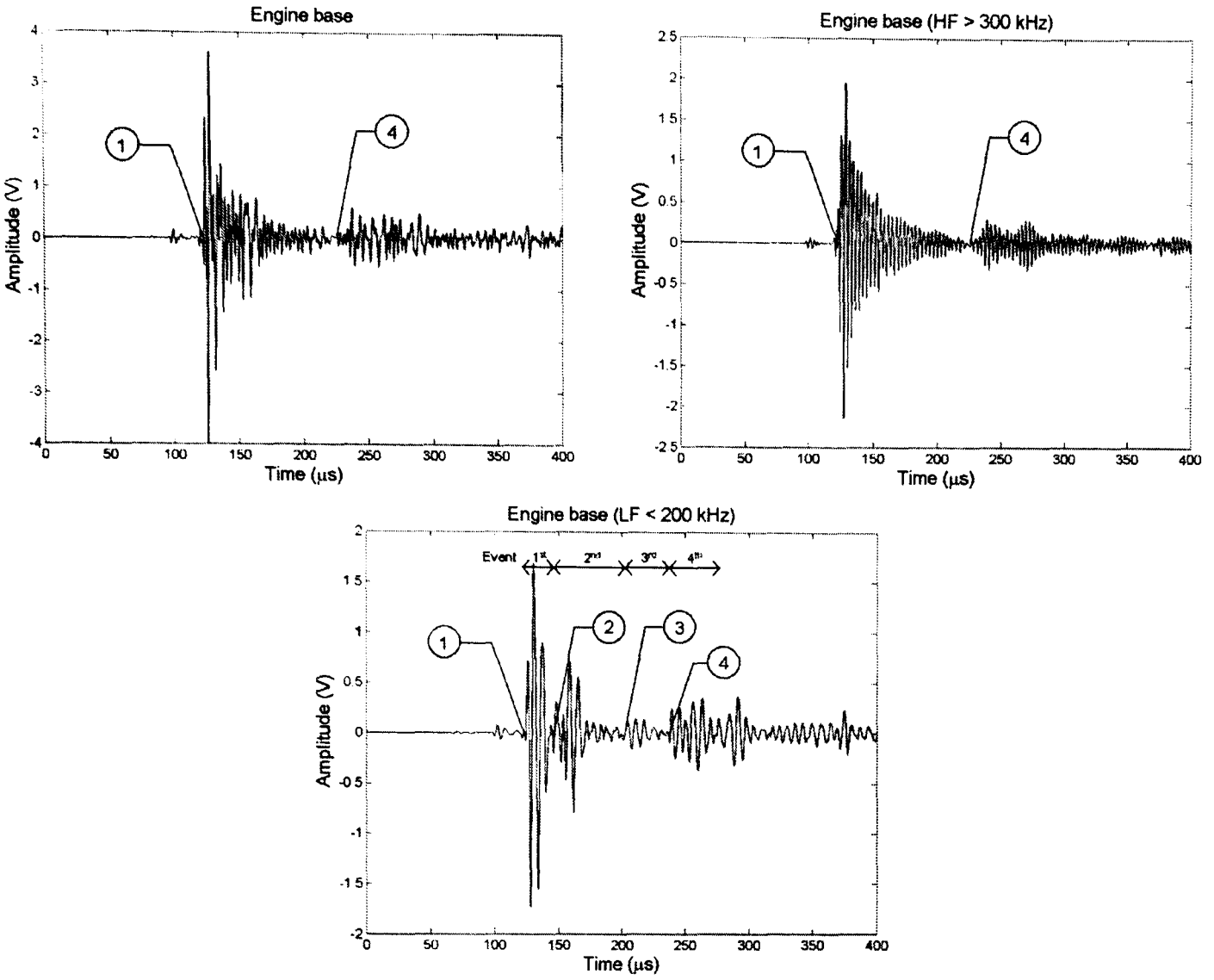

Figure 5.20: Measured raw AE signals acquired on the engine base with source-sensor distance = 0.3 m, showing effect of filtering on the signal.

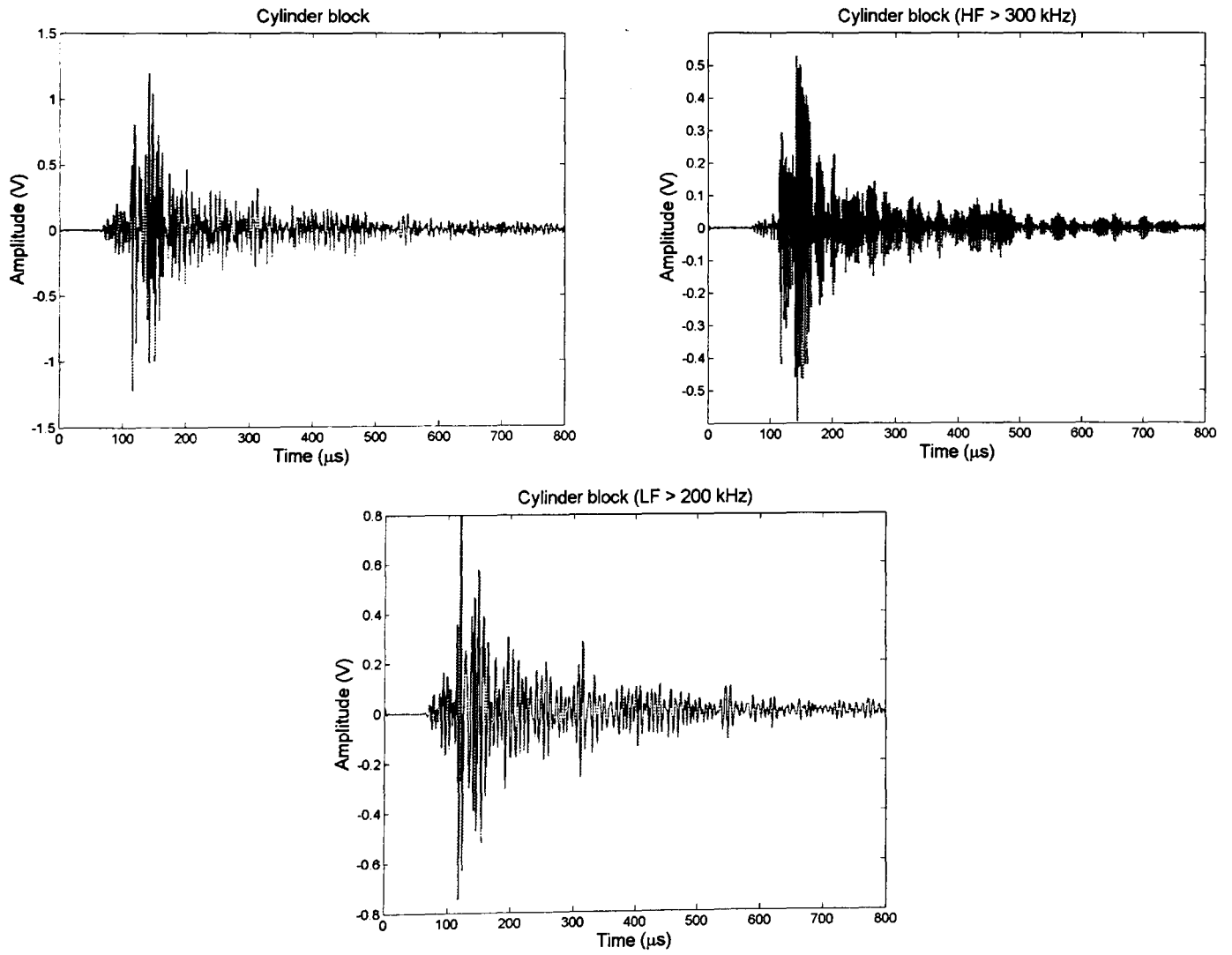

Figure 5.21: Measured raw AE signal acquired on the cylinder block with source-sensor distance = 0.3 m, showing effect of filtering on the signal.

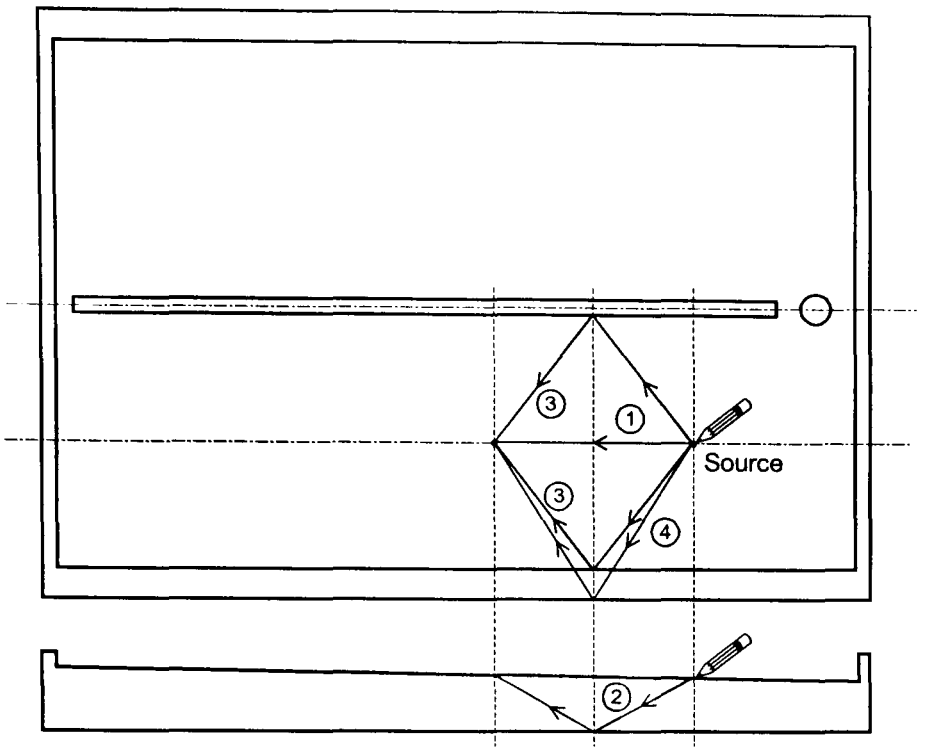

Figure 5.22: Drawings of the engine base showing possible propagation paths.

Clearly, the recorded signal from a pencil lead break can contain some reflections which depend on the complexity of the structure and may involve propagation in surface and body modes, all of which will affect the amount of energy recorded in the signal. In order to illuminate this effect, a sliding time window (Sections 5.2.3 and Figure 5.5) was used to show how the attenuation factor varied with the duration of the signal analysed. Figures 5.23 and 5.24 show the attenuation factor, k for the unfiltered signal and signals filtered with the low-pass (<200 kHz) and high pass (>300 kHz) bands against time window duration. These results were averaged from five individual lead breaks for each condition, zero (on the time scale) corresponding to the beginning of the slow wave. The results for the four simple blocks and paths can be seen in Figure 5.23 and for the four complex blocks and paths in Figure 5.24. As can be seen, all values of attenuation factor settle to a relatively constant value within about 300 μs of the wave arrival. Most of the blocks show similar behaviour between the two bands although, in some cases, the attenuation factor for the HF component goes through a maximum about 50 μs into the signal corresponding roughly to the end of the fast wave. For most other cases, the attenuation factor drops monotonically with time into the signal.

In Figure 5.23, it can be seen that the attenuation factor for simpler transmission paths is around 10 on the thicker engine base and the surface table, and is around 12 on the thinner (36 mm thick) engine panel. The attenuation on the thin narrow strip is very low and this may be due to a more reverberant field being present. The attenuation factor is much higher for the low frequency filtered results on the engine base and the surface table while it is lower for the thinner engine panel (36 mm thick) and the strip.

However, the engine panel has a web on the surface inside the engine, opposite to that where the sensors were placed.

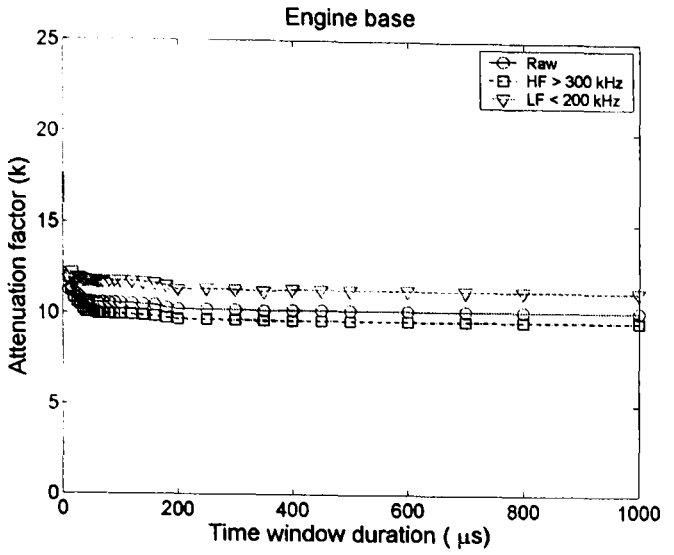

(a) Engine base

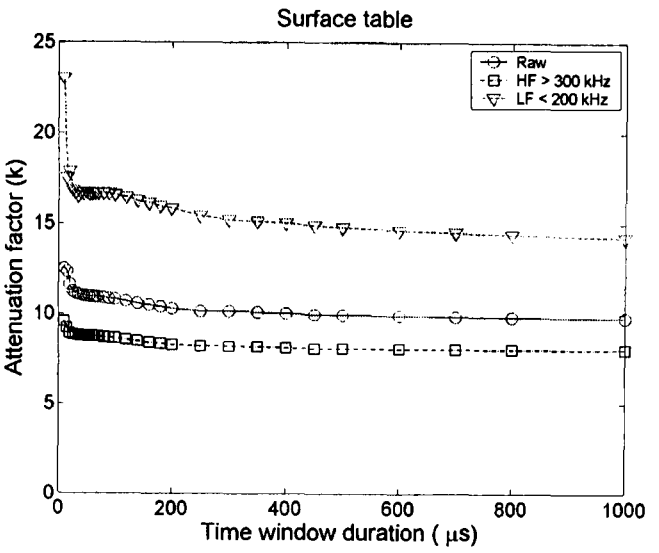

(b) Surface table

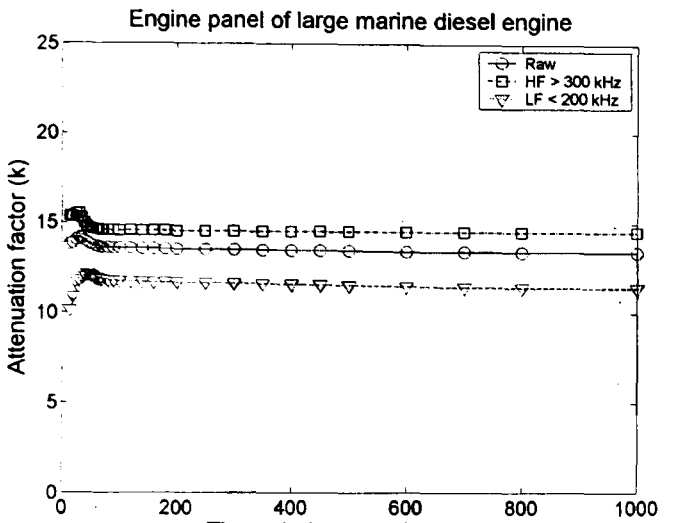

(c) Engine panel

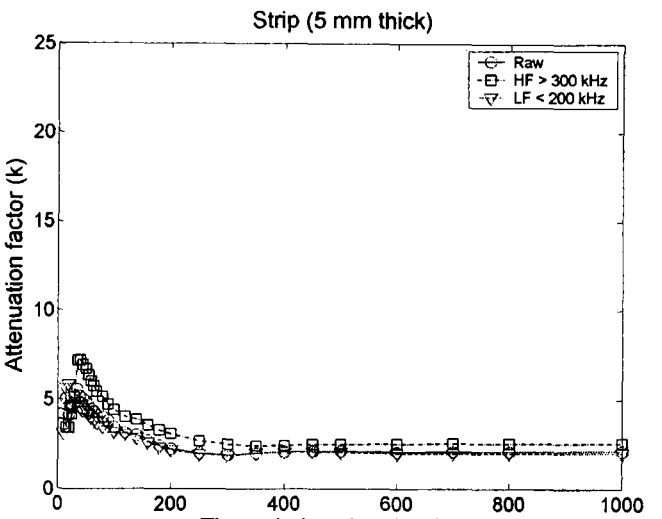

(d) Strip (5 mm thick)

Figure 5.23: Plot of apparent attenuation factor (k) as a function of time window duration, for filtered and unfiltered time-series from four simple objects and paths.

Similar results are shown in Figure 5.24 for the attenuation factor calculated where the transmission path is more complicated. The attenuation across the webs on the surface table is almost tripled to k ≈ 30 and doubled on the engine base to k ≈ 18.5. The attenuation on the cylinder block (8 mm thick) is around 12, more like the simpler shapes. The dimensions of the sections making up the cylinder block are about 100 mm long/wide and 8 mm thick, which is more like the thin, narrow strip so similar effects associated with a more reverberant wave field (more reflections) may reduce the attenuation of the signals. In all of these cases the higher frequency energy is attenuated more quickly, although in some marginally so.

The difference between the attenuation on the engine base (Figure 5.24(b)) and the surface table (Figure 5.24(c)) can be attributed to the fact that the web structure on the

engine base is on the test surface, whereas it is underneath the test surface for the surface table. The attenuations of unfiltered and filtered signals on the engine base seem to be similar, unlike the surface table. The width of web on the surface table also has an effect on attenuation as can be seen from the difference between the unfiltered and filtered signals, where the larger web width increases the attenuation coefficient significantly.

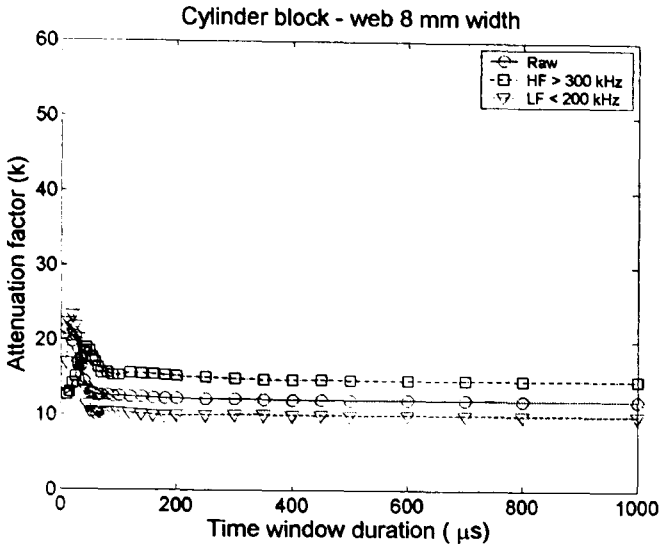

(a) Cylinder block – web 8 mm width

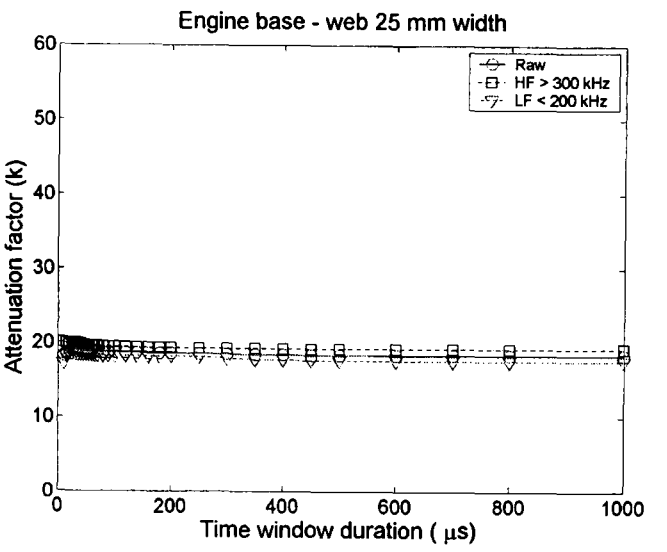

(b) Engine base – web 25 mm width

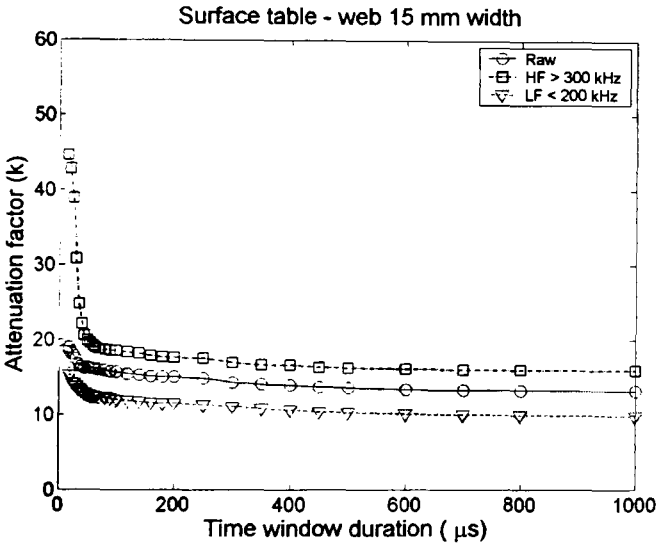

(c) Surface table – web 15 mm width

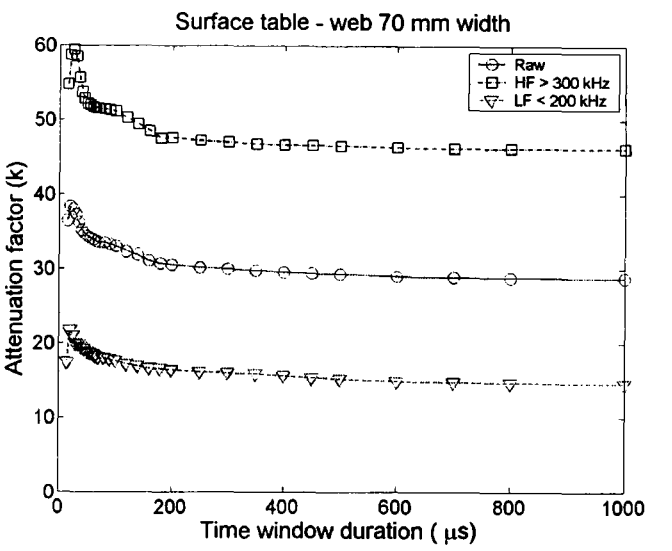

(d) Surface table – web 70 mm width

Figure 5.24: Plot of apparent attenuation factor (k) as a function of time window duration, for filtered and unfiltered time-series from four complex objects and paths.

Overall, it can be seen that the attenuation factor of all of the objects examined depends on the source-sensor path and the complexity of the object geometry. Thicker objects of simple geometry give a higher value of attenuation factor than thinner ones and thicker webs provide greater "leakage" in complex geometries. In simple geometries, most of the transmitted energy is in two frequency bands, 100-200 kHz and 300-350 kHz, while the lower frequencies tend to dominate at longer distances or where more leakage paths are present.

The analysis technique used in this section will be applied to analyse the data obtained from more complex structures such as the cylinder head and block of the diesel engine in order to determine attenuation factors for the remaining transmission tests. The fast wave (4500 m/s) and slow wave (2650 m/s) speeds will be used to determine source-sensor distance in the next section.

5.4 Results and discussion of 3D transmission tests on the small HSDI diesel engine blocks

Figures 5.25-5.36 and Tables 5.4-5.10 summarise the results of AE propagation from sources at injectors, inlet valves, exhaust valves and cylinder liners to various sensor arrays on the cylinder head and the cylinder block as described in Section 4.4. The results are discussed here as cylinder head sources and in-cylinder sources, respectively, using horizontal arrays, and then for vertical arrays. The findings of Section 5.3 have been used to avoid excessive repetition of analysis. The attenuation factors for all tests were determined using the best fit straight line (Equation (3.16)).

5.4.1 Transmission tests from cylinder head sources to horizontal sensor arrays on cylinder head and cylinder block

The data acquired using the simulated source was used to investigate the source-sensor distance and the attenuation factors, which could then be compared with the results in Section 5.3 and the results of engine running tests in Chapter 6. It is important to be able to estimate the source sensor distance reliably because this will then be used to study the attenuation of the AE energy with distance and calculate the attenuation factors for AE propagating on diesel engine blocks.

Figure 5.25 shows a comparison of measured transmission path lengths from transmission tests on the cylinder head to the horizontal sensor array on the cylinder head with those estimated from a 3D straight line. Each 3D straight line (d_s) was calculated from the co-ordinates of each source (x_1, y_1, z_1) and each receiver sensor (x_2, y_2, z_2) in 3D space using:

$$d_s = \sqrt{(x_2 - x_1)^2 + (y_2 - y_1)^2 + (z_2 - z_1)^2} \tag{5.3}$$

Path lengths were estimated from the acquired signal using fast wave and slow wave speeds as determined from the cylinder block in Section 5.3.1 (4500 m/s and 2650 m/s, respectively) and then multiplying by the arrival time of each wavefront as described in Section 5.2.4. The threshold level for slow waves was 0.2 of maximum signal amplitude and, for fast waves, it was set by eye because of the difficulty in setting a single threshold level for the lower signal to noise ratios. The dotted line in Figure 5.25 represents the reference 3D straight line ($y_{ref} = x$), the solid line represents the best-fit straight line for the measured transmission path length using the slow wave speed (y_s) and the dashed line that using the fast wave speed (y_f). Both the best-fit straight lines for the fast and slow waves were determined using linear regression with zero intercept:

$$y_f = C_f . y_{ref} \tag{5.4}$$

and

$$y_s = C_s . y_{ref} \tag{5.5}$$

where C_f and C_s are coefficients from the linear fit, which can be regarded as correction factors for the fast and slow wave speeds, respectively, containing uncertainties in wave speed, path length or both, arising out of the dispersive nature of the waves.

Figure 5.25 therefore gives a comparison between the two distances estimated using fast and slow wave speeds and the straight line distance for various source positions on injectors (INJ), inlet valves (IV) and exhaust valves (EV). As can be seen, all of the measured data estimates a distance greater than the straight line distance and the deviation of both estimates increases with distance from the source. This effect is most obvious for the inlet valve.

The correlation coefficients for the best fit straight lines through the data (R^2) can be used to assess the applicability of a simple straight-line propagation model. It can be seen that the results for the exhaust valve (Figure 5.25(b)) give a better correlation and this is probably because the artificial source was applied to the exhaust valve spring seat on the cylinder head and deviations from the reference may be only associated with a change of path and geometry rather than a change of speed [11]. However, when the pencil lead is broken on the injector body or inlet valve stem, the wave travels across a number of boundaries to the sensor array and this causes increased AE energy

attenuation through reflection and also, possibly, through wave mode conversion, potentially affecting both path length and effective wave speed. It has been mentioned [11] that, if AE propagates across boundaries between dissimilar materials or if mode conversion from one wave propagation mode to another mode occurs, then there will be a change in speed.

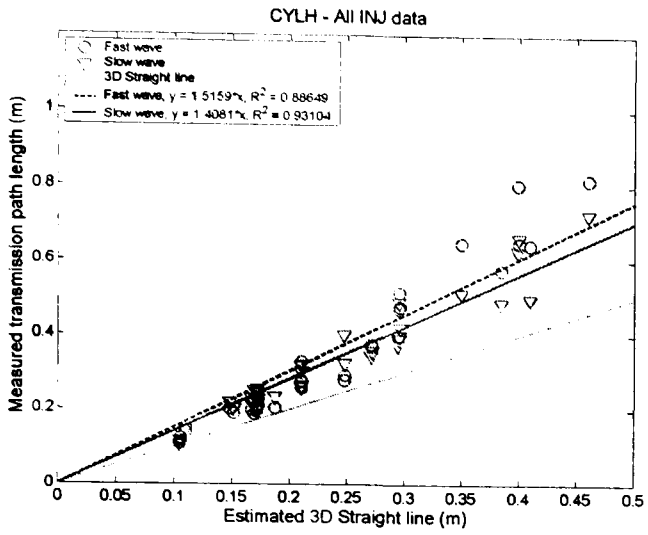

(a) Injectors (INJ)

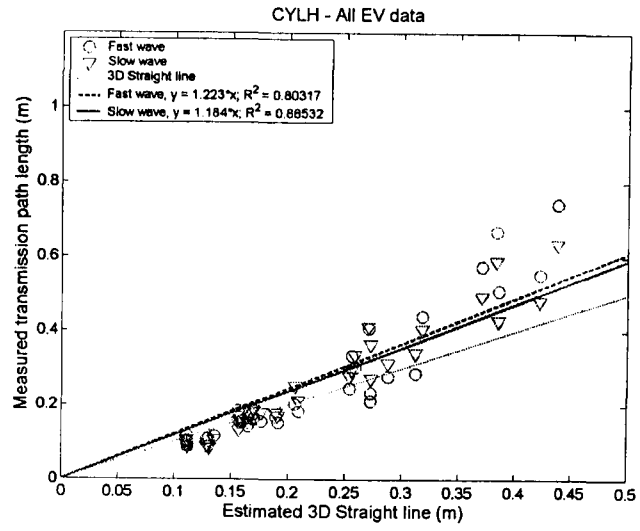

(b) Exhaust valves (EV)

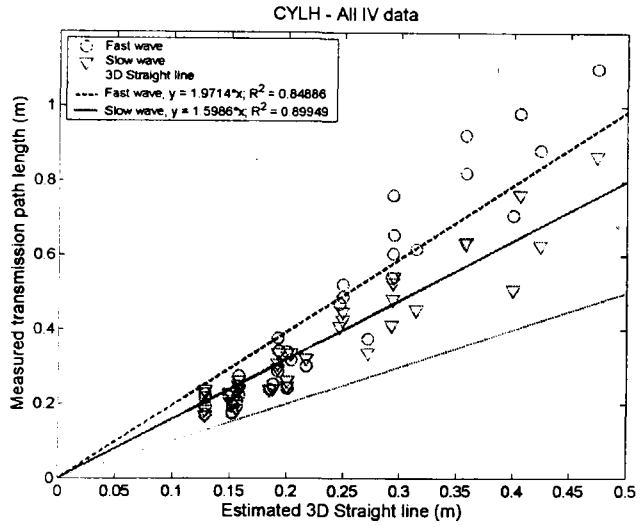

(c) Inlet valves (IV)

Figure 5.25: Comparison of various measured transmission paths with estimated 3D straight line from transmission tests for cylinder head sources using the cylinder head array.

In addition, assuming that both fast and slow wave speeds through the cylinder head are constant, the error in estimated distance relies only on the arrival time difference between source and sensor. As can be seen in Figure 5.25, the scatter and error in estimated distance is greater for the straight-line distances beyond 0.3 m. This is because the rise time of the AE signal increases with a propagating distance and, when using a threshold crossing technique, the apparent arrival time becomes less easy to determine as dispersion makes the distinction between different groups less clear. Other

authors, e.g. Pollock [13] and Ying *et al* [104], have also found that the accuracy of determination of time differences depends on the rise time of the AE signal.

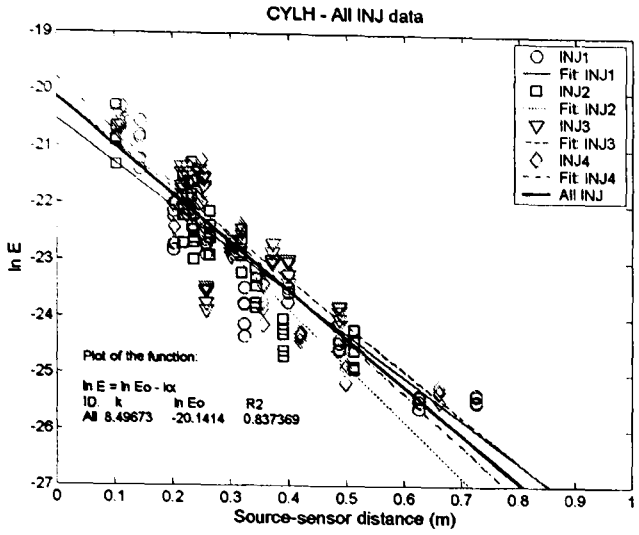

(a) Injector (INJ)

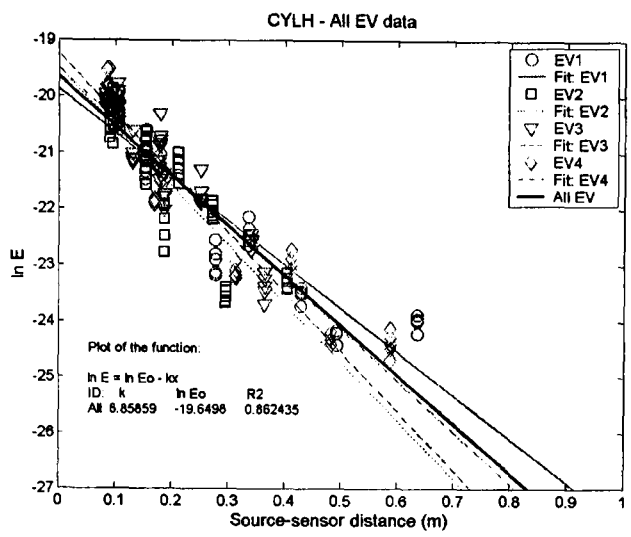

(b) Exhaust valve (EV)

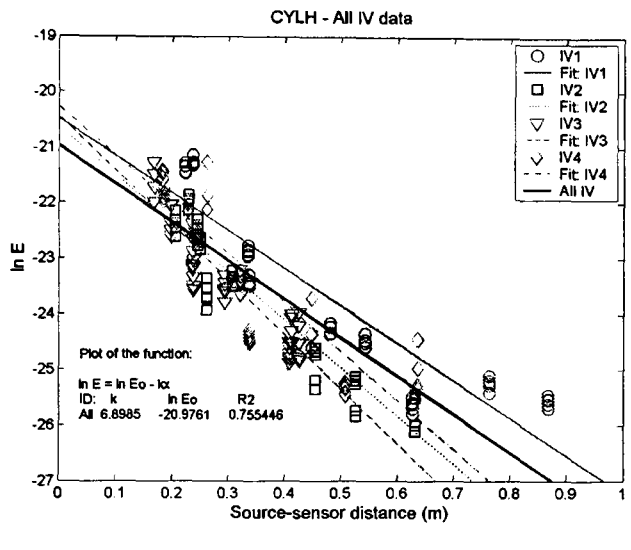

(c) Inlet valve (IV)

Figure 5.26: Plot of $\ln E$ versus source-sensor distance for transmission tests from simulated sources on injectors, inlet valves and exhaust valves to the cylinder head array.

In this work, it was found that the most consistent method of estimating source-sensor distance was to use a threshold to identify the arrival time of the low frequency, low speed, high amplitude wave together with the wave speed (slow wave, 2650 m/s) measured on the cylinder block shown in Figure 5.14(b). Using this source-sensor distance, the attenuation factors for AE energy for each of the source positions at the injector bodies, exhaust valve spring seats and inlet valve stems can be seen in Figure 5.26, where the five records for each source-sensor pair are plotted individually. The sliding time window technique described in Section 5.2.3 was used to determine time window duration for calculating AE energy. It was found that, in most cases, a time window duration of 2000 μs (10000 points) was appropriate for energy analysis (Table 5.1). The best-fit straight line for each source was calculated using the technique

described in Section 5.2.1 and this is represented by the solid line, those for the individual cylinders being shown in various dotted lines in Figure 5.26. Table 5.4 summarises the data illustrated in Figure 5.26. The averaged attenuation factors for each test are 8.5, 9 and 7, respectively, with the correlation coefficients all above 70%. It might be noted at this point that the variation in attenuation factors between source types on different cylinders is greater than the variation between the source types. Since the individual cylinder measurements (e.g. injector on cylinder 1) are themselves averaged, it seems likely that the transmission path might be affected by factors such as the position of the piston and the valve opening position.

Source positions	k	$\ln E_o$	R^2
Injector – 1	7.5788	-20.5305	0.8734
Injector – 2	9.9680	-19.8882	0.8662
Injector – 3	8.0914	-20.1121	0.6967
Injector – 4	9.2762	-19.8045	0.8739
All injectors	**8.4967**	**-20.1414**	**0.8374**
Exhaust valve – 1	7.8233	-19.8659	0.8773
Exhaust valve – 2	10.4826	-19.4971	0.7749
Exhaust valve – 3	10.6391	-19.2366	0.8852
Exhaust valve – 4	9.2872	-19.4948	0.9108
All exhaust valves	**8.8586**	**-19.6498**	**0.8624**
Inlet valve – 1	6.7437	-20.4827	0.8427
Inlet valve – 2	8.6514	-20.6500	0.8918
Inlet valve – 3	9.8196	-20.4460	0.8637
Inlet valve – 4	8.8092	-20.2739	0.8215
All inlet valves	**6.8985**	**-20.9761**	**0.7554**

Table 5.4: Summary of effective attenuation factor (k), apparent source energy on logarithmic scale ($\ln E_o$) and coefficient of determination (R^2) for transmission tests on cylinder head with source positions on injectors, IV and EV using the best-fit straight line ($\ln E = \ln E_o - kx$).

Using the best-fit straight lines according to Equations (5.4) and (5.5), it was possible to re-calculate both wave speeds from C_f and C_s, yielding an effective fast wave ($V_{f,eff}$) and an effective slow wave ($V_{s,eff}$) speed, respectively:

$$V_{f,eff} = \frac{V_f}{C_f} \tag{5.6}$$

and

$$V_{s,eff} = \frac{V_s}{C_s} \tag{5.7}$$

where V_f and V_s are measured fast wave and slow wave speeds (4500 m/s and 2650 m/s, respectively) on the cylinder block, as shown in Figure 5.14.

Table 5.5 shows a summary of slow and fast wave speeds, attenuation factors and correction factors (C_f and C_s) from the linear fit to the results shown in Figures 5.25-5.26. Clearly, there is some systematic relationship between correction factors and apparent wave speed, with slower speed being associated with larger correction factors. If, instead of correcting for speed, one corrects for distance, the attenuation factors can be corrected, for example as shown in the last column of Table 5.5. As can be seen, this yields values of k'_{slow} for slow wave, which can be quite close to that obtained for the simple geometry. Overall, this suggests that the "error" in complex geometric objects has more to do with the assumption of straight-line path length than the assumption of constant speed, although the effect of boundaries is not acknowledged by this.

Experiments	**Attenuation factor (k)**	**Fast wave (m/s)**	C_f	**Slow wave (m/s)**	C_s	k'_{slow}
Simple geometry[1]	12	4500	-	2650	-	
Source at exhaust valves (EV)[2]	8.8586	3680	1.2230	2238	1.1840	10.4886
Source at injectors (INJ)[2]	8.4967	2969	1.5159	1882	1.4081	11.9642
Source at inlet valves (IV)[2]	6.8985	2283	1.9714	1658	1.5986	11.0279

Table 5.5: Summary of wave speed[1] and effective wave speed[2] from various tests.

So, the effective wave speed on the cylinder head is generally lower than is measured on simpler geometric objects and this is thought to be due to the combined effects of indirect wave transmission paths, mode conversions and dispersion, which affect the phase of the wave arriving at the sensors. The effective wave speeds for the fast component and slow component are almost equally affected with the slow component being consistently slightly less so. This shows that dispersion is a minor, if consistent component of the apparent wave speed changes. In summary, AE waves travel through the cylinder head with an effective fast wave speed of between 2200-3700 m/s and an effective slow wave speed of between 1600-2300 m/s with the confidence level in both results being over 80%.

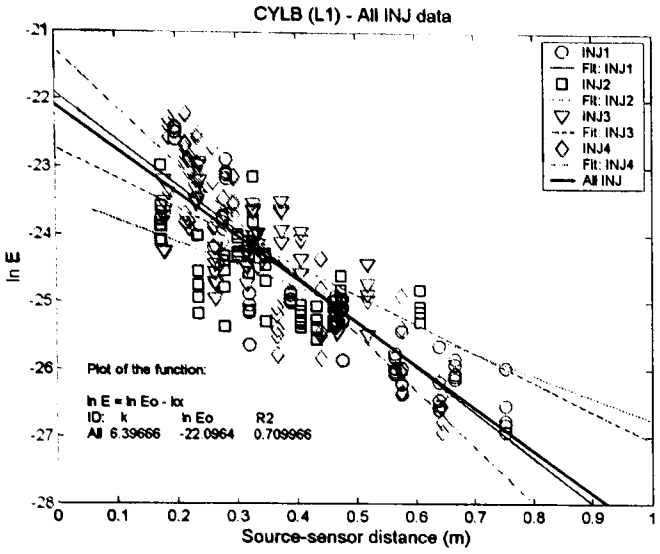

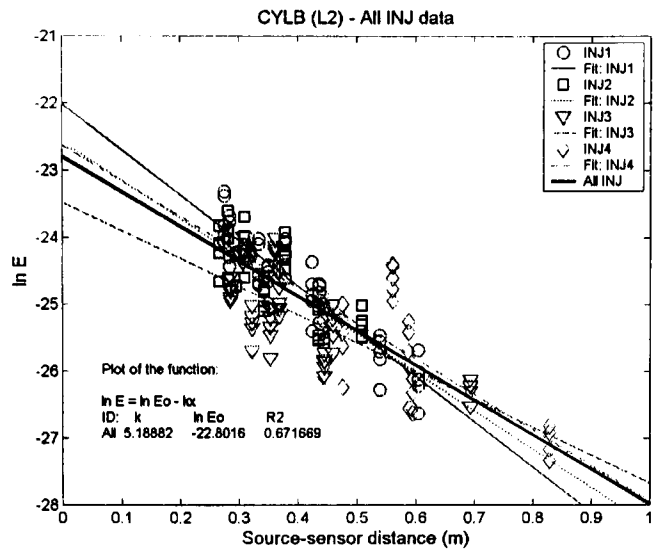

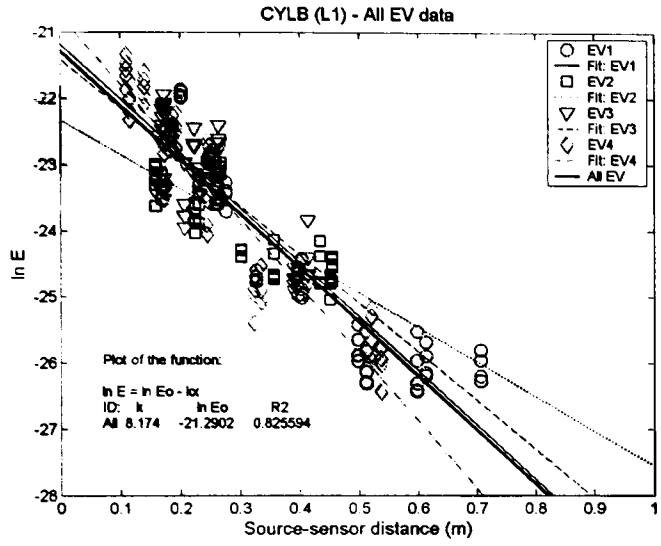

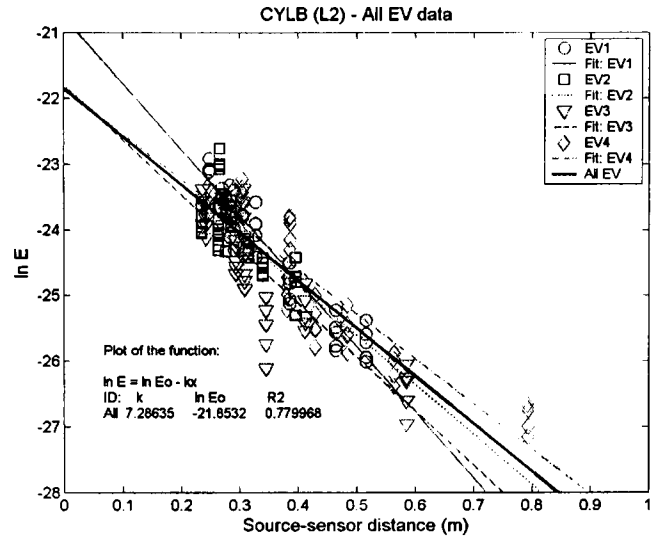

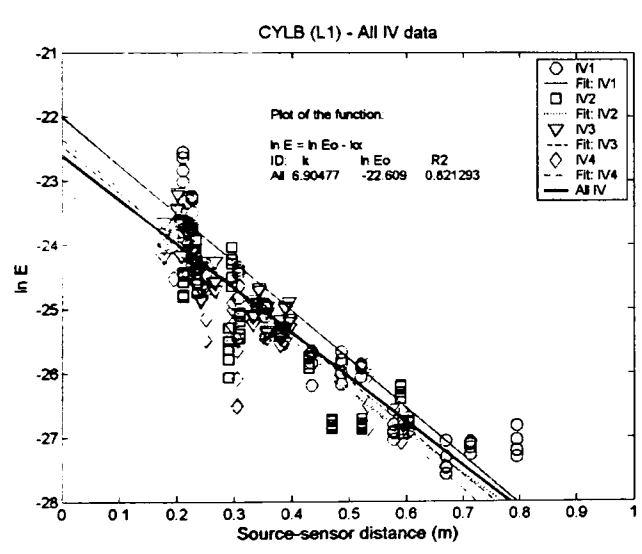

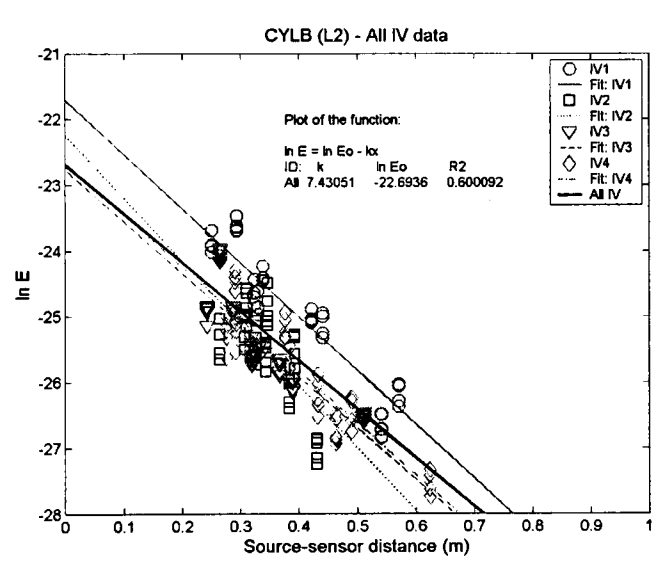

(a) Cylinder block – level 1

(b) Cylinder block – level 2

Figure 5.27: Plot of $\ln E$ versus source-sensor distance from various simulated sources (injectors, EVs and IVs) on cylinder head to two horizontal sensor arrays on cylinder block.

Figure 5.27 shows $\ln E$ versus source-sensor distance for the transmission tests with cylinder head sources (at injectors, EV spring seats and IV stems) using the two horizontal sensor arrays on the cylinder block, which were 0.03 m (L1) and 0.12 m (L2) below the top surface of the cylinder block (Figure 4.10). It is clear that there is some transmission from the cylinder head to the cylinder block, since all sensors at both horizontal arrays were able to detect an AE signal from the simulated sources on the cylinder head. The results given in Figure 5.27 and Table 5.6 show that the attenuation

factors for the arrays on the cylinder block are generally similar to those for the corresponding source as seen by the array on the cylinder head (Table 5.4), but that the E_o values are substantially smaller. This would suggest that the effect of straight-line metallic path is similar for the two types of array positions, but that there is a substantial drop associated with transmission from cylinder head to cylinder block. For injectors, the attenuation factors for both arrays on the cylinder block are smaller than on the cylinder head. This might be because the transmission paths of AE waves propagating from the injector to the cylinder head and to the cylinder block are more complicated, perhaps, involving the cylinders themselves.

Sources	Sensor array position					
	Cylinder block – level 1			Cylinder block – level 2		
	k	$\ln E_o$	R^2	k	$\ln E_o$	R^2
Injector – 1	6.7719	-21.9064	0.8198	6.7749	-22.0189	0.8239
Injector – 2	3.3157	-23.4448	0.3893	5.7396	-22.5767	0.6106
Injector – 3	4.3414	-22.7257	0.4198	4.1918	-23.4800	0.5296
Injector – 4	8.4180	-21.2650	0.8172	5.3185	-22.6261	0.7318
All injectors	**6.3967**	**-22.0964**	**0.7100**	**5.1888**	**-22.8016**	**0.6717**
Exhaust valve – 1	8.2216	-21.1861	0.8584	10.0280	-20.7693	0.9201
Exhaust valve – 2	5.2320	-22.3266	0.7092	7.5910	-21.8053	0.4875
Exhaust valve – 3	7.3704	-21.4128	0.5646	8.2606	-21.8088	0.7688
Exhaust valve – 4	10.2035	-20.7580	0.8909	6.8564	-21.8567	0.8476
All exhaust valves	**8.1740**	**-21.2902**	**0.8256**	**7.2863**	**-21.8532**	**0.7800**
Inlet valve – 1	7.5546	-22.0076	0.8858	8.2248	-21.7130	0.8703
Inlet valve – 2	6.3499	-23.1258	0.7815	9.5300	-22.2438	0.4566
Inlet valve – 3	7.3361	-22.4579	0.7854	7.8642	-22.7716	0.7452
Inlet valve – 4	7.8226	-22.3447	0.7680	7.9217	-22.6648	0.8504
All inlet valves	**6.9048**	**-22.6090**	**0.8213**	**7.4305**	**-22.6936**	**0.6001**

Table 5.6: Summary of effective attenuation factor (k), apparent source energy on logarithmic scale ($\ln E_o$) and coefficient of determination (R^2) for transmission tests from sources on injectors, IV and EV to horizontal sensor arrays on cylinder block using the best-fit straight line ($\ln E = \ln E_o - kx$).

5.4.2 Transmission tests from cylinder liner to horizontal sensor arrays on cylinder block

From the engine running cycle, there are some potential mechanical and fluid flow events arising within the cylinder, such as combustion, piston slap and liner scuffing. Using a simulated source on the liner, it can be seen that AE waves can propagate from the inner surface of the cylinder to both sensor arrays on the cylinder block (L1 and L2). Figures 5.28 and 5.29 show the relationship between $\ln E$ and source-sensor distance using the technique described in Section 5.2.1 for transmission tests from cylinder liner

to the two horizontal sensor arrays with and without water in the gallery. The calculated values of $\ln E$ for the two source positions at A1 and A3 (see Figure 4.11) on each of cylinder liners 1-4 are plotted against the source-sensor distance calculated using the slow wave speed with a threshold level at 0.2 of maximum signal amplitude to find wave arrival time automatically as described in Section 5.25.

The results and the best linear fit (solid line) for the tests on the cylinder block shown in Figures 5.28(a) and 5.28(b) are summarised in Table 5.7. The attenuation factors for the individual cylinders to both sensor arrays without water in the block vary from 9.9 to 14.7 with a good correlation (generally over 80%). It can be seen that, the attenuation coefficients for source position A1 are systematically lower than those for A3 and that Level 2 coefficients are systematically lower than Level 1. The collected values give an overall average attenuation coefficient ($k =$ 11.8) which is consistent with the corrected results shown in Table 5.5

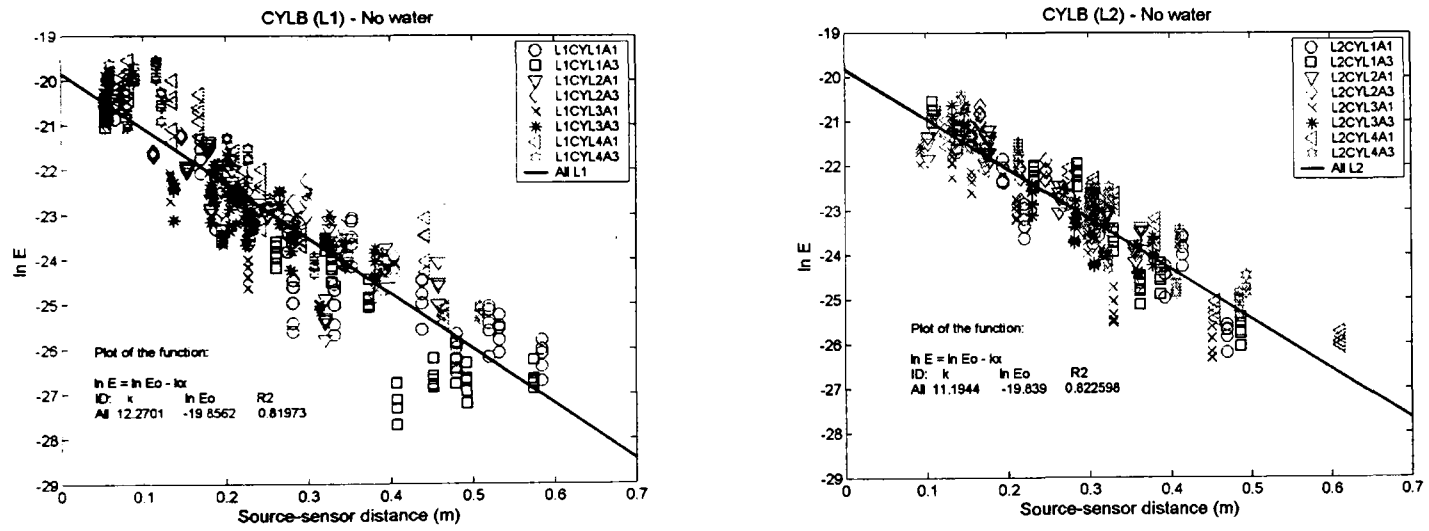

(a) Sensor array – level 1

(b) Sensor array – level 2

Figure 5.28: Plot of $\ln E$ versus source-sensor distance for various sensor positions on cylinder block for sensor arrays at level 1 and level 2 without water inside the gallery. Source positions were at A1 and A3 inside each cylinder liner.

Figures 5.29(a) and 5.29(b) and Table 5.8 show the equivalent results with the cylinder block water gallery filled. In these figures, the best fit straight line (solid line) and $\ln E$ were only calculated for sources at cylinder no. 1. Nevertheless, it is evident that attenuation factors are slightly larger for the equivalent cylinder and source position to either array where the water gallery is filled giving an averaged attenuation factor of 12.7. It would appear, therefore, that the presence of water in the gallery gives more opportunity for geometric scattering of the AE waves and hence greater attenuation over the same nominal path.

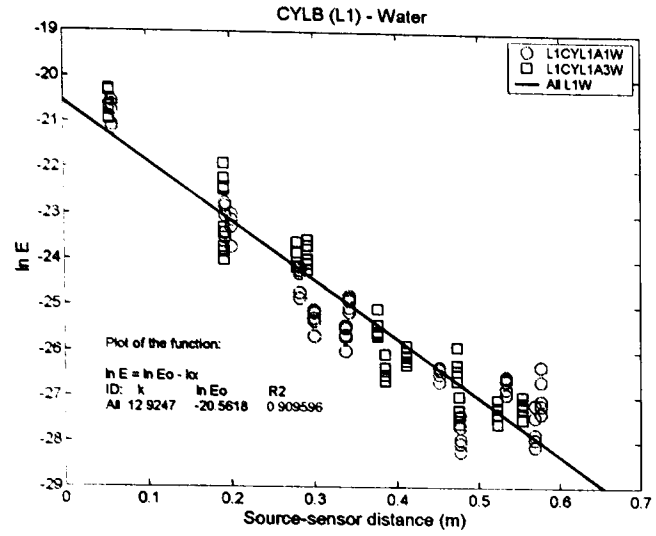

(a) Sensor array – level 1

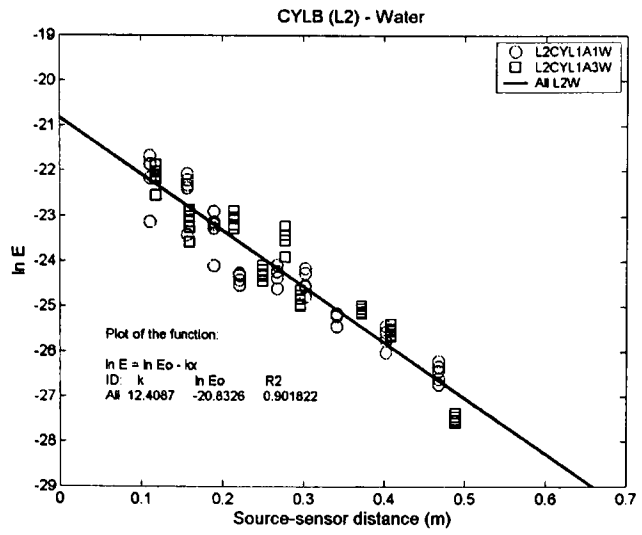

(b) Sensor array – level 2

Figure 5.29: Plot of $\ln E$ versus source-sensor distance for cylinder block arrays with water inside the gallery. Source positions were at A1 and A3 on surface of cylinder liner no. 1.

No	Array position	Cyl. no.	Pos	k	$\ln E_o$	R^2
1	Level 1	1	A1	10.2202	-20.5803	0.8040
2	Level 1	1	A3	12.3399	-20.5160	0.8562
3	Level 1	2	A1	10.4281	-20.3336	0.7665
4	Level 1	2	A3	9.9671	-20.3403	0.8457
5	Level 1	3	A1	12.9245	-20.1615	0.6953
6	Level 1	3	A3	11.9356	-20.1244	0.7945
7	Level 1	4	A1	12.1275	-19.2543	0.9004
8	Level 1	4	A3	12.7752	-19.1608	0.9015
9	Level 2	1	A1	11.4657	-20.0148	0.7991
10	Level 2	1	A3	13.1477	-19.6799	0.8461
11	Level 2	2	A1	11.1747	-19.9608	0.8644
12	Level 2	2	A3	13.6376	-19.0914	0.9246
13	Level 2	3	A1	9.8782	-20.0021	0.8939
14	Level 2	3	A3	14.7385	-18.7874	0.9028
15	Level 2	4	A1	11.8310	-20.4005	0.8519
16	Level 2	4	A3	14.1302	-19.2341	0.8842
17	Level 1	1,2,3,4	All A1	11.4657	-20.0148	0.7991
19	Level 1	1,2,3,4	All A3	13.1477	-19.6799	0.8461
18	Level 2	1,2,3,4	All A1	10.2761	-20.1777	0.8053
20	Level 2	1,2,3,4	All A3	12.6046	-19.3459	0.8649
21	Level 1	1,2,3,4	All A1/A3	12.2701	-19.8562	0.8197
22	Level 2	1,2,3,4	All A1/A3	11.1944	-19.8390	0.8226
23	Level 1&2	1,2,3,4	All data	11.7590	-19.8544	0.8103

Table 5.7: Summary of effective attenuation factor (k), apparent source energy on logarithmic scale ($\ln E_o$) and coefficient of determination (R^2) for transmission tests on cylinder block with two horizontal sensor arrays on cylinder block (no water inside water gallery) using the best-fit straight line ($\ln E = \ln E_o - kx$).

No	Array position	Cyl. No.	Pos	k	$\ln E_o$	R^2
1	Level 1	1	A1	12.1113	-20.9031	0.8934
2	Level 1	1	A3	13.8561	-20.1867	0.9333
3	Level 2	1	A1	12.0160	-20.9963	0.9009
4	Level 2	1	A3	12.9499	-20.6315	0.9073
5	Level 1	1	All A1/A3	12.9247	-20.5618	0.9096
6	Level 2	1	All A1/A3	12.4087	-20.8326	0.9018
7	Level 1&2	1	All data	12.6690	-20.6986	0.9110

Table 5.8: Summary of effective attenuation factor (k), apparent source energy on logarithmic scale ($\ln E_o$) and coefficient of determination (R^2) for transmission tests on cylinder block with two horizontal sensor arrays on cylinder block (water gallery filled) using the best-fit straight line ($\ln E = \ln E_o - kx$).

5.4.3 Results of transmission test across head gasket using vertical sensor array

Figures 5.30 and 5.31 show $\ln E$ versus source-sensor distance from transmission tests across the head gasket with source positions on the injector, the exhaust valve and the inlet valve of cylinder no 3. Sensors were mounted along a vertical axis at various positions on the cylinder head and cylinder block, and the vertical dashed line shown in each figure represents the head gasket location. The AE energy was calculated using the method described in Section 5.2.1, and the source-sensor distance was measured using the threshold crossing technique described in Section 5.2.4 using the slow wave with the threshold level set at 0.2 of the maximum signal amplitude.

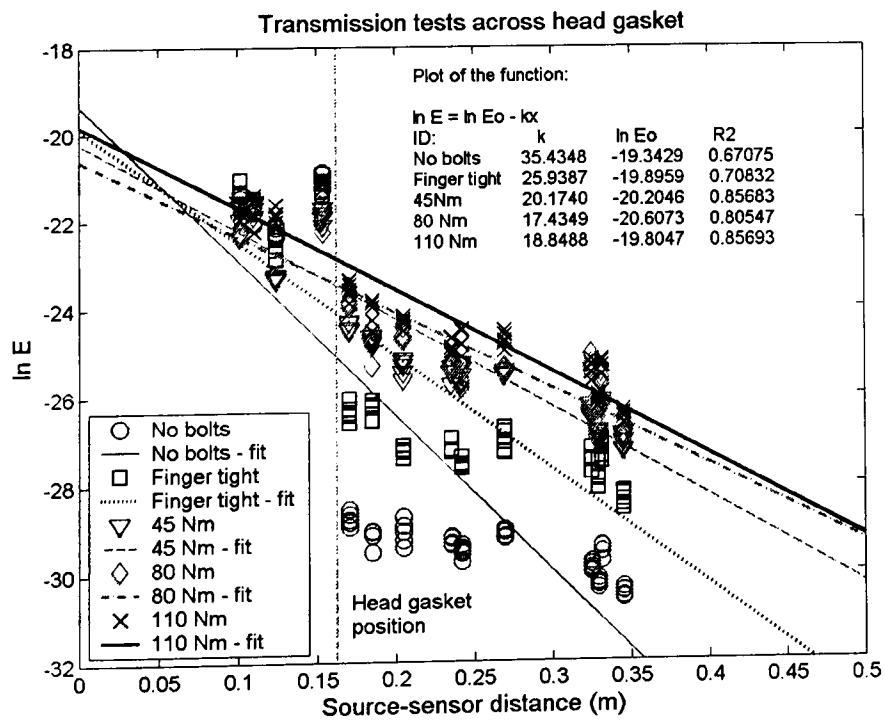

Figure 5.30: Plots of $\ln E$ versus source-sensor distance and their best-fit straight line for transmission tests across the cylinder head gasket with various bolt torques using a vertical sensor array. Source position was on IV3.

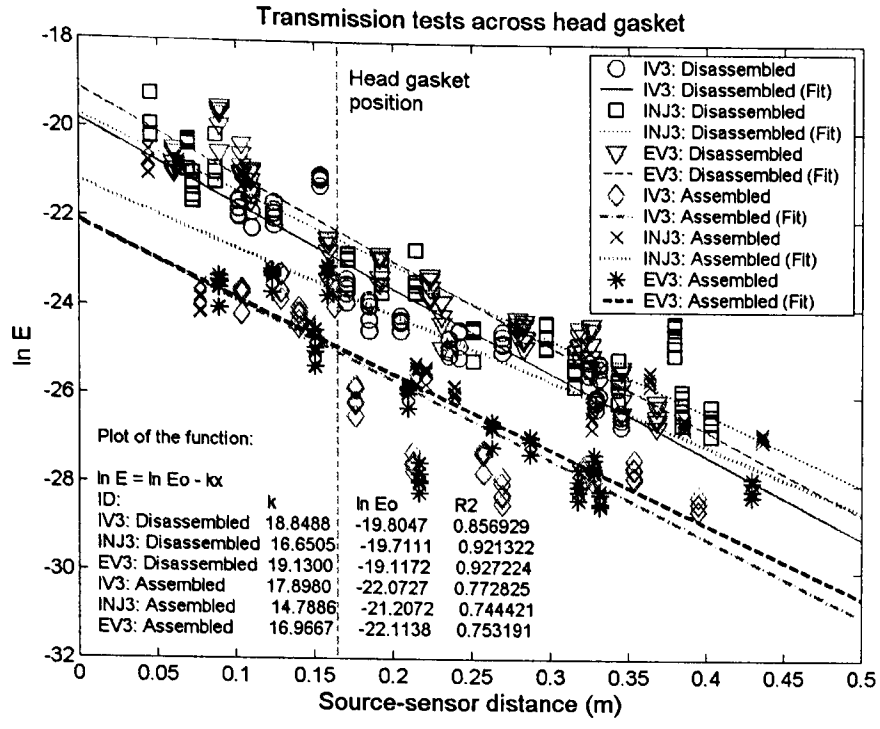

Figure 5.31: Plots of $\ln E$ versus source-sensor distance and their best-fit straight lines for transmission tests across the cylinder head gasket using the vertical sensor array, for the disassembled and assembled engines. Source positions were on INJ3, IV3 and EV3.

Figure 5.30 shows the results for various bolt clamping conditions (no bolts, bolts finger-tight, bolt torque at 45, 80 and 110 Nm) with the source on the inlet valve stem of cylinder no. 3. Figure 5.31 shows the results from the vertical sensor array on the two different engine blocks with the bolt torque at 110 Nm with sources on the injector, the exhaust valve and the inlet valve of cylinder no. 3 (Figures 4.12 and 4.13). The first test was on the disassembled engine block (no ancillary equipment) with no water inside the gallery, and the second was on the assembled engine (a running engine) with the water gallery filled. Table 5.9 summarises all coefficients from the best-fit straight lines for all transmission tests across the head gasket with and without water inside the gallery. From Figure 5.30, it is clear that there is a discontinuity in transmission when the cylinder head bolts are absent or loose and this is reflected in the large values of attenuation factor. However, once the bolts are fully torqued down, this discontinuity is not so apparent (Figure 5.31) although, attenuation factors are still larger than for the horizontal arrays. This effect has been investigated for simulated bolted joints by Shao and Mechefske [121] who studied attenuation of vibration transmitted through static metal to metal interfaces of steel, aluminium, stainless steel and copper. Simply supported beams (individual and stacked two, three and four layers thick of a single material) were used and the beams were held together with bolts at both ends. Impulsive vibration sources were generated by dropping a steel ball at mid-span. It was shown that, as the number of interfaces (number of beams in stack) increased, the attenuation increased gradually for tightly clamped interfaces, and significantly for loosely clamped

interfaces, especially at the first interface. They also noted that this effect was independent of material properties.

Transmission tests	k	$\ln E_o$	R^2
IV3: No bolts (Disassembled engine)	35.4348	-19.3429	0.6708
IV3: Finger tight (Disassembled engine)	25.9387	-19.8959	0.7083
IV3: 45 Nm (Disassembled engine)	20.1740	-20.2046	0.8568
IV3: 80 Nm (Disassembled engine)	17.4349	-20.6073	0.8055
IV3: 110 Nm (Disassembled engine)	18.8488	-19.8047	0.8569
INJ3: 110 Nm (Disassembled engine)	16.6505	-19.7111	0.9213
EV3: 110 Nm (Disassembled engine)	19.1300	-19.1172	0.9272
IV3: (Assembled engine)	17.8980	-22.0727	0.7728
INJ3: (Assembled engine)	14.7886	-21.2072	0.7444
EV3: (Assembled engine)	16.9667	-22.1138	0.7532

Table 5.9: Summary of effective attenuation factor (k), apparent source energy on logarithmic scale ($\ln E_o$) and coefficient of determination (R^2) for transmission tests across head gasket using the best-fit straight line ($\ln E = \ln E_o - kx$).

The effect of water filling seems this time to be to reduce attenuation factors and the injector, IV, and EV seem each to have systematically different attenuation factors which are consistent for the two engines. In addition, it can be seen that the effective source energy for the tests with water are smaller than the tests without water. This can again be explained by the acoustic impedance mismatch between cast iron and water being less than that to air (25 to 1, Table 3.2) so some AE energy is transmitted (lost) to the water reducing the amplitude at the sensor array positions. This effect has also been mentioned by Pollock [13] who suggested that, for pressure vessels and storage tanks, contained water could extract energy from AE waves propagating in the metal.

5.4.4 Summary of transmission tests on diesel engine blocks

Figures 5.32-5.35 show a conglomeration of $\ln E$ versus source sensor distance results for the various transmission tests on cylinder heads and cylinder blocks as described in Sections 5.4.2 and 5.4.3. It has been possible to detect simulated sources (pencil lead breaks) not only from various positions on the cylinder head but also on the inner surface of the cylinder liner at almost any point on the surface of the engine block or cylinder head. Figure 5.32 shows only the results of transmission tests from cylinder head sources at injectors, exhaust valves and inlet valves to various horizontal and vertical sensor array positions on the cylinder head and the cylinder block. It is evident that the attenuation of AE waves to the vertical array is significantly greater than that to the horizontal arrays.

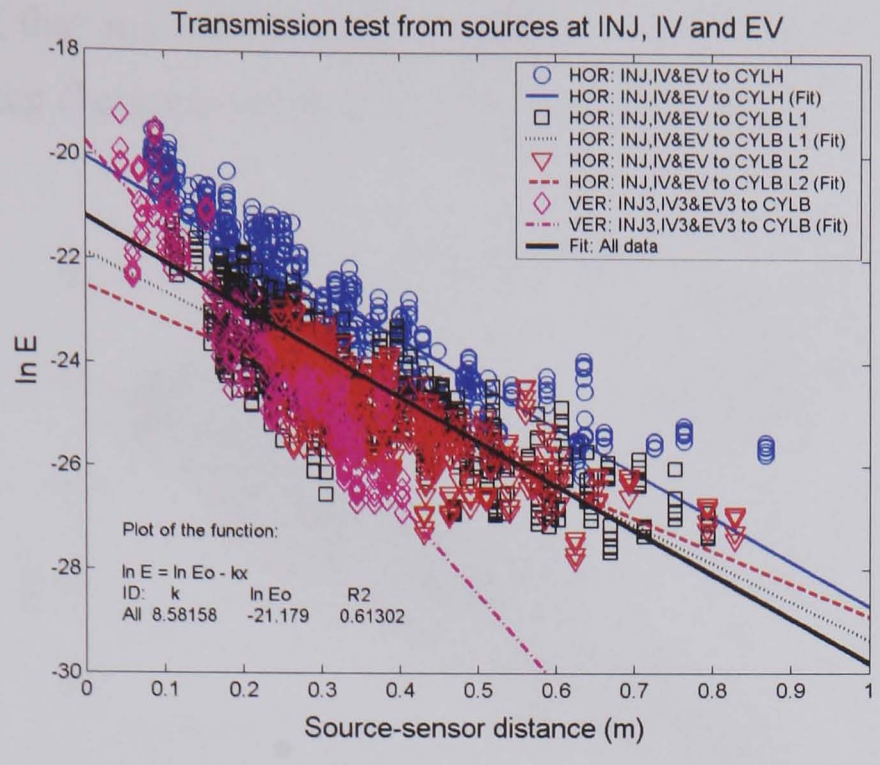

Figure 5.32: Comparison of $\ln E$ for transmission tests from cylinder head source to the various horizontal and vertical sensor arrays on the cylinder head and the cylinder block without water.

Figure 5.33 shows the results of transmission tests from sources at injectors, exhaust valves, inlet valves and the surface of cylinder liners to arrays on the cylinder head and block without water inside the gallery. It can be seen that the attenuation of AE energy is slightly greater for sources inside the cylinders than for cylinder head sources.

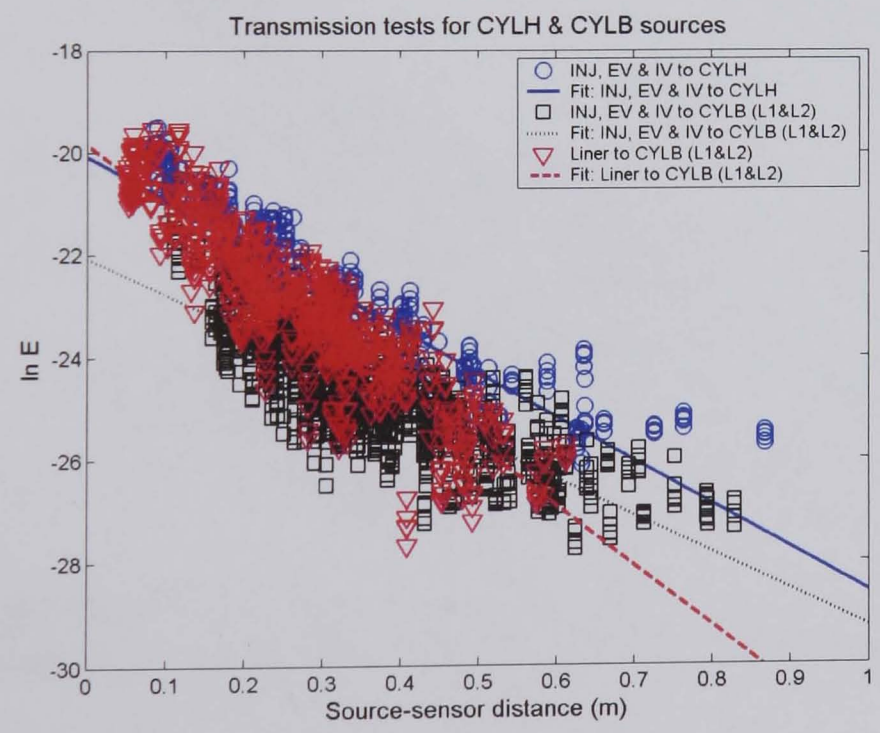

Figure 5.33: Comparison of $\ln E$ for various transmission tests from cylinder head and cylinder liner sources to horizontal arrays on the cylinder head and block without water inside gallery.

As mentioned in Section 5.4.3, energy can leak to the water when the gallery is filled. It can be seen in Figure 5.34 for horizontal arrays and Figure 5.35 for the vertical array that the overall energy content for water-filled engines is lower with a small increase in

slope, confirming that any leakage occurs gradually with transmission distance as well as there being a step change in intercept (apparent source energy).

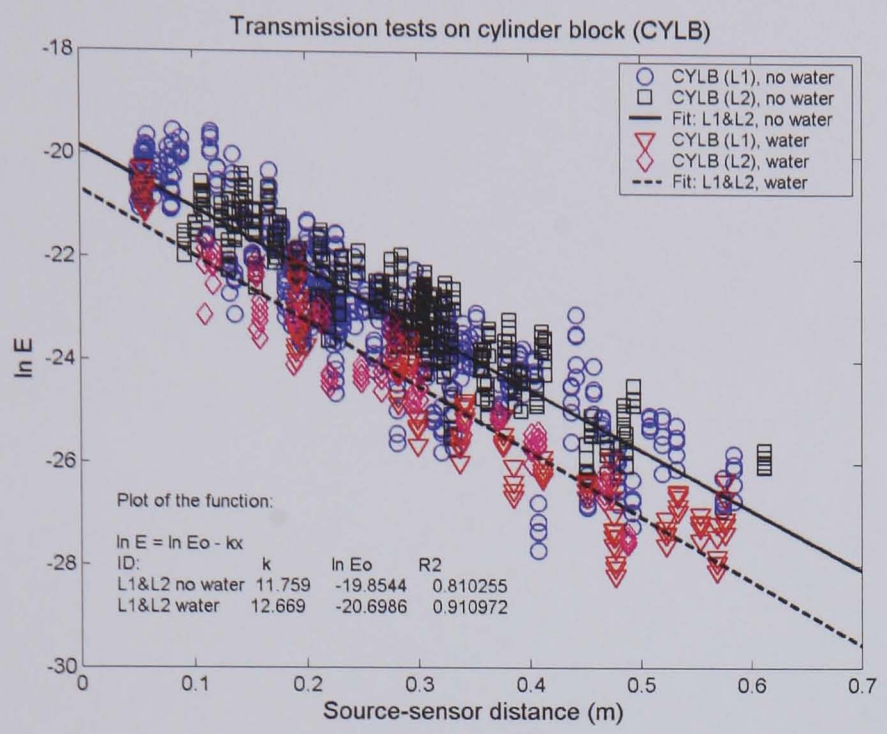

Figure 5.34: Comparison of $\ln E$ for cylinder liner sources to horizontal arrays on the cylinder block with and without water inside gallery.

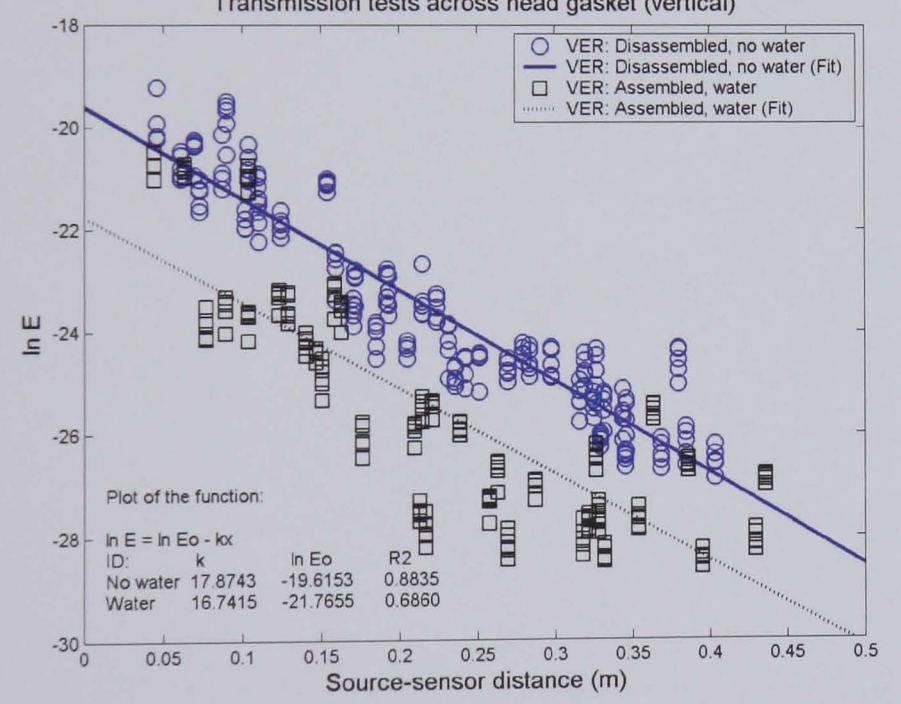

Figure 5.35: Comparison of $\ln E$ for various transmission tests across head gasket using vertical sensor arrays with and without water in gallery. Source was on INJ3, EV3 and IV3.

From Table 5.10, it is evident that attenuation factors for the vertical arrays are somewhat higher than for the horizontal arrays, suggesting that the effects of the two components might usefully be separated. On the basis that the three levels of horizontal array (on the cylinder head, 0.08 m below the source, at Level 1, 0.14 m below the source and at Level 2, 0.23 m below the source) would, in principle, yield parallel

attenuation curves with an offset whose value depends on the vertical position, Figure 5.36 shows a plot of $\ln E_o$ for cylinder head sources against vertical distance for each of the levels. By determining the best fit straight line, it can be seen that the attenuation factor ($k = 15.8$) is similar to the attenuation factor obtained from the vertical array as seen in Figure 5.35 and Table 5.10. It might be noted that the propagation of AE energy in the horizontal direction is more complicated than the vertical direction having a number of possible paths from source to sensor. The overall effect of reduced apparent attenuation of the horizontal component is probably similar to that seen in the narrow strip where multiple reflections contribute to the energy seen at the sensor.

Transmission tests	k	$\ln E_o$	R^2
HOR: INJ, EV and IV (1-4) to cylinder head, no water	8.5101	-20.0848	0.8157
HOR: INJ, EV and IV (1-4) to cylinder block (L1), no water	7.4300	-21.8822	0.7329
HOR: INJ, EV and IV (1-4) to cylinder block (L2), no water	6.3630	-22.5571	0.5615
HOR: INJ, EV and IV (1-4) to cylinder block (L1&L2), no water	7.1969	-22.0689	0.68217
All CYLH sources to all HOR arrays, no water	8.3961	-21.1817	0.6187
HOR: Liner 1 – 4 (A1&A3) to cylinder block (L1), no water	12.2701	-19.8562	0.8197
HOR: Liner 1 – 4 (A1&A3) to cylinder block (L2), no water	11.1944	-19.8390	0.8226
HOR: Liner 1 – 4 (A1&A3) to cylinder block (L1&L2), no water	11.7590	-19.8544	0.8103
HOR: Liner 1 (A1&A3) to cylinder block (L1), water	12.9247	-20.5618	0.9096
HOR: Liner 1 (A1&A3) to cylinder block (L2), water	12.4087	-20.8326	0.9018
HOR: Liner 1 (A1&A3) to cylinder block (L1&L2), water	12.6690	-20.6986	0.9110
VER: INJ3, EV3 and IV3 to cylinder block, no water	17.8743	-19.6153	0.8835
VER: INJ3, EV3 and IV3 to cylinder block, water	16.7415	-21.7655	0.6860
All CYLH sources to all HOR and VER arrays, no water	8.5816	-21.1790	0.6130

Table 5.10: Summary of effective attenuation factor (k), apparent source energy on logarithmic scale ($\ln E_o$) and coefficient of determination (R^2) for all transmission tests on the cylinder head and the cylinder block with/without water filling using the best-fit straight lines ($\ln E = \ln E_o - kx$).

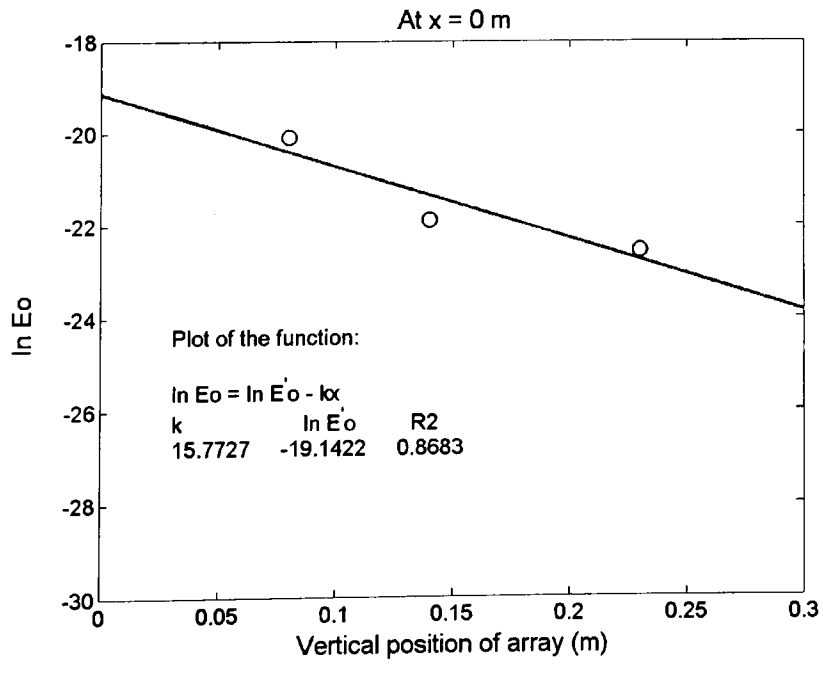

Figure 5.36: Plot of $\ln E$ from the results of various transmission tests using various horizontal sensor arrays versus vertical distance from sources.

Most AE attenuation studies have been based on maximum amplitude, and have been carried out on plate-like structures [11, 85, 101, 102], and have used a power law function [11] or exponential function [103]. The relatively few studies which use energy attenuation (e.g. Mba and Hall, [86]), are focused on making quantitative use of the energy for diagnostic purposes as is the case in the current work. Most of this work has concentrated on determining the maximum distance at which AE sensors can detect a signal in order to optimise sensor spacing for source location.

A summary of the averaged attenuation factors from all of the results discussed in Section 5.4 can be seen in Table 5.10. For real complex structures such as an engine, when an AE source is generated, the wave type and transmission path cannot be controlled, and the resultant distortion in the source time-frequency characteristic is unavoidable and has to be accepted [11]. In this section, only estimated transmission path lengths using the slow wave speed and measured arrival times are used in the analysis and these will also be used to interpret the engine running tests in the next chapter. The attenuation factors for AE transmission from various sources on the cylinder head (Tables 5.6 and 5.10) will be compared with the results from real engine sources and will subsequently be used for spatial reconstitution and location of sources using sensors on the cylinder head of the small HSDI diesel engine.

5.5 Results and discussion of transmission tests on 10 MW marine diesel engine

The transmission tests on the 10 MW marine diesel engine (see Figures 4.14 and 4.15) were carried out to assess the generic application of the work and, as such, are less exhaustive than those on the small HSDI engine. Figure 5.37 shows the results of transmission tests from an injector to cylinder block calculated using the method described in Section 5.2.1. Figures 5.38-5.41 and Table 5.11 are the results of the transmission tests on the large cylinder liner which is made of cast iron. The analysis techniques were modified to suit this application because of its large extent and Sections 3.3 and 5.2.1 describe how this was done. The results are discussed in this section and will be used to analyse some selected engine running tests in the next chapter.

5.5.1 Transmission test from injector to cylinder block

Figure 5.37 shows $\ln E$ versus source sensor distance for transmission tests from injector to cylinder block (with the sensor mounted on a web or on a flat panel) on the 10 MW engine using a simulated source (an automatic centre-punch). The energy content of each signal was calculated using Equation (3.14) using the method described in Section 5.2.1 and Table 5.1. However, the energy at the source (the injector) position was not included in the calculation. The energy for the signals acquired at the valve housing (P1b), the exposed area of the upper part (P2) and the lower part (P3) of the cylinder liner, and the flat panel (P4a & P5a) or web (P4b & P5b) of the cylinder block were used (see Figure 4.14). The attenuation factor was calculated using best-fit straight line (Equation (3.16)), and the source-sensor distance was estimated from a drawing. Ten records for each source-sensor pair were plotted and the best-fit straight line was determined. The averaged attenuation factor for both tests is around 2.7 and this was slightly lower for the flat panel surface than the web surface. It is significant to note that the correlation is significantly better over these large distances and the attenuation factor is considerably lower. This might reasonably be attributed to the large size of the metallic components (less geometric spreading) with a proportionately small effect of interfaces and boundaries.

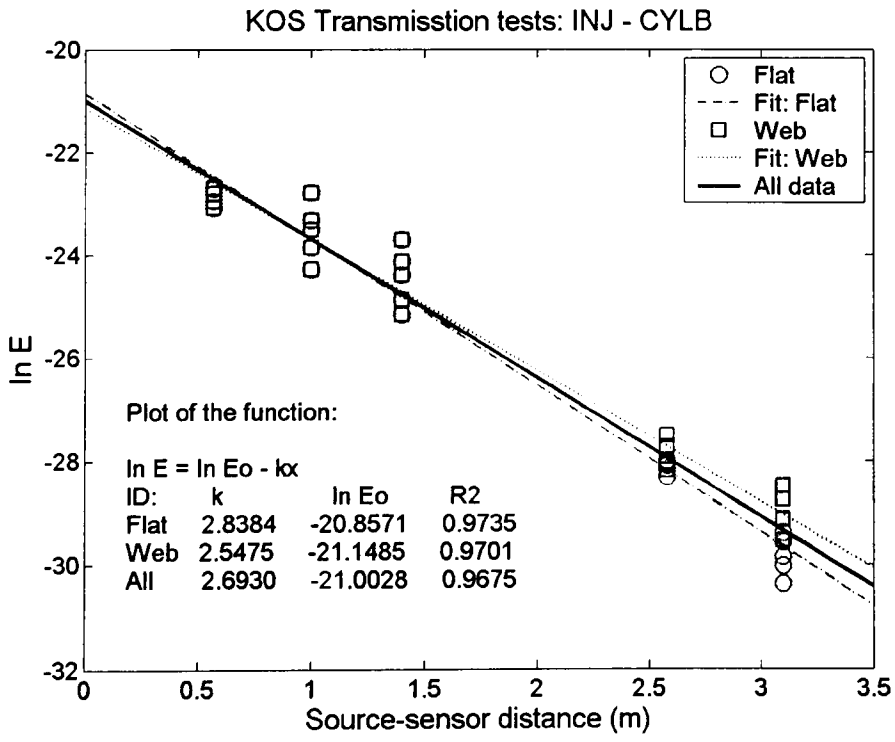

Figure 5.37: Plot of $\ln E$ versus source-sensor distance for transmission test from injector to cylinder block on 10 MW marine diesel engine.

5.5.2 Transmission test on cylinder liner

Example plots of three raw signals are shown in Figure 5.38 recorded from receiver sensors S2, S3 and S4 (Figure 4.15) where sources were generated at 0.05, 0.51 and 1.8m from the top surface of the cylinder liner. A typical signal at short source-sensor distance is shown in Figure 5.38(a) whereas Figure 5.38(b) is typical of a source on a surface with some complicated geometric feature (such as around the oil groove). Figure 5.38(c) shows a typical signal where the source was generated far from the receiver sensors (source at bottom of liner, receiver at top). One general observation is that the wave modes seem clearer for transmission over short distances but the effects of reflections, damping and multiple waves make the waveform very complicated over longer transmission paths.

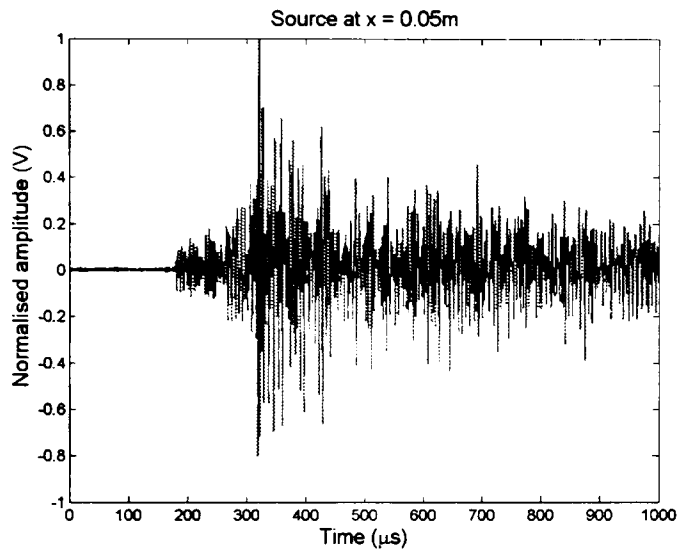

(a)

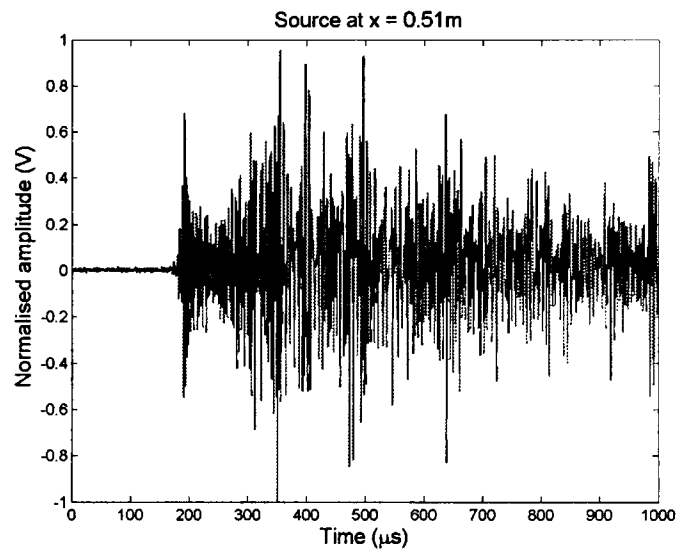

(b)

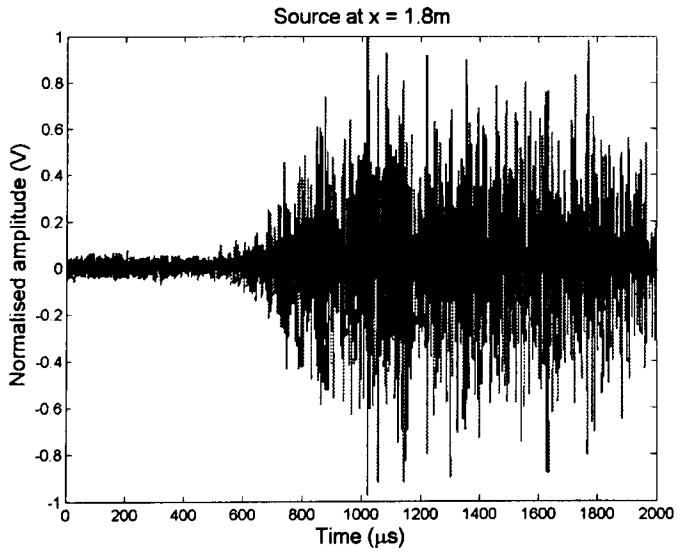

(c)

Figure 5.38: Measured raw AE signals for source positions at 0.05, 0.51 and 1.8 m, for (a) short source-sensor distance, (b) source generated on surface of complex geometry, and (c) long source-sensor distance.

Figure 5.39 shows $\ln E$ versus source–sensor distance for the signals acquired from all positions on the liner. Source-sensor distance was estimated as the shortest direct transmission path from a drawing, and each line shown was determined using best-fit straight line. It can be seen that the energy content separates into two groups; the signals acquired from positions S2 and S4, and the signals acquired at S3 (Figure 4.15). The attenuation factors for all tests are relatively similar at around 2.1-2.3 as seen in Figure 5.39 and Table 5.11.

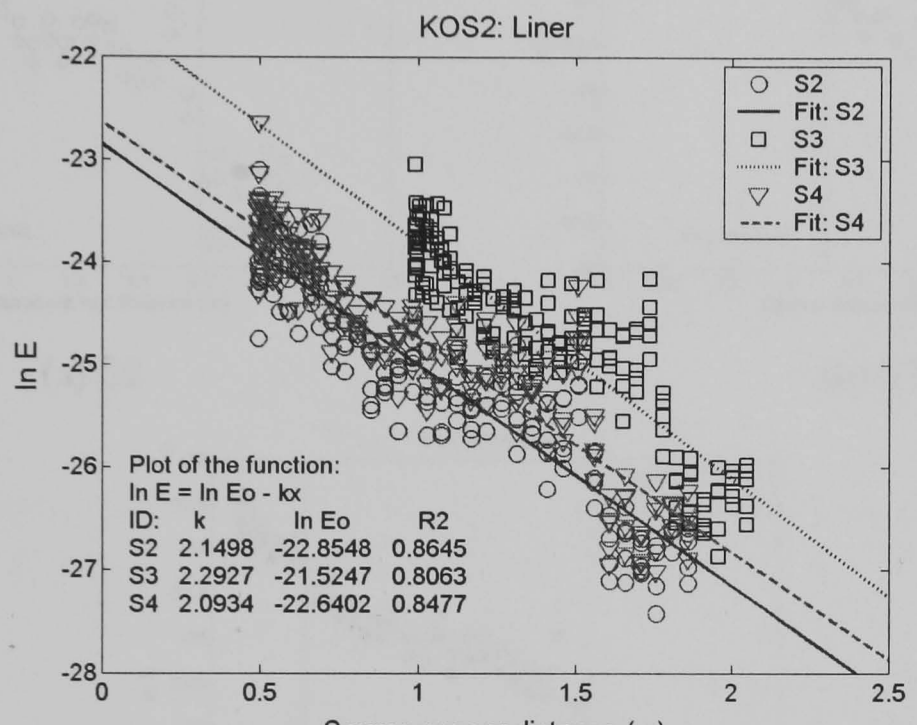

Figure 5.39: Plot $\ln E$ versus source – sensor distance for various sensor positions on cylinder liner of 10 MW marine diesel engine.

The influence of waves travelling in different directions is seen in Figure 5.39 where, for S3, the energy is higher for a given source-sensor distance, say 1m, than at sensors S2 and S4. Supposing two waves to travel from the source in opposite directions around the circumference of the liner, one can imagine two stronger waves to arrive at S3 after travelling 1 m while one strong wave (travelling 0.57 m) and one weak wave (travelling 1.7 m round the liner) to arrive at S2 (or S4) resulting in lower amplitude. To compensate for the effect of two waves, the results in Figure 5.39 were normalised to give an energy content for the shorter distance, x_s. Thus, from Equations (3.18) and (3.19), the normalised energy content at receiver sensors at S2 and S4 becomes

$$E(x) = E_o e^{-kx_s} \cdot [1 + e^{-kc} \cdot e^{2x_s}] = E_s \cdot [1 + e^{-kc} \cdot e^{2x_s}]$$

$$E_s = \frac{E(x)}{[1 + e^{-kc} \cdot e^{2x_s}]} \tag{5.8}$$

and, for the receiver sensor at S3 ($x_s = x_l$), the normalised energy content is given by:

$$E_s = \frac{E(x)}{2} \tag{5.9}$$

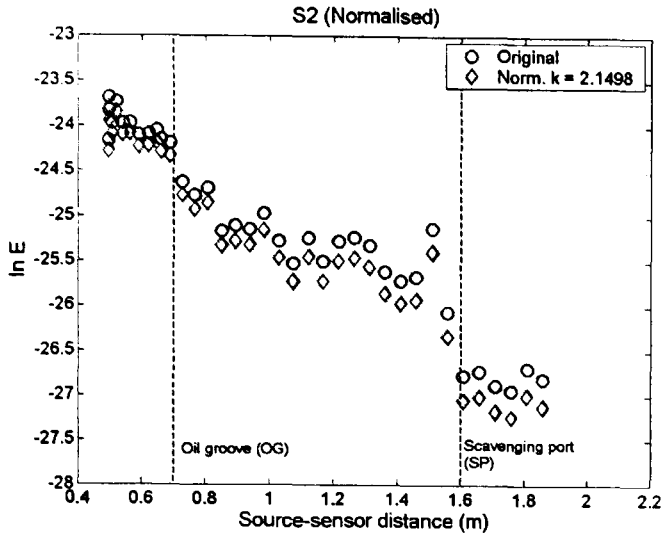

(a) S2

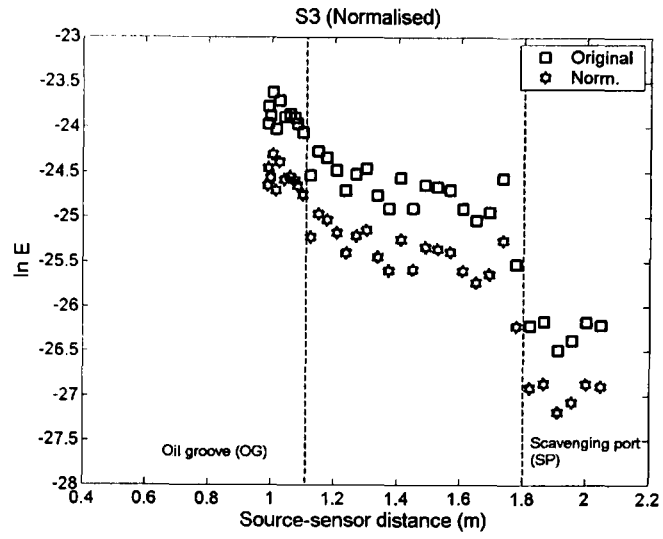

(b) S3

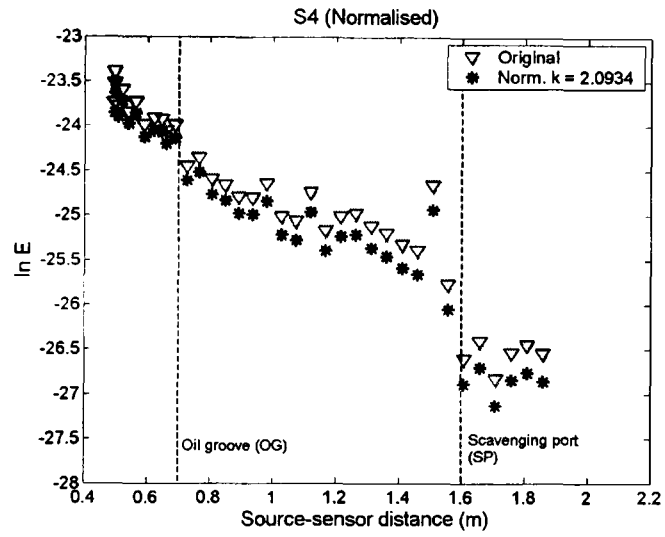

(c) S4

Figure 5.40: Normalised $\ln E$ versus source-sensor distance for large diesel cylinder liner using Equation (3.19). Sensor positions at S2 (a), S3 (b) and S4 (c)

Using Equation (5.8) with $k =$ 2.1498 and 2.0934 for S2 and S4, respectively, and Equation (5.9) for S3, the normalised energy content of each sensor was averaged from five records and the results are shown in Figure 5.40. The vertical dashed lines represent the positions of the oil groove (OG) and scavenging port (SP) and it can be seen that the energy content drops at both positions, more so at the scavenging where the geometry is much more complicated. Figure 5.41 shows the best fit straight line of each sensor. As can be seen, the data do not "line-up" exactly although this may be due to sensitivity to sensor position (the sensors were not moved during the test) and/or effects of local geometric features in the liner. Overall, the attenuation factor remains similar with attenuation factors for each sensor of around 2.3 as seen in Figure 5.41 and Table 5.11.

Generally, this analysis shows that a wave generated in the internal surface of a large cylinder liner can travel both axially and circumferentially and that internal features in the liner will lead to discontinuities in energy.

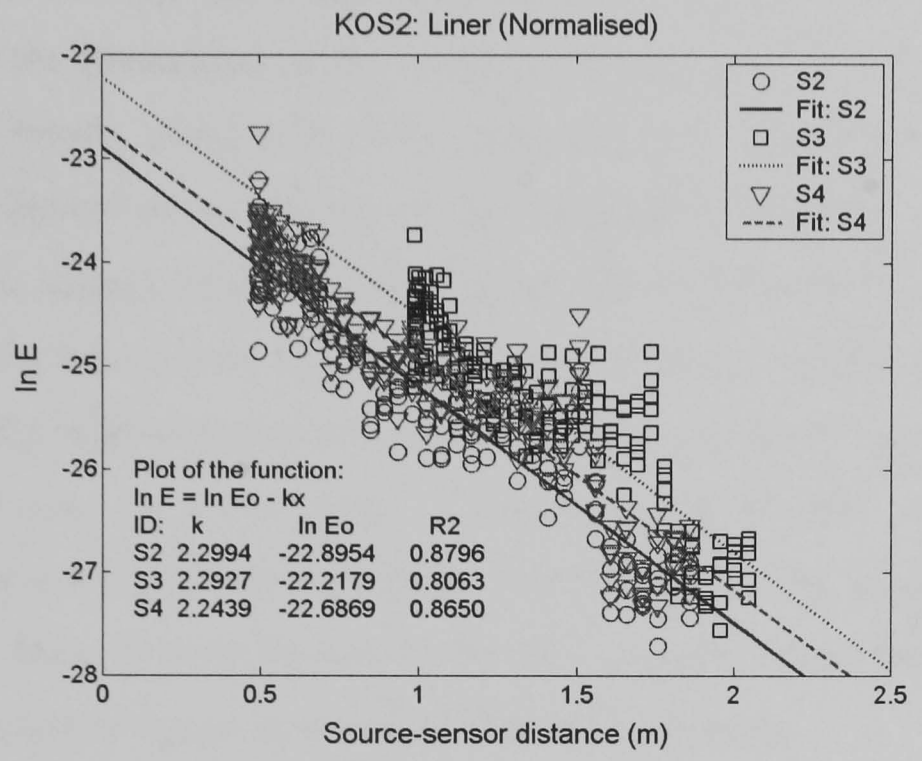

Figure 5.41: Plot of Normalised $\ln E$ versus source – sensor distance (for S2 and S4, k = 2 and for S3, $x_s = x_l$), for various source positions on cylinder liner of 10 MW diesel engine.

Sensor position	$\ln E$			**Normalised** $\ln E$		
	k	$\ln E_o$	R^2	k	$\ln E_o$	R^2
S2	2.1498	-22.8548	0.8645	2.2994	-22.8954	0.8796
S3	2.2927	-21.5248	0.8063	2.2927	-22.2179	0.8063
S4	2.0934	-22.6402	0.8477	2.2439	-22.6869	0.8650

Table 5.11: Summary of attenuation factor (k), $\ln E_o$ and coefficient of determination (R^2) from Figures 5.39 and 5.41.

The analysis techniques used in small diesel engines have been used successfully to determine attenuation of AE energy on a large marine diesel engine. The results of this section will be used to help analyse some selected results obtained from engine running tests to provide a demonstration of scale-up effects.

5.6 Summary of findings for transmission tests

This chapter has been concerned with the propagation of AE waves through simple (plate-like) structures and more complicated structures, such as the cylinder head and the cylinder block of small and large diesel engines. A simple absorption law has been used to describe the attenuation of the energy as given in Section 3.3 (Equations (3.14)-(3.16)) and two waves, along with their associated wave speeds have been identified. The attenuation factors found depend on the geometric complexity, although, even for very complicated objects, there can be good correlation between the measured data and the simple model chosen here if the attenuation coefficient is known. It is recognised that, when dealing with complex structures, there is a potential error in source-sensor distance, arrival time or wave speed, or indeed a combination of all three due to dispersion, reflection and mode conversion. The findings of this chapter will be applied to data obtained from running engines in the next chapter, where the exact sources and therefore source-sensor distances are more difficult to estimate.

Chapter 6 Engine running tests

6.1 Introduction

This chapter describes and discusses the results of the laboratory engine running tests on the small 76 kW HSDI diesel engine and the in-service industrial tests for the large 10 MW diesel engine, both described in Chapter 4. The sensor arrays typically used were similar to those for the transmission tests discussed in Chapter 5. The analysis techniques used in this chapter are described in the next sub-section, and were developed to extract significant features from the detected signals. Accordingly, they are based mostly on relatively simple statistical signal processing techniques in the time domain, the crank angle domain, and a combination of the crank angle and frequency domain. The analysis is aimed at understanding AE wave propagation of real sources in running diesel engines under various conditions in order to improve the capacity of AE to identify source characteristics in a multi-source, multi-sensor system. The injector (INJ) and exhaust valve opening (EVO) events are the main ones discussed in this chapter, and the results are compared with those of the transmission tests using simulated sources in Chapter 5. The final section shows the application of these techniques on the large two-stroke diesel engine.

6.2 Analysis techniques for engine running tests

The main objective of the analysis was to develop signal processing techniques to describe the nature of AE events from a sensor signal recorded after the wave has propagated through the engine structure. Typical AE sources in engines are mechanical and fluid activities from the injection process, the combustion process, valve operation and ancillary equipment. The analysis techniques developed were based on time domain, crank angle domain, and a combination of crank angle and frequency domain processing.

6.2.1 Crank angle domain analysis

For running diesel engine signals, the time series could be resampled to the crank angle domain by using the signal acquired from the digital shaft encoder including the reference pulse (TDC position). The crank angle domain has the advantage that it is tied to certain mechanical events in the engine cycle and it therefore permits the introduction of deterministic methods into the signal processing. The resampled signal was always referred to the crank angle at top dead centre (TDC) of cylinder no. 1 on its firing stroke. Using the timing signal, the number of data points in each degree of crank angle was found, and, assuming that the engine speed was constant within each individual degree of rotation, the data could be resampled directly from the time domain to the crank angle domain until the entire engine cycle (720 degrees) was obtained. In this way, all AE signals irrespective of local or average engine speed, were mapped onto the same scale and the signals associated with mechanical events could be therefore compared with each other.

For the running diesel engine tests, the energy content of each mechanical event in a time domain signal could be determined using Equation (3.14). However, as mentioned above, the signal energy can be more meaningfully determined from the crank angle domain signal given its mechanical significance and the fact that it compensates for slight variations in engine speed within and between cycles. Thus, Equation (3.14) can be re-expressed for an event window from θ_1 to θ_2, by the following equation,

$$E(\theta) = \int_{\theta_1}^{\theta_2} v^2(\theta)\, d\theta \tag{6.1}$$

For a typical running diesel engine, there are various predictable source events associated, for example, with injectors, inlet valves, exhaust valves, combustion and other ancillary equipment. The signal was windowed with a suitable angle range and the energy content was calculated using Equation (6.1). For transmission analysis, the energy content for each sensor array position was determined and then plotted against source-sensor distance so that the best-fit straight line and attenuation factor could be obtained using Equation (3.16). Source-sensor distance was taken as the estimated distance from the slow wave speed (2650 m/s) determined in the transmission tests using simulated sources in Section 5.4, which, in turn, assumes that the sources were on

injector bodies, exhaust valve spring bases and the tops of inlet valve stems. This process was carried out for all running test conditions on the small HSDI diesel engine and large marine diesel engine as described in Sections 4.5 and 4.7. Table 6.2.1 summarises all the engine running tests for the small and large diesel engine, including speeds, load conditions and crank angle ranges used in the analysis.

Engine running tests	Speed (rpm)	Load condition	Crank angle range (reference to TDC of each cylinder)
Small HSDI engine: CYLH sources to CYLH array (Section 4.5.1)	800/1200	No load/ 30 Nm	INJ: 40 degs (-10° to +30°) EVO: 20 degs (110° to 130° ± 10°)
Small HSDI engine: CYLH sources to CYLB (L1) array (Section 4.5.2)	800/1200	No load/ 30 Nm	INJ: 40 degs (-10° to +30°) EVO: 20 degs (110° to 130° ± 10°)
Small HSDI engine: CYLH sources to CYLB (L2) array (Section 4.5.2)	800/1200	No load/ 30 Nm	INJ: 40 degs (-10° to +30°) EVO: 20 degs (110° to 130° ± 10°)
Small HSDI engine: CYLH sources (Cylinder no. 3) to vertical array (Section 4.5.3)	800	No load/ 30 Nm	INJ: 40 degs (-10° to +30°) EVO: 20 degs (110° to 130° ± 10°)
Large marine diesel engine, industrial site (Section 4.7)	136	9 MW	INJ: 40 degs (-10° to +30°) Scavenging: 5 degs (+120° to +125°)

Table 6.1: Summary of experimental conditions and data analysis for engine running tests

6.2.2 Signal to noise ratio (SNR) determination

For the engine running tests, there was a relatively constant background noise level and the signal amplitudes for some mechanical events at some sensor positions only barely exceeded that background level. In order to avoid such weak signals distorting the analysis, the signal to noise ratio (SNR) for each window at each sensor was determined and a threshold set for the minimum acceptable value. SNR was calculated as the ratio between the maximum value of energy content in a small crank angle ($\Delta\theta$) and the mean energy content of the signal in a specific window in which the event is expected to occur (from θ_1 to θ_2) as seen in Equation (6.1):

$$SNR = \frac{\max\left(E_{\Delta\theta_i}\right)}{E_w} = \frac{\max\left(\int_{\theta_i}^{\theta_{i+\Delta\theta}} V^2 d\theta \Big/ \Delta\theta\right)}{\left(\int_{\theta_1}^{\theta_2} V^2 d\theta\right) \Big/ (\theta_2 - \theta_1)} \tag{6.2}$$

where $E_{\Delta\theta_i}$ is energy content of a small crank angle ($\Delta\theta$), i = 1, 2, 3, … n;

and E_w is mean energy of the whole signal in a specific window from θ_1 to θ_2.

In general, $E_{\Delta\theta_i}$ was calculated for one degree of crank angle and the minimum SNR was set at 2, any detected signal below this level being excluded from the analysis.

6.2.3 Crank angle – frequency analysis

Because the acquired signal from a running diesel engine involved multiple sources of various types, frequency analysis of the entire signal is unlikely to be useful, so time-frequency analysis techniques such as the Short-Time Fourier Transform (STFT) [58, 64, 122] were applied to look for evidence of different mechanical phenomena in the signal. The STFT uses a short data window centred at time τ, and the process works by multiplying the signal, $s(t)$ by a window function, $\gamma(t)$ to determine spectral coefficients which describe frequency components for a short length of data at time *t*. Then, the window is moved to a new position and the process is repeated. The STFT is given by:

$$STFT(\tau,\omega) = \int_{-\infty}^{+\infty} s(t)\cdot\gamma(t-\tau)\cdot e^{-j\omega t}\,dt \tag{6.3}$$

The STFT can also be used to determine frequency components in the crank angle domain (resampled signal) and the results can be shown as a 3D plot of time, frequency and amplitude, for example, as a contour plot. The calculation process is the same as previously mentioned and was performed on a short data window of approximately one degree centred at a crank angle, θ until the entire engine cycle (720 degrees) was obtained.

6.3 Engine running tests on small HSDI diesel engine

The tests on the running HSDI engine were carried out with various source and sensor positions as described in Section 4.5. Figures 6.1-6.16 and Table 6.2 show examples of the results recorded at each element of the horizontal and vertical sensor arrays for one engine running condition, after having been resampled from the time domain into the crank angle domain. Each plot shows degrees after TDC of cylinder no. 1 firing on the scale, according to the techniques described in Section 6.2.1.

Figures 6.1-6.3 show examples of the mapping against crank angle of the AE signals acquired at the horizontal sensor arrays on the cylinder head and the cylinder block at L1 and L2, respectively. The sensor positions, P1-P9 or P1-P12, indicated on the right are the sensor positions shown in Figures 4.9 and 4.10, and the mapping of mechanical events onto crank angle is shown along the bottom of each figure; injector (INJ) events, exhaust valve opening (EVO) and closing (EVC) events and inlet valve opening (IVO) and closing (IVC) events, the numbers 1-4 indicating cylinder number so that, for example, EVO4 denotes exhaust valve opening on cylinder no. 4. The vertical dotted lines represent TDC for firing of each cylinder at crank angles of 0, 180, 360 and 540 degrees after TDC1, and show the firing order 1-3-4-2. The scale of amplitude of the signals is given in the plot such as ± 10, ± 5, and ± 2 for Figures 6.1, 6.2 and 6.3 respectively. The test condition for each plot was normal running with an engine speed of 800 rpm and no load.

A number of observations are immediately apparent from these figures. Firstly, the INJ events are clearly the strongest in the cycle at all three arrays. The only other events that are clearly and consistently observed, are the EVO events of which the EVO4 appears to be the strongest, irrespective of array level. The EVO4 events seem also to be most evident at the upper cylinder block array, an amplification which does not seem to be shown by the EVO1 event, although it must be acknowledged that the examples shown relate only to one cycle. The other major observation is that the intensity of any observed event shows clear changes with sensor position. This can be appreciated by looking at, say, the INJ1 and INJ4 events in Figure 6.1 to 6.3 where it can be seen that the INJ1 is most intense at array positions 1, 2, 8, 9 (1, 2, 11, 12 in Figure 6.2) and that the INJ4 is most intense at array positions 4, 5, 6 (6, 7, 8 in Figure 6.2). Generally, it appears that, as might be expected, array positions closest to the event yield the strongest signal.

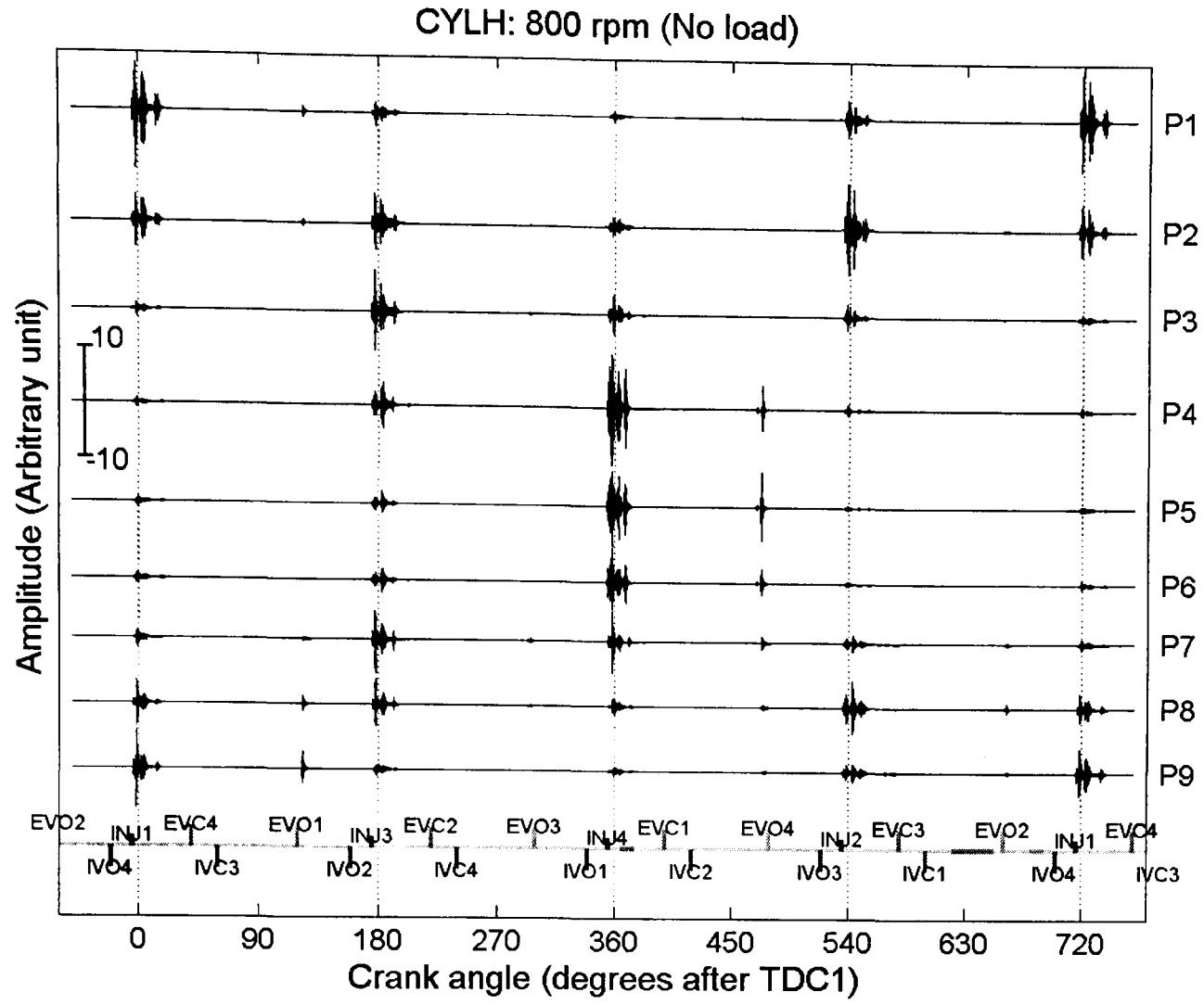

Figure 6.1: Raw AE signal versus crank angle from the running engine acquired at the horizontal sensor array on the cylinder head. Speed 800 rpm, no load. Dotted lines represent TDC firing for each cylinder.

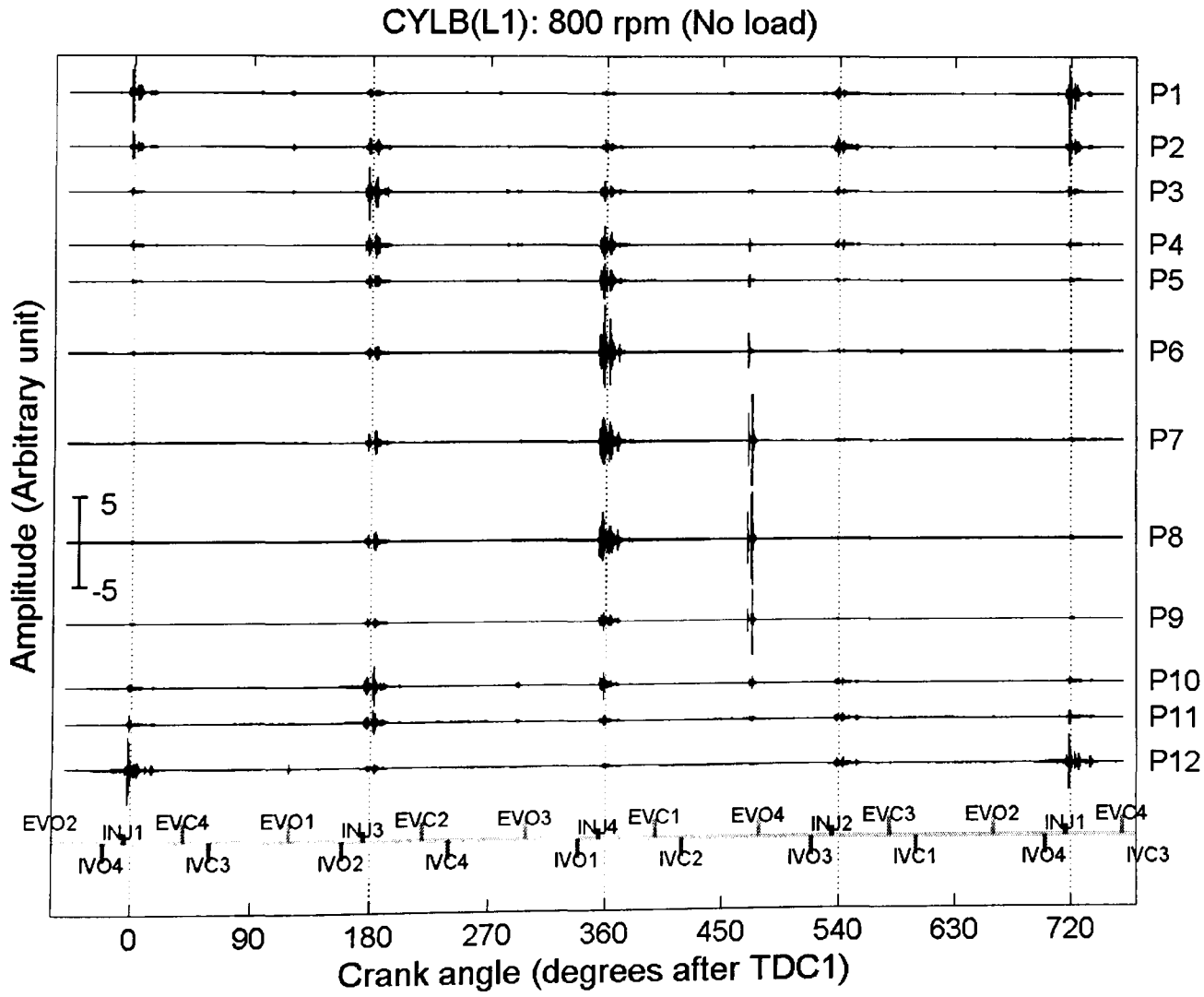

Figure 6.2: Raw AE signal from the running engine at the sensor array on the cylinder block at level 1. Speed 800 rpm, no load.

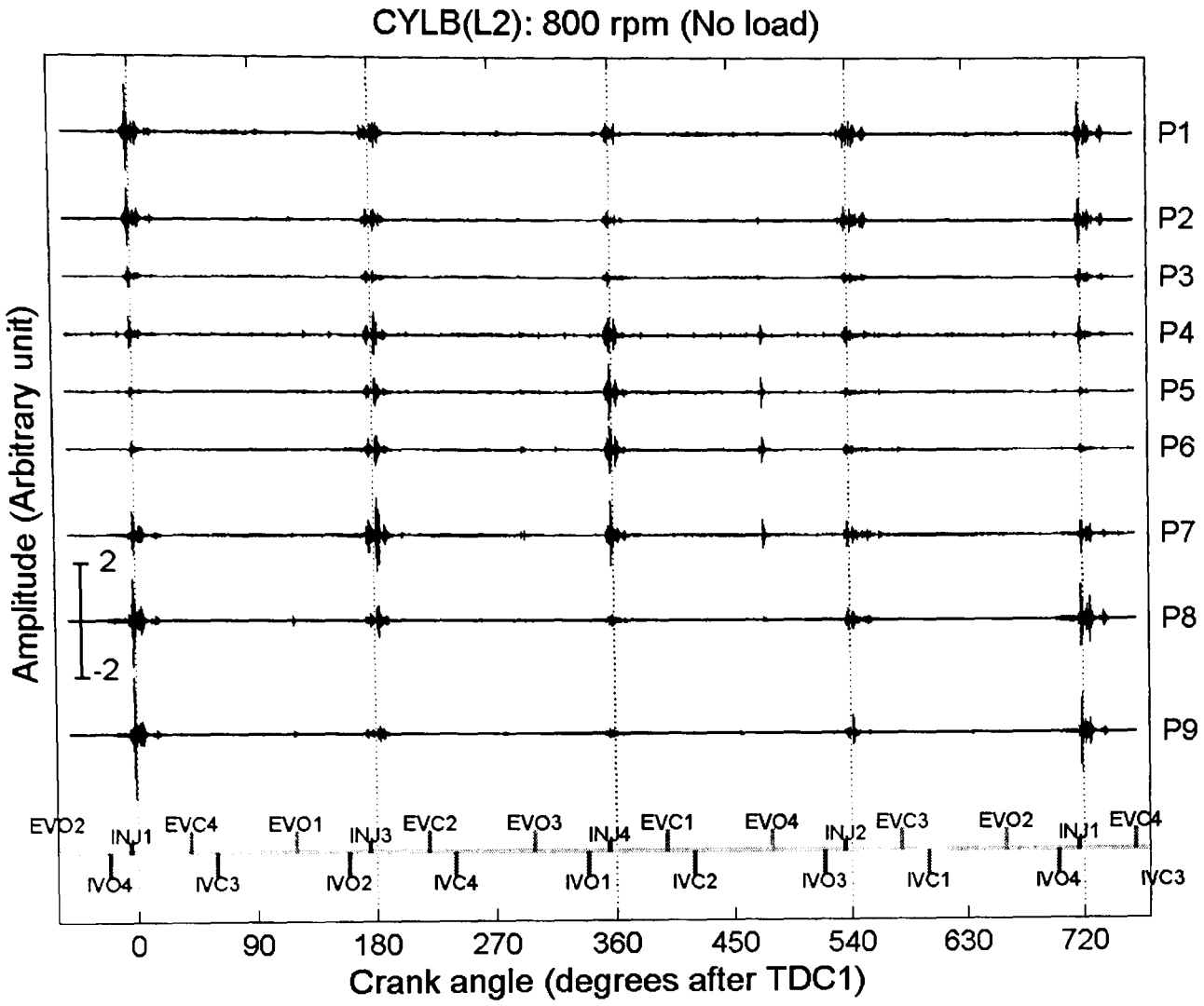

Figure 6.3: Plot of raw AE signal from the running diesel engine acquired at the sensor array on the cylinder block at level 2. Speed 800 rpm, no load.

However, the signals shown in Figures 6.1-6.3 contain more information than can be illustrated in a single plot. Accordingly, Figures 6.4-6.5, 6.6-6.7, and 6.8-6.9 show examples of the INJ, EVO, EVC, IVO and IVC events at each cylinder from the three arrays, respectively. For greater resolution, the amplitude of each signal in the plots was enveloped and normalised by its maximum amplitude (varies from 0 to 1), although relative intensities at each sensor position are no longer evident. The mapping of mechanical events onto crank angle is again shown along the bottom of each plot. Figures 6.4, 6.6 and 6.8 confirm that the INJ signals are visible above the background at all sensor positions in all three arrays. In addition, it can be seen that there are significant time differences between the same event observed at different array positions, most clearly seen by comparing the INJ1 and INJ4 signals; these time delays are in general accord with the intensity effects observed in Figure 6.1 to 6.3 in that signals from sources close to the sensor are apparently earlier in the cycle than those further away, in some cases by a few degrees. The EVO events also exhibit time delays and, unlike the INJ events, some array positions do not register the EVO event above the background noise. Figures 6.5, 6.7 and 6.9 show the weaker events, the IVO, EVC and IVC amplified digitally as indicated above, and here the question is whether or not

the event can be detected at all above the background. The SNR method described in Section 6.2.2 was specifically designed to search within specific time windows around the expected event using an appropriate threshold above the ambient background level.

The injector and EVO events are the main mechanical events in the signals but closer examination reveals that there is information which might be useful throughout the whole signal. The injector events acquired from the cylinder head are the strongest, and the detailed structure of the characteristic for each cylinder is slightly different, depending, presumably, on the condition and operation of the injector. For the injector events detected at sensors on the cylinder block, it appears that there might be interference from other sources because the shape of the signals is dissimilar to that recorded on the cylinder head including some unknown sub-events, particularly evident at lower sensor positions on the cylinder block (below L2, Figure 6.8). It is possible that the injector signals include components coming from the combustion process and possibly even the bearings and gudgeon pins. The EVO events acquired from the cylinder head array are consistent, again unlike the arrays on the cylinder block where some unknown sub-events appear in the signals, which might be associated with the mechanical operation of the valves. The EVC events only appear in some sensor positions in each of the arrays, whereas it is only possible to see the IVO and IVC events at array positions on the cylinder block. Again, there are some unidentified events seen in these signals which might be due to mechanical moving components such as the camshaft, tappets, pushrods or rocker arm.

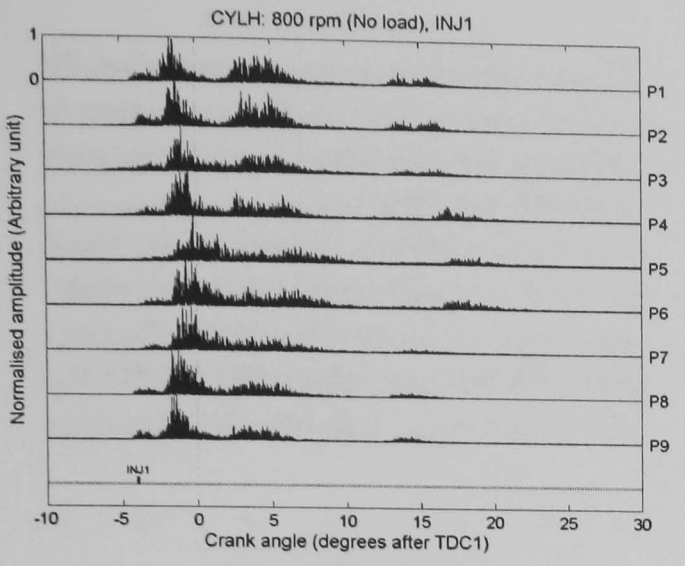

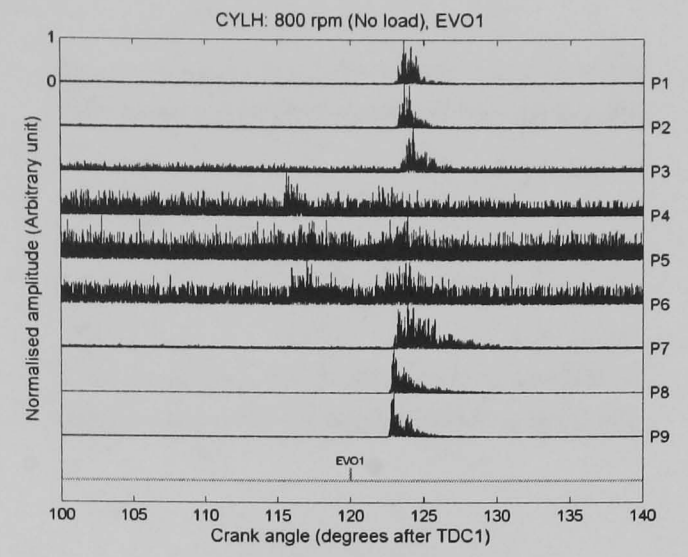

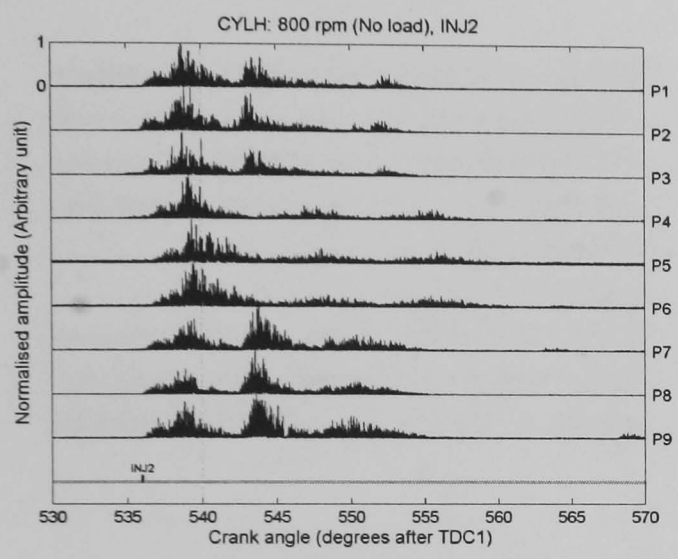

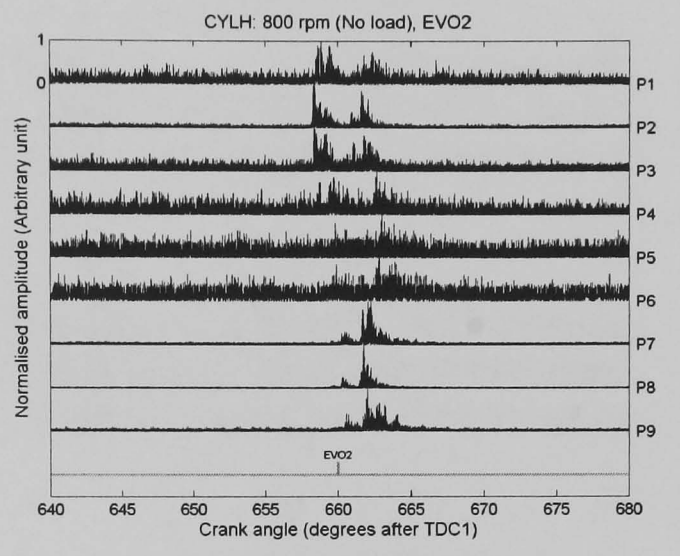

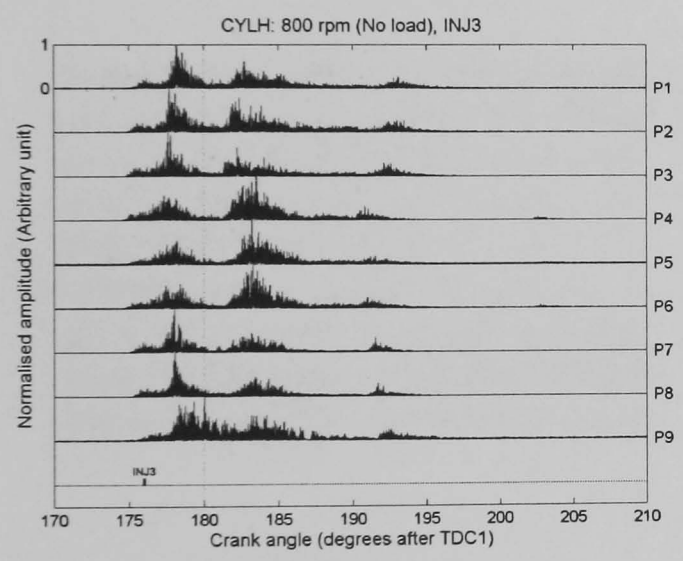

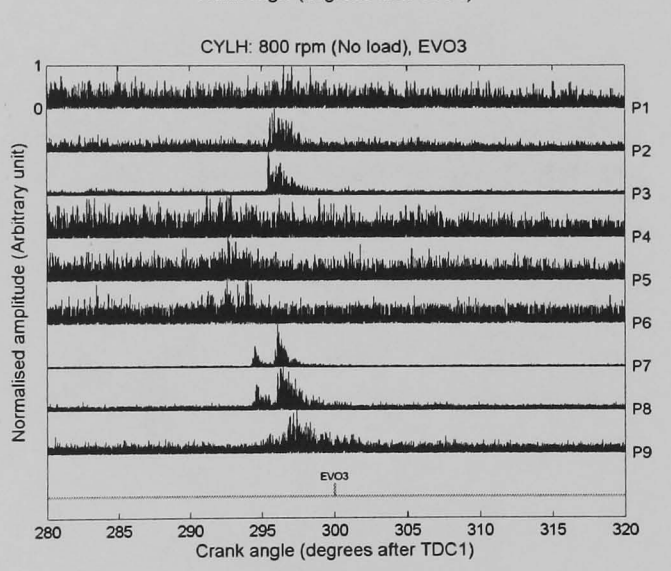

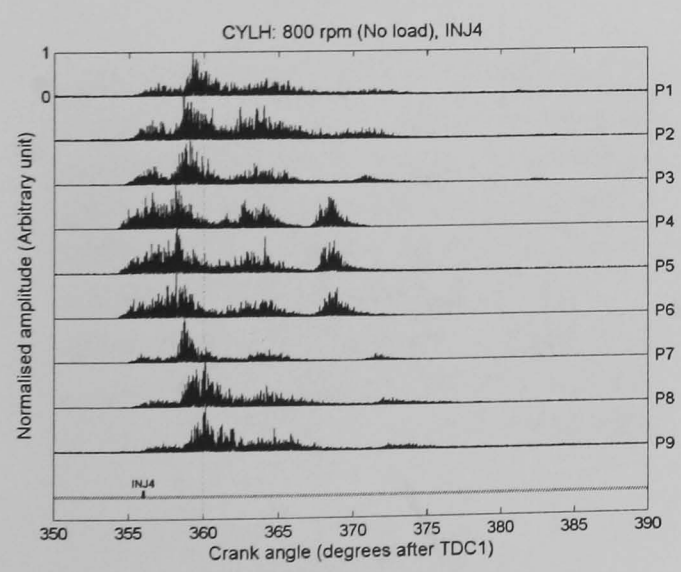

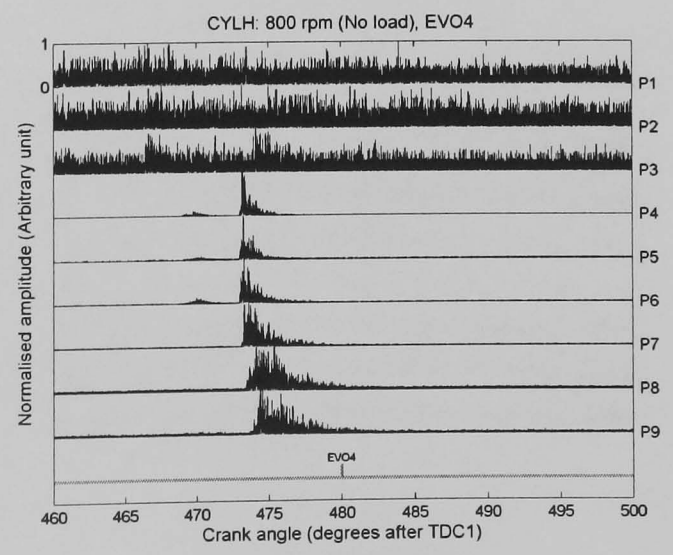

(a) Injector events

(b) EVO events

Figure 6.4: Plot of normalised AE signal for injector and EVO events for cylinders 1-4 versus crank angle (shown in Figure 6.1) acquired from sensor array on cylinder head.

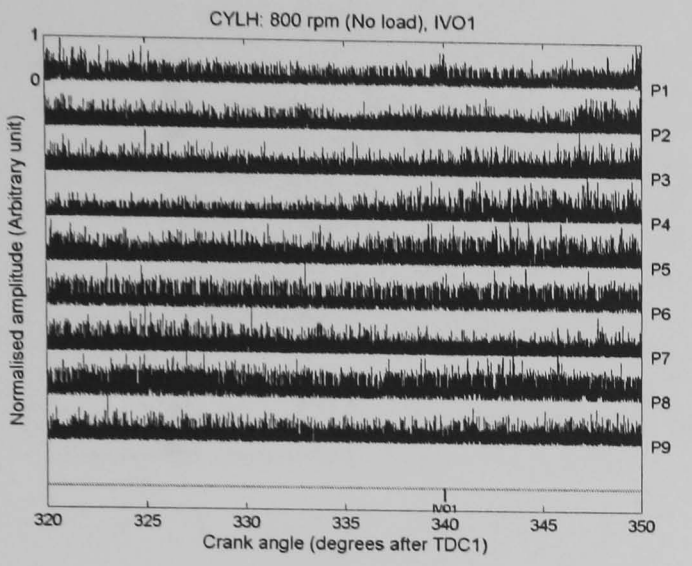

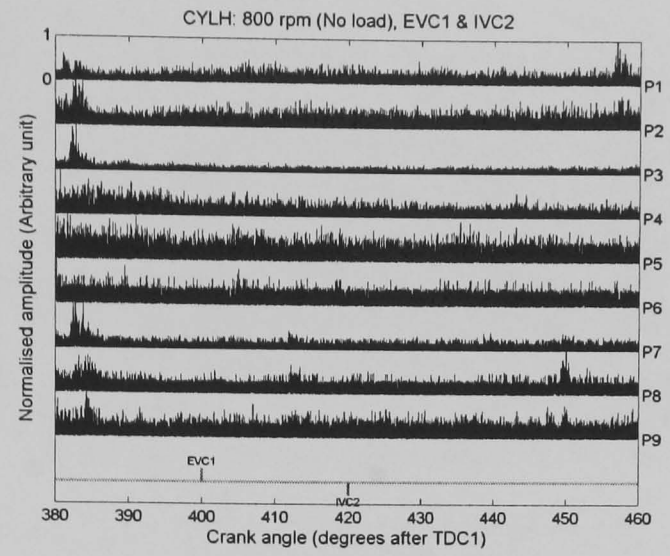

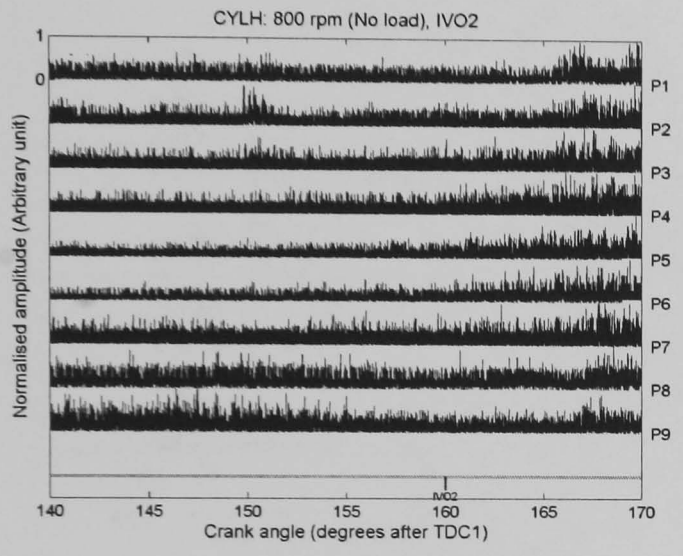

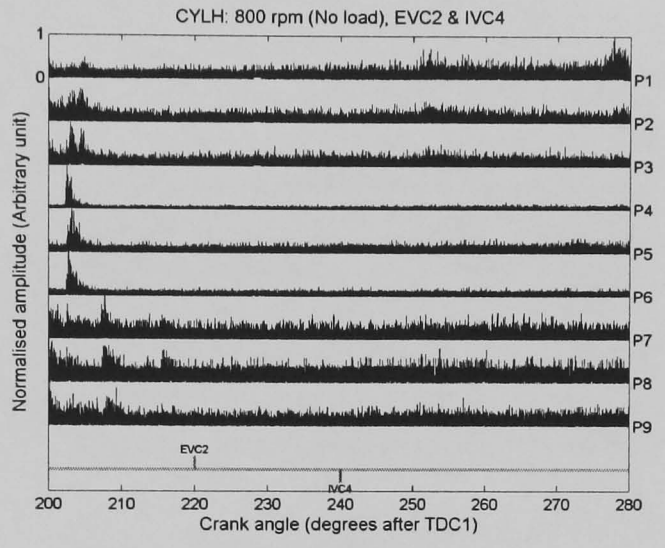

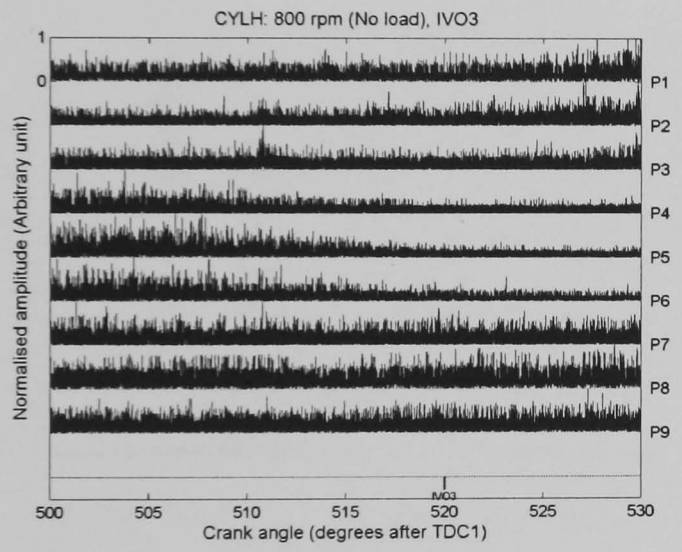

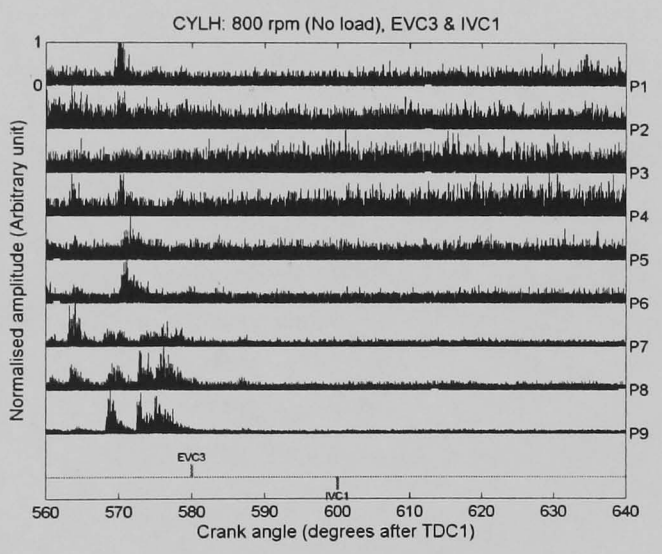

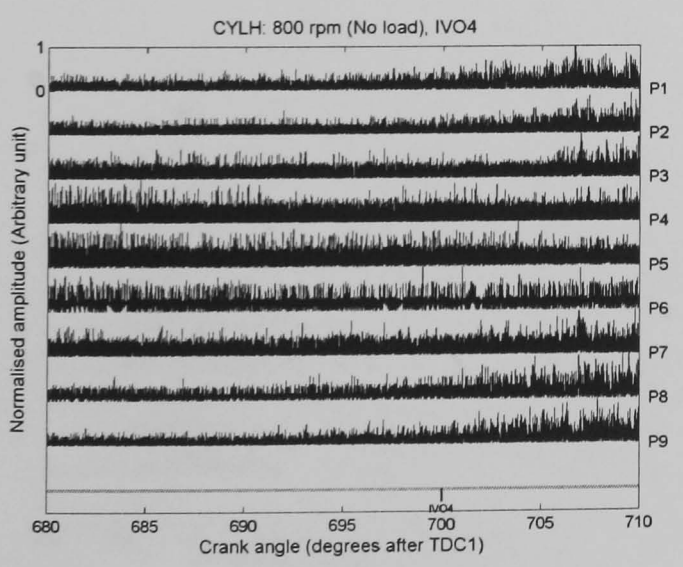

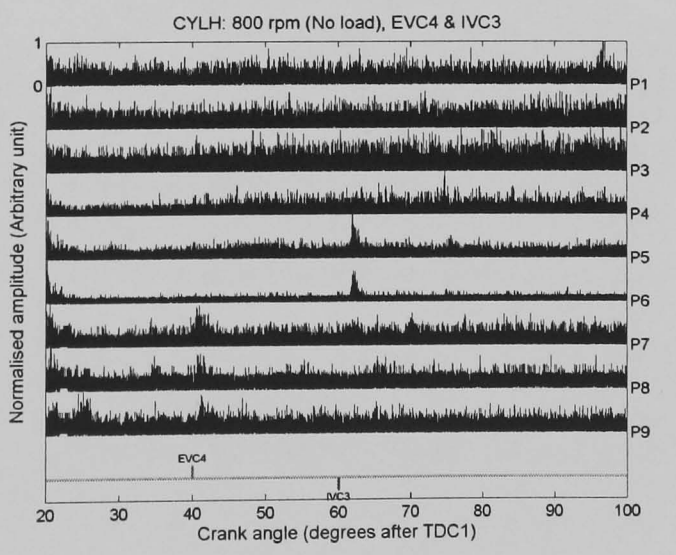

(a) IVO events

(b) EVC & IVC events

Figure 6.5: Plot of normalised AE signal for IVO, IVC and EVO events for cylinders 1-4 versus crank angle (shown in Figure 6.1) acquired from sensor array on cylinder head.

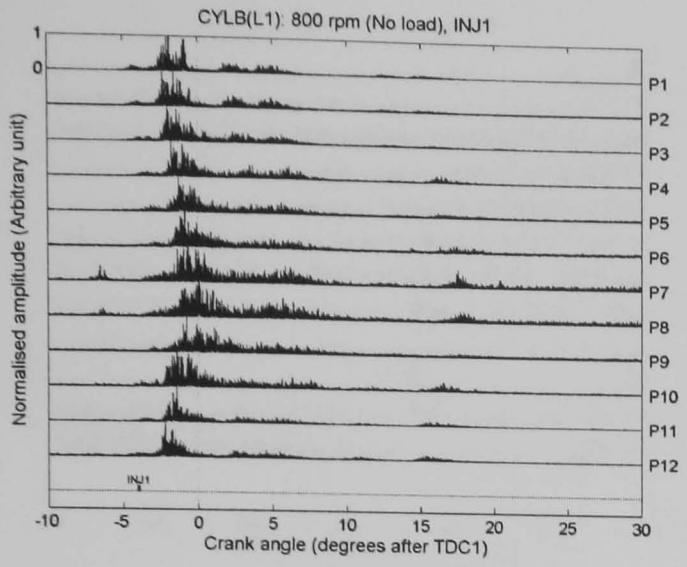

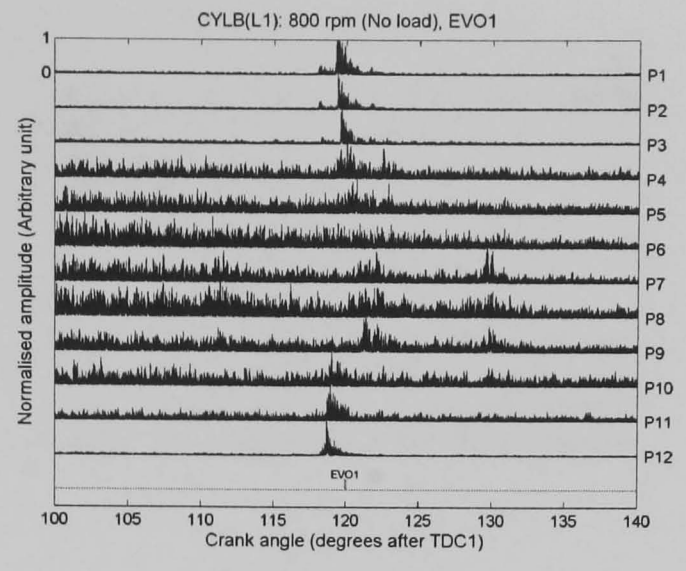

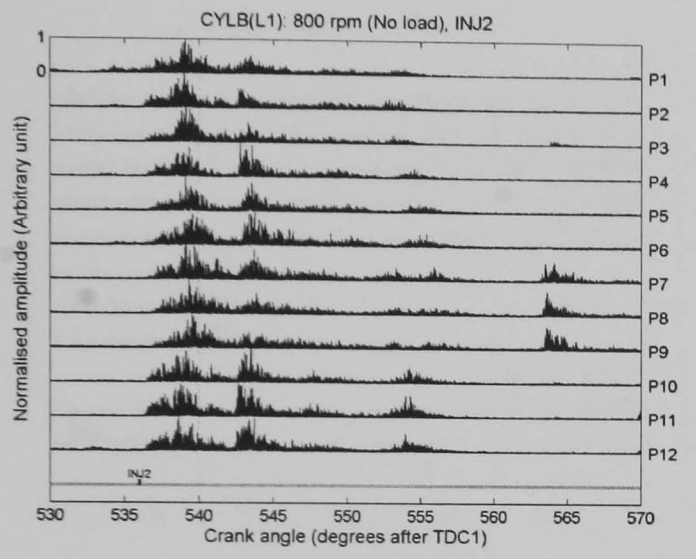

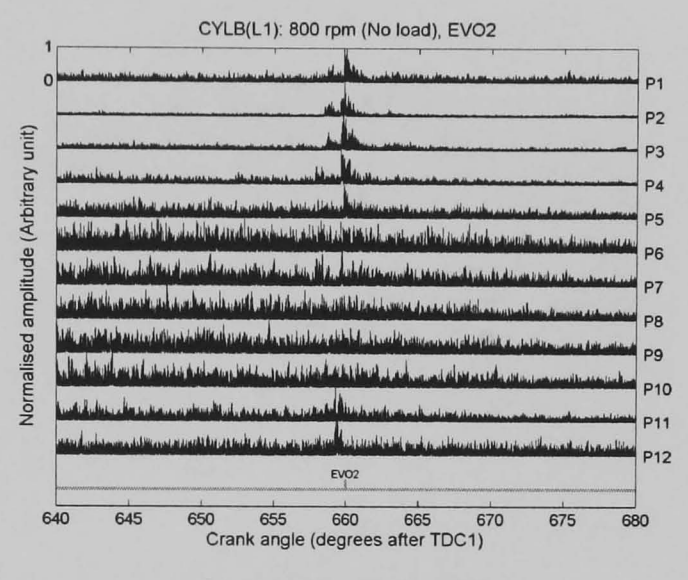

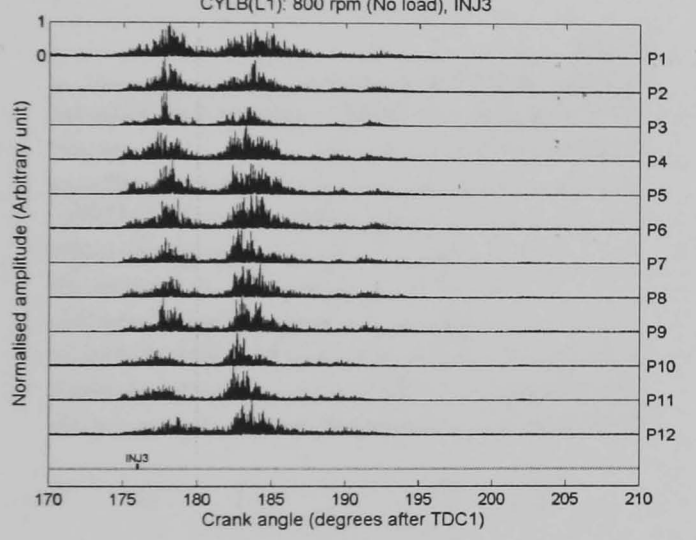

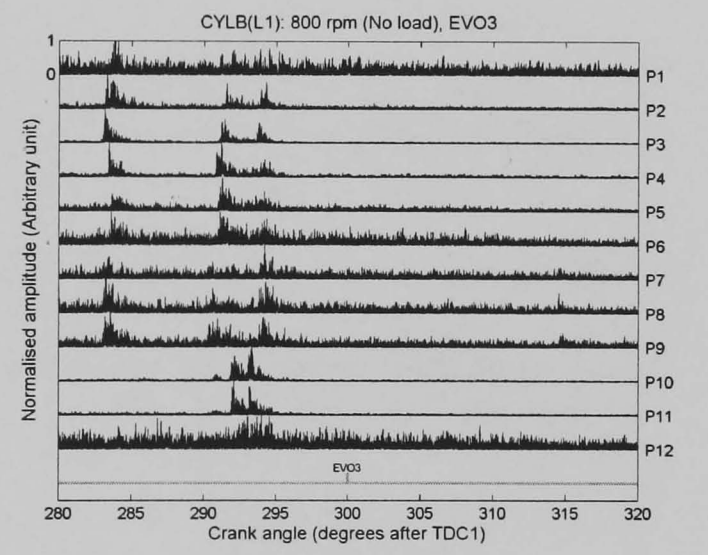

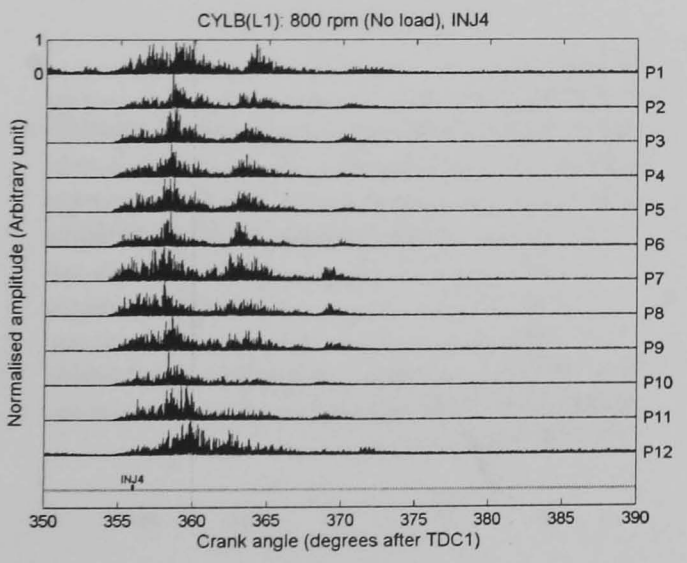

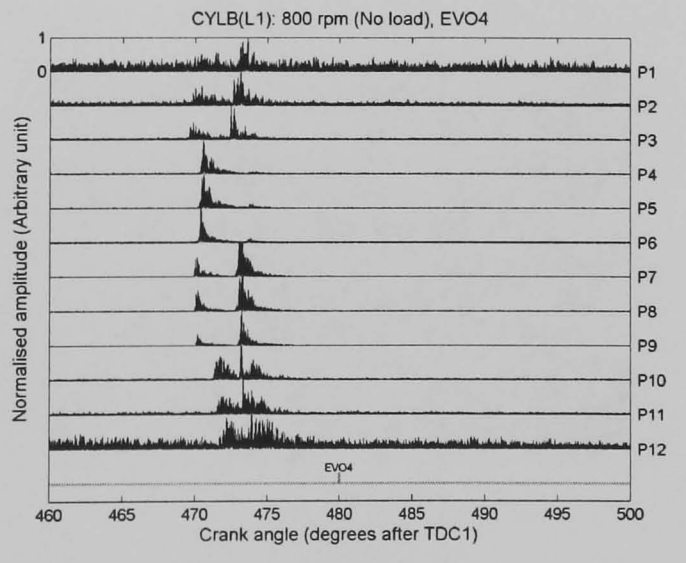

(a) Injector events

(b) EVO events

Figure 6.6: Plot of normalised AE signal for injector and EVO events for cylinders 1-4 versus crank angle (shown in Figure 6.2) acquired from sensor array on cylinder block (L1).

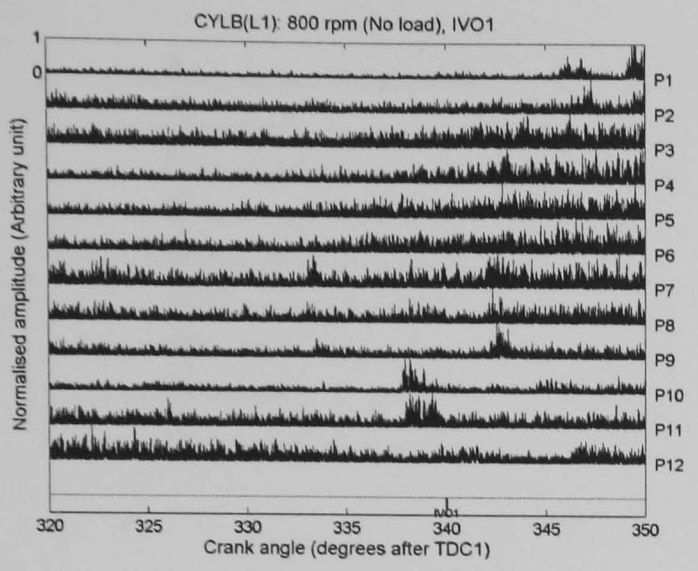

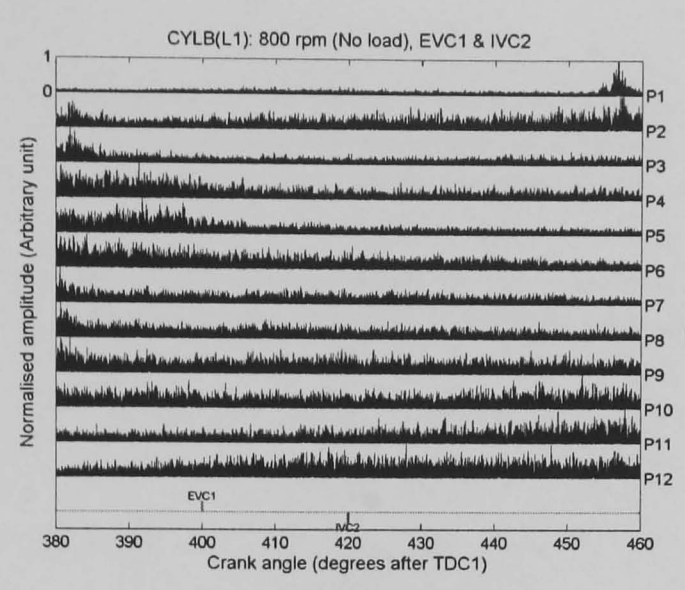

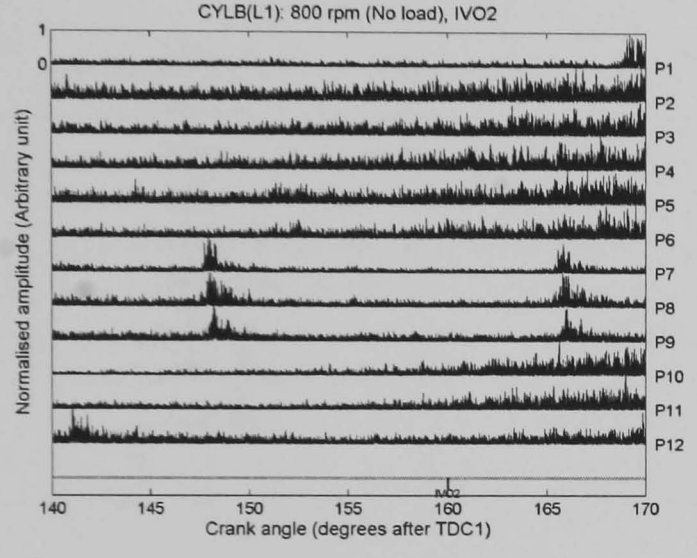

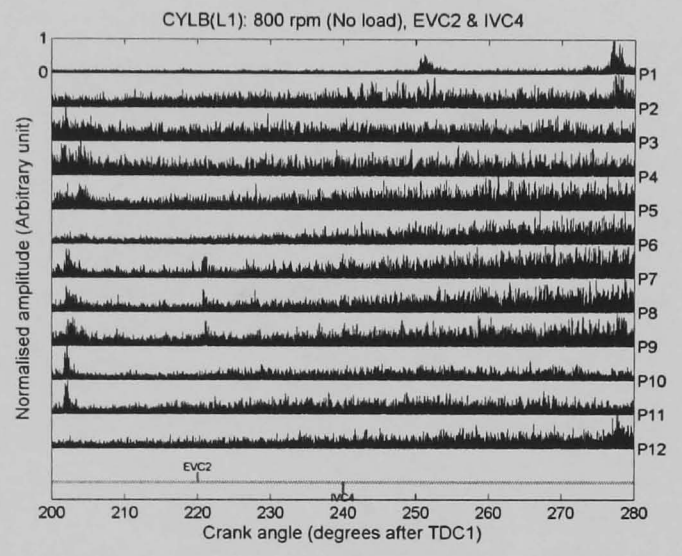

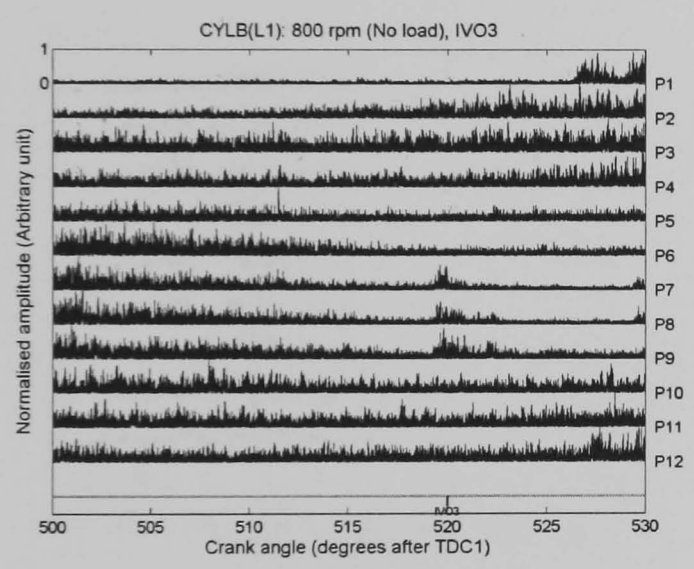

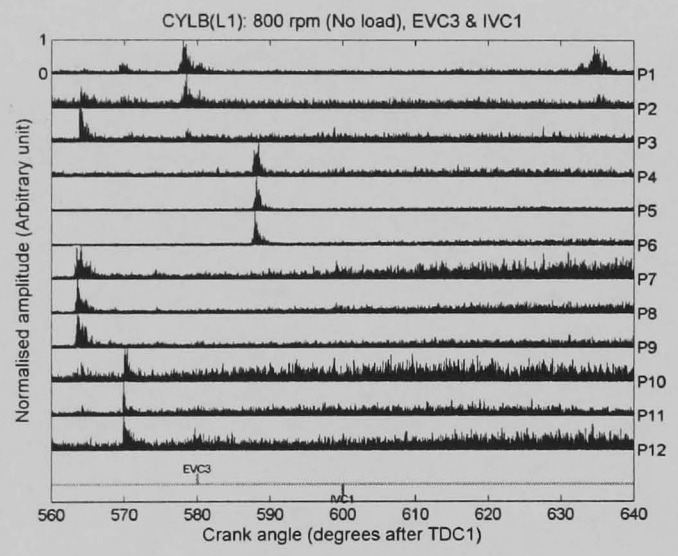

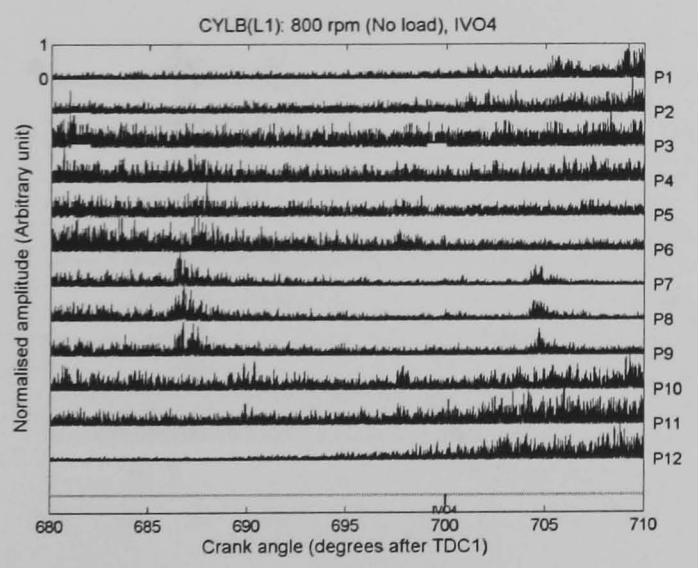

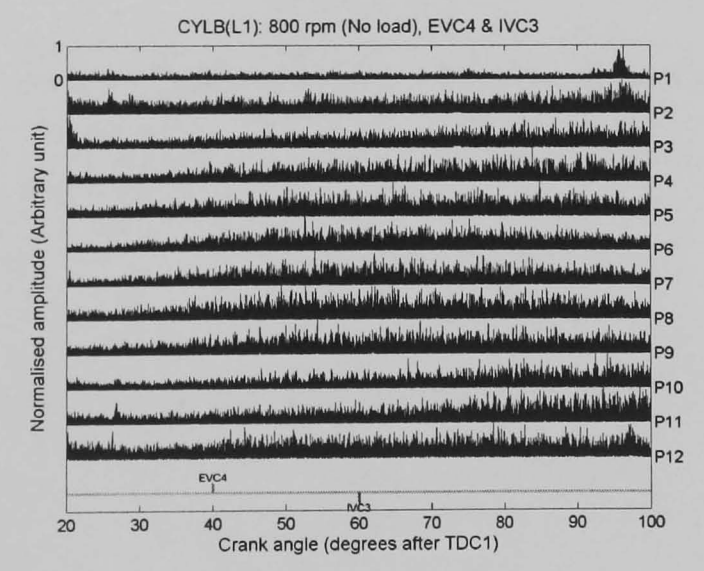

(a) IVO events

(b) EVC & IVC events

Figure 6.7: Plot of normalised AE signal for IVO, IVC and EVC events for cylinders 1-4 versus crank angle (shown in Figure 6.2) acquired from sensor array on cylinder block (L1).

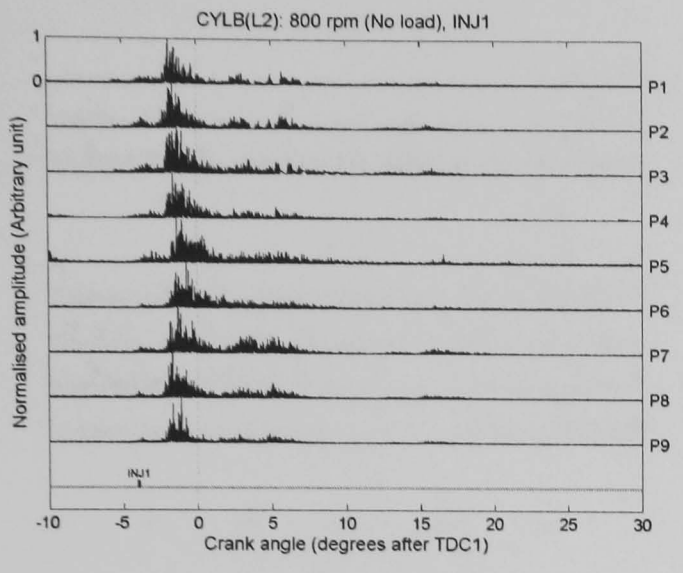

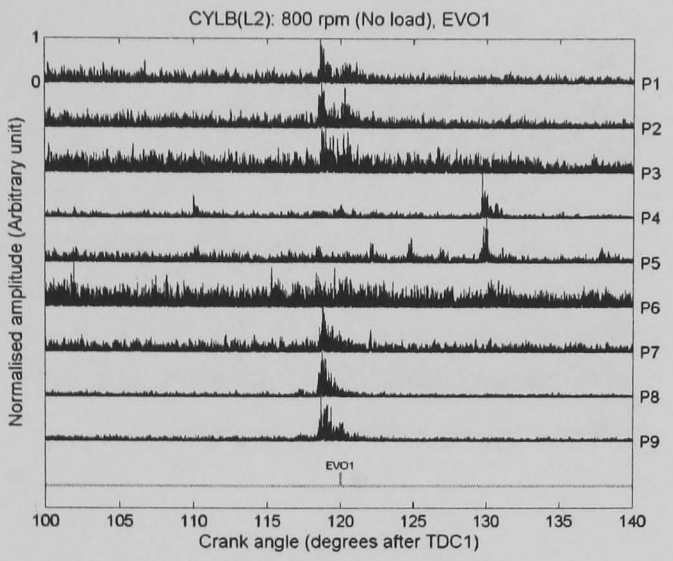

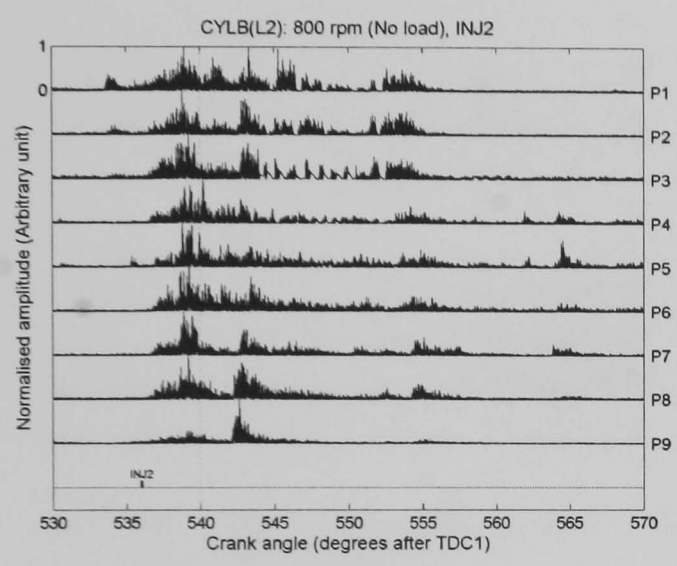

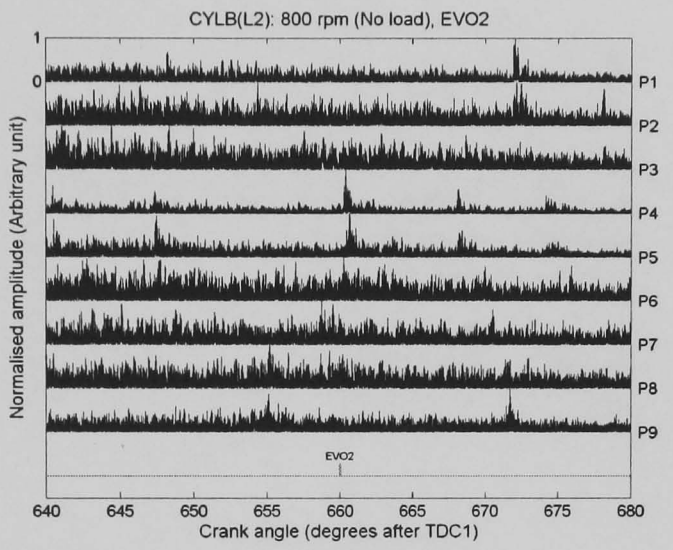

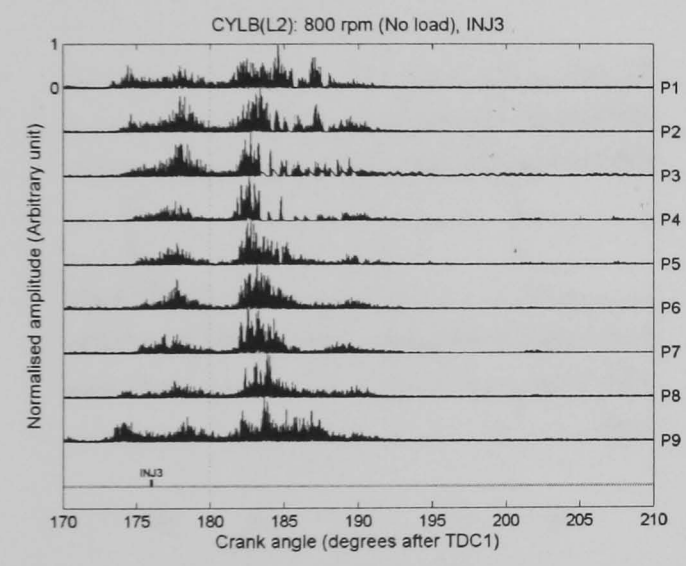

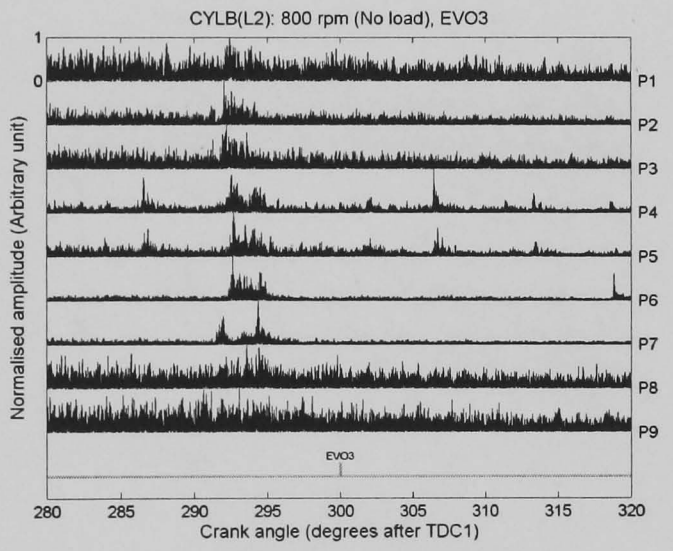

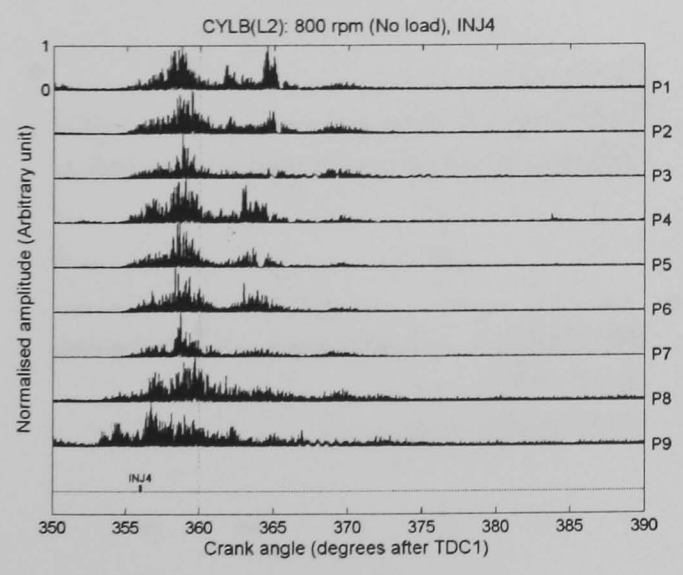

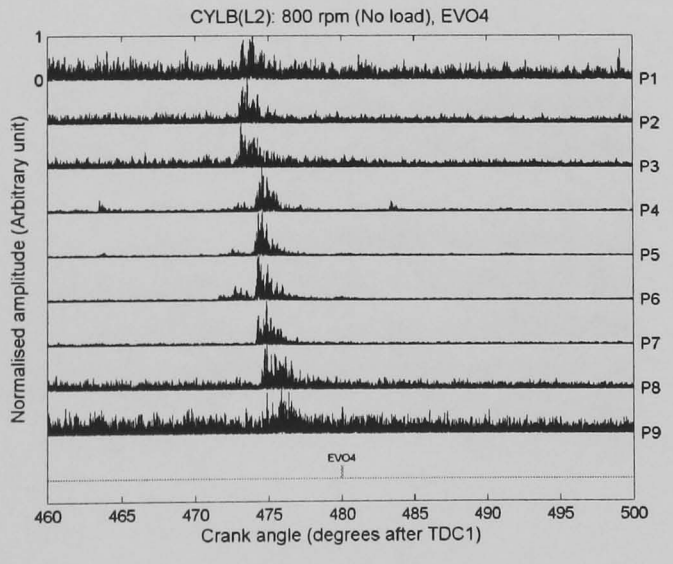

(a) Injector events

(b) EVO events

Figure 6.8: Plot of normalised AE signal for injector and EVO events for cylinders 1-4 versus crank angle (shown in Figure 6.3) acquired from sensor array on cylinder block (L2).

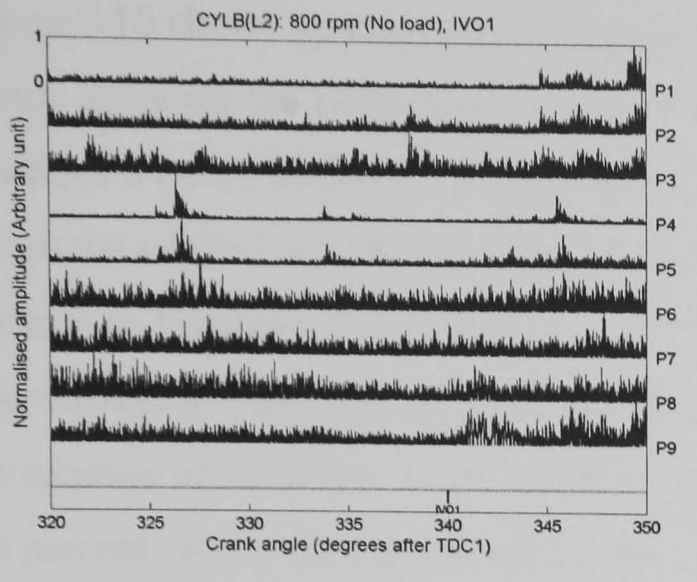

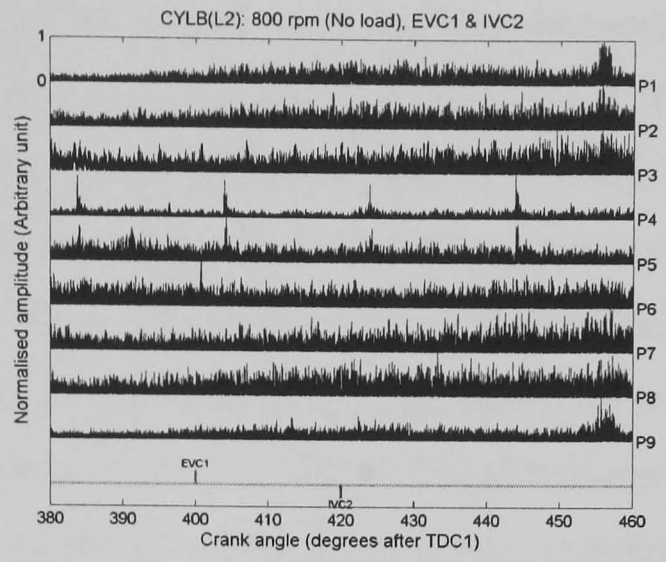

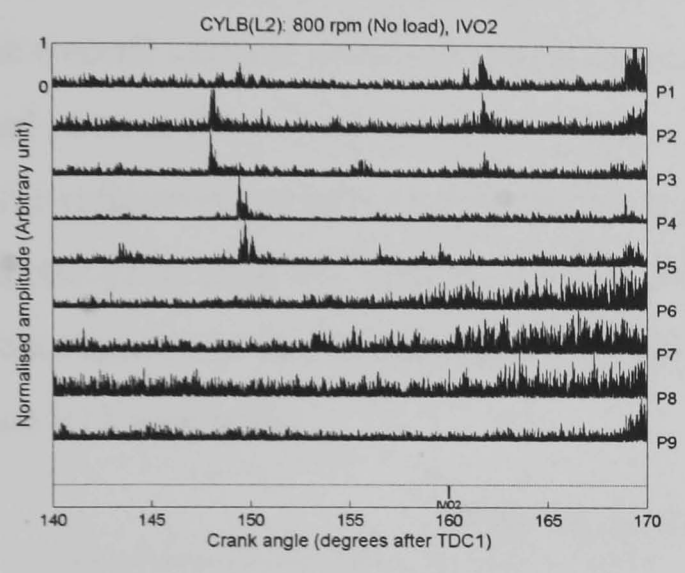

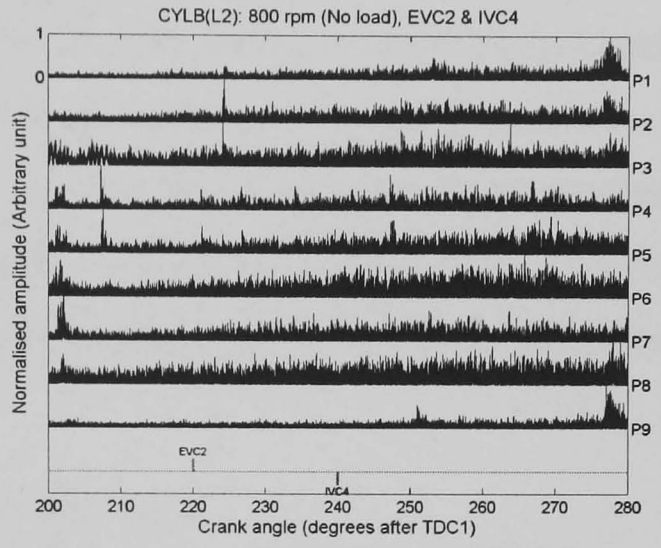

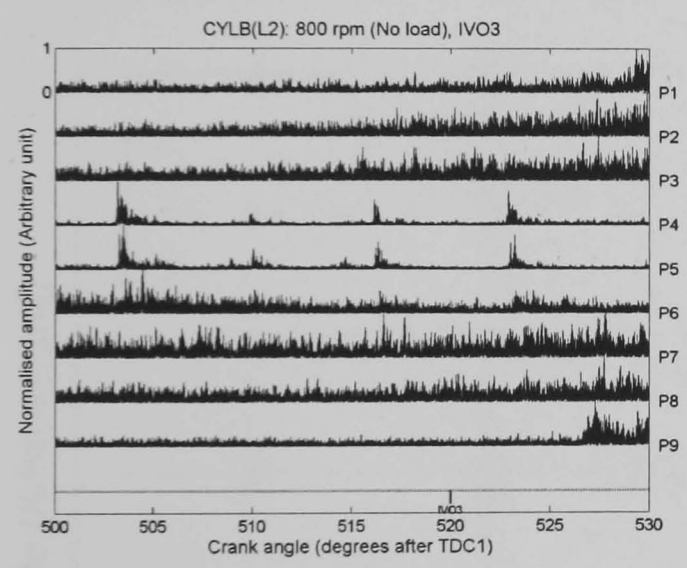

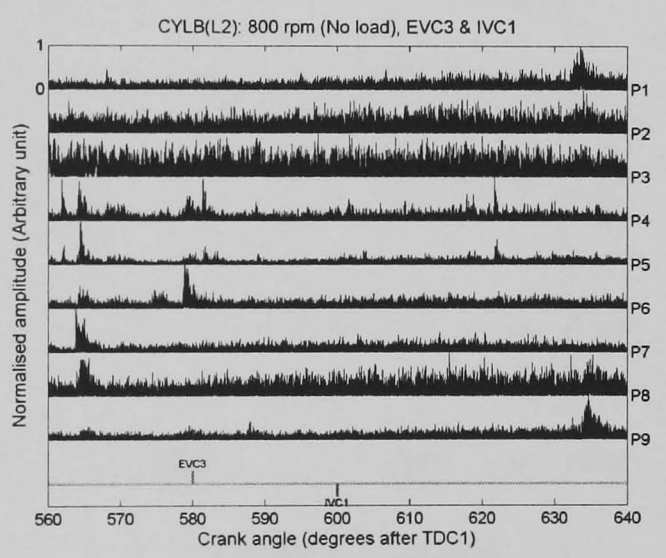

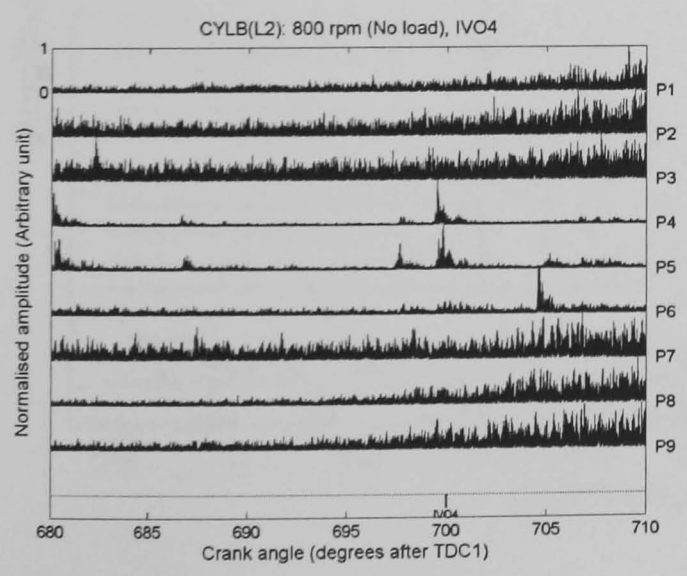

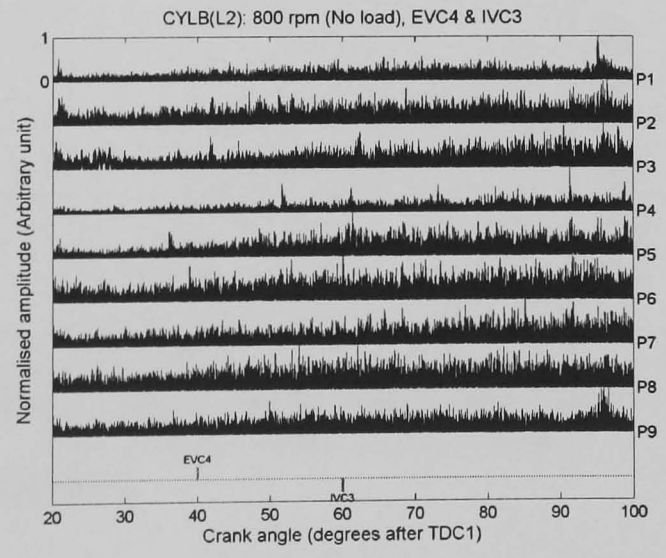

(a) IVO events

(b) EVC & IVC events

Figure 6.9: Plot of normalised AE signal for IVO, IVC and EVC events for cylinders 1-4 versus crank angle (shown in Figure 6.3) acquired from sensor array on cylinder block (L2).

Figure 6.10 shows an example of mapping of the AE signals acquired from the vertical sensor array on the running engine operating at a speed of 800 rpm and no load. The positions P1-P12 indicated on the right are the sensor positions shown in Figure 4.13, where the vertical section is centred on cylinder no. 3. Figure 6.10 exhibits some similar features to Figures 6.1-6.3, in that the INJ events are the strongest with the EVO being next strongest, although this time the EVO3 was the strongest of these consistent with the location of the array. At positions P5 and below, a number of small amplitude events are present, and only some of these are even tentatively attributable to the event map. The overall vertical attenuation appears to centre all of the main events at P4, but with a dead area at P3, where the AE energy is very small and this may be due to effects of wave reflection, which can reduce the amplitude of the signal, or due to local structural effects, or it may be because sensor positioning was difficult. The small amplitude events appear to be coming from the bottom of the engine, as they decrease in amplitude from P12 upwards.

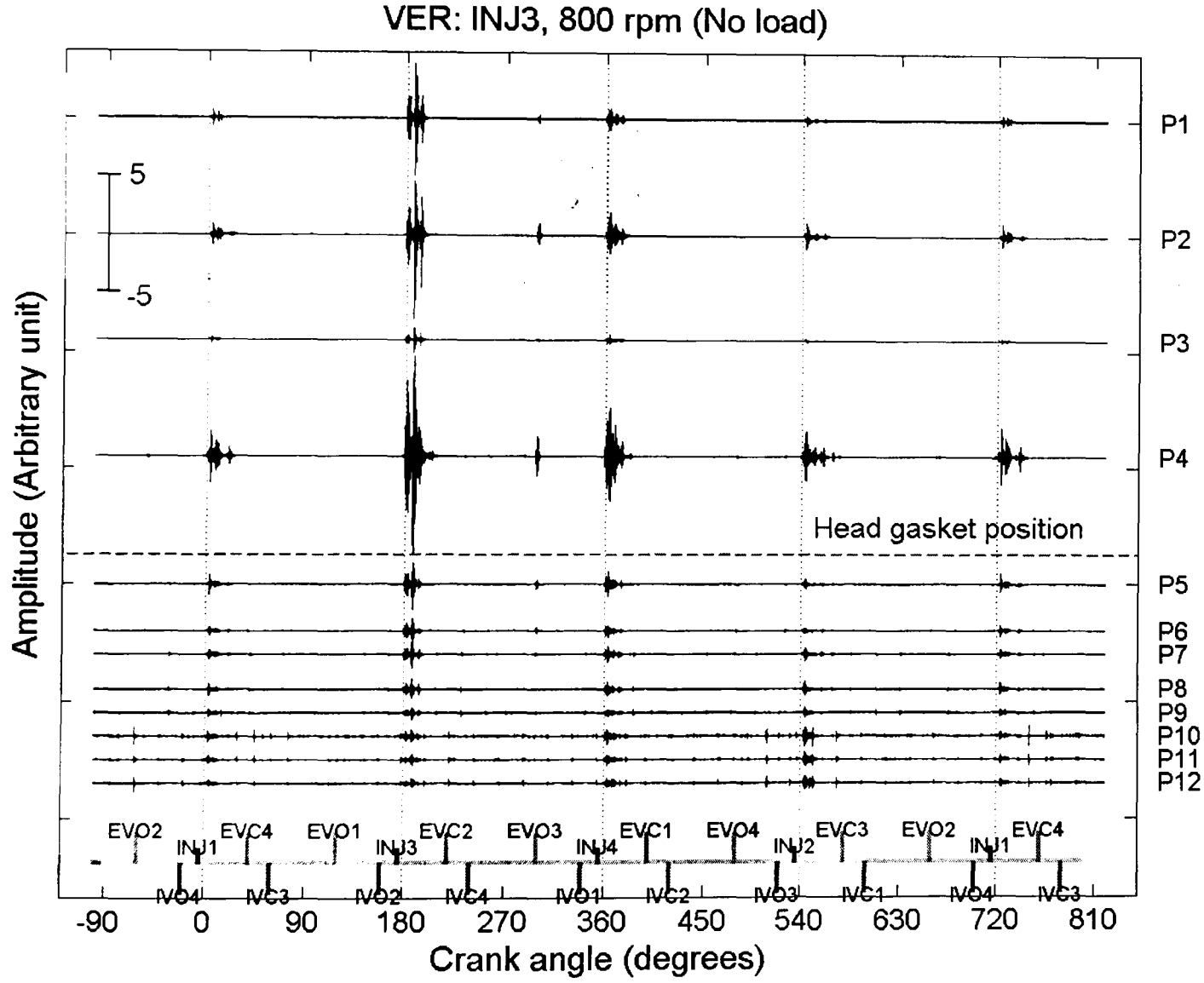

Figure 6.10: Plot of raw AE signal versus crank angle acquired at vertical sensor array from running engine at speed of 800 rpm with no load. Dotted vertical lines represent TDC firing for each cylinder, and dashed horizontal line indicates the location of the cylinder head gasket.

In order to obtain a detailed view of these signals, they were enveloped (square root of squared signal) and normalised to their maximum amplitude as before so that the INJ, EVO, EVC, IVO and IVC events of each cylinder could be seen against ambient background as seen in Figures 6.11 and 6.12. From Figure 6.11, it is obvious that the two main events, INJ and EVO, can be seen in the signals acquired down to P6 in roughly the same way as with the horizontal sensor arrays. However, for the signals acquired below P6, both injector and EVO events seem to be associated (Figure 6.12) with other unknown events pitched at approximately 10 degrees either side of them. For IVO, IVC and EVC events, these are again visible at some sensor positions and appear to become clearer and stronger at positions below P5. Events at about 15-20 degrees either side of the valve events may well be coming from the camshaft, tappets and other moving parts around the lower part of the cylinder block such as the bearings, lubricating pump, or drive gears.

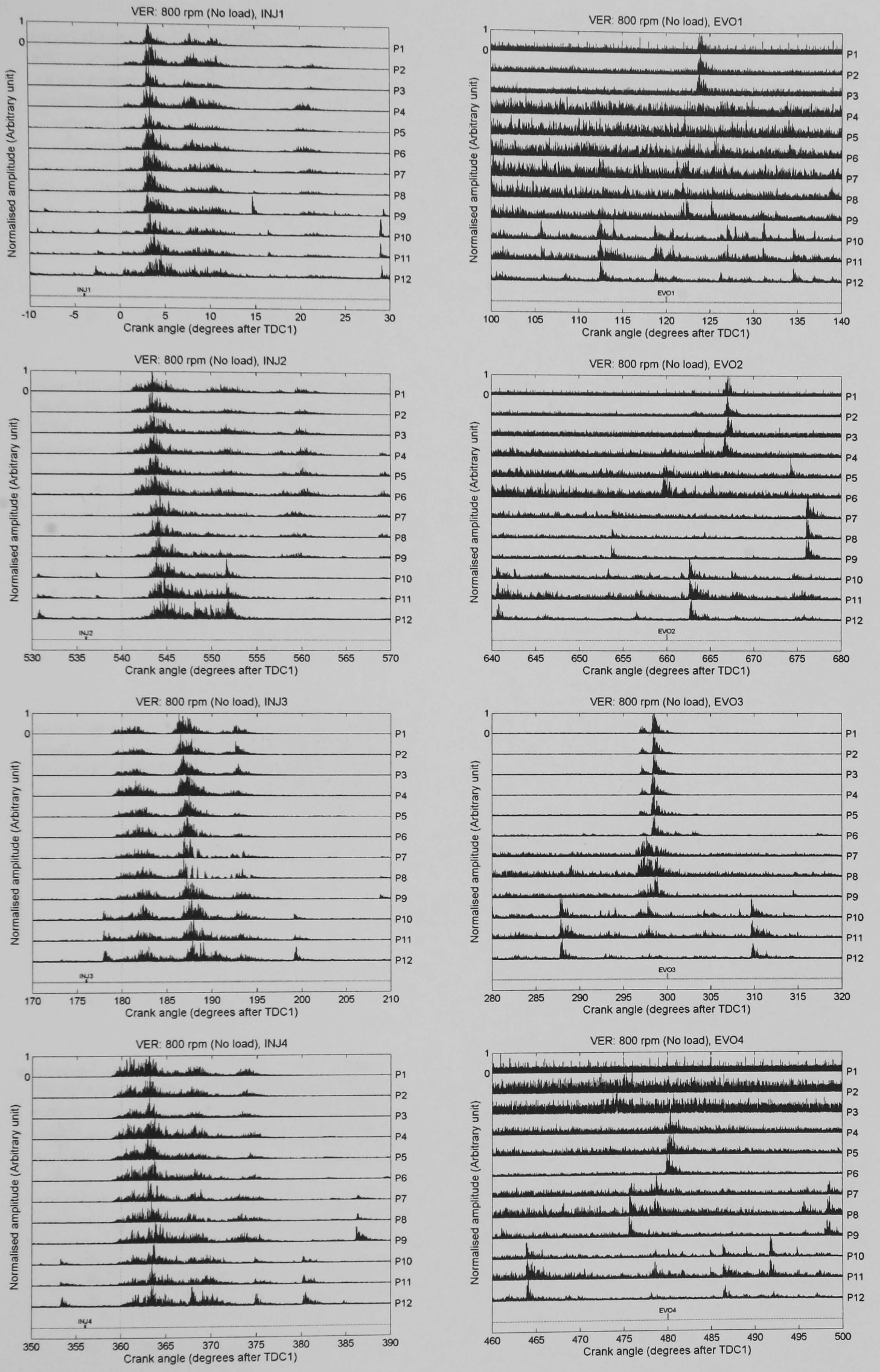

(a) Injector events

(b) EVO events

Figure 6.11: Plot of normalised AE signals from injector and EVO events on cylinders 1-4 versus crank angle (enhancement of Figure 6.10) using vertical sensor array.

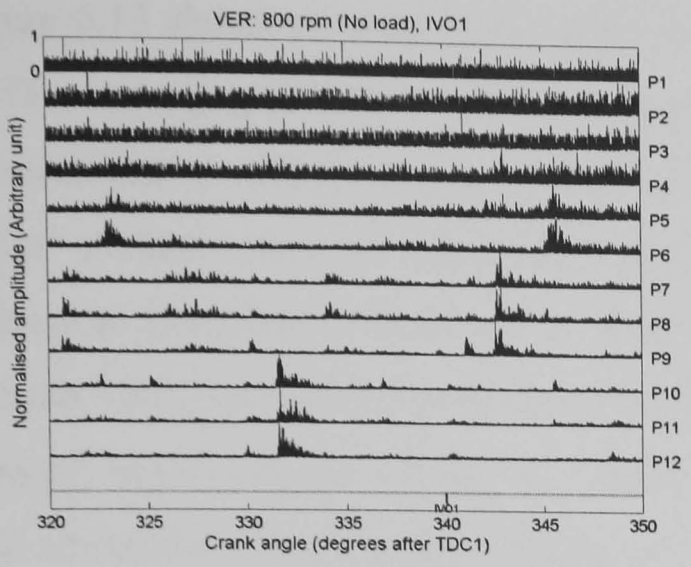

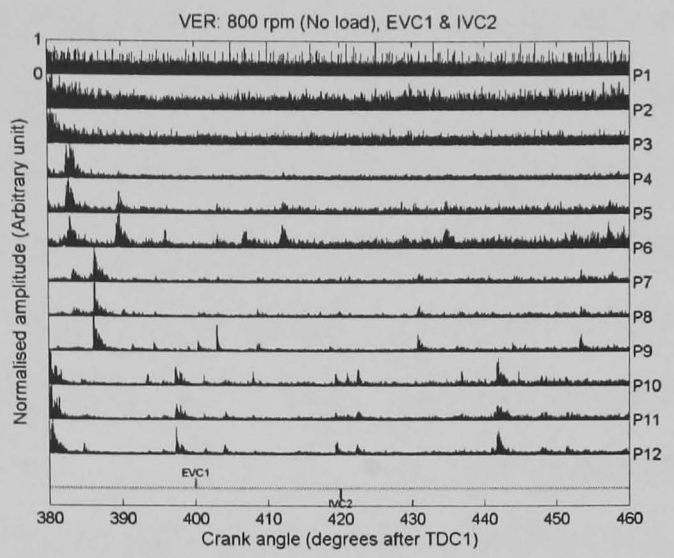

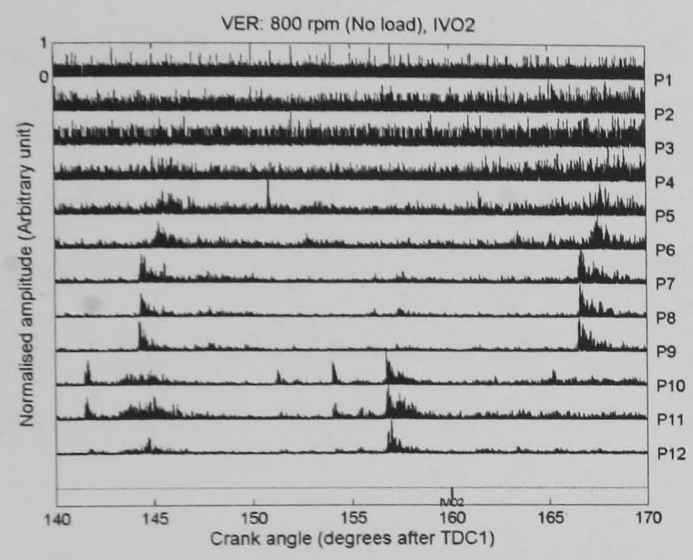

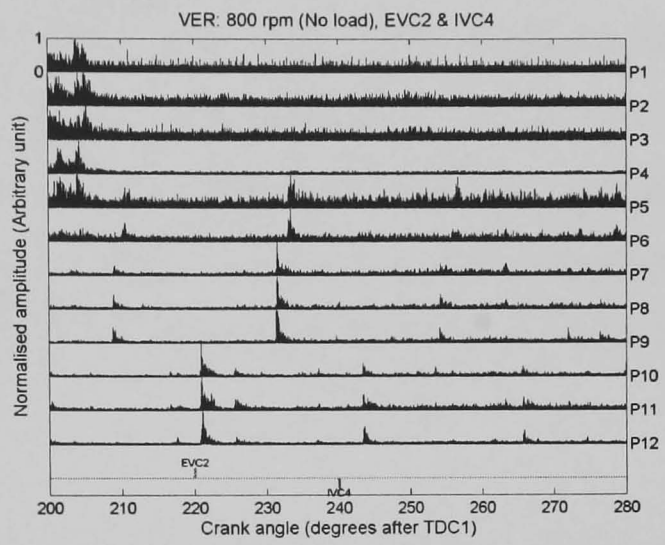

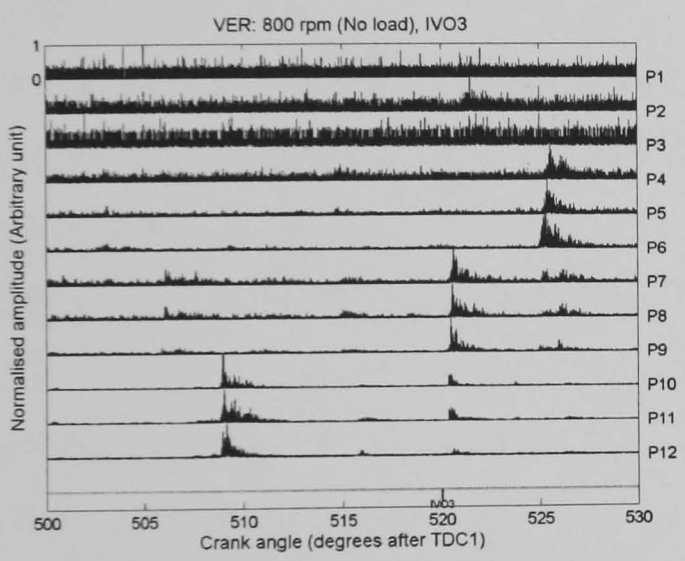

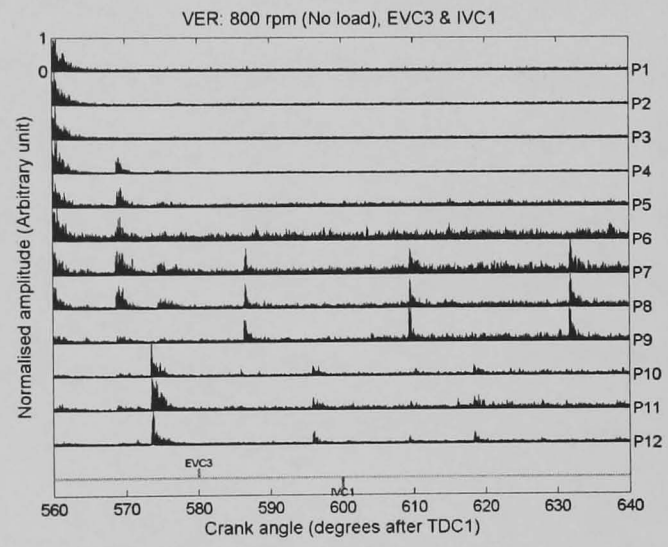

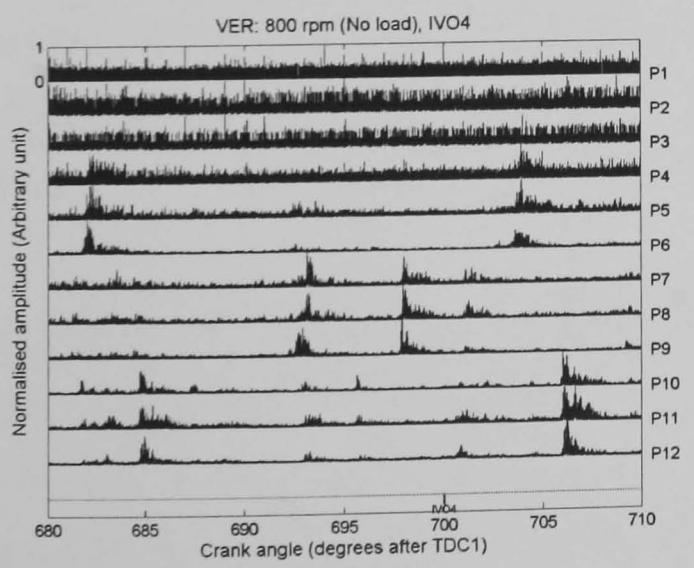

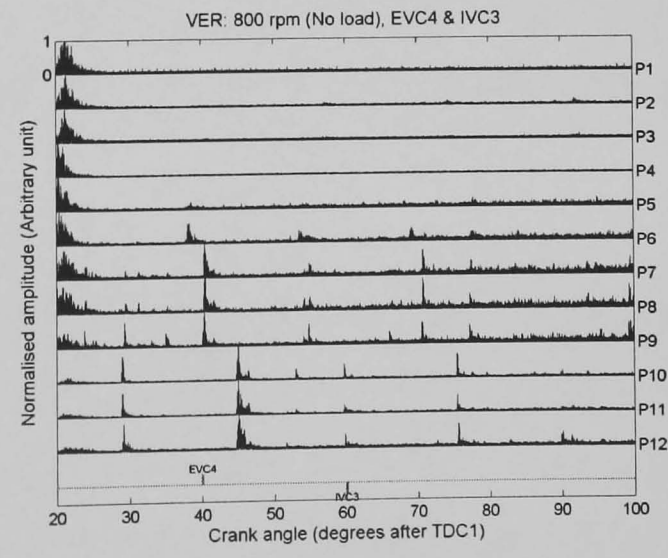

(a) IVO events

(b) EVC & IVC events

Figure 6.12: Plot of normalised AE signals for IVO, IVC and EVC events on cylinders 1-4 versus crank angle (enhancement of Figure 6.10) using vertical sensor array.

Figure 6.13 shows plots of $\ln E$ versus source-sensor distance for the injector and the EVO events acquired from the horizontal sensor arrays on the cylinder head and the cylinder block, with the engine operating at a speed of 800 rpm under no load. Source-sensor distance was the same as obtained from transmission tests using simulated sources as described in Section 5.4, where the sources were actually on injector bodies, exhaust valve spring bases and the top of the inlet valve stems. The exact sources on the running engine are not known so a small error is introduced here. The energy content was calculated using Equation (6.1) according to the method described in Section 6.2.1, over a crank angle width of 40 degrees (from -10° to 30°) around TDC of each cylinder for the injector events and over a crank angle width of 20 degrees from 110° to 130° ($\pm 10^{\circ}$) after TDC of each cylinder for the EVO events as shown in Table 6.1. Twenty records of each injector and EVO event were used and these are plotted individually on the graphs. The best-fit straight lines (the solid lines) shown in Figure 6.13 were determined using Equation (3.16).

In order to avoid the attenuation curves being unduly affected by signals close to the ambient background level, a method was developed to remove weak signals (see Section 6.2.2). Figure 6.14 shows signal to noise ratio (SNR) against sensor position for both injector events and EVO events acquired from various sensor positions on the cylinder head and the cylinder block. The dotted line is the reference SNR level (SNR = 2), below which signals were excluded from consideration. The SNR was calculated using Equation (6.2) using the method described in Section 6.2.2. As can be seen, the SNR for the injector events is always above 2 but falls below 2 for some EVO events at some sensor positions. The SNR values for the EVO events are generally more variable than the INJ events and become noticeably lower as the array is moved down the engine.

The plots of $\ln E$ against source-sensor distance for the INJ and EVO events shown in Figure 6.13, with the weak signal removed, generally confirm the observations made earlier that energy decreases with increasing distance from the source. This is most consistent for injector events observed from the cylinder head array and from the Level 1 cylinder block array and correlations are extremely poor on the Level 2 cylinder block array for either type of event. The correlations are also weak generally for the EVO events and this seems to be due to the rather different behaviour of EVO4. It might be noted in this context that, in terms of source-sensor distance, Figure 6.13 is based on the

assumption that the sources of the INJ and EVO signals are on the injector body and on the EV spring seat respectively, and implicitly that all of the sources of a given type (INJ 1-4 or EVO 1-4) are of equal strength.

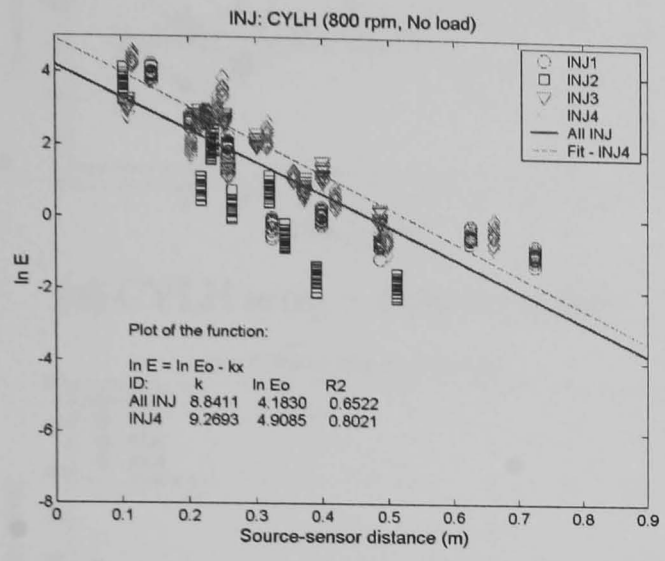

(a) CYLH array – Injector events

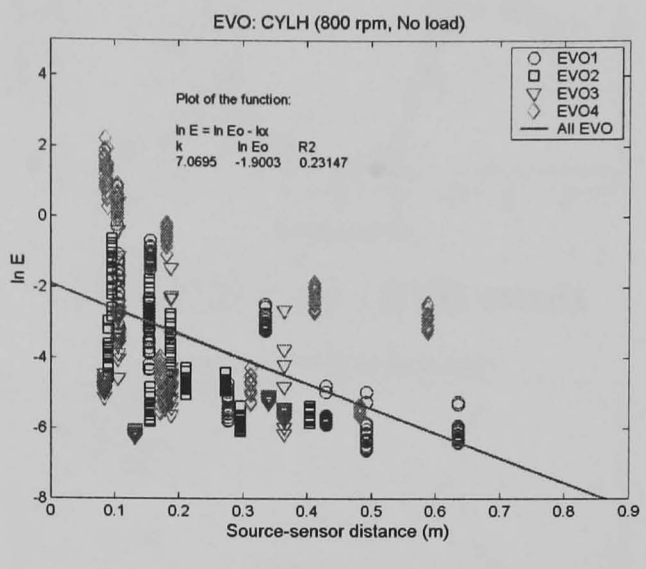

(b) CYLH array – EVO events

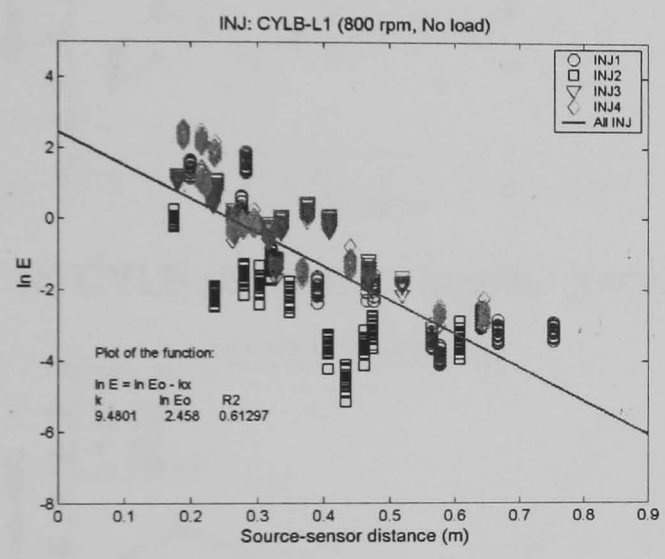

(c) CYLB(L1) array – Injector events

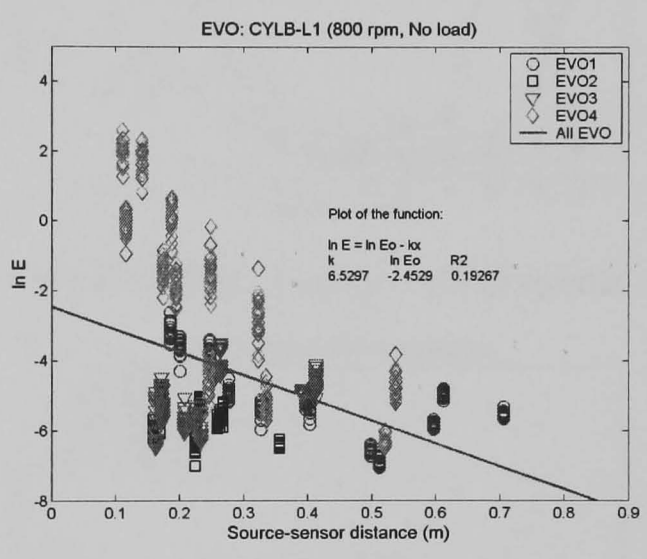

(d) CYLB(L1) array – EVO events

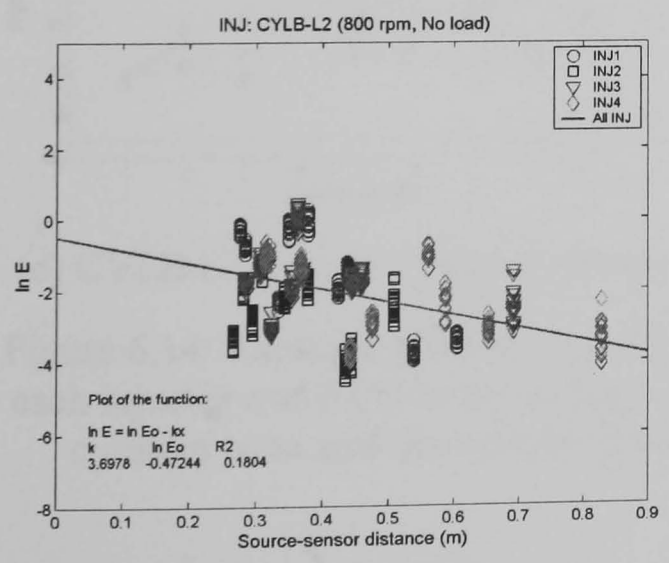

(e) CYLB(L2) array – Injector events

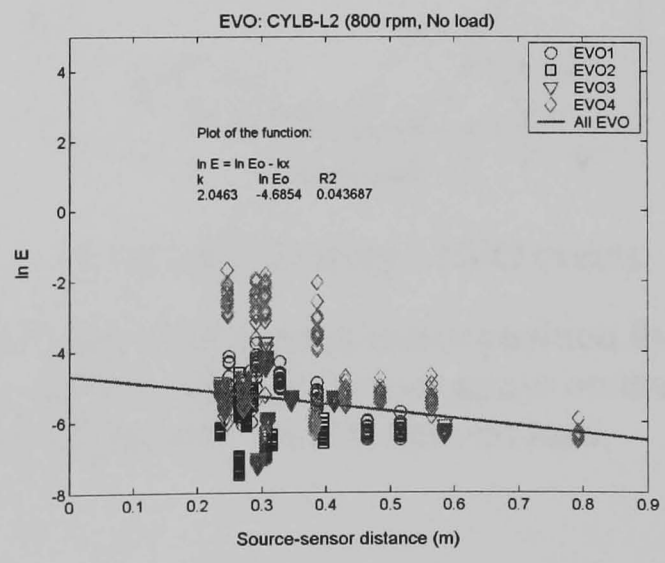

(f) CYLB(L2) array – EVO events

Figure 6.13: Plots of $\ln E$ versus source-sensor distance for the injector and EVO events acquired from various horizontal sensor arrays on the cylinder head and the cylinder block with engine speed at 800 rpm, no load.

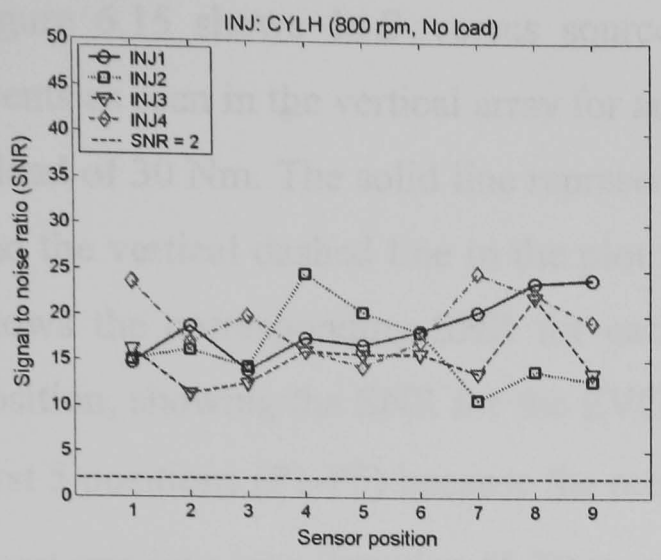

(a) CYLH array – Injector events

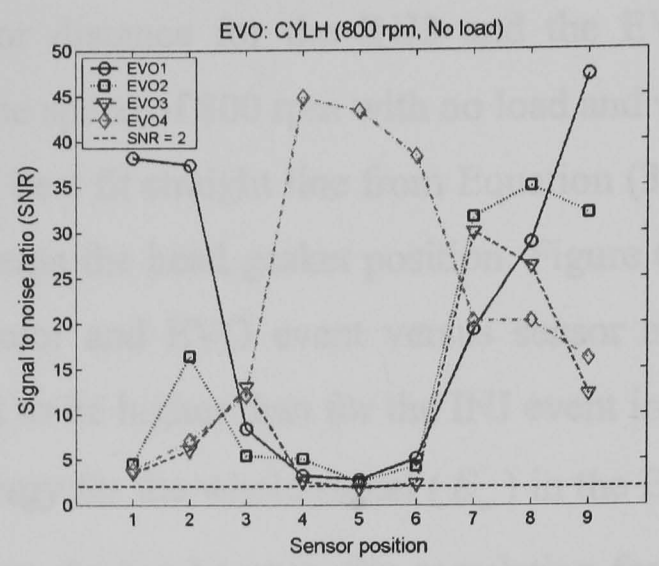

(b) CYLH array – EVO events

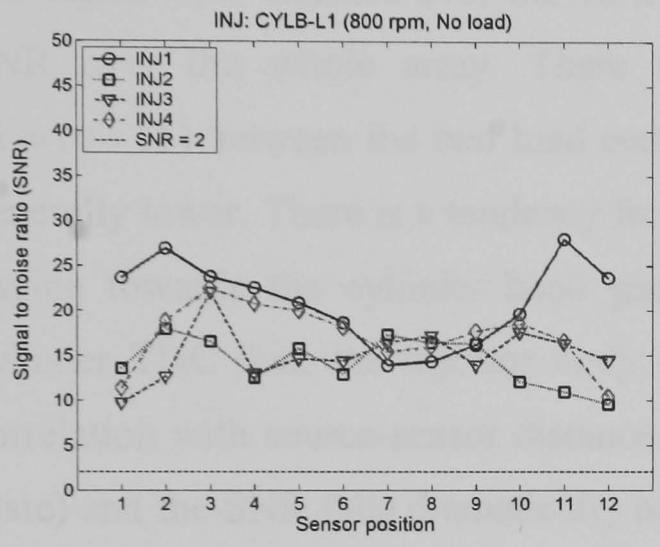

(c) CYLB (L1) array – Injector events

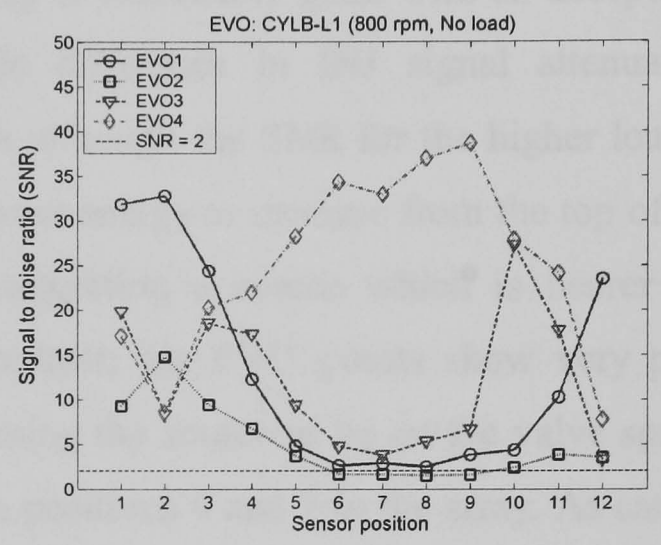

(d) CYLB (L1) array – EVO events

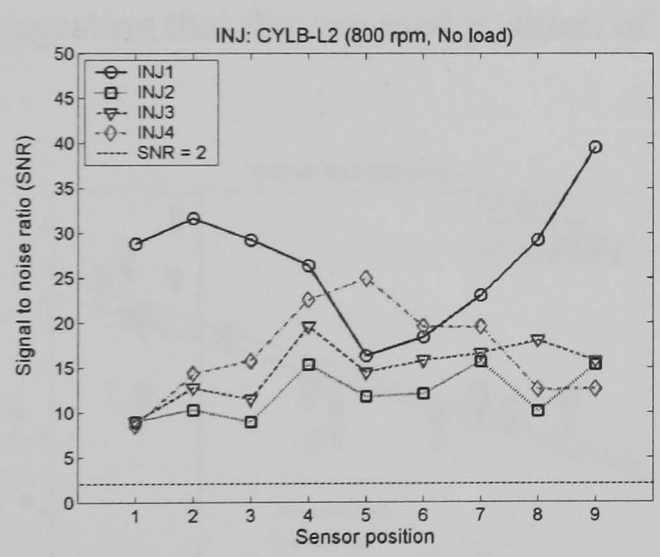

(e) CYLB (L2) array – Injector events

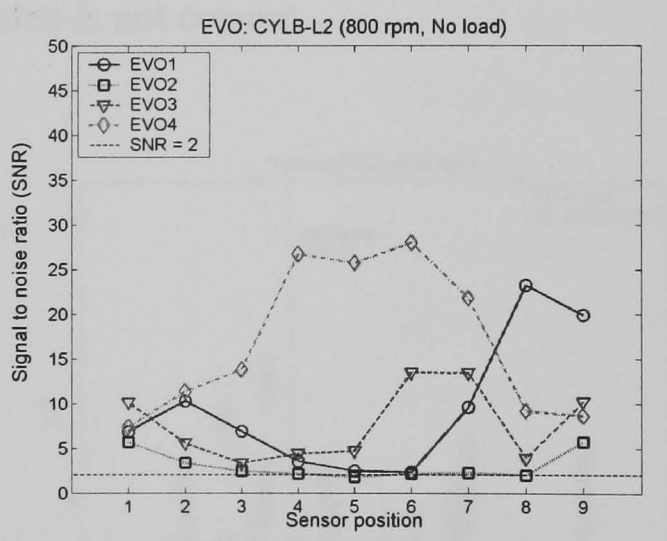

(f) CYLB (L2) array – EVO events

Figure 6.14: Example plots of signal to noise ratio (SNR) versus sensor position for each injector and EVO event acquired from various horizontal sensor arrays on the cylinder head and the cylinder block with engine speed at 800 rpm, no load.

Figure 6.15 shows $\ln E$ versus source-sensor distance for the INJ3 and the EVO3 events as seen in the vertical array for an engine speed of 800 rpm with no load and with a load of 30 Nm. The solid line represents the best fit straight line from Equation (3.14) and the vertical dashed line in the plot represents the head gasket position. Figure 6.16 shows the corresponding SNR for each injector and EVO event versus sensor array position, showing the SNR for the EVO event to be higher than for the INJ event in the first 5 positions (P1-P5) because the mean energy for the whole signal (E_w) in the EVO event window (see Equation (6.2)) was smaller. As can be seen, the correlation for the INJ signal with distance over the vertical array is reasonably good with an acceptable SNR over the whole array. There is little difference in INJ signal attenuation ($k \approx 10-11$) between the two load conditions although the SNR for the higher load is generally lower. There is a tendency for the event energy to increase from the top of the engine towards the cylinder head gasket, suggesting a source which is nearer the cylinder TDC than the injector body. By contrast, the EVO events show very poor correlation with source-sensor distance (assuming the source to be on the valve spring plate) and the SNR falls dramatically between positions 4 and 7 in the array. As can be seen in Figure 6.15(b), the energy appears to increase with source-sensor distance again suggesting that the assumed position of the source is not correct.

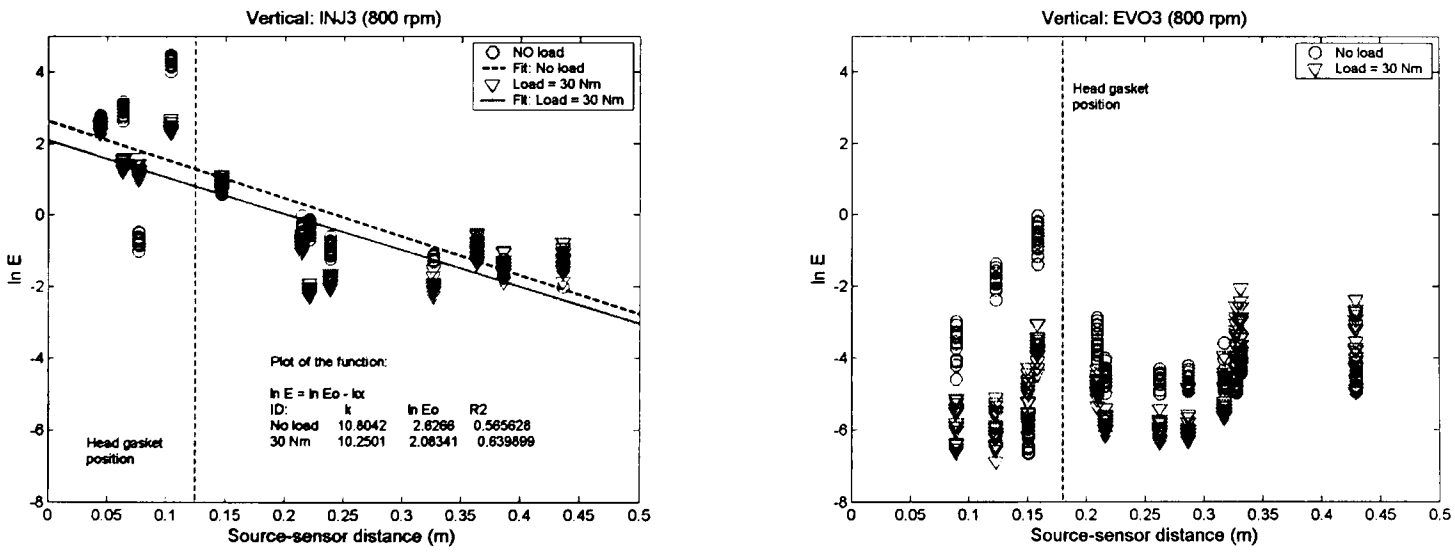

(a) Injector event (b) EVO event

Figure 6.15: Plots of $\ln E$ versus source-sensor distance for the injector and EVO events acquired at the vertical sensor array. The engine was operated with no load and under a load of 30 Nm, running with speed 800 rpm.

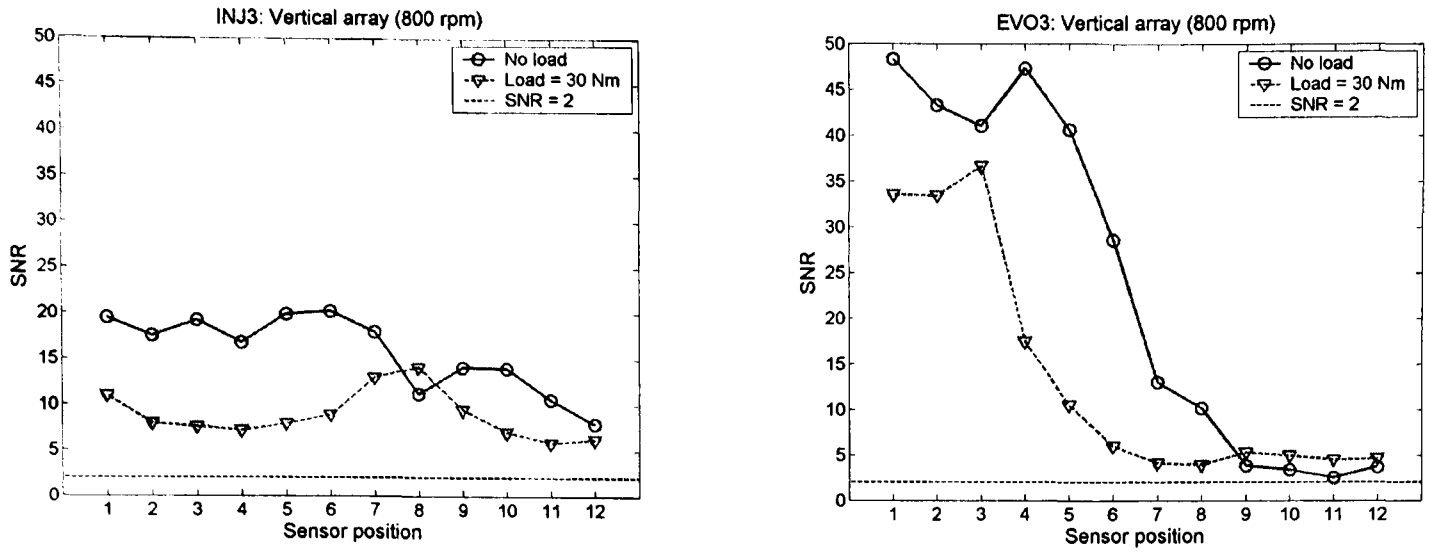

(a) Injector event

(b) EVO event

Figure 6.16: Plots of SNR versus vertical sensor array position for injector and EVO events from the running diesel engine test (800 rpm) with no load and with load at 30 Nm.

Table 6.2 summarises the attenuation factors (k), $\ln E_o$ and coefficient of determination (R^2) for the best fit straight lines for the injector and the EVO events from all engine running tests using horizontal and vertical sensor arrays. Generally, these confirm the observations made on Figures 6.13 and 6.15 that the best correlation is obtained for the INJ signals but that they are relatively poor for the Level 2 horizontal array. It is thought that other mechanical and fluid flow activities around the cylinder block (e.g. bearing, cam shaft, lubrication pump and fuel pump) interfere with the signals acquired at Level 2. Correlations are generally poor for the EVO signals and the variation of the measured attenuation factors rather high. It is possible that the EVO events at some array positions include a number of events associated with impacts of the rocker arm with the push rod or valve tappet or from mechanical moving components such as camshaft or rocker shaft, and this is also evident in the AE signals where the actual timing of the events can vary slightly. The large variation in the calculated attenuation factors is normally associated with a poor correlation with supposed source-sensor distance and is therefore likely to be due to uncertainty in the actual location of the source. For the best results (i.e. greatest certainty of source position) for horizontal arrays, the measured attenuation factors for the injector events for four engine running conditions are reasonably consistent with $k \approx$ 7-9.5 and correlation coefficients between 57 and 77%. For the EVO events, the measured attenuation factors are reasonably consistent ($k \approx$ 5-7) but the correlations are poor, generally below 36%. For the vertical array, the attenuation factors for the injector events from the two engine running conditions are consistent ($k \approx$ 10-11) with

correlation coefficients between 55 and 65%. However, for the EVO events, correlation coefficients are generally poor and the value of attenuation factor is around 6.

Sensor array	Speed rpm	Load	Injector events (1 – 4)			EVO events (1 – 4)		
			k	$\ln E_o$	R^2	k	$\ln E_o$	R^2
Cylinder head	800	No load	8.8411	4.1830	0.6522	7.0695	-1.9003	0.2315
Cylinder head	800	30 Nm	9.4276	4.6751	0.7585	5.7948	-2.0628	0.2623
Cylinder head	1200	No load	9.0616	5.3165	0.7716	4.9761	-2.1316	0.1908
Cylinder head	1200	30 Nm	8.3997	5.3666	0.7410	7.0254	-1.3728	0.3593
Cylinder block (L1)	800	No load	9.4801	2.4580	0.6130	6.5297	-2.4529	0.1927
Cylinder block (L1)	800	30 Nm	8.4913	2.4175	0.5784	3.3540	-3.7634	0.1036
Cylinder block (L1)	1200	No load	8.2269	3.2259	0.6424	4.7706	-1.6991	0.2527
Cylinder block (L1)	1200	30 Nm	7.3460	3.4985	0.6117	2.7564	-2.7819	0.0924
Cylinder block (L2)	800	No load	3.6978	-0.4724	0.1804	2.0463	-4.6854	0.0437
Cylinder block (L2)	800	30 Nm	4.6800	0.6282	0.3729	3.2975	-3.9839	0.1905
Cylinder block (L2)	1200	No load	4.2317	1.1415	0.3795	1.6638	-3.4012	0.0184
Cylinder block (L2)	1200	30 Nm	1.4612	0.6161	0.0404	2.9325	-3.5076	0.1215
Vertical array*: Cyl3	800	No load	10.8042	2.6266	0.5656	5.8911	-2.5296	0.1633
Vertical array*: Cyl3	800	30 Nm	10.2501	2.0834	0.6399	-2.7066	-5.1290	0.1083

Remark: * For vertical sensor array, only injector 3 and EVO 3 events were used in the analysis.

Table 6.2: Summary of effective attenuation factor (k), apparent source energy in logarithmic scale ($\ln E_o$) and coefficient of determination (R^2) using the best-fit straight line ($\ln E = \ln E_o - kx$) for the injector and EVO events from engine running tests using horizontal and vertical sensor arrays on the cylinder head and the cylinder block.

Figure 6.17 shows a comparison of attenuation factors for artificial and real sources generated at injectors and exhaust valves in bar chart format. The values shown in the figure combine the results for horizontal sensor arrays on the cylinder head and the cylinder block for the running diesel engine tests under all test conditions (Table 6.2) and the pencil lead break tests (Tables 5.4, 5.6, 5.7 and 5.9), where the error-bar shown represents the mean, maximum and minimum values of attenuation factors.

For the injector events, the cylinder head array generally gives results that are consistent with pencil lead breaks on the injector body, with only a slight tendency to higher effective attenuation. The injector events observed at the upper cylinder block array give consistently high effective attenuation coefficients (relative to the reference on the injectors) with the effect being greater at lower speeds and lower loads. In contrast, the effective attenuation coefficients at the lower cylinder block array are consistently lower than the reference ($k \approx 5.5$) on the injectors. All the effective coefficients measured for the Level 2 array, engine running source and simulated source, are lower than found for the other arrays. In addition, for both cylinder block arrays, it is clear that the effective

attenuation coefficients are less than the reference on the cylinder liners in all conditions. It would appear therefore that many of the events (or parts thereof) have associated sources at the bottom of the engine, leading to an overestimate of source-sensor distance for at least part of the energy.

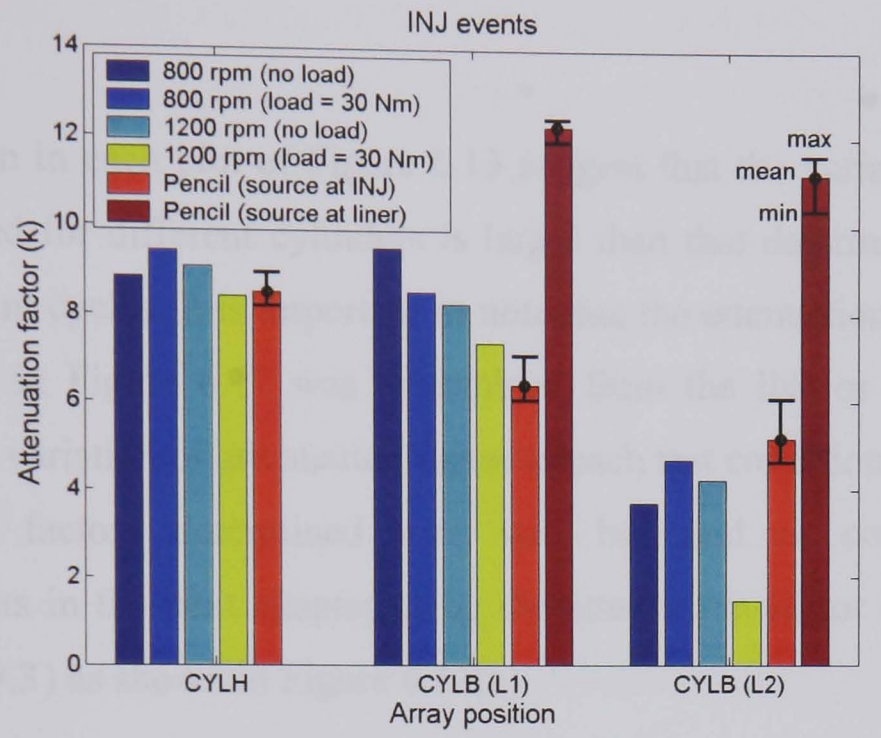

(a) INJ events

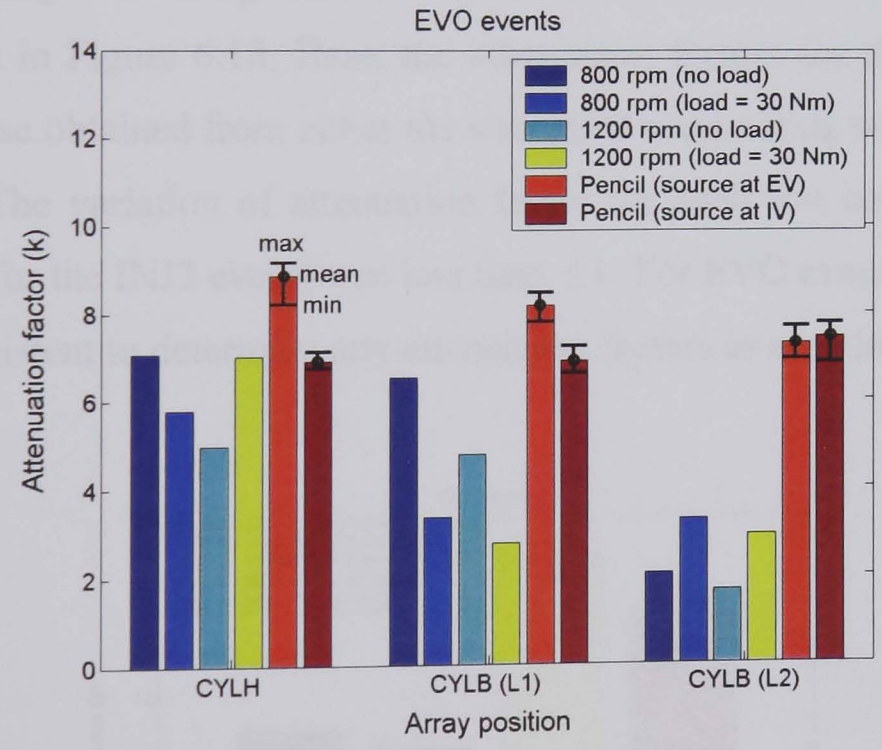

(b) EVO events

Figure 6.17: Comparison of attenuation factors between engine running tests and transmission tests from sources at injectors and exhaust valves to various sensor arrays on cylinder head and cylinder block of small diesel engine.

For the EVO events, the cylinder head array result is most consistent with the value obtained for the pencil lead breaks, although the results vary a little more with load and speed and all give low effective attenuation coefficients compared with a source at the EV, although this is less so with respect to a reference on the IV. For the upper block

array L1, the results for different loads and speeds are highly variable and are below both simulated source results (pencil). The Level 2 array again gives lower effective attenuation coefficients, and the results for different loads and speeds are variable around $k \approx 1.6\text{-}2.3$ with poor correlations. Again, the lower apparent attenuation coefficients at L2 would suggest some parts of the source to be at the bottom of the engine.

The results shown in each plot of Figure 6.13 suggest that the variation of attenuation factors determined for different cylinders is larger than that determined for individual source for different cycles. It is important to note that the attenuation factor at each test condition shown in Figure 6.17 was determined from the INJ or EVO event of all cylinders and the variation of attenuation factor in each test condition was less than ± 3. The attenuation factors determined here will be used in comparison for the reconstitution tests in the next chapter using the attenuation factor determined for the INJ4 event ($k \approx 9.3$) as shown in Figure 6.13(a).

The results for engine running tests and simulated source tests for the vertical sensor array are shown in Figure 6.18. Here, the attenuation factors for the running tests are smaller than those obtained from either the simulated source tests with or without water in the gallery. The variation of attenuation factor for each test condition (which was calculated only for the INJ3 event) was less than ± 1. For EVO events, the data were not sufficiently consistent to determine any attenuation factors as seen in Figure 6.15(b).

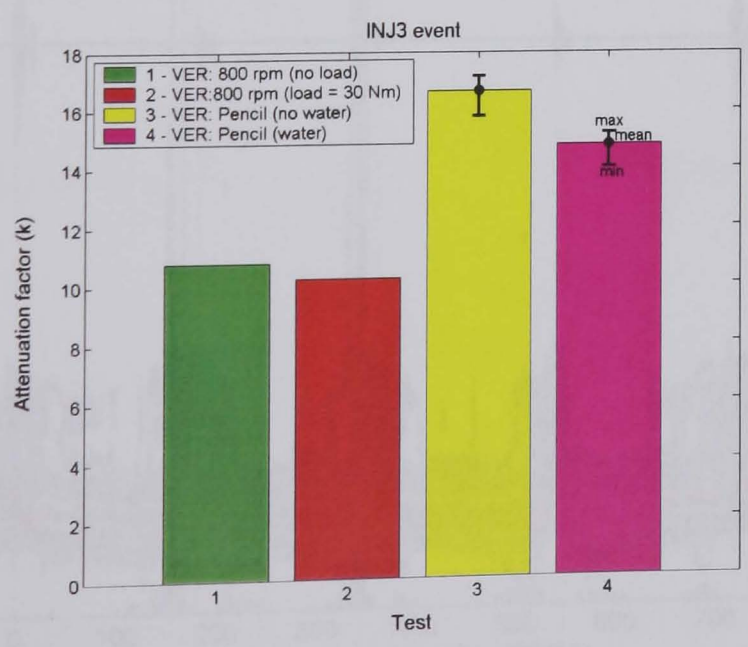

Figure 6.18: Comparison of attenuation factors between engine running tests and transmission tests from sources at injector of cylinder no. 3 to vertical sensor array positions.

The limited success obtained by using the relatively coarse event windows in the foregoing suggests that a more detailed analysis of the events might be useful. Accordingly, Figure 6.19 shows a contour plot using the STFT as described in Section 6.2.3, for a receiver sensor at P1 on the cylinder head of the running diesel engine at 800 rpm with no load. Frequency content was normalized using the maximum amplitude of the frequency spectrum and the power therefore varied from 0 to 1 as seen on the scale to the right of the figure. The top of the figure shows the comparison of the raw signal and the mechanical event map, and the vertical dotted lines represent TDC (firing) for each cylinder at 0, 180, 360 and 540 degrees (firing order 1-3-4-2). It can be seen that there are two main frequency bands at around 100-250 kHz (low frequency band) and 250-400 kHz (high frequency band). The low frequency band is generally present through the entire engine cycle (720 degrees) and this is thought to be associated with mechanical activity of moving parts around the cylinder head. On the other hand, the high frequency band is most strongly present at the TDC of each cylinder and, by implication, the INJ events and this may be associated with the fuel flow activity at the injectors. El-Ghamry *et al* [7] and Fog *et al* [8] have observed that the high frequency component of AE signals from engines, may be associated with fluid-flow activity for a number of sources such as exhaust valve leakage on a two stroke marine diesel engine and a cylinder head gasket leak on a four stroke, HDSI diesel engine, respectively.

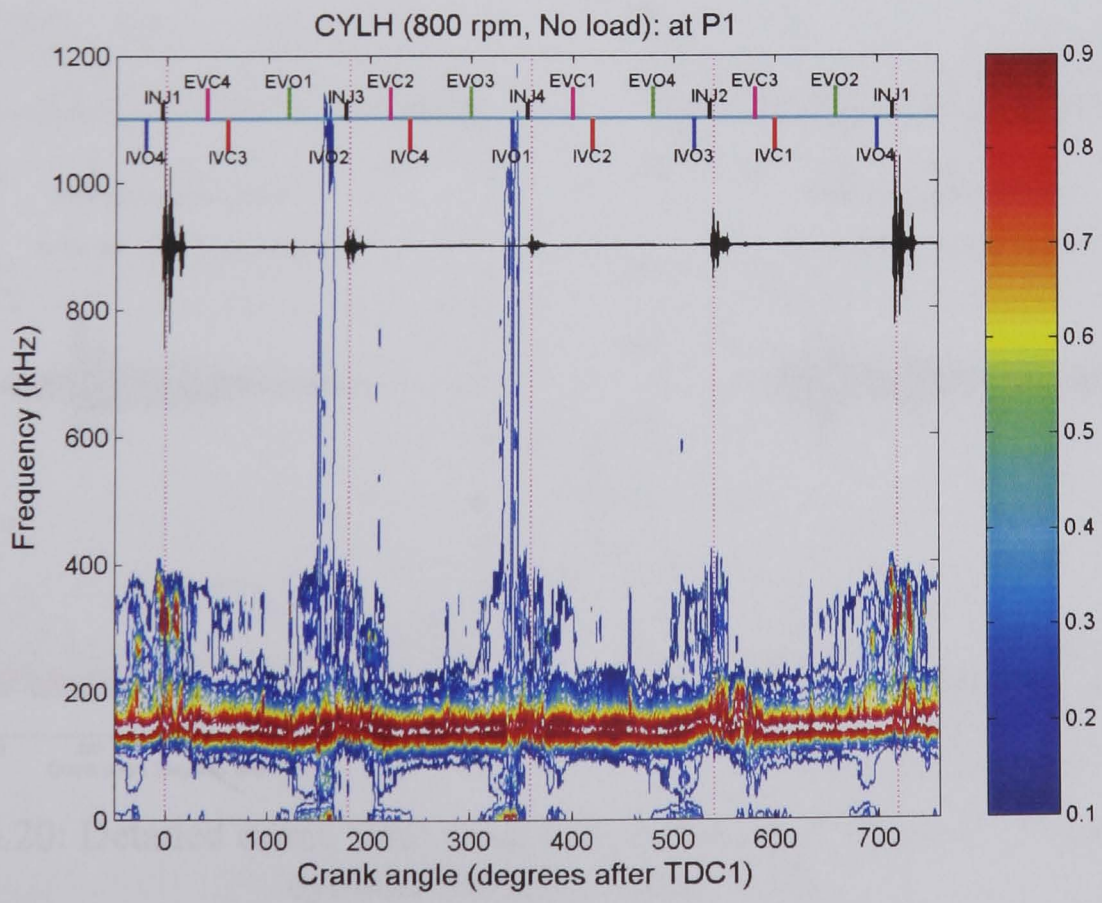

Figure 6.19: Contour plot of crank angle, frequency and normalised magnitude for a running signal recorded at sensor position at P1 on the cylinder head of the small diesel engine.

The fine structure of the injector signals is shown in Figure 6.20, which focuses on the four injector events from Figure 6.19. There appear to be four components in the injector event, associated with different mixes of low and high frequency. The switch between low and high frequency bands can, however, only be seen clearly for the injector event of cylinder no. 1. The injectors used in the HSDI small diesel engine are single stage spring type injectors, for which four components can be identified (1) pressure build up in the injector (which probably includes a small impact between needle and valve seat before the full needle opening); (2) needle lift (mechanical impact between needle and its backstop and activity of fluid flow through injector nozzle); (3) needle closing (mechanical impact between needle and its seat and activity of fluid flow through injector nozzle) and (4) back pressure fluctuations in the fuel line (bouncing of backpressure between needle and plunger of fuel injection pump in the fuel delivery line after needle closing). The location of this last event depends on the length of the fuel delivery line and its duration depends on the residual pressure in the fuel delivery line.

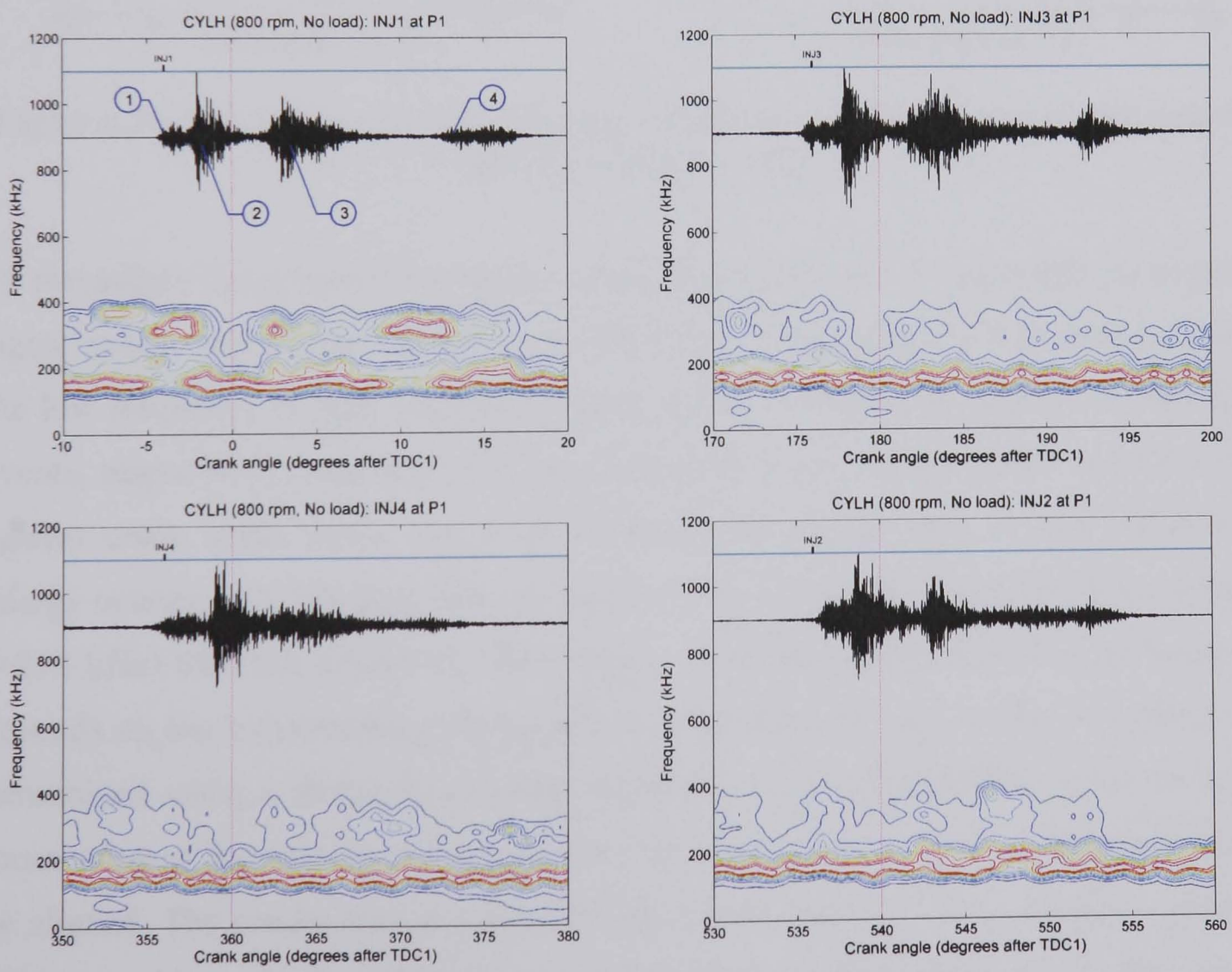

Figure 6.20: Detailed event, time, frequency structure of injection events for each cylinder (detail of Figure 6.19).

The EVO signals also have some interesting fine structures, and an example for the EVO1 and EVO2 events is shown in Figure 6.21 (the EVO3 and EVO4 events are not seen in the signal), although only that from cylinder no. 1 can be seen clearly. Again a switch between low and high frequency can be seen in the EVO1 event, and again, the low frequency band is generally continuous throughout the signals, probably associated with mechanical activity of moving parts related to valve operation. It is expected that the high frequency band is associated with the high pressure exhaust gas flowing over the valve face.

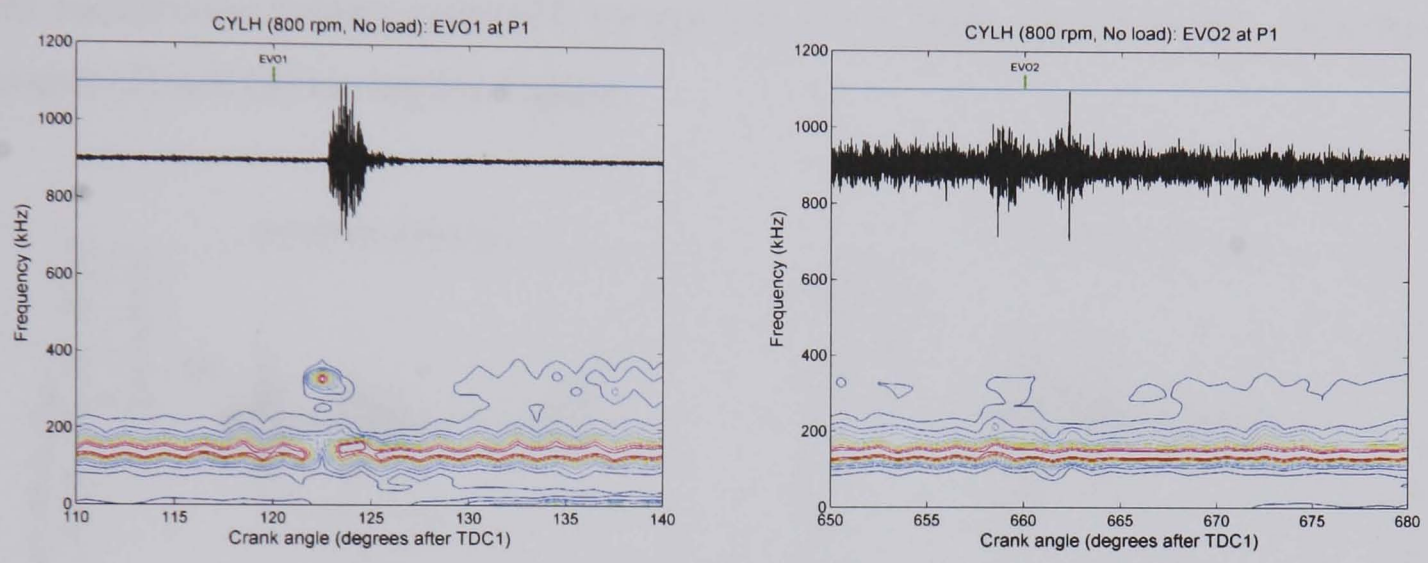

Figure 6.21: Detailed event, time, frequency structure of EVO events for each cylinder (detail of Figure 6.19).

To investigate the potential for more detailed diagnostic information within an event the signal energy was divided between two frequency bands. Figures 6.22 and 6.23 show the low frequency to high frequency signal energy ratio for the injector and the EVO events, respectively, acquired from the horizontal sensor array on the cylinder head, against crank angle across the event window. The energy ratio is that between the energy content of a low-pass filtered signal (<250 kHz) and a high-pass filtered signal (>250 kHz) for each degree of crank angle. Since the arrival time at a given sensor depends on the transmission path length, the time delay of each event in the array was determined using a threshold crossing technique (with the threshold value set at the mean value of the enveloped raw signal for the event window) so that the records could be aligned. The results shown were calculated from the tests with an engine speed of 800 rpm with no load, and the energy ratios were averaged from 20 records (i.e. 20 cycles). The raw signal shown at the top of each plot is that acquired from the sensor closest to each cylinder, although the energy ratios are plotted for all 9 sensor positions (P1-P9) and the average for all positions is shown as a dotted line.

As can be seen in Figure 6.22, each injector is slightly different, mostly likely due to its specific characteristics of spring stiffness, fuel pressure and timing as well as the condition of the nozzle (clean/blocked) or needle (sticking). The energy ratios show similar trends with three or four different peak locations, which are associated with the aforementioned aspects of injector action. The first is a small peak that occurs around 4-6 degrees before TDC of each cylinder. The second is the main peak that occurs at crank angle around 0, 180, 360 and 540 degrees and is also associated with TDC of each cylinder. The other peaks vary slightly at crank angles around 5-10 and 15-20 degrees after TDC of each cylinder. The energy ratios broadly follow those peaks with the background (before event (1)) having a very low energy ratio and the space between events (2) and (3) having the highest.

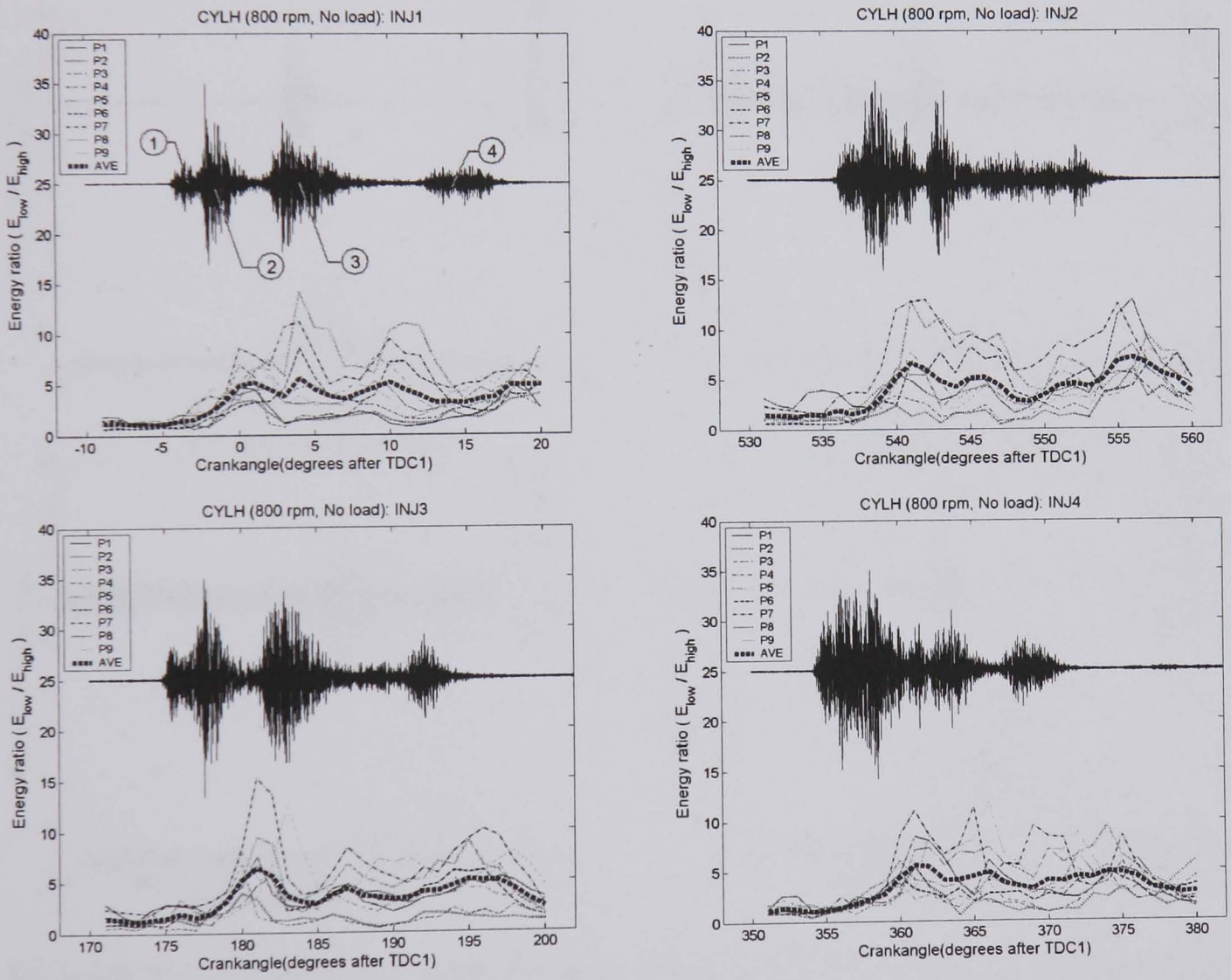

Figure 6.22: Plot of energy ratio between signal energy of low frequency band signal (< 250 kHz) and high frequency band signal (>250 kHz) versus crank angle for each injection process event. The numbers 1-4 indicate the main events in the injection process.

Typically, the injection process in diesel engines involves a combination of needle impacts and the high-pressure fuel flow within the injector body. Gu *et al* [44, 45] have studied needle behaviour in the diesel engine injection process, and have developed a dynamic model for the needle motion of a typical single-stage, hole-type injector of a

direct injection diesel engine and compared it with experimental results of the vibration response from an injector body. They described the characteristic of the injector behaviour for three series of transients during the injection cycle; fluid excitation commencing prior to needle opening impact, needle opening impact and needle closing impact. For the injector closing impact, they found it was difficult to distinguish fluid activity and mechanical impact in the vibration signal. From Figure 6.20, however, it appears that each type of activity can be seen separately in the AE record during the injector closing impact. Gill *et al* [9] have also observed that the activity commencing with the build-up of fuel pressure in the high-pressure pipe prior to the opening of needle valve could be detected by AE but was not visible in the vibration signal.

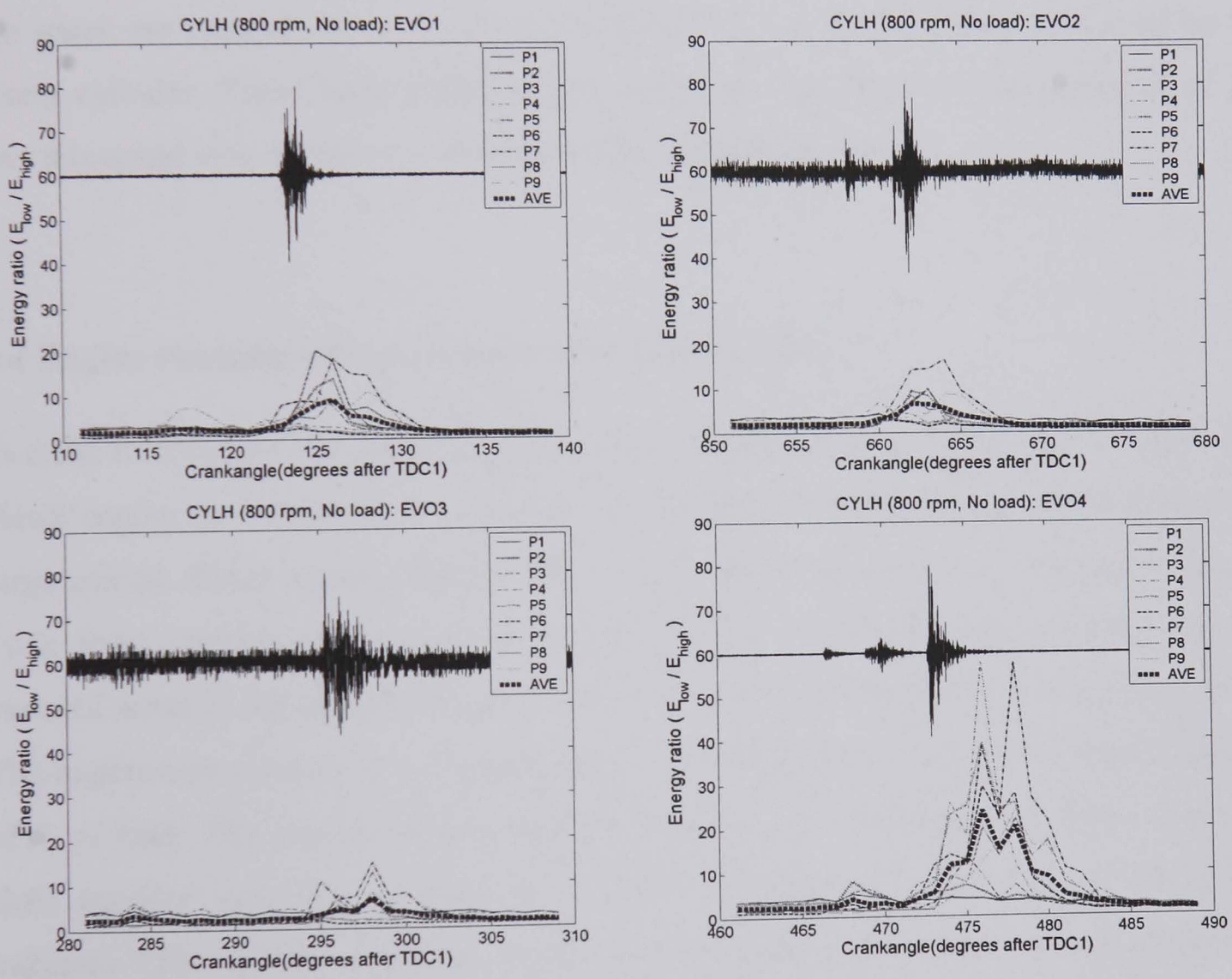

Figure 6.23: Plot of energy ratio between signal energy of low frequency band signal (100 – 250 kHz) and high frequency band signal (250 – 400 kHz) versus crank angle for each EVO event.

A similar analysis of the energy ratios is shown for the EVO events in Figure 6.23. The AE signals appear to contain one or two events, the timing of which can vary over 5–10 degrees. This might be due to varying condition of the individual exhaust valves or other related mechanical moving parts. The event at crank angles around 120-130 degrees after TDC of each cylinder show high proportions of low frequency energy,

perhaps associated with the impact of the rocker arm and the top of the exhaust valve stem. After the exhaust valve is fully opened, the proportion of high frequency energy increases again and this may be due to the excitation of exhaust gas flow.

The injector and EVO event frequency detail is most clearly seen in signals from sensors closest to the source position (Figures 6.20 and 6.21) whereas the other events have a lower mean frequency. This might be caused by attenuation and structural filtering of the high frequency band due to the complex geometry of the engine block.

As mentioned earlier, the EVC, IVC and IVO events are rarely seen in the signals. This difference for the EVO events can be explained because, when the exhaust valve opens, the gases are typically at a pressure of around 3-4 bar [123], further enhanced by the rising cylinder. These high pressure fluid activities may be the main generator of AE and this could also explain the strength of the injector signals.

6.4 Engine running tests on large marine diesel engine

In order to illustrate the generic nature of the approach the methods used for the small diesel engine have been used to extract information from AE signals obtained from the large marine diesel engine. Figure 6.24 shows typical AE signals acquired for a single cycle from various sensors placed on the injector body, the valve housing, and the exposed areas of the upper and lower parts of the cylinder liner (Figures 4.14 and 4.15). The engine was running at a constant speed at 136 rpm and was under approximately 9 MW of load. The signals shown were resampled onto crank angle domain using the shaft encoder and TDC signals as described in Section 6.2.1 and the dotted line indicates TDC of this cylinder. Four main events can be identified immediately in Figure 6.24 as the injector, EVO, EVC and the ring pack passing the scavenging port. Douglas *et al* [21] have described these events in much more detail and the purpose here is merely to show the application. Douglas *et al* [21] noted that the needle actions at fuel injection start and end could be identified as well as some high frequency signals between the two and some other mechanical impacts (see Figure 2.5). It was also shown that, during the compression and expansion strokes, the "background" AE level increased as the contact force between piston rings and cylinder liner increased due to the high in-cylinder pressure associated with the compression and combustion processes

and an AE event associated with the ring-pack passing over the oil groove in the cylinder liner was seen at around 55 degrees after TDC.

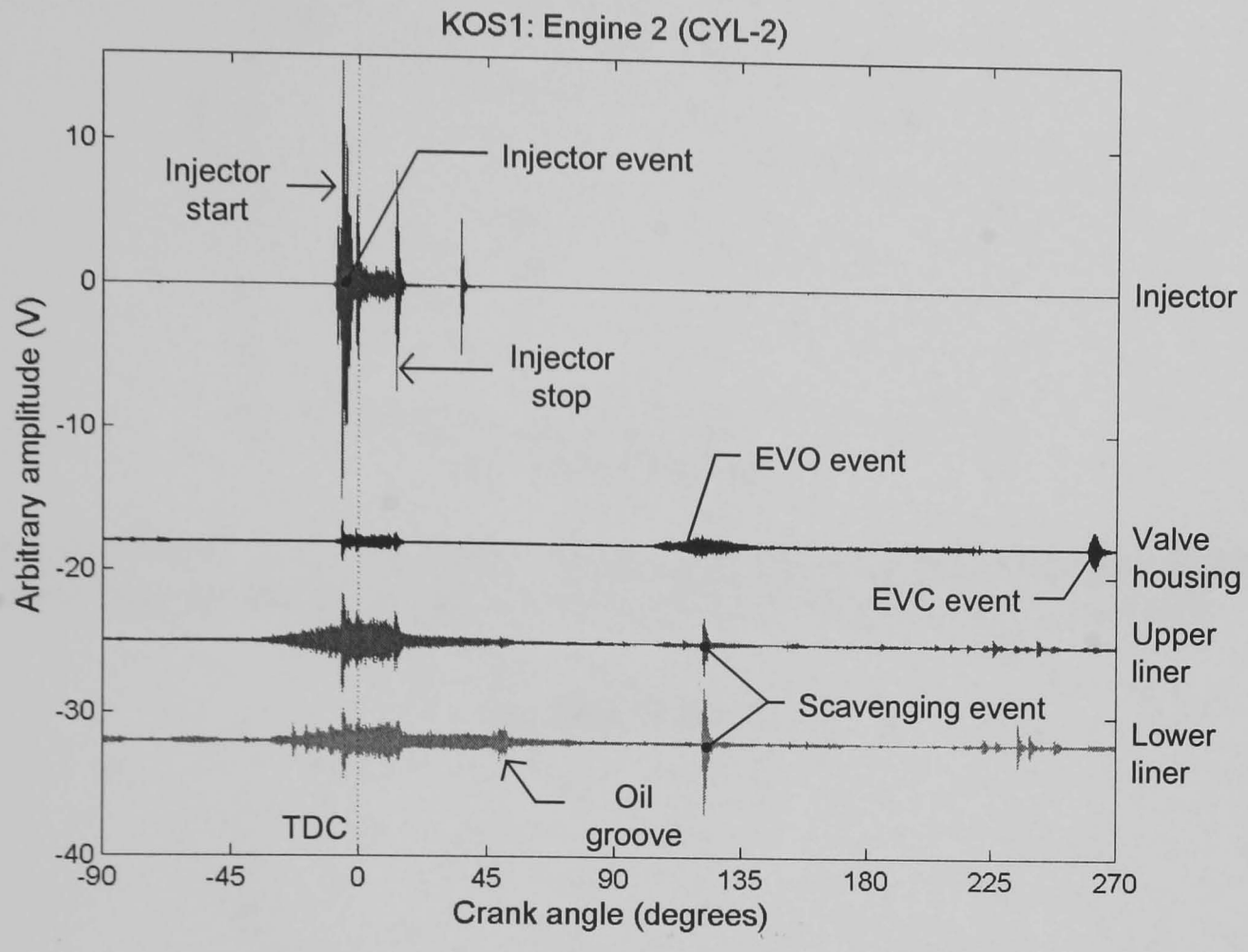

Figure 6.24: Raw AE signal acquired from various sensor positions on a large marine diesel engine (Kos power plant) at speed 136 rpm and load 9 MW.

As with the results on the small engines, the strongest signals are obtained from sensors closest to the source of the AE, although the large distances involved mean that the character, and even presence, of events can be very different when viewed by different sensors. The signals are attenuated as the source-sensor distance increases but the large distances involved cause problems relating to noise levels. The injector and scavenging port events are consistent and AE energy of each event can be determined using Equation (6.1) as described in Section 6.2.1, and Figures 6.25 and 6.26 show plots of $\ln E$ versus source-sensor distance for each of these events. The labels INJ, VH, UL and LL indicate sensor positions on the injector body, valve housing, and the exposed areas of the upper and lower parts of the cylinder liner as shown in Figure 4.14. The energy content was calculated over a crank angle width of 40 degrees (from -10^{o} to 30^{o}) around TDC for the injector events and over a crank angle width of 5 degrees from 120^{o} to 125^{o} after TDC for the scavenging port event. Source-sensor distance was estimated from a drawing and was the same distance used for the transmission tests discussed in Section 5.5.

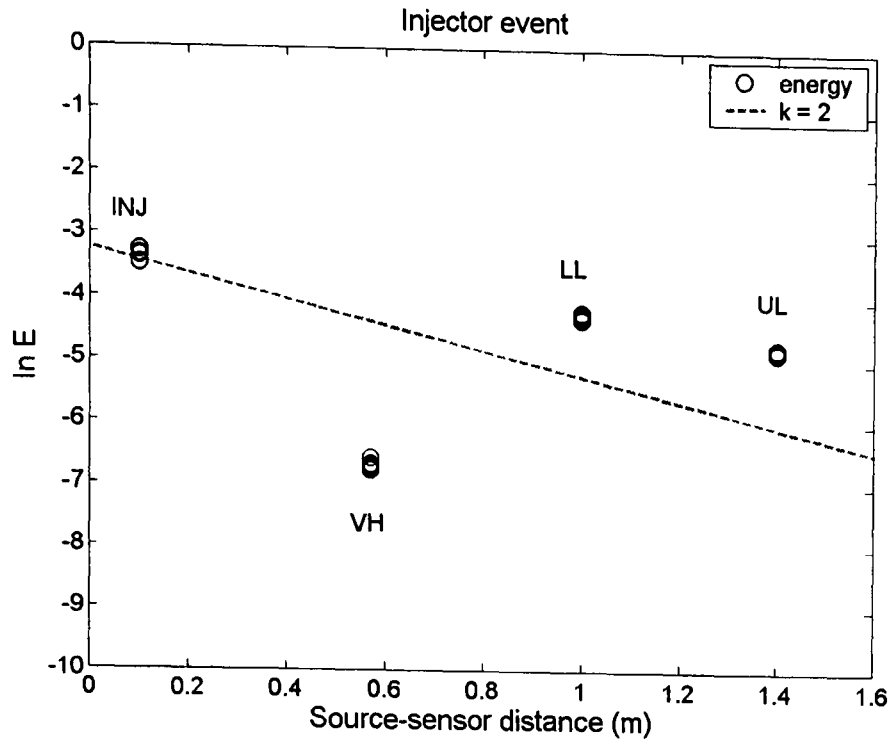

Figure 6.25: Plot of $\ln E$ versus source-sensor distance for the injector event acquired from large marine diesel engine (sensor positions at INJ, VH, UL and LL).

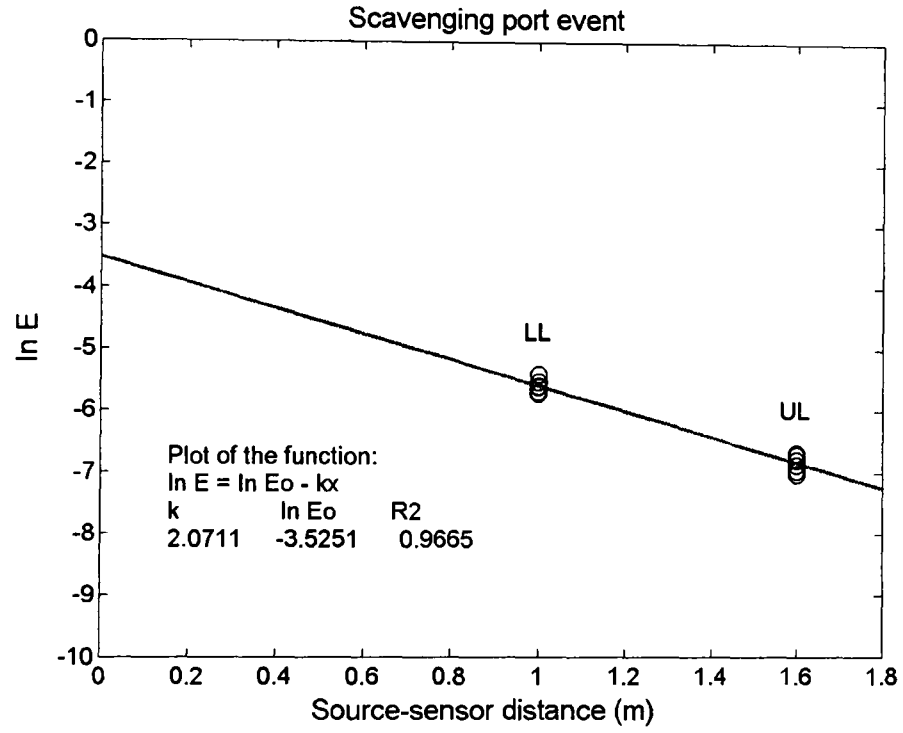

Figure 6.26: Plot of $\ln E$ versus source-sensor distance for scavenging port event acquired from large marine diesel engine (sensor positions at LL and UL).

For the injector event shown in Figure 6.25, it can be seen that the AE energy obtained from the sensor placed at the VH is much lower than one might expect from the other positions. It is thought that the transmission path for this sensor position is more complicated as AE waves have to travel across several boundaries from injector to cylinder cover and then to valve housing. Looking at the record for this sensor position, it is evident that it shows a very different profile to the other positions, particularly with regard to valve actions. For sensors placed at UL and LL, the injector event is clearly affected by other AE sources such as combustion process, piston movement and piston ring/cylinder liner interaction as seen in Figure 6.24. Nevertheless, if we draw a line of

slope $k = 2$ through the injector sensor position, it is seen that the UL and LL energies lie just above this line. The scavenging port event could not be isolated from the signal recorded at the VH because the signal from exhaust valve operation is coincident, and the event does not show an acceptable signal to noise ratio at the injector sensor position. Thus, only sensor positions at UL and LL could be plotted in Figure 6.26, although, these are also consistent with an attenuation factor, $k \approx 2$, as observed in the transmission tests using a simulated source (Section 5.5.2).

6.5 Summary of findings for engine running tests

For the case of small diesel engines, attenuation factors for engine running tests on the cylinder head array are consistent with transmission tests on the same array with $k \approx$ 8-10 for the injector events and $k \approx$ 5-7 for the EVO events. However, for other arrays, the injector and EVO events need to be described in more detail to identify other AE sources with the events so that results could be improved. For example the mechanical impact and fluid flow taking place during injection and valve operation processes can be seen in more detail using the STFT analysis. The analysis method used to determine the attenuation factor in small diesel engines can be applied to large marine diesel engines, with broad agreement with the attenuation factor determined using a simulated source. The effect of detailed structure of the events, and overlaps of temporally simultaneous events, is more evident in the larger engine showing that analysis would benefit more from spatial location techniques.

The findings of this chapter will be used for spatial reconstitution in order to improve resolution of multi-source signals acquired from both small and large diesel engines. The next chapter will demonstrate the method of reconstitution for the examples of the injector signal acquired from the small diesel engine and the scavenging port signal from the large marine diesel engine.

Chapter 7 Application of source location and signal reconstitution in diesel engines

7.1 Introduction

This chapter is concerned with source location for the small HSDI diesel engine and signal reconstitution for the small and large diesel engines. Typical AE signals acquired from the engines are multiple-source signals associated with mechanical and fluid flow activities during the engine cycle which can be identified by segmenting in time and space domains using the methods discussed in Chapter 6. The findings of Chapters 5 and 6, in particular the attenuation factors and wave speeds, are used to improve fidelity of the multiple-source signals in this chapter. Two source location techniques, velocity-based and energy-based, are used with triangular sensor arrays to locate source positions on the cylinder head. The techniques are described in the next section and applied to the transmission tests using simulated sources (Sections 4.4.1 and 5.4.1) and to the engine running tests (Sections 4.5.5 and 6.3) and the results are compared. Signal reconstitution is also demonstrated where an attempt to reproduce the source signal from the signal acquired at each array position is made.

7.2 Source location in a small HSDI diesel engine

Two source location techniques, each based on the intersection of two hyperbolae are compared here. The traditional velocity-based technique [11], which has been described in Section 3.4.2, uses arrival time differences between sensors and wave speed to determine source location. For an energy-based technique, the absorption model, attenuation factor, and energy content of the signals can be used to locate the source position and this is described in the following sub-section, and then applied to sources generated from the injector and the exhaust valve of cylinders 2 and 4, using the horizontal array on the cylinder head, for both simulated sources (pencil lead break) and engine running tests. The results of the source location calculations were plotted on a 2D projected view of the cylinder head. For array given position, there is a possible 2mm error associated with the 3D geometry of the cylinder head, but this is small compared to the sensor diameter of 10 mm.

7.2.1 Source location using energy technique

Typically, planar source location in two dimensions uses a triangular sensor array to determine the intersection of two hyperbolae as shown in Figure 3.8. The technique uses arrival time difference for a wave arriving at the sensors, wave speed, and distance between the sensors and source location is determined by solving simultaneously Equations (3.25) and (3.26) as described in Section 3.4.2. This technique can be applied relatively easily for sources on objects with simple geometry, such as plate-like structures, because wave speed and time-of-flight can be measured accurately, as discussed in Chapter 3. However, for complex geometries and paths such as around the cylinder head of an engine, wave speed and time-of-flight are more difficult to measure because of distortion of the AE waveform by attenuation, reflection, refraction, dispersion and mode conversion of the waves. Also, for a real running engine, the signals acquired can be complicated, including more than one source, so it might be difficult to establish the arrival time for each source. As an alternative solution, the absorption model (Equation (3.15)), using AE energy, transmission path (source-sensor distance) and attenuation factor can be used to develop an energy-based technique to determine the location of a source, without recourse to wave speed or measurement of wave arrival times.

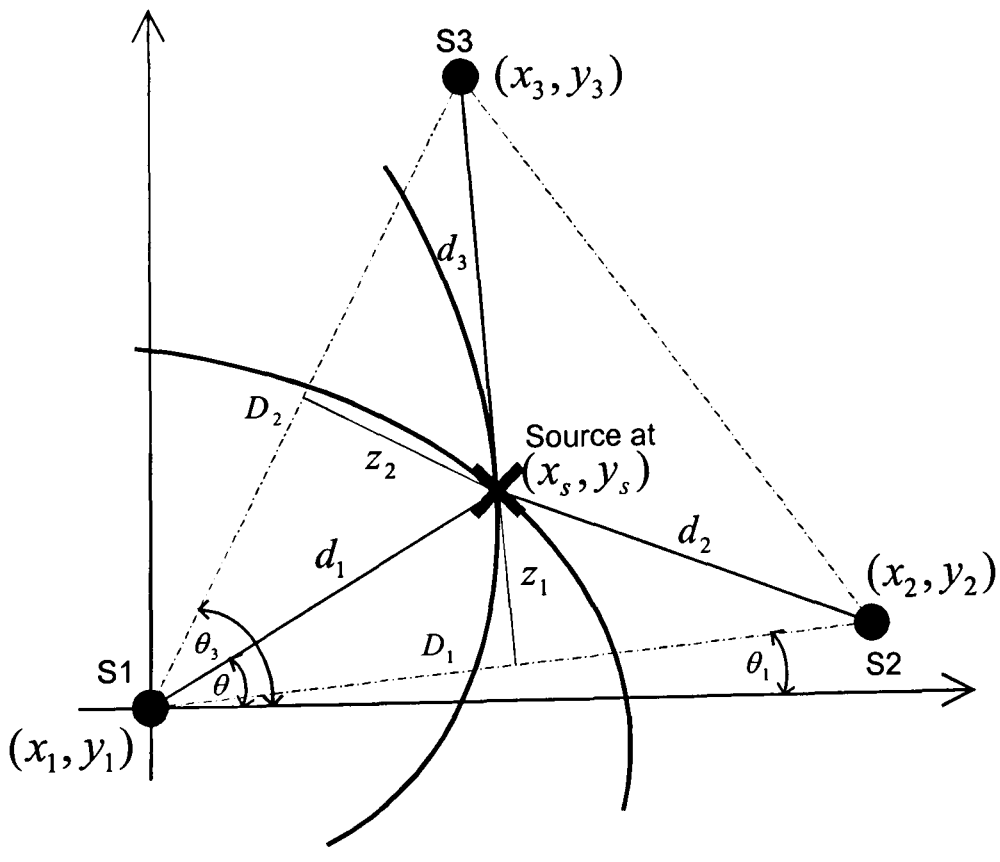

Figure 7.1: Schematic diagram of energy-based source location technique using a triangular array.

This energy-based technique uses three sensors mounted on the side of the cylinder head as a triangular array where sensors S1, S2, and S3 are located at (x_1, y_1), (x_2, y_2) and (x_3, y_3), respectively, as shown in Figure 7.1. It assumes that source locations are in an area bounded by the triangle and the sequence of arrival at the sensors is S1-S2-S3. By determining energy contents of the signals from the three AE signals in the array, two hyperbolae can be defined and the intersection gives a source location at (x_s, y_s) as seen in Figure 7.1.

From Equation (3.16), the source-sensor distance, d_i or transmission path can be obtained using the relationship between energy on a logarithmic scale, $\ln E_i$ and attenuation factor, k;

$$d_i = \frac{\ln E_o - \ln E_i}{k} \tag{7.1}$$

Then, calculating the energy difference between sensors S1-S2 and S1-S3, two hyperbolae (with the foci at S1-S2 and S1-S3) can be defined

$$\delta_1 = d_2 - d_1 = \Delta t_1 \cdot c = \frac{\ln E_1 - \ln E_2}{k} \tag{7.2}$$

and

$$\delta_2 = d_3 - d_1 = \Delta t_2 \cdot c = \frac{\ln E_1 - \ln E_3}{k} \tag{7.3}$$

where δ_1 and δ_2 are constant;

Δt_1 and Δt_2 are arrival time difference for a wave arriving at the sensors;

and c is a wave speed

For sensors S1 and S2, the distance, d_1 between source and S1 (Figure 7.1) can be determined using z_1, thus:

$$z_1 = d_1 \cdot \sin(\theta - \theta_1) \tag{7.4}$$

$$z_1^2 = d_2^2 - \left(D_1 - d_1 \cos(\theta - \theta_1)\right)^2$$

$$d_1^2\left(\sin^2(\theta - \theta_1)\right) = d_2^2 - \left(D_1^2 - 2D_1 d_1 \cos(\theta - \theta_1) + d_1^2 \cos^2(\theta - \theta_1)\right)$$

$$d_1^2 = d_2^2 - D_1^2 + 2D_1 d_1 \cos(\theta - \theta_1) \tag{7.5}$$

By substituting $d_2 = \delta_1 + d_1$ from Equation (7.2), Equation (7.5) becomes

$$d_1^2 = d_1^2 + 2d_1\delta_1 + \delta_1^2 - D_1^2 + 2D_1 d_1 \cos(\theta - \theta_1)$$

$$d_1 = \frac{D_1^2 - \delta_1^2}{2(\delta_1 + D_1 \cos(\theta - \theta_1))} \tag{7.6}$$

Similarly, for sensors S1 and S3, z_2 is given by

$$z_2 = d_1 \cdot \sin(\theta_3 - \theta) \tag{7.7}$$

and, using Equations (7.3) and (7.7), another expression for, d_1 can be written:

$$d_1 = \frac{D_2^2 - \delta_2^2}{2(\delta_2 + D_2 \cos(\theta_3 - \theta))} \tag{7.8}$$

By solving Equations (7.6) and (7.8) simultaneously to satisfy the input condition, the distance between source and sensor, d_1 is obtained and the source location can be given by:

$$x_s = x_1 + d_1 \cos\theta \tag{7.9}$$

$$y_s = y_1 + d_1 \sin\theta \tag{7.10}$$

7.2.2 Source location on the cylinder head using simulated sources

Both source location techniques (energy- and velocity-based) were applied to the experimental data from the simulated source tests described in Section 4.4.1. The velocity-based technique uses Equations (3.25) and (3.26) and slow wave speed of 2650 m/s (as determined in Section 5.4) to locate the source, and the second technique uses Equations (7.6) and (7.8) and the relevant attenuation factors for the various source positions, such as the injectors and the exhaust valves, as shown in Table 5.4. Four simulated source positions were used; two on the injector (INJ) bodies and two on the surface of exhaust valve (EV) spring bases of cylinders 2 and 4. For presentation

purposes, source location is plotted on a 2D development of the cylinder head where the vertical surfaces projected onto a 2D plane. The range of source locations thus obtained indicate a zone in which the sources were generated.

Figures 7.2 and 7.3 show examples of normalised AE signals for each sensor position (P1 to P9) with simulated sources at INJ4 and EV4, respectively. Each signal shown in these figures is normalised by its maximum amplitude in order to illustrate the relative structures of the signals. The vertical dashed line in each plot indicates the arrival time of the signal, determined using the threshold crossing technique with a threshold value at 0.2 of maximum amplitude. The time-of-flight (referred to P4 for the INJ4 source and P5 for the EV4 source) and energy content of the entirety of each signal are also shown in each plot. It can be seen that the AE energy attenuates as distance from the source increases; the weaker signals seem to appear at sensor positions P1, P2, P8 and P9 for the INJ4 source and at sensor positions P1, P2, and P9 for the EV4 event. The AE energy for the EV4 source is generally higher than that for INJ4 source, probably because the EV4 event was generated at the surface of the exhaust valve spring base (on the cylinder head) so AE waves travel only through the cylinder head, whereas waves generated in the injector body travel across a number of interfaces (from the injector to the cylinder head) and AE energy is more attenuated. Rise times and decay times of all signals also increase as distance from the source increases, and a sharp rising edge (short rise time) can be seen in signals acquired from sensors placed close to the sources (i.e. P4, P5 or P6) making arrival time easier to determine. Figure 7.4 shows the SNR for the INJ2, INJ4, EV2 and EV4 events as determined at each sensor position. As can be seen, the SNRs for both events are well above the reference value (SNR = 2) and, as might be expected, higher values of SNR appear at sensors placed close to the sources.

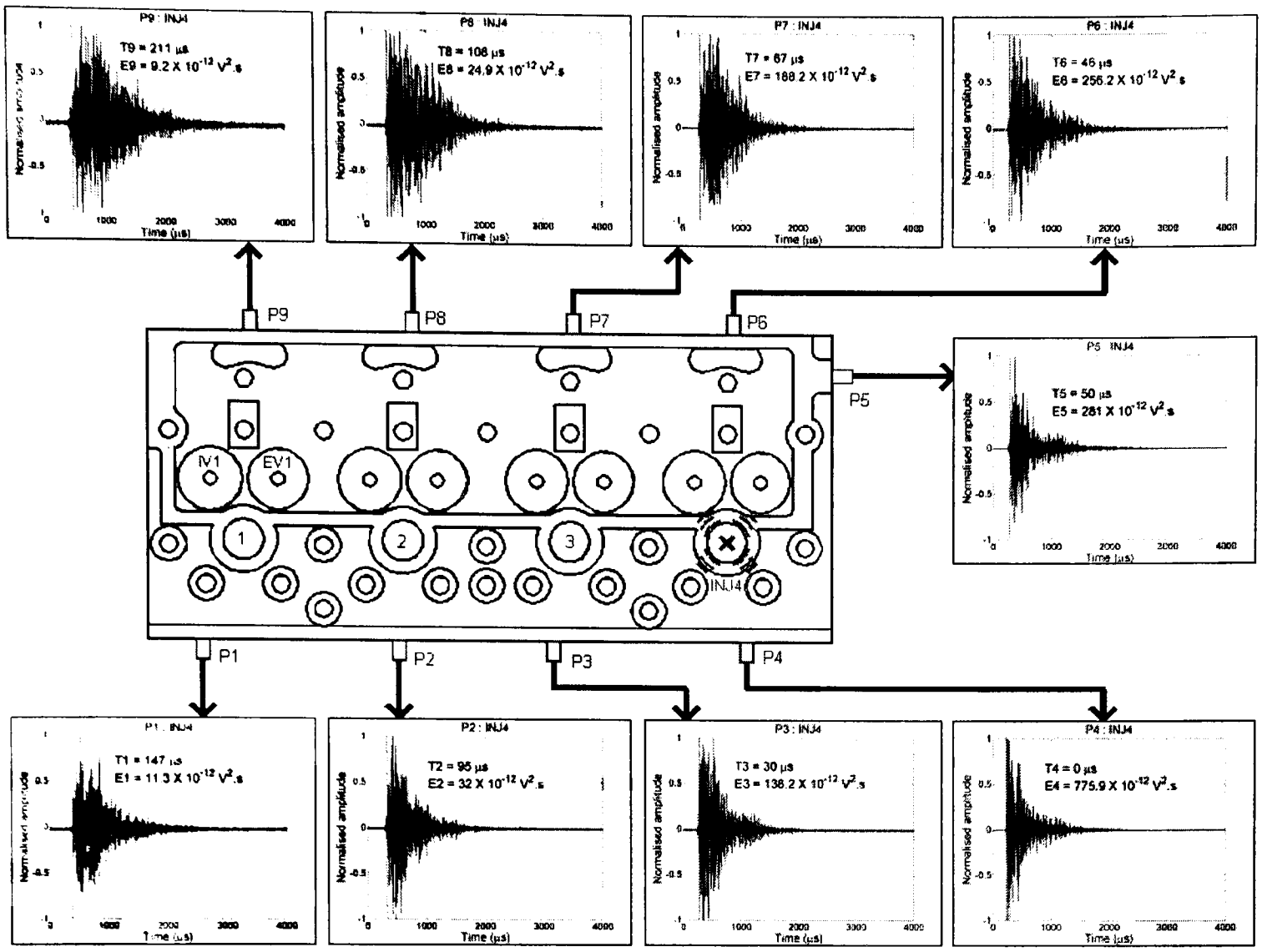

Figure 7.2: Example plots of normalised AE signals recorded at cylinder head array from a simulated source at injector no. 4.

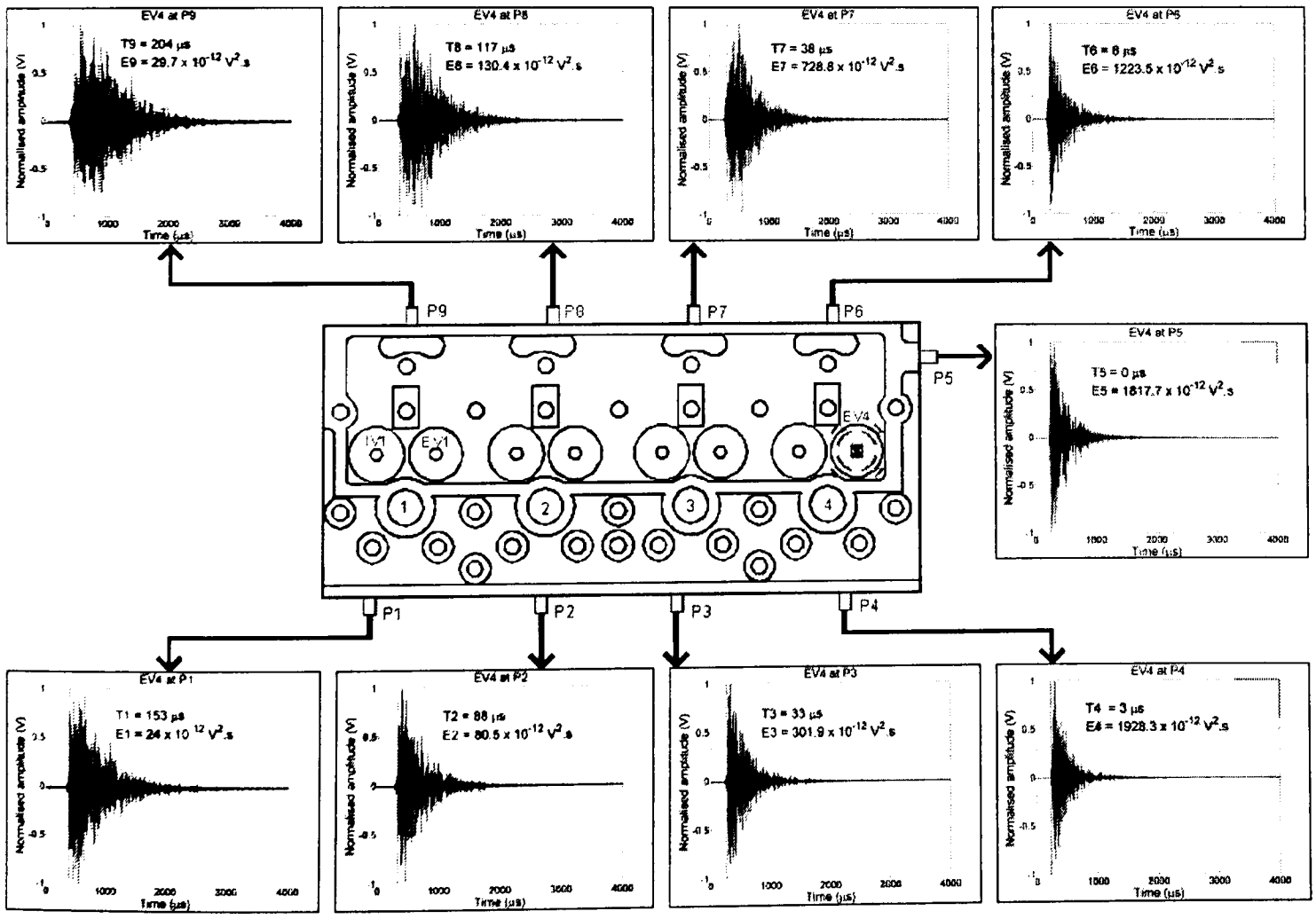

Figure 7.3: Example plots of normalised AE signals recorded at cylinder head array from a simulated source at exhaust valve no. 4.

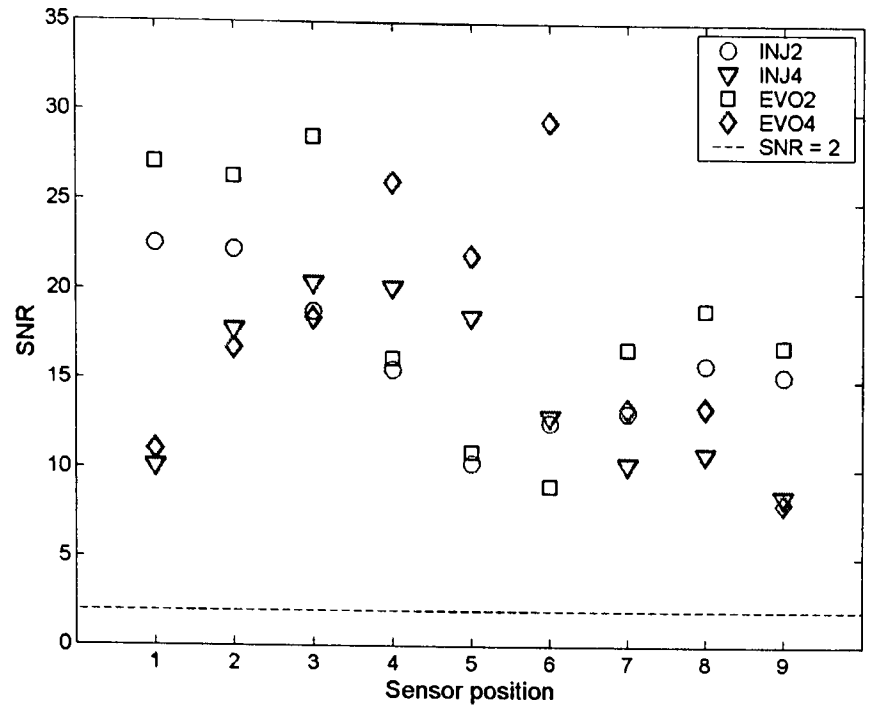

Figure 7.4: SNR for simulated sources acquired at cylinder head array.

It is possible to identify roughly the source location (zone location [11]) simply by eye using maximum peak amplitude or AE energy, remembering that the signals shown in Figures 7.2 and 7.3 are normalised. Using AE energy (given as a number in Figures 7.2 and 7.3), it can be seen by inspection that the source is located around cylinder no. 4 and close to P4 and P5. The results of a more precise source location using the velocity-based technique with triangular arrays is shown in Figure 7.5 for the data acquired from transmission tests on the cylinder head (Section 4.5.1) for the INJ2, INJ4, EV2 and EV4 sources. Two triangular sensor arrays on the cylinder head were chosen with sensor configurations of P1, P4 and P8 for sources at INJ2 and EV2 and P5, P6 and P4 for sources at INJ4 and EV4. Using the slow wave speed of 2650 m/s (determined in Section 5.4) and arrival time difference between sensors, source locations can be determined by solving simultaneously Equations (3.25) and (3.26) so that the calculated locations satisfy the input condition (minimum difference between calculated locations from both equations was set at less than 1mm) to obtain the location of the source with reference to P1 (for the INJ2 and the EV2) or P5 (for the INJ4 and the EV4) by using Equations (7.9) and (7.10). Five records were used for each array and the results obtained are shown in Figure 7.5 including the location of source, injectors, EVs, IVs and sensor positions. The points labelled predicted-1 and predicted-2, shown in Figure 7.5 such as for array configuration of P1, P4 and P8 indicate the predicted location of the source obtained from Equations (3.25) and (3.26), respectively. It can be seen that sources can generally be located using the wave velocity-based technique and that best accuracy is obtained for the results of the EV2 and EV4 events.

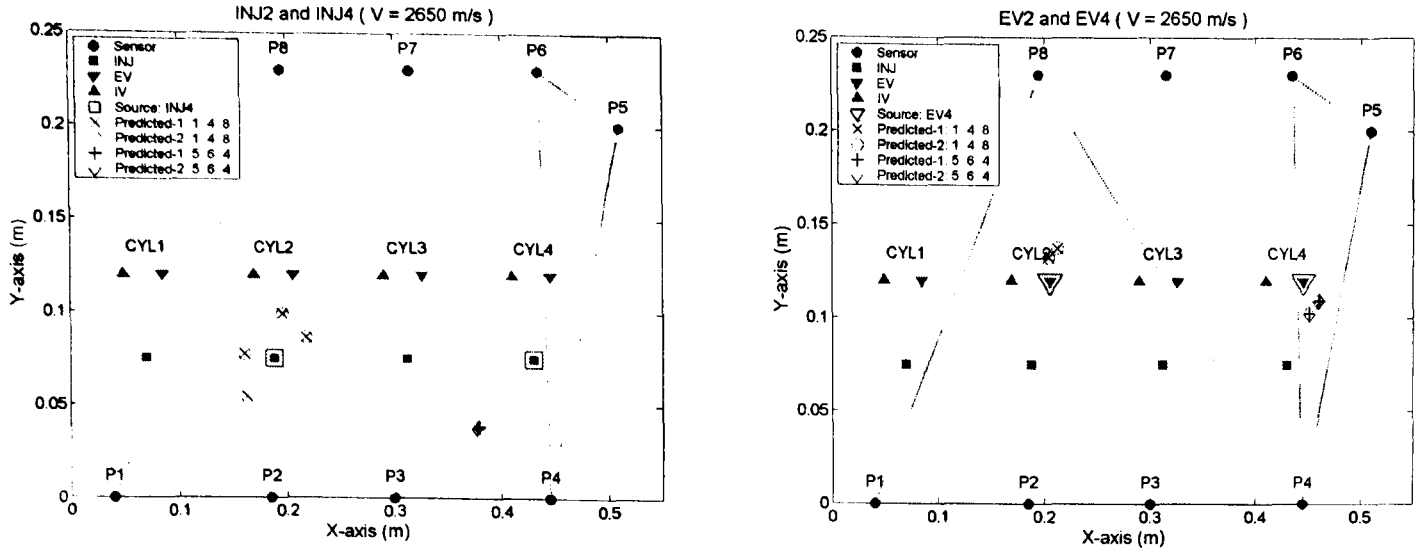

(a) Source at injectors (■) (b) Source at exhaust valves (▼)

Figure 7.5: Velocity-based source location technique using triangular arrays on the cylinder head for simulated tests.

Source locations for the same data using the energy-based technique as described in Section 7.1, are shown in Figure 7.6. The energy content of each signal was determined using the method described in Section 5.2.1 and was calculated from the arrival time of the signal to the end of the signal using a time window size of 2000 μs (10000 points). The wave arrival was determined using the threshold crossing technique with a threshold value at 1.5 times the maximum amplitude of the noise signal as described in Section 5.2.1. The attenuation factor (k) of each event can be seen in Table 5.4; $k \approx$ 10, 9.3, 10.5 and 9.3 for the INJ2, INJ4, EV2 and EV4 events, respectively. The sources were then located by using the triangular array configurations of P1, P4 and P8 for sources at INJ2 and EV2, P4, P5 and P6 for source at INJ4, and P5, P6 and P4 for source at EV4. By solving simultaneously Equations (7.6) and (7.8), the output results (θ and d_1 as shown in Figure 7.1) satisfying the input condition (minimum difference between calculated locations of both equations was set at less than 1mm) were used to obtain the location of the source with reference to P1 (for INJ2 and EV2), P4 (for INJ4) or P5 (for EV4) by means of Equations (7.9) and (7.10). As can be seen in Figure 7.6, sources can be located using the energy-based technique, but they are not generally as accurate as the velocity-based technique, and choice of array triangle can be very important.

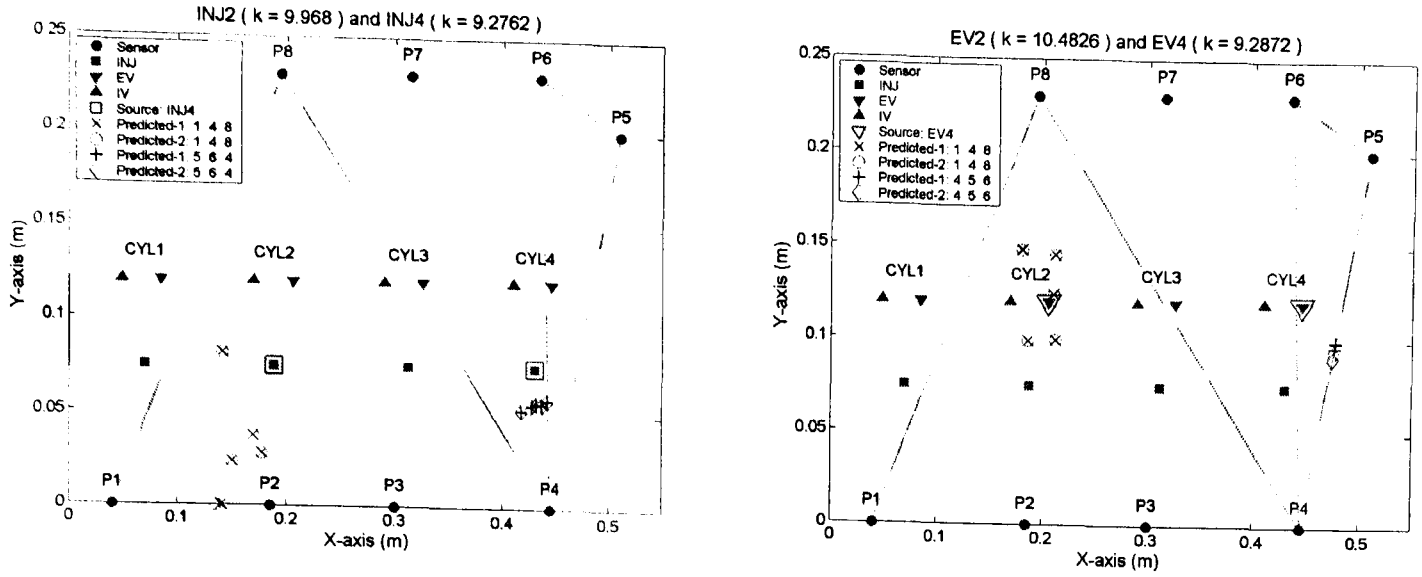

(a) Source at injectors (■) (b) Source at exhaust valves (▼)

Figure 7.6: Energy-based source location technique using triangular arrays on the cylinder head for simulated sources.

With either source location technique, it can be seen that the predicted source is normally located inside the triangular array. However, in some cases, the predicted location lay outside the triangle, although the predicted position was invariably on the side opposite the reference position. For example, for the INJ4 event (array positions of P5, P6 and P4) seen in Figure 7.6(b), the predicted positions are at the side opposite the reference position (P5).

The error in source location using both techniques for all array configurations is summarised in Table 7.1, where the error is simply defined as the distance (mm) between actual and predicted source positions expressed as mean, maximum, and minimum of the 5 records. It can be seen that the mean errors are similar for both techniques, and are recognisably lower for the EV sources using the velocity-based technique.

Source	Array	Arrival time difference technique				Energy difference technique			
		Speed (m/s)	Source location error (mm)				Source location error (mm)		
			Mean	Max	Min	k	Mean	Max	Min
INJ2	P148	2650	28	32	25	9.9680	58	89	42
INJ4	P564	2650	64	65	63	9.2762	21	26	19
EV2	P148	2650	14	19	13	10.4826	24	37	6
EV4	P564	2650	18	19	18	9.2872	38	38	37

Table 7.1: Summary of error in source location for simulated sources using a cylinder head array.

The accuracy of the velocity-based technique depends on two factors; arrival time difference and wave speed. Successful source location using the time-based techniques has been demonstrated for simple structures using, for example: arrival time difference

between sensors [83, 104]; arrival time difference between two wave modes (i.e. high-pass and low-pass signals) using a single sensor [81, 85]; and arrival time difference of waves propagating with a group velocity determined using wavelet transform [69]. In these simpler cases, wave speed can be reasonably assumed to be constant as AE waves travel without encountering surfaces and so the predicted source location depends only on the accuracy of determining arrival time difference. In the case of complex structures such as the cylinder head, it is difficult to determine wave speed because transmission paths are more complex leading to quite a lot of dispersion and complexity in path length. These effects can be seen particularly in the results for the INJ sources where the waves propagate across a number of interfaces and through different materials from the injector to the cylinder head, where the acoustic impedances of the materials are not perfectly matched. In contrast, AE waves generated at EV positions propagate through one material so the wave speeds are probably constant, although dispersion due to different path length can still occur. The results shown in Figure 7.5(b) also give better source location because the EV2 and EV4 events give a sharp rising edge (short rise time) so that the arrival time of signals can be detected more accurately than for injector events.

To overcome these uncertainties, the optimum wave speed (or effective wave speed) to give the most precise source location has been determined for the example of the INJ4 event using the triangular array configuration of P5, P6 and P4 as shown in Figure 7.5(a). This was done using the velocity-based technique and decreasing the wave speed from 2650 m/s in steps of 100 m/s and determining iteratively the velocity at which the minimum error is obtained. Figure 7.7 shows the plot of the wave speed against error and, as can be seen, a wave speed of around 1150 m/s gives the minimum error of 20 mm for the INJ4 event. This process might be used to determine "effective" wave speeds for other events in order to improve accuracy of source location using the velocity-based technique. As mentioned before, the AE waves propagate across a number of interfaces and through different materials for the INJ4 event so the wave speeds are different to the slow wave speed used at 2650 m/s and, in theory, depend on the material properties [11].

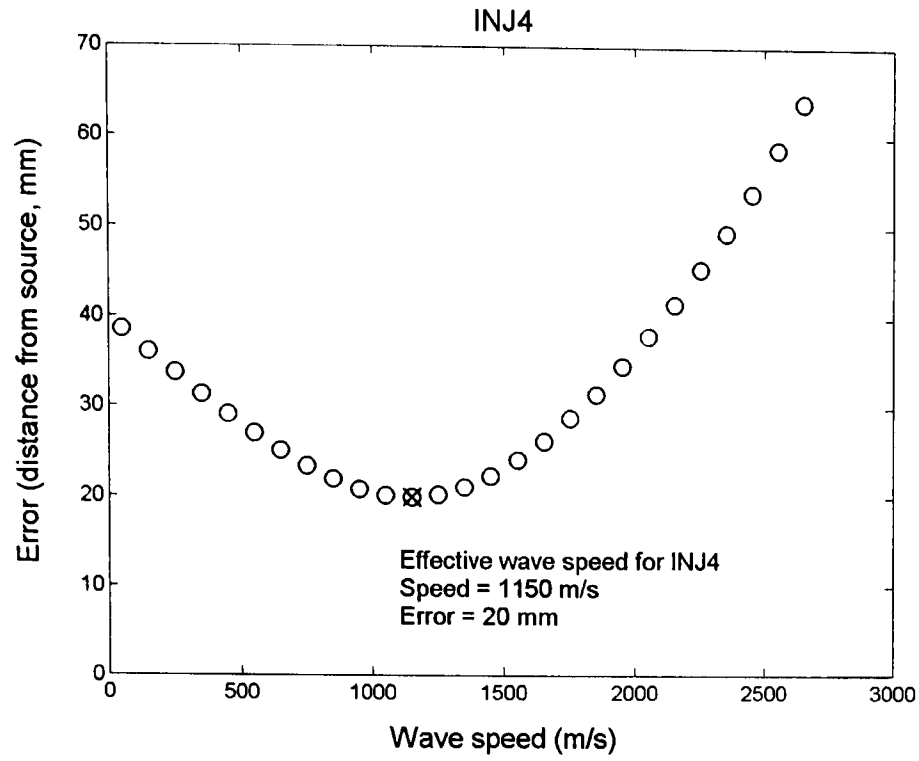

Figure 7.7: Effective wave speed for the INJ4 event for minimisation of location error

For the energy-based technique, the accuracy of a predicted location depends on an attenuation factor which was determined using source-sensor distances estimated from the slow wave speed of 2650 m/s and ultimately, arrival time difference between signals using the threshold crossing techniques, all as described in Section 5.4. The wave speed used may not be accurate, precisely because of the effects of wave propagation mentioned for the velocity-based technique. Thus, the more accurately the transmission path length is known, the more accurate the attenuation factor will be. Figures 7.5 and 7.6 show that, for single sources, location using the velocity-based technique is generally more accurate than the energy-based technique.

7.2.3 Source location on the cylinder head of a running diesel engine

Figures 7.8 and 7.9 show normalised AE signals with their maximum signal amplitudes for the INJ4 and EVO4 events acquired from the horizontal sensor array on the cylinder head (P1-P9) for the engine running at 800 rpm with no load. The vertical dashed line shown in each plot indicates the arrival time of the "signal" determined using the threshold crossing technique with a threshold value of 0.2 times the maximum amplitude, and the energy content of the "event window" is also given in the plots. It is important to note that the signals shown in Figures 7.8 and 7.9 were not all acquired for the same cycle (being acquired in groups of 3 sensor positions) causing some variations. Nevertheless, it can be seen that AE energy decreases as distance from the source increases and the arrival time of the signal increases with propagation distance. As already discussed, the INJ4 event shown in Figure 7.8 is a combination of multiple

sources associated with the mechanical movements and fluid flow phenomena during the injection process, the combustion process and other movements of ancillary equipment. Some variation in the four main peaks can be seen in the plots and this may be because AE waves travel from the various sources to each sensor following slightly different transmission paths, as well as the fact that the signatures of these different cycles are being propagated.

For the EVO4 event shown in Figure 7.9, a clear signal can only be seen at the sensors placed close to the source (P4, P5 and P6) and around the rear side of the cylinder head (P7, P8 and P9). The signals at sensor positions P1, P2 and P3 are not sufficiently strong to determine the location of the source reliably. For sensor positions P4, P5 and P6, the signals were acquired for the same cycle and are composed of three main peaks. The large peak is the main exhaust valve opening process and it is thought that the smaller peaks may be associated with other related moving components during the exhaust valve operating period such as push rod, rocker arm, rocker shaft and cam movement.

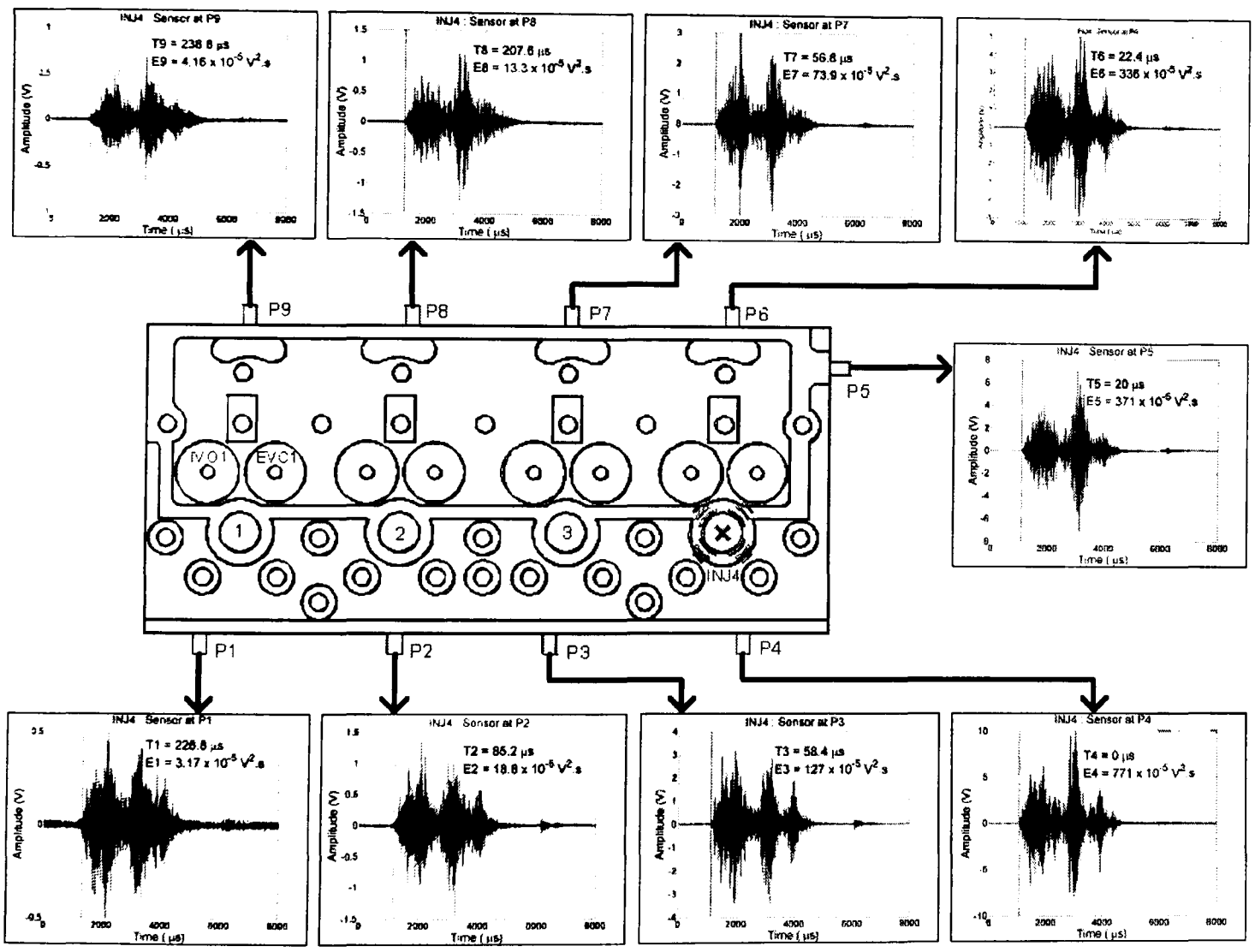

Figure 7.8: Schematic plot of normalised injector event at cylinder no. 4 acquired using the sensor array on the cylinder head (P1-P9) from the diesel engine running at 800 rpm with no load.

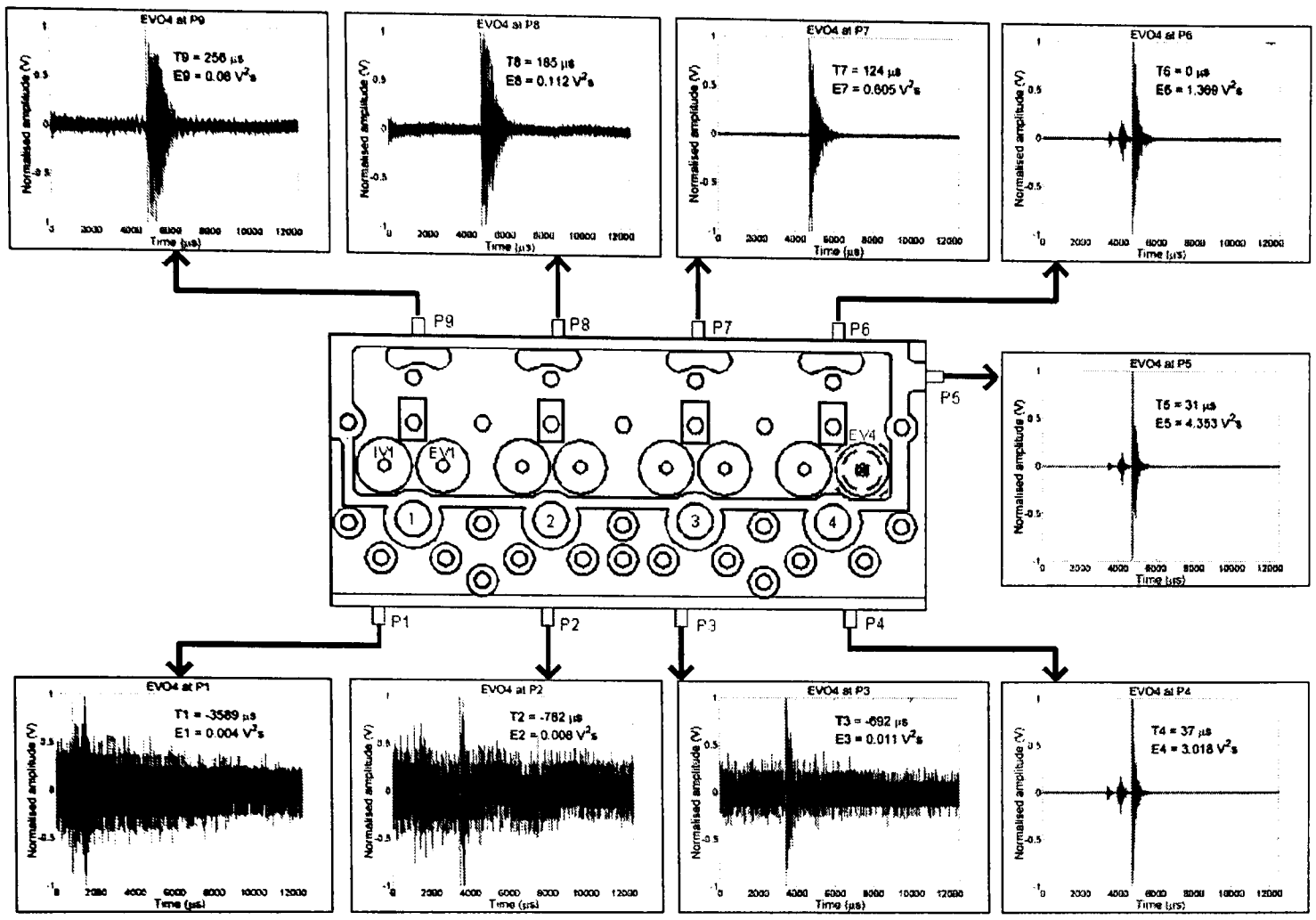

Figure 7.9: Schematic plot of normalised EVO event at cylinder no. 4 acquired using the sensor array on the cylinder head (P1-P9) from the diesel engine running at 800 rpm with no load.

The source location techniques described earlier can be used to predict the location of real sources from the running engine using triangular arrays on the cylinder head, preferably using records acquired from the same engine cycle. The signals shown in Figures 7.8 and 7.9 were not acquired from the same cycle and so a specific test with the engine running at speed of 800 rpm with no load was carried out as described in Section 4.5.4. In this experiment, all groups of three signals included sensor position P4 as a reference. This resulted in the acquisition of data from 3 groups of 4 array positions (i.e. P1,2,3,4; P5,6,7,4 and P6,8,9,4). Due to some adjustments in valve clearance, the EVO4 signals in this special test were not exactly the same as in the test results shown in Figure 7.9, and, as can be seen in Figure 7.10, the EVO4 signals shown are weaker and only appear clearly on the sensor positions placed close to the source (P4, P5 and P6). However, for the INJ4 event, the signals acquired in this way were similar to those shown in Figure 7.8. The experimental data from this auxiliary test will be used for the application of source location in this section and signal reconstitution in the next section.

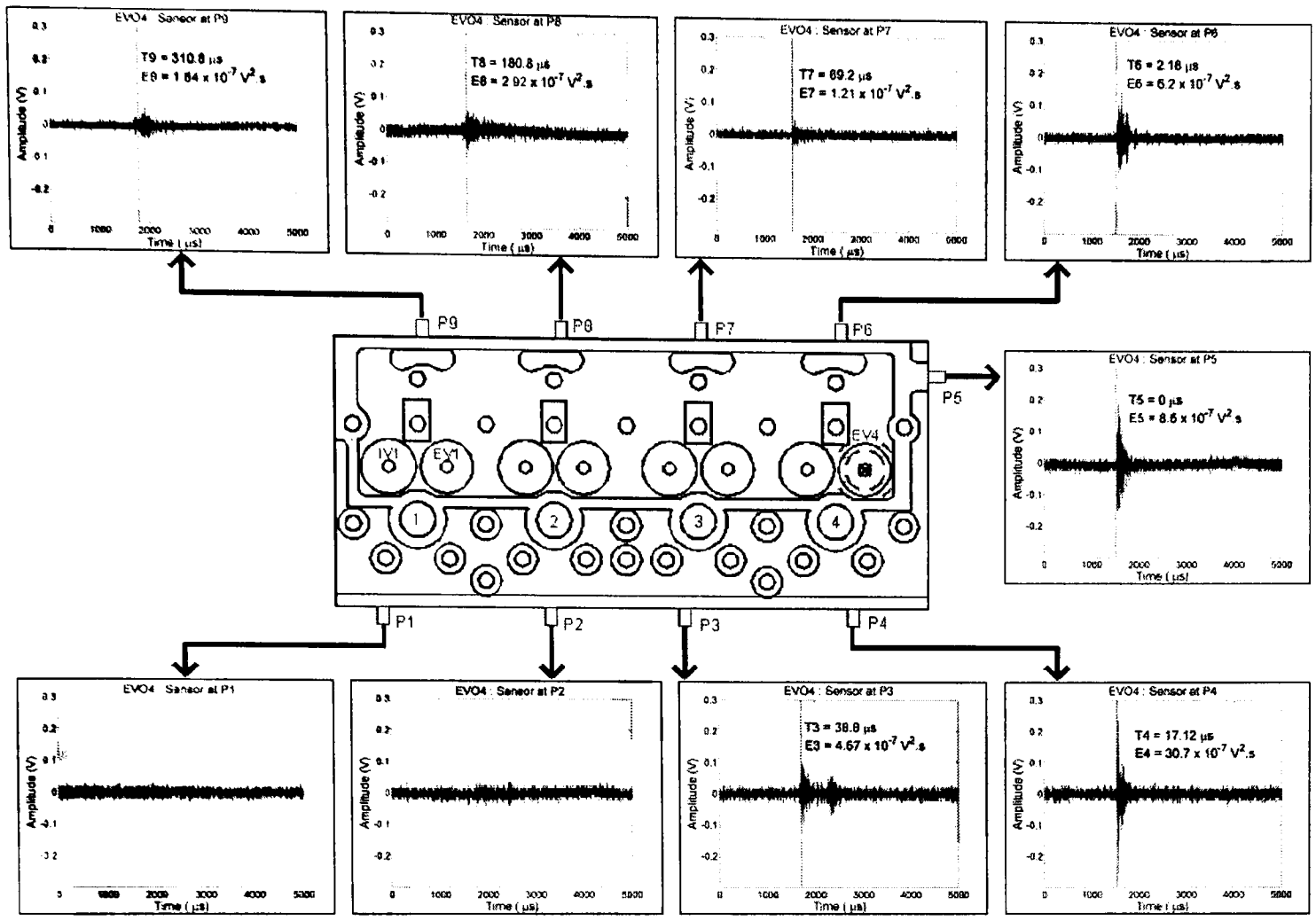

Figure 7.10: Schematic plot of normalised EVO event at cylinder no. 4 acquired using the sensor array on the cylinder head (P1-P9) from the diesel engine running at 800 rpm with no load (after adjusting valve clearance).

In order to use this data to source locate, the attenuation factors for the INJ2, INJ4, EVO2 and EVO4 were determined, and in order to allow the maximum number of simultaneous AE recordings, shaft encoder and TDC signals were not used in these last experiments so the window of each event was chosen by inspection and then the attenuation factor was calculated using the method described in Section 5.2.1, with a threshold value of 1.5 of maximum noise amplitude. Source-sensor distances used were the same as those used in the transmission tests on the cylinder head described in Section 5.4.1. The SNR was also considered in order to eliminate weak signals and the value of the SNR against sensor position for each event can be seen in Figure 7.11, where the SNRs for the INJ2 and INJ4 events are everywhere greater than 2 whereas they are less than 2 at some sensor positions for EVO, for example P1, P4 and P5 for the EVO2 event and P1 for the EVO4 event. Using an SNR over 2 as a minimum requirement, the attenuation factors for each event were determined (Figure 7.12) to be around 11 for INJ events and around 6 for EVO events. These attenuation factors will be used for source location using the energy-based technique and for signal reconstitution. In addition, the sensor positions, P1 to P9 shown in Figure 7.12 represent

sensor positions on the cylinder head array for INJ4 events which will be used in discussion for signal reconstitution.

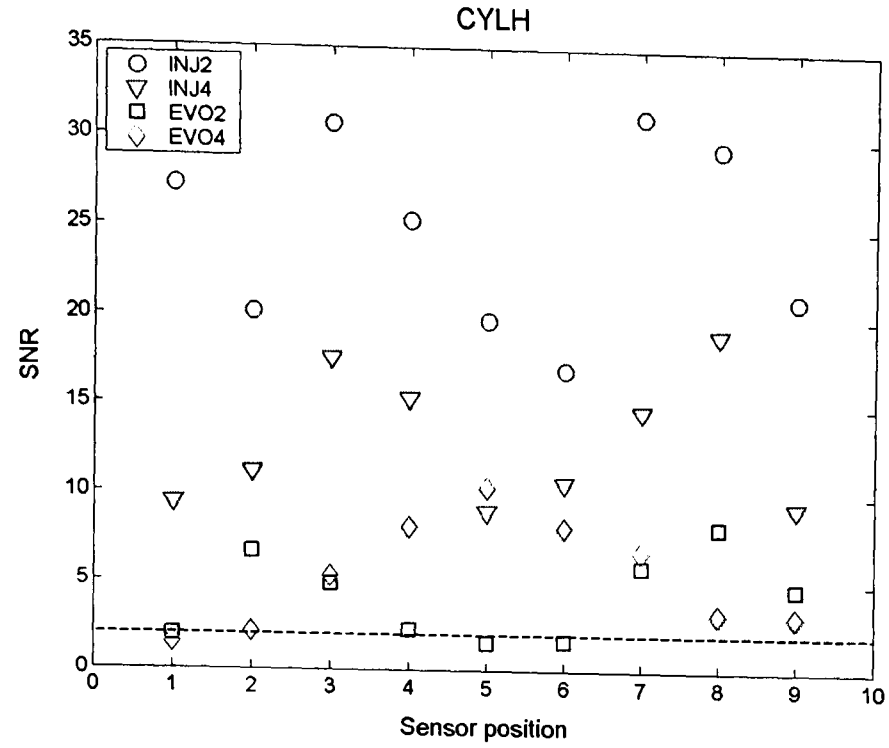

Figure 7.11: SNR versus sensor position for the INJ2, INJ4, EVO2, and EVO4 events.

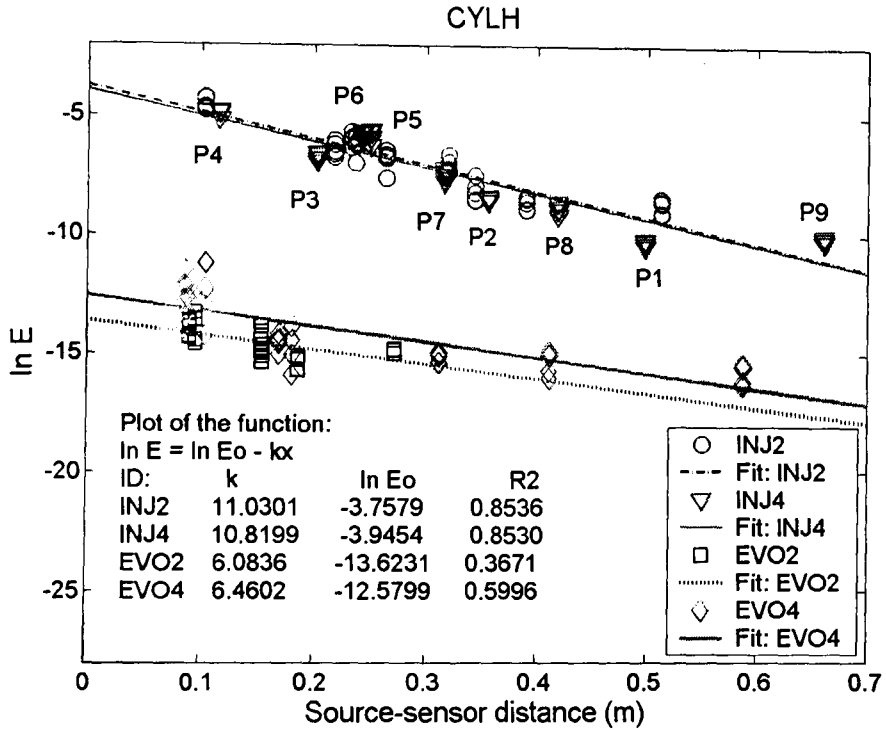

Figure 7.12: Energy, as $\ln(E)$ versus source-sensor distance and the coefficients from best-fit straight lines for the INJ2, INJ4, EVO2, and EVO4 events.

The triangular arrays used for source location are the same as in the previous section; sensor positions at P1, P4 and P8 for the INJ2 and EVO2 events and sensor positions at P5, P6 and P4 for the INJ4 and EVO4 events. Figure 7.13 shows plots of SNRs for the various sensors and events considered. The data relating to the EVO2 event acquired at P4 had an SNR below 2 and was not used in Figure 7.14.

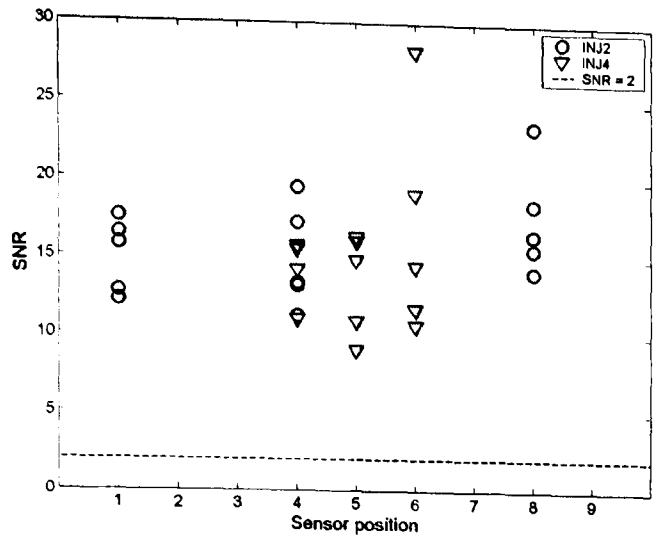

(a) The injector events

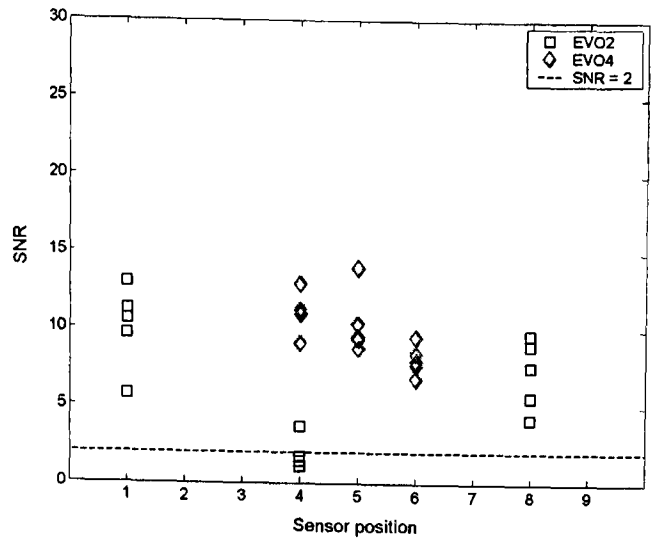

(b) The EVO events

Figure 7.13: Plot of SNR (for the INJ and EVO events of cylinders nos. 2 and 4) versus sensor position for the signals acquired from two triangular arrays (P1-4-8 and P5-6-4).

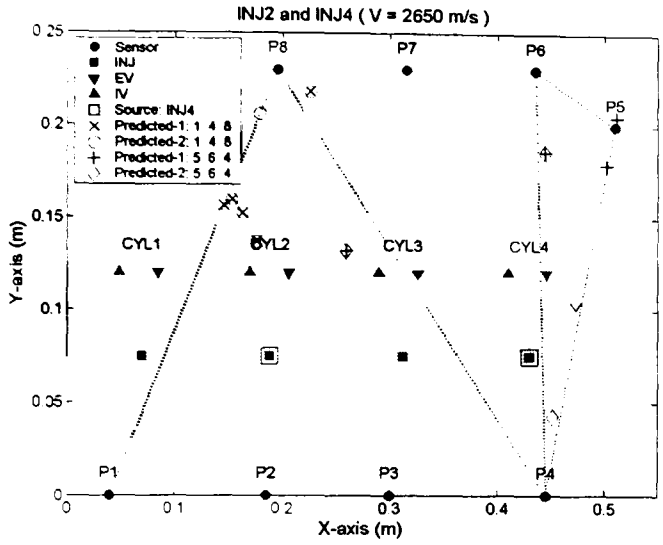

(a) Source at injectors (▣)

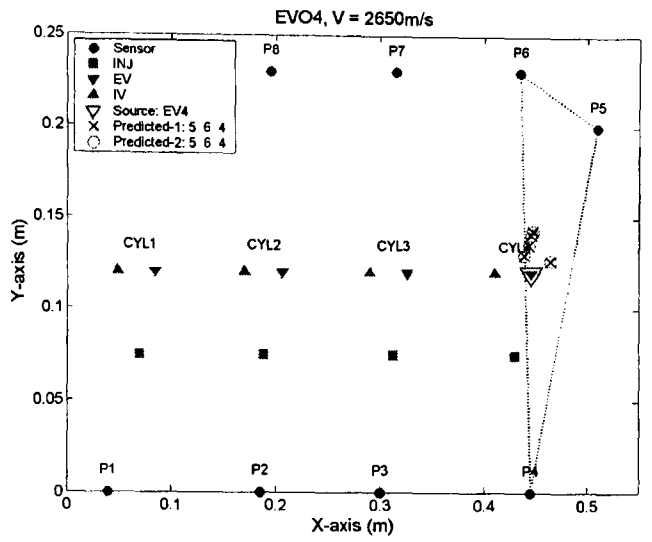

(b) Source at exhaust valves (▽)

Figure 7.14: Velocity-based source location technique using triangular arrays on the cylinder head for engine running tests at speed of 800 rpm with no load.

The results of source location using the velocity-based technique for the engine running at 800 rpm with no load can be seen in Figure 7.14. The arrival time of each signal was determined using the threshold crossing technique with a threshold value at 0.2 of maximum amplitude and a wave speed of 2650 m/s. The predicted locations of sources shown in the plot were calculated for 5 engine cycles are generally much further from the actual source than for the simulated source, especially for the INJ events. This may be because the injector events are combination of multiple sources and effects of wave attenuation, reflection, refraction and mode conversion may have distorted the AE signals. In Figure 7.14(b), the source at the EVO4 can be located rather more accurately because the AE waves generated had a sharp rising edge (short rise time) which probably comes from the exhaust valve opening impact and high pressure fluid flow during valve opening, so that the arrival time may be detecting the same wave modes.

The errors are summarised in Table 7.2; another factor contributing to these errors may be that the wave speed is still that used for the simulated source, which would lead to a systematic error if the real source were to be at a different location to the simulated one.

Figure 7.15 shows the results of source location using the energy-based technique for the same arrays as mentioned before, the predicted locations again having been calculated from 5 cycles. The calculation method used was the same as discussed in Section 7.2.2 for the simulated source, and used the individual attenuation factors obtained for each source location (INJ2, INJ4 and EVO4) shown in Figure 7.12. As can be seen, this method is much more accurate than the velocity-based approach, although the location of EVO4 is poorer, probably because the energy variation between cycles for EVO events is much larger than for INJ events (Figure 7.12) resulting in a larger random error.

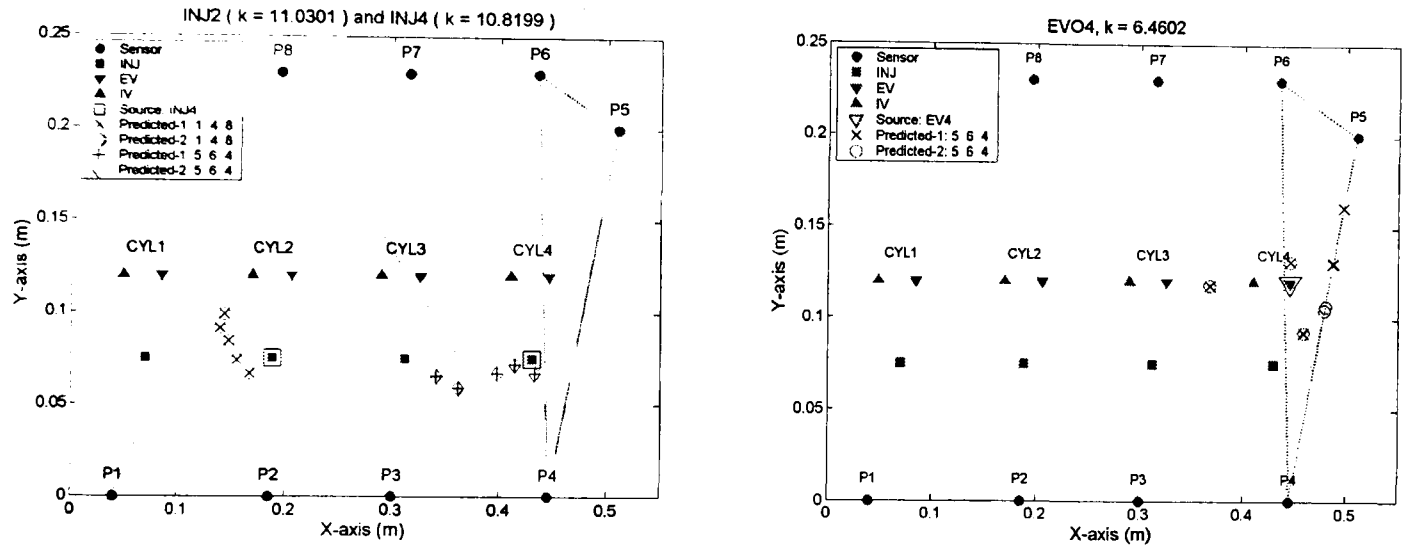

(a) Source at injectors (■) (b) Source at exhaust valves (▼)

Figure 7.15: Energy-based source location technique using triangular arrays on the cylinder head for engine running tests at speed of 800 rpm with no load.

Source	Array	Arrival time difference technique				Energy difference technique			
		Speed	Source location error (mm)			k	Source location error (mm)		
			Mean	Max	Min		Mean	Max	Min
INJ2	P148	2650	96	148	63	11.0201	40	51	23
INJ4	P564	2650	165	205	111	10.8199	43	89	8
EV4	P564	2650	18	23	12	6.4602	41	79	11

Table 7.2: Summary of error in source location using data acquired from engine running tests with a sensor array on the cylinder head.

Overall, in the case of multiple sources, better results are obtained for source location using the energy-based technique because this technique concentrates on energy content of the entire event and is not so dependent on precise identification of arrival time. In

addition, the accuracy of both techniques depends on other parameters such as accuracy of the wave speed, attenuation factor or adequate SNR, including the assumptions made in the determination of the fundamental location parameters, attenuation factor and velocity.

7.3 Application to Signal Reconstitution

Typical AE signals detected on diesel engines are time-series with multiple-source signals which overlap in time and space, and relate to events associated with mechanical moving components (e.g. valves, injectors, bearings, and ancillary equipment) and fluid flow activities (e.g. combustion, fuel injection and gas flow), which all combine to produce complicated signals. The signals can be segmented and mapped onto various events associated with the injection process, the combustion process, and valve operations as has been described in Chapter 6. It is clear that the detected signals (or events) attenuate as distance from the source increases and that the time-of-flight also increases directly with distance. The stronger signals contain more detailed information about each process, especially for sensors placed closer to the sources, although other, lower intensity signals may contain some useful information as well. Signal reconstitution should help to enhance the resolution of the signals and also improve diagnostic outcomes. In a practical deployment, only a few sensors are likely to be used and signal reconstitution will enable optimisation of the array positions chosen.

7.3.1 Signal reconstitution technique

As already noted, the signals acquired from the cylinder head array (P1-P9) shown in Figures 7.8-7.10 attenuate as distance from source increases and the time-of-flight also increases with distance. For signals acquired at relatively large distances such as the INJ4 event recorded at P1 shown in Figure 7.8, it may be possible to obtain more information from this signal by reconstituting it to the "original" source at INJ4 or at least to the signal recorded at the sensor placed closest to the source (in this case, at P4). Pelesskaya and Vangeli [109] have used a mathematical model to reconstruct an AE signal from a single source from a signal received at a sensor, concentrating on the effect of AE wave attenuation and a single reflection from a boundary. However, it is impractical to use this method to reconstitute the multiple-source signals which are typical in diesel engines. Steel and Reuben [12] have suggested that the process of

signal reconstitution requires adjusting the timing and signal amplitudes which could be implemented using time-of-flight, a model for the transmission path (distance), an attenuation factor and knowledge of machine operation. Here, we wish to reconstitute a signal acquired at a sensor placed close to a source (P1 at distance x_1) from another signal acquired at a sensor placed further from the source (P2 at distance x_2), as illustrated schematically in Figure 7.16. Two processes are applied, being the adjustment of amplitudes and of timing, using the fundamental parameters, attenuation factor, k, and velocity, c. Amplitudes for the reconstituted signal can be determined using the energy-based technique (Equation (7.14)).

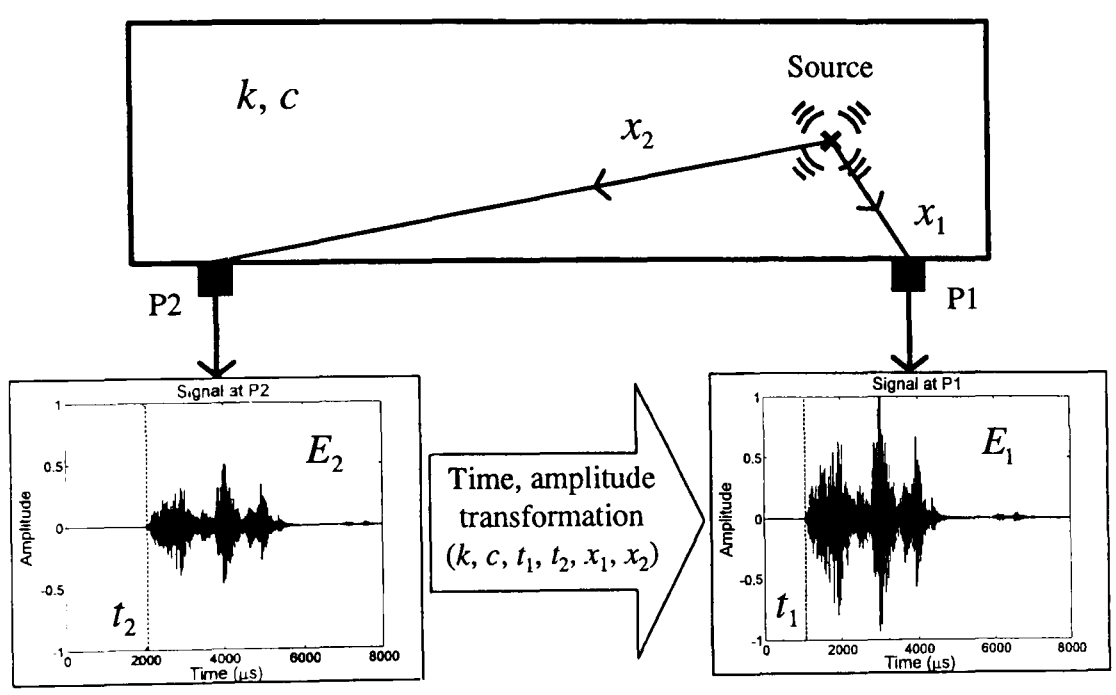

Figure 7.16: Schematic diagram for signal reconstitution from P2 to P1 and various parameters.

The energy content of each signal can be determined using Equation (3.14), (although, it can also be determined using Equation (3.15)). Thus, the energy content for each signal becomes

$$E_1 = \int A_{1i}^2(t)dt = E_o \cdot e^{-kx_1} \tag{7.11}$$

$$E_2 = \int A_{2i}^2(t)dt = E_o \cdot e^{-kx_2} \tag{7.12}$$

where E_1 and E_2 are energy content for the signals acquired at P1 and P2;

$A_{1i}(t)$ and $A_{2i}(t)$ are amplitude of the signals at time, t;

E_o is a constant apparent source energy;

k is the attenuation factor;

and x_1 and x_2 are source-sensor distances.

Using Equations (7.11) and (7.12), the energy ratio between the signals is determined so that the reconstituted signal from P2 at P1 can be obtained:

$$\frac{E_1}{E_2} = \frac{E_o \cdot e^{-kx_1}}{E_o \cdot e^{-kx_2}} = e^{k(x_2 - x_1)}$$

$$E_1 = e^{k(x_2 - x_1)} \cdot E_2 \tag{7.13}$$

By substituting E_1 and E_2 from Equations (7.11) and (7.12) into Equation (7.13), the amplitudes of the reconstituted signal at P1 from a record at P2 can be obtained:

$$\int A_{1i}^2 dt = e^{k(x_2 - x_1)} \cdot \int A_{2i}^2 dt = \int \left(\sqrt{e^{k(x_2 - x_1)}} \cdot A_{2i} \right)^2 dt$$

$$A_{1i}^2 = \left(\sqrt{e^{k(x_2 - x_1)}} \cdot A_{2i} \right)^2$$

$$A_{1i} = \sqrt{e^{k(x_2 - x_1)}} \cdot A_{2i} \tag{7. 14}$$

To adjust timing, the arrival time of each signal (t_1 and t_2) is determined using, for example, a threshold crossing technique and the reconstituted signal can be adjusted using the arrival time difference between the signals at t_2 and t_1.

The reconstitution error percentage (REP) can be used to measure performance of the signal reconstitution process. By segmenting the original and reconstituted signal into N time windows, the RMS energy of each window can be calculated using Equation (2.2). Thus, by comparing the RMS energy for each window, the REP can be obtained from:

$$REP(\%) = \frac{\sum_{i=1}^{N} \left| Erms_{1i} - Erms_{2i} \right|}{\sum_{i=1}^{N} Erms_{1i}} \times 100 \tag{7.15}$$

where $Erms_{1i}$ and $Erms_{2i}$ represent RMS energy in each window, $i = 1,2,3,...,N$ for the original signal and reconstituted signal, respectively. Obviously, the REP will depend upon the window width.

The next two sub-sections demonstrate respectively, signal reconstitution applied to the injector event for the small HSDI engine and the scavenging port event for the large marine diesel engine.

7.3.2 Signal reconstitution for HSDI diesel engine

This section demonstrates the signal reconstitution technique applied to the small HSDI diesel engine focusing on the INJ4 event acquired using the cylinder head array. To reconstitute the signal at P4, each of the other signals in the array was acquired with reference to P4 as described in Section 4.4.5 in order that reconstituted signals could be obtained for the same cycle as the reference. Figure 7.17 shows the results of reconstitution of signals from P1-P3 and P5-P7 and P8-P9 to the signal at P4 of which there are three separate examples. Three signals are shown in each plot, which are the original signal detected at P4, the original signal detected at each sensor and the reconstituted signal. Equation (7.14) was used to adjust amplitude for each reconstituted signal using the relevant attenuation factor shown in Figure 7.12 ($k = 10.8$) and using the same source-sensor distance as was used for calculating the attenuation factors. For the timing adjustment, the threshold crossing technique was used to determine the arrival time of each signal using a threshold value at the mean of each enveloped signal. Using the arrival time difference, all the signals shown in Figure 7.17 were adjusted with reference to P4.

The signal at P4 varies slightly from cycle to cycle and can have 3 or 4 main peaks as seen in the three examples in Figure 7.17. The reconstituted signals appear consistent for sensors placed close to the source, such as at positions P5 and P6. The medium distance signals from P7, P8 and P9 seem to give reasonable reconstitution, whereas for positions P1, P2 and P3, it appears that the signals can be reconstituted best for the first two peaks while the other two peaks seem to have been lost. This may be because of different attenuation factors for different sources, different transmission paths, or other effects of AE wave propagation, including differential attenuation with frequency (structural filtering), reflection, refraction and mode conversion, all of which will lead to greater distortion at longer distances.

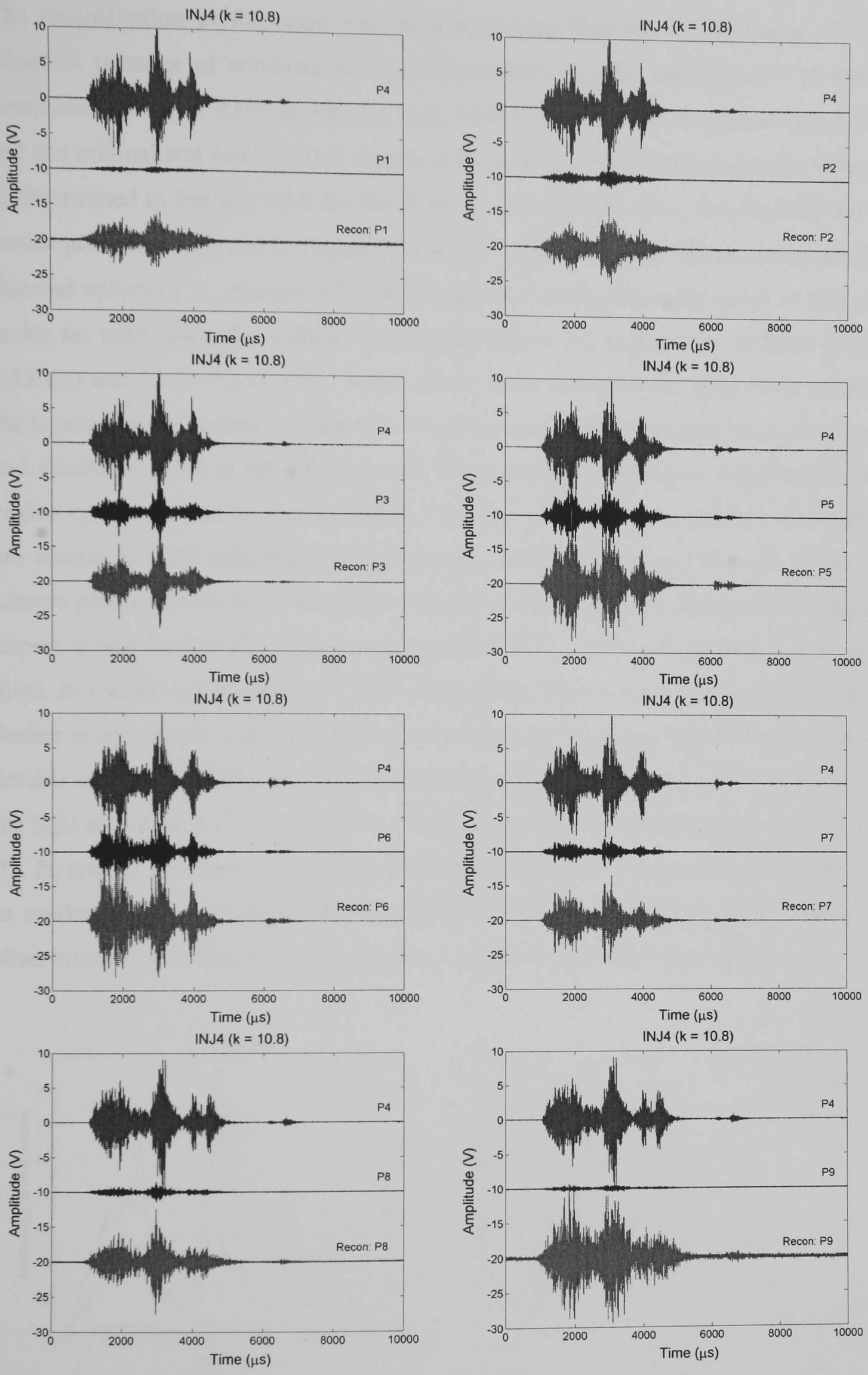

Figure 7.17: Reconstituted signals for the INJ4 event from the cylinder head array.

The reconstitution performance was calculated using Equation (7.15) using $N = 50$ windows (number of windows for calculating RMS energy), and Figure 7.18 shows comparison plots of RMS energy for each window between the reference signal (P4) and the original and reconstituted signals at P1 and P5, respectively, using the value of k determined in Section 7.2.3 for the INJ4 running engine source, and the REP for all sensor positions is shown in Figure 7.19 which also shows REP values obtained using selected values of k, namely 9.3 (for the engine running tests with speed at 800 rpm under no load using the cylinder head array where the source was at INJ4 (Figure 6.15(a))) and 13 ($\approx 9.3 \times 1.4081$) which is the value corrected for slow wave speed of the injector events shown in Table 5.5. The error bar shown represents mean, maximum and minimum value of the REP for each sensor position which was calculated from 5 engine cycles. As can be seen in Figure 7.19, the REPs for the unreconstituted signals are around 35-95% indicating large differences and it is clear that they are poorer for sensors placed further from the source. Using $k = 10.8$, the reconstitution of the signals improves and the REPs generally vary around 20-60%. Neither of the other values of k gives an overall improvement in REP although the higher value tends to improve the further array signals and the lower tends to improve the closer signals (both with the notable exception of P9). The improvement in REPs using $k = 10.8$ should be seen in the light of Figure 7.12, where P1, P2, P3, P7 and P8 lie below the best-fit line whereas P5, P6 and P9 lie above. This observation suggests that there is a limitation in REP due to random error, a situation which could be improved by increasing the number of observations for k and by averaging over a number of cycles for reconstitution.

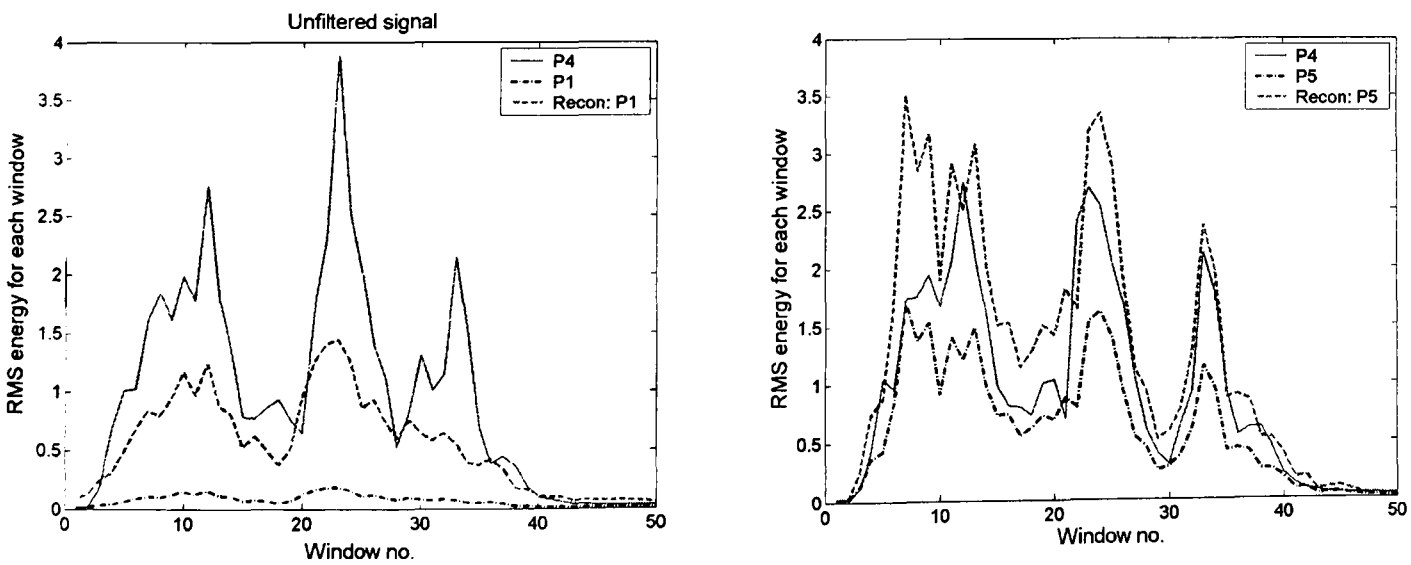

Figure 7.18: Example plots of RMS energy at each window for original (P4) and reconstituted signals (P1 and P5) using $k \approx 10.8$.

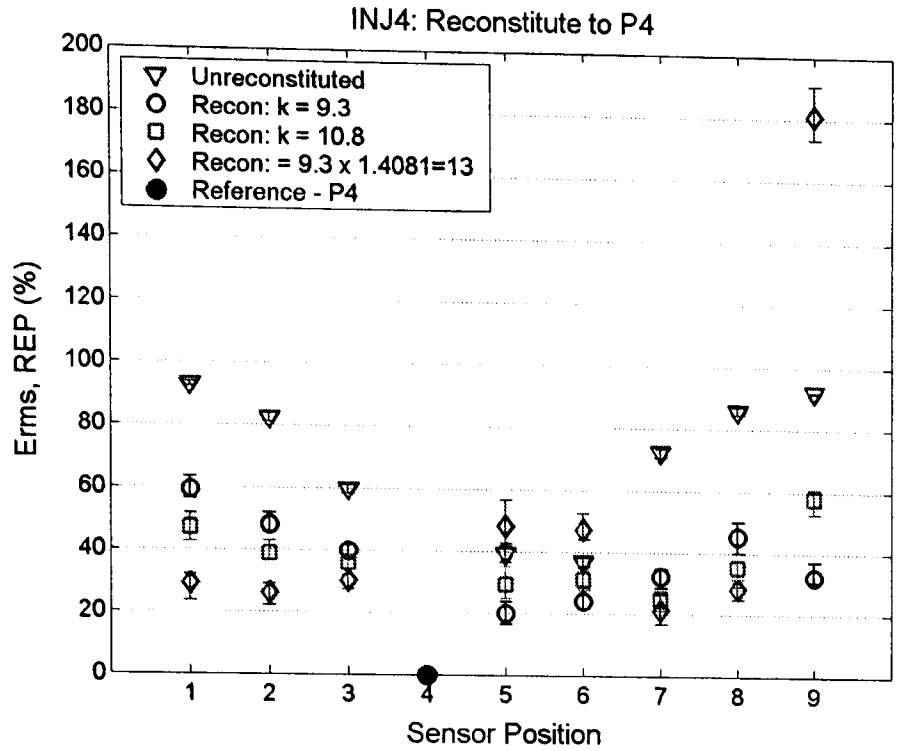

Figure 7.19: Comparison of REP for reconstituted signals using various attenuation factors

It is possible that further improvements in reconstitution might be possible by allowing variable attenuation in the frequency domain. For example, it is clear that the initial stage (up to window 10) of the signal at P5 is less heavily attenuated than the rest and that much of the error is associated with over-correction up to window 10. This might be because of lower attenuation of the high frequency component of the first part of the INJ signal (Figure 6.2.2). If the higher frequency component were to have a different attenuation factor, the use of an averaged (over frequency) attenuation factor could account for this distortion obtained.

7.3.3 Signal reconstitution for large marine diesel engine

This section shows a demonstration of the technique developed in Section 7.3.1 to reconstitute signals for the large marine diesel engine. The mechanical and fluid flow activities related to a two-stroke cycle have been discussed in Section 6.4, and the scavenging port signal was chosen to demonstrate the possibility of signal reconstitution on a scale up application because it was the most consistent event between cycles thus minimising the difficulties with averaging alluded to in the small engine. It is thought that the sources are generated near BDC and are due to the piston rings passing the scavenging ports as illustrated in Figure 4.15 and some attenuation data for this event was already available [124]. This signal was detected at the sensors placed on the upper and lower part of the exposed area of the liner as mentioned before (Section 6.4) and the stronger signal was acquired at the lower sensor position. In this case, the scavenging

port lower liner (LL) signal can be reconstituted from the upper liner (UL) signal as shown in Figure 7.20, using Equation (7.14), with the attenuation factor for the scavenging port event, $k \approx 2$ as shown in Figure 6.26, and using a transmission path estimated from drawings. The unreconstituted signals at the LL and UL positions are shown in Figure 7.20 along with the reconstituted LL signal derived from the UL signal for 6 different engine cycles. Again, the REPs were determined from Equation (7.15) using 50 windows and it was found that the REPs of the reconstituted signal improved by around 5% (REP $\approx$ 29-36% and 24-34% for unreconstituted and reconstituted signals, respectively). This signal improvement may be because both of the sensors were placed quite far from the source and so the signal reconstitution did not improve as much as seen in the injector signal for the small diesel engine. Further work could be carried out to acquire scavenging port signals at sensors placed close to the scavenging port with consequent improvement of signal reconstitution, but this is not discussed further here. The unreconstituted and reconstituted signals for the six examples are similar although, in some cases (the last two plots in Figure 7.20), the UL signal appears to be contaminated with other sources which may come from areas such as the cooling water pipe around upper parts of the liner or the exhaust valve port. There are other differences between the signals acquired at the different locations which may indicate multiple sources not all in the same place.

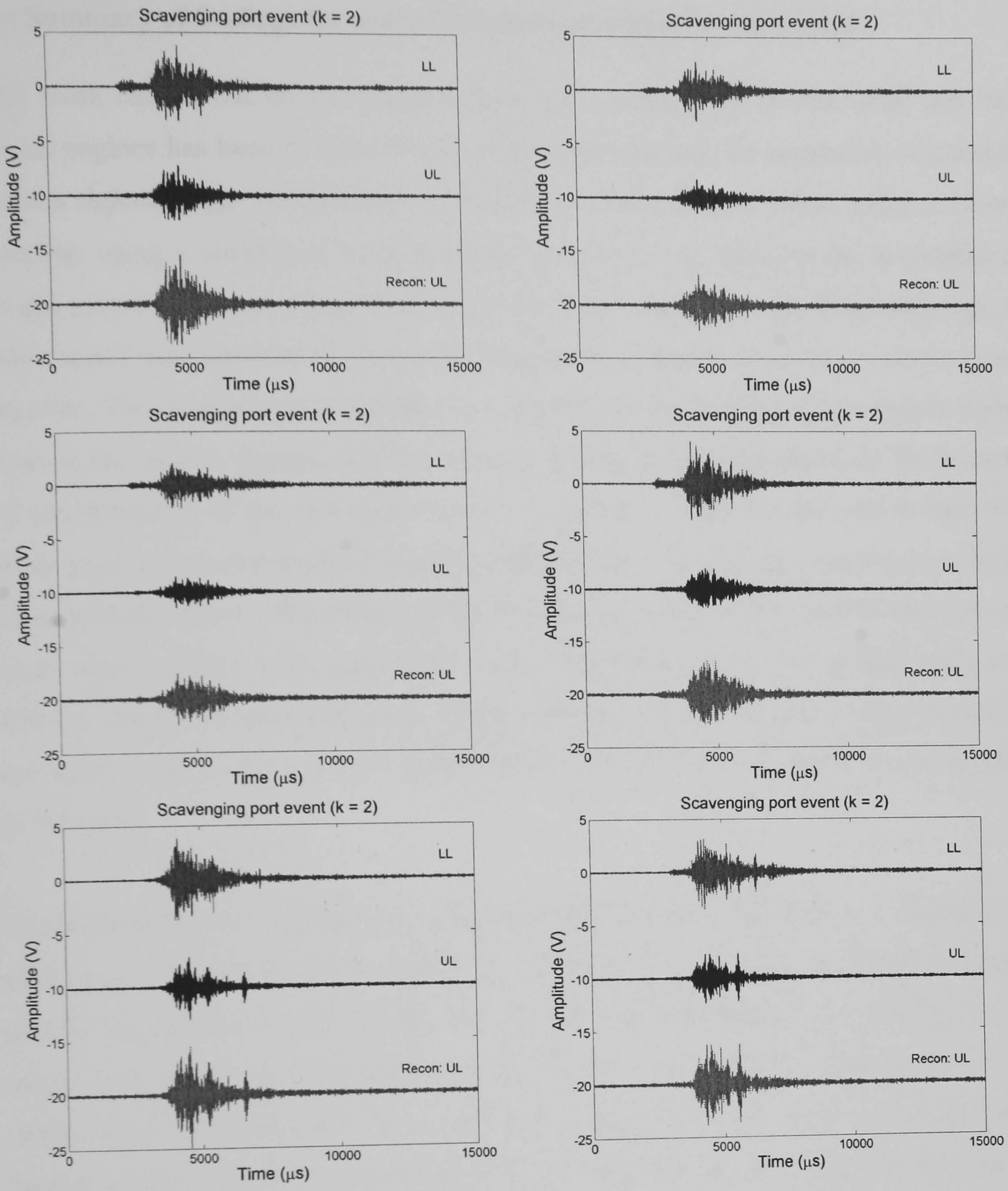

Figure 7.20: Reconstituted signal for scavenging port event on a large marine diesel engine.

7.4 Summary of findings for source location and signal reconstitution.

The work carried out on transmission tests and running tests on the small and large diesel engines has been developed here to demonstrate how the resolution of multiple-source signals might be enhanced for condition monitoring of diesel engines. Source location using a traditional velocity-based technique was found to be successful for single source signals or segments with a sharp rising edge (short rise time), although the wave speed used needs to be known for the particular structure to allow accurate source location. The energy-based technique was found to be useful for multiple-source signals such as the injector signals, and the accuracy of this technique depends on the accuracy of determination of the attenuation factor. In addition, SNR can be used to eliminate weak signals from the analysis avoiding false alarms which might otherwise be caused by amplifying noise. The source location techniques have been demonstrated on the small diesel engine with geometries and boundaries which are complicated, and, whereas results are generally good, further research on the effects of frequency and on averaging would improve the performance and accuracy of both source location techniques.

Signal reconstitution has also been demonstrated, and has been shown to improve the resolution, of multiple-source signals in the time and space domains. By segmenting specific signals, these could be reconstituted from a remote position to one closer to the source, and hence of high fidelity, by adjusting amplitudes and timing. The results clearly show the possibility of reconstituting signals for both small and large diesel engines so that optimum information can be obtained from the detected AE signals, although, again, further work on averaging and differential frequency effects could improve performance.

Chapter 8 Discussion, conclusions and future work

8.1 Discussion and conclusions

As presented in the preceding chapters, this work has developed techniques to handle semi-continuous, multiple source AE signals using sensor arrays. In particular this research has:

- developed an AE attenuation model for wave propagating on diesel engines using a simple absorption law,
- developed a means of segmenting (mapping) the signals from running engines in time and space so that individual events in the engine cycle can be identified and located, and
- developed techniques for enhancing the resolution of multi-source signals from running engines using attenuation factors and time-of-flight, called "spatial reconstitution".

AE was already known to be a useful tool for monitoring of diesel engine conditions such as exhaust valve leakage, head gasket leakage, combustion, injector faults and liner scuffing. Typical signals detected during engine operation are multiple-source signals coming from mechanical and fluid flow activities during the engine cycle such as injectors, valves, combustion, and ancillary equipment. The attenuation of AE has been reported qualitatively by Gill *et al* [6], El-Ghamry *et al* [7] and Douglas *et al* [21] but no systematic studies of this attenuation have been investigated on diesel engines. For such complex structures, AE wave propagation is complicated and distortion can occur due to the effects of scattering, absorption, dispersion, reflection, refraction and mode conversion at microstructural features, interfaces and boundaries. In this research, the attenuation of AE energy was handled using a simple absorption law to determine attenuation factors based on studies using simulated and real sources. Some simple and more advanced signal processing techniques have been developed to segment the signals and extract information such as attenuation factors, time-of-flight, wave speeds and transmission paths and these were used to improve resolution of multiple-source signals for diesel engines. The results have been applied to source location and signal

reconstitution which has been demonstrated on small HSDI diesel engines and a large marine diesel engine.

The detailed conclusions from the transmission tests on various simple and complex cast iron objects are:

- The attenuation of AE energy propagating through cast iron objects can generally be modelled using a simple absorption law where AE energy decays as an exponential function with distance as described by Equation (3.15). The attenuation increases as distance from the source increases and more complicated transmission paths and geometries give higher attenuation factors. In structures of small extent, such as the thin, narrow strip, a more "reverberant" wave field led to very low attenuation.
- AE propagation is sensitive to geometrical features such as boundaries of objects where AE energy drops significantly when the wave propagates across webs, corners, edges and discontinuities.
- For the simulated sources used here, AE waves recorded at the sensors have a lower energy, fast wave preceding the main signal which carries the peak amplitude (slow wave). The arrival time difference $(t_2 - t_1)$ between the fast wave and slow wave increased directly with source-sensor distance in all test objects, and the measured fast wave and slow wave speeds were 4500 and 2650 m/s, respectively. Although useful in fundamental studies of propagation, this distinction was of less value when dealing with real sources on engines.
- The frequency content of the AE signals from simulated sources recorded by the sensor used here were predominantly in two frequency bands around 100-200 kHz (low frequency band) and 300-350 kHz (high frequency band). It was found that AE waves in one frequency band, say 100-200 kHz, can convert to another frequency band, say 300-350 kHz at boundaries. In more complicated objects, the higher frequency signal (HF > 300 kHz) energy attenuates more quickly than the lower frequency energy (LF < 200 kHz).

The detailed conclusions from the transmission tests on the small HSDI diesel engines and the large marine diesel engine using simulated sources are:

- Whereas detailed analysis of AE wave propagation in diesel engines would be very difficult not least because the nature of the source is unknown, studies of AE wave speed and attenuation have enabled application of the simple attenuation model for AE energy, and thence to an energy analysis approach.
- It has been found that arrival times of high amplitude slower AE waves can be measured relatively accurately. Measuring these arrival times and assuming the wave speed determined in the simple structures allows calculation of source-sensor distance.
- By plotting AE energy level against calculated source-sensor distance, it has been possible to determine effective attenuation factors. Good correlation between measured data and the best fit logarithmic decay has been found where k is typically around 8 to 12 for the small engine block and source positions considered here, and around 2 for the large engine structure.
- In this work, the most consistent method was to use the slow wave speed (2650 m/s) and arrival time difference between detected signals to estimate source-sensor distances for various sources and sensor arrays. It was found that the distances so measured were longer than the 3D straight-line (the reference distance).
- For source positions on the cylinder head, attenuation factors for the signals acquired at various sensor positions around the cylinder head were more consistent and the better correlated. As the sensor array is moved down the cylinder block, away from the sources, the measured attenuation factors tend to decrease slightly.
- It is clear that some of the AE propagates from the cylinder head sources to the cylinder block array positions by passing through the cylinder head bolts. However, the transmission of AE energy has been found to increase directly as the bolts are tightened to an increasing torque, but even at full tightening there is a significant drop in transmitted AE energy at this interface. This is in good agreement with Shao and Mechefsake [121] who found that attenuation of vibration signal increased as number of tight interfaces (number of beams in stack) increased. The attenuation of signals in the vertical direction is generally greater than in the horizontal direction.
- In the case of AE propagation through the engine with water inside the water gallery, the attenuation was slightly higher than without water. Since the times of flight are similar, it is concluded that the added water increases the "losses" from the system but the dominant transmission paths are through the cast iron structure of the engine block.

- When the technique was applied on the cylinder liner of the large marine diesel engine, attenuation factors of 2-2.3 were found, and, when applied to the whole engine structure values were between 2.5 and 2.8. The lower attenuation in the large structure is attributed to the lower geometric complexity per unit propagation distance.

The detailed conclusions from the engine running tests on the small HSDI diesel engine and the large marine diesel engine are:

- The detected AE signals emanate from a number of sources associated with mechanical and fluid flow processes during the engine cycle, such as injection, combustion and valve operation processes, including other moving components related to the engine cycle. The signals can be mapped from the time domain onto the crank angle domain using a reference signal such as a crank angle encoder and TDC pulses so that the mechanical events during the engine cycle can be identified. The injector and EVO events were the most consistently detected for all sensor positions, and the signals varied in nature depending on the condition of the injectors and the exhaust valves. The other valve operation events were observed at some sensor positions, although they were not consistent and had a poor signal to noise ratio. It is interesting to note that, for the sensor positions lower down the cylinder block, some other events related to the engine cycle could also be detected in the signals, although their detailed identification was not pursued.
- Using the absorption model, attenuation factors for the injector and EVO events could be determined for a given source using a suitable window in the crank angle domain. The most consistent results were for the cylinder head array where similar results to those in the transmission tests using the simulated source were found. The SNRs of the signals needed to be used to eliminate weak signals in order to improve the correlation of the model for attenuation factors, which were around 8-10 for the injector events and 5-7 for the EVO events.
- Time-frequency analysis was used to reveal the mechanical and fluid flow activities for the injector and EVO events. It is thought that the low frequency band signals around 100-250 kHz are associated with mechanical impact and that the high frequency signals around 250-400 kHz are associated with fluid flow activities during the engine cycle.

- The techniques developed to analyse the signals acquired from the small diesel engine was applied to analyse signals from the large marine diesel engine. Attenuation factors could also be determined using the absorption model applied to the most consistent events yielding results similar to the transmission tests with simulated sources.

The detailed conclusions from the application of source location on the small HSDI diesel engines and signal reconstitution for the small and large diesel engines are:

- Source location using velocity-based and energy-based techniques using triangular sensor arrays to determine the intersection of two hyperbolae was found to be possible for sources on the cylinder head of the small diesel engines using an array on the cylinder head. The energy method was found to be generally a little less successful from the velocity-based technique for simulated sources.
- Source location using the velocity-based technique is most effective for single source signals with a sharp rising edge (short rise time) and the accuracy of predicted location depends on accuracy of arrival time, a good SNR and known wave speed.
- The energy-based source location technique is better for multiple source signals because it is not directly dependent on arrival time measurement and wave speed. Using an appropriate attenuation factor and the energy content of the entire signal, it is possible to determine the location of the source and the accuracy depends on the attenuation factor.
- Signal reconstitution can be used to enhance resolution of multiple-source signals for the small and large diesel engine applications. By using time-of-flight, attenuation factor, transmission path length and the absorption model, a signal can be reconstituted to its source and this was demonstrated for a subset of the data.
- The success of source location and reconstitution would appear currently to be limited by random error in the absorption features and could also be potentially improved by accounting for differential frequency effects.

The main aim of this work has been achieved in that a relatively simple model of AE propagation (characterised by a single wave speed and a single attenuation factor) has

been developed and applied to simple and complicated structures such as the cylinder head and the cylinder block of diesel engines. The AE energy, wave speed, time-of-flight and source-sensor distance estimation have been described and used successfully on applications of source location and signal reconstitution on diesel engines.

The techniques developed here can be used to study attenuation of AE waves propagating in other type of engines as well as machinery in order to enhance information obtained from detected signals. It is uneconomical to use individual sensors placed close to each source for a real application and this work will allow optimisation of sensor arrays and improved resolution of multiple-source signals obtained during machine operation. For example, in application to a large diesel engine, it may be possible to monitor the condition and performance of each cylinder using a single AE sensor placed on the cylinder liner or the cylinder cover but only once the detailed source-sensor relationship are known. Source location techniques (velocity based and energy based) using a triangular array make it possible to locate sources on complicated structures such as the cylinder head of small diesel engines and this could be extended for signal mapping and source location using AE on other machinery such as compressors. The findings of this work, together with existing AE monitoring knowledge will also enable future developments of engine management systems to monitor conditions and improve performance of engines.

8.2 Future work

The following recommendations are suggested for further research:

- The measurement of transmission path length on the 3D engine blocks: The attenuation factor is one of the main parameters used here to study AE wave propagation, source location and signal reconstitution on the diesel engine block. It is possible to use 3D solid modelling and ray tracing techniques [125] to determine possible transmission paths from source to sensor arrays in order that transmission paths can be more quantitatively modelled to improve the accuracy of the attenuation factor. There is also scope to reduce the random error in path determination and to account for differential frequency effects.

- The measurement of needle valve position: Simultaneous measurement of needle valve position, fuel line pressure and raw AE signal from the injector process would help to elucidate the various processes occurring during the injector events. With this information, it may then be possible to extract more information of the mechanical and fluid flow activities inside injectors and other related components using other advanced signal processing techniques.
- Frequency filtering: The typical AE signals acquired from diesel engines are multiple-source signals (i.e. mechanical and fluid flow activities) such as injector signals. Using frequency filtering techniques, it may be possible to separate flow-related and mechanical elements of complex events.
- Reconstitution of engine running signals: The signal reconstitution has shown the potential to improve resolution of multiple-source signals. It may be possible to implement the signal reconstitution technique to monitor fault conditions in diesel engines simply by searching for out-of-normal signatures. Such an approach requires long-term monitoring of reconstituted signals.
- Cylinder pressure reconstitution: The power output of an engine is an indicator of performance. It has been shown that the AE signal can be used to reconstruct a cylinder pressure waveform [23]. For AE signals acquired from small diesel engines, it may be possible to reconstitute the pressure for each cylinder using a pressure reconstruction technique involving the attenuation model and a reconstitution of the AE signal so that the power output of each cylinder can be monitored.
- Piston ring and liner interaction: Liner scuffing which tends to affect large-bore engines, can reduce the engine compression ratio and the power output. It may be possible to use a source location technique to determine location of scuffing and piston ring/liner interaction [21] in a cylinder liner. Equally, good reconstitution of other sources would allow their subtraction from the signal leaving behind the cylinder liner interaction signal.
- Engine management: The techniques developed for monitoring using AE have been shown to have the capacity to yield useful information indicating performance as well as faults for diesel engines. With clear approaches to reconstitution, it should be possible to implement an on-line engine management system using AE based techniques and artificial intelligence techniques such as pattern recognition and neural networks to enhance performance of diesel engines.

- Valve performance: Although valve signatures on the small engines are weak relative to the injector signatures, it is clear from the changes once clearances were adjusted that useful information can be obtained. It is worthwhile, therefore, pursuing the effect of valve clearance and leakage on signals on the basis that valves should normally be "silent", any signature being indicative of an out-of-normal condition.

References

[1] BSI, "Condition monitoring and diagnostics of machines - Vocabulary," *British Standard, BS ISO 13372:2004*, 2004.

[2] Hutton, R. W., "Condition monitoring - the way forward," *Handbook of Condition Monitoring, 1st Edition*, edited by B. K. N. Rao, Elsevier Science, 1996, pp. 37-48.

[3] Long, B. R. and Boutin, K. D., "Enhancing the process of diesel engine condition monitoring," *Proceeding of Technical Conference, American Society of Mechanical Engineers, Internal Combustion Engine Division (Publication) ICE*, Vol. 27, No. 1, 1996, pp. 61-68.

[4] Gu, F., Li, W., Ball, A. D., and Leung, A. Y. T., "The condition monitoring of diesel engines using acoustic measurements, Part 1: Acoustic characteristics of the engine and representation of the acoustic signals," *SAE 2000 World Congress, Session: Noise & Vibration, Detroit, USA (SP-1514)*, 2000, pp. 51-57.

[5] Ball, A. D., Gu, F., and Li, W., "The condition monitoring of diesel engines using acoustic measurements, Part 2: Fault detection and diagnosis," *SAE 2000 World Congress, Session: Noise & Vibration, Detroit, USA (SP-1514)*, 2000, pp. 57-64.

[6] Gill, J. D., Reuben, R. L., Scaife, M., Brown, E. R., and Steel, J. A., "Detection of diesel engine faults using acoustic emission," *Proceedings of the 2nd International Conference: Planned Maintenance, Reliability & Quality,* 1998, pp. 57-61.

[7] El-Ghamry, M. H., Reuben, R. L., and Steel, J. A., "The development of automated pattern recognition and statistical feature isolation techniques for the diagnosis of reciprocating machinery faults using acoustic emission," *Mechanical Systems and Signal Processing*, Vol. 17, No. 4, 2003, pp. 805-823.

[8] Fog, T. L., Brown, E. R., Hansen, H. S., Madsen, L. B., Sorensen, P., Hansen, E. R., Steel, J. A., Reuben, R. L., and Pedersen, P. S., "Exhaust valve leakage detection in marine diesel engines," *Proceeding of the 11th International Conference on Condition Monitoring and Diagnostic Engineering Management, COMADEM, Australia*, 1998, pp. 269-278.

[9] Gill, J. D., Reuben, R. L., and Steel, J. A., "A study of small HSDI diesel engine

fuel injection equipment faults using acoustic emission," *Proceedings of the 24th European Conference on Acoustic Emission Testing, EWGAE, France*, 2000, pp. 281-286.

[10] Shuster, M., Combs, D., Karrip, K., and Burke, D., "Piston ring cylinder liner scuffing phenomenon studies using acoustic emission technique," *Advances in Powertrain Tribology, SP-1548, SAE*, 2000, pp. 23-35.

[11] Miller, R. K. and McIntire, P., *Non-Destructive Testing Handbook Vol.5 - Acoustic Emission,* American Society for Non-Destructive Testing,USA, 1987.

[12] Steel, J. A. and Reuben, R. L., "Development of condition monitoring of engines using acoustic emission," *Proceedings of the Institution of Mechanical Engineers, Part L: Journal of Strain Analysis for Engineering Applications* (In press 2005).

[13] Pollock, A. A., "Classical wave theory in practical AE testing," *Progress in Acoustic Emission III - JAP Society of Non-Destructive Testing*, 1986, pp. 708-721.

[14] Kolsky, H., *Stress Wave in Solids,* Dover, New York, USA, 1963.

[15] Rao, B. K. N., "Vibration monitoring," *Handbook of Condition Monitoring, 1st Edition*, edited by B. K. N. Rao, Elsevier Science, 1996, pp. 49-80.

[16] Liu, Y., Liu, Z., Xie, Y., and Yao, Z., "Research on an on-line wear condition monitoring system for marine diesel engine," *Tribology International*, Vol. 33, No. 12, 2000, pp. 829-835.

[17] Reuben, R. L., "The role of acoustic emission in industrial condition monitoring," *International Journal of COMADEM*, Vol. 1, No. 4, 1998, pp. 35-46.

[18] Frances, A. K., Gill, J. D., Reuben, R. L., and Steel, J. A., "A study of the variability of acoustic emission signals from a medium size marine diesel engine under service conditions," *Proceedings of the 16th International Congress, Condition Monitoring and Diagnostic Engineering Management, COMADEM, Sweden,* 2003, pp. 503-512.

[19] Douglas, R. M., Steel, J. A., Reuben, R. L., and Fog, T. L., "On-line power estimation of large diesel engines using acoustic emission and instantaneous crankshaft angular velocity," *Submitted to IMechE, Internaltional Journal of*

Engine Research, 2004.

[20] Pontoppidan, N. H., Larsen, J. L., and Fog, T., "Independent component analysis for detection of condition changes in large diesel engines," *Proceeding of the 16th International Conference on Condition Monitoring and Diagnostic Engineering Management, COMADEM, Sweden,* 2003, pp. 493-502.

[21] Douglas, R. M., Hymers, D. A., Steel, J. A., and Reuben, R. L., "Source identification of piston ring and cylinder liner interaction using acoustic emission," *Proceeding of the 17th International Conference on Condition Monitoring and Diagnostic Engineering Management, COMADEM, Cambridge, UK,* 2004, pp. 305-314.

[22] Gao, Y. and Randall, R. B., "Reconstruction of diesel engine cylinder pressure using a time domain smoothing technique," *Mechanical Systems and Signal Processing*, Vol. 13, No. 5, 1999, pp. 709-722.

[23] El-Ghamry, M. H., Performance and condition monitoring of reciprocating machines using acoustic emission, Heriot-Watt University, Edinburgh, UK, 2000.

[24] Koike, N., Kumagai, Y., and Nakamura, K., "Development of detection system for abnormal wear of engine bearings," *JSAE Review*, Vol. 19, No. 1, 1998, pp. 27-32.

[25] Fog, T. L., Hansen, L. K., Larsen, J., Hansen, H. S., Madsen, L. B., Sorensen, P., Hansen, E. R., and Pedersen, P. S. "On condition monitoring of exhaust valves in marine diesel engines," *Neural Networks for Signal Processing - Proceedings of the IEEE Workshop: Proceedings of the 9th IEEE Workshop on Neural Networks for Signal Processing (NNSP'99), USA*, 23-25 Aug 1999, pp. 554-564.

[26] Gill, J. D., Douglas, R. M., Neo, Y. S., Reuben, R. L., and Steel, J. A., "Examination of plate valve behaviour in a small reciprocating compressor using acoustic emission," *Proceeding of the 24th European Conference on Acoustic Emission, EWGAE, France*, 2000, pp. 133-138.

[27] Twiddle, J. A. and Jones, N. B., "A high-level technique for diesel engine combustion system condition monitoring and fault diagnosis," *Proceedings of the Institution of Mechanical Engineers. Part I: Journal of Systems and Control Engineering*, Vol. 216, No. 2, 2002, pp. 125-134.

[28] Twiddle, J. A. and Jones, N. B., "Fuzzy model-based condition monitoring and fault diagnosis of a diesel engine cooling system," *Proceedings of the Institution of Mechanical Engineers. Part I: Journal of Systems and Control Engineering*, Vol. 216, No. 3, 2002, pp. 215-224.

[29] Neill, G. D., Reuben, R. L., Sandford, P. M., Brown, E. R., and Steel, J. A., "Detection of incipient cavitation in pumps using acoustic emission," *Proceedings of the Institution of Mechanical Engineers, Part E: Journal of Process Mechanical Engineering*, Vol. 211, No. 4, 1997, pp. 267-277.

[30] Miettinen, J. and Siekkinen, V., "Acoustic emission in monitoring sliding contact behaviour," *Wear*, Vol. 181-183, No. 2, 1995, pp. 897-900.

[31] Ferguson, I. G., Gill, J. D., Reuben, R. L., Steel, J. A., Brown, E. R., and Roosch, E., "Condition monitoring of rotating seals using acoustic emission," *Proceedings of the 23th European Conference on Acoustic Emission Testing, EWGAE, TÜV Austria, Vienna,* 6-8 May 1998, pp. 281-286.

[32] Gill, J. D., Brown, E. R., Twite, M., Horner, G., Reuben, R. L., and Steel, J. A., "Monitoring of a large reciprocating compressor," *Proceeding of the 11th International Conference on Condition Monitoring and Diagnostic Engineering Management, COMADEM, Australia,* 1998, pp. 317-326.

[33] McFadden, P. D. and Smith, J. D., "A signal processing technique for detecting local defects in a gear from the signal average of the vibration," *Proceedings of the Institution of Mechanical Engineers, Part C: Journal of Mechanical Engineering Science*, Vol. 199, No. 4, 1985, pp. 287-292.

[34] Staszewski, W. J., W. K., and Tomlinson, G. R., "Time-frequency analysis in gearbox fault detection using the Wigner-Ville distribution and pattern recognition," *Mechanical Systems and Signal Processing*, Vol. 11, No. 5, 1997, pp. 673-692.

[35] Dellomo, M. R., "Helicopter gearbox fault detection: a neural network based approach," *Journal of Vibration and Acoustics, Transactions of the ASME*, Vol. 121, No. 3, 1999, pp. 265-272.

[36] Al-Balushi, K. R. and Samanta, B., "Gear fault diagnosis using energy-based features of acoustic emission signals," *Proceedings of the Institution of Mechanical Engineers. Part I: Journal of Systems and Control Engineering*, Vol. 216, No. 3, 2002, pp. 249-263.

[37] Hardman, W., Hess, A., and Blunt, D., "USN drivetrain diagnostics and prognostics development strategy and demonstration," *Proceedings of the 13th International Congress, Condition Monitoring and Diagnostic Engineering Management, COMADEM, Houston, Taxas, USA,* 2000, pp. 287-296.

[38] Neill, G. D., Benzie, S., Gill, J. D., Sandford, P. M., Brown, E. R., Steel, J. A., and Reuben, R. L., "The relative merits of acoustic emission and acceleration monitoring for the detection of bearing defects," *Proceeding of the 11th International Conference on Condition Monitoring and Diagnostic Engineering Management, COMADEM, Australia,* 1998, pp. 643-650.

[39] Choudhury, A. and Tandon, N., "Application of acoustic emission technique for the detection of defects in rolling element bearings," *Tribology International*, Vol. 33, No. 1, 2000, pp. 39-45.

[40] Yoshioka, T., "Diagnosis of machinery using acoustic emission techniques," *Acoustic Emission - Beyond the millennium*, edited by T. Kishi, M. Ohtsu, and S. Yuyama, Elsevier, UK, 2000, pp. 215-230.

[41] Zuluaga-Giraldo, C., Mba, D., and Smart, M., "Acoustic emission during run-up and run-down of a power generation turbine," *Tribology International*, Vol. 37, No. 5, 2004, pp. 415-422.

[42] Grimmelius, H. T., Meiler, P. P., Maas, H. L. M. M., Bonnier, B., Grevink, J. S., and Van Kuilenburg, R. F., "Three state-of-the-art methods for condition monitoring," *IEEE Transactions on Industrial Electronics*, Vol. 46, No. 2, 1999, pp. 407-416.

[43] Hountalas, D. T. and Kouremenos, A. D., "Development and application of a fully automatic troubleshooting method for large marine diesel engines," *Applied Thermal Engineering*, Vol. 19, No. 3, 1999, pp. 299-324.

[44] Gu, F. and Ball, A. D., "Diesel injector dynamic modelling and estimation of injection parameters from impact response. Part I; modelling and analysis of injector impacts," *Proceedings of the Institution of Mechanical Engineers, Part D: Journal of Automobile Engineering*, Vol. 210, No. 4, 1996, pp. 293-302.

[45] Gu, F., Ball, A. D., and Rao, K. K., "Diesel injector dynamic modelling and estimation of injection parameters from impact response. Part 2: prediction of injection parameters from monitored vibration," *Proceedings of the Institution of Mechanical Engineers, Part D: Journal of Automobile Engineering*, Vol. 210,

No. 4, 1996, pp. 303-312.

[46] StatSoft, I., Electronic Statistics Textbook, Tulsa, OK: StatSoft Web Resource: http://www.statsoft.com/textbook/stathome.html, 2004.

[47] Weisstein, E. W., Probability and Statistics, MathWorld: A Wolfram Web Resource, http://mathworld.wolfram.com/topics/moments.html, 2004.

[48] NIST/SEMATECH, e-Handbook of Statistical Methods, Web Resource: http://www.itl.nist.gov/div898/handbook, 2004.

[49] Freund, J. E. and Walpole, R. E., *Mathematical Statistics, 4th edition,* Prentice-Hall, New Jersey, USA, 1987.

[50] ASTM, "ASTM E 1316-99a: Standard terminology for nondestructive examinations," *Annual Book of ASTM Standards*, Vol. 3.03, 1999.

[51] BSI, "Non-destructive testing - Terminology, Part 9: Terms used in acoustic emission testing," *British standard, BS EN 1330-9:2000*, 2000, pp. 1-31.

[52] Harris, D. O. and Bell, R. L., "The measurement and significance of energy in acoustic emission testing," *Experimental Mechanics*, Vol. 17, No. 9, 1977, pp. 347-353.

[53] Beattie, A. G. and Jaramillo, R. A., "The measurement of energy in acoustic emission," *Review of Scientific Instruments*, Vol. 45, No. 3, 1974, pp. 352-357.

[54] Scott, I. G., *Basic acoustic emission,* Gondon and Breach Science, USA, 1991.

[55] Matthews, J. R., *Acoustic Emission,* Gordon and Breach Science, USA, 1983.

[56] Duncan, H. A., "Energy processing techniques for stress wave emission signals," *Journal of the Acoustical Society of America*, Vol. 65, No. 6, 1979, pp. 1556-1561.

[57] Cochran, W. T., Cooley, J. W., Favin, D. L., Helms, H. D., Kaenel, R. A., Lang, W. W., Maling, G. C., Nelson, D. E., Rader, C. M., and Welch, P. D., "What is Fast Fourier Transform," *IEEE Transactions on Audio and Electroacoustics*, Vol. 15, No. 2, 1967, pp. 45-55.

[58] Qian, S. and Chen, D., *Joint Time Frequency Analysis: Methods and Application,* Prentice-Hall, New Jersey, USA, 1996.

[59] Welch, P. D., "The use of Fast Fourier Transform for the estimation of power spectra: A method based on time averaging over short, modified periodograms,"

IEEE Transactions on Audio and Electroacoustics, Vol. 15, No. 2, 1967, pp. 70-73.

[60] Mathworks, *MATLAB, Signal Processing Toolbox User's Guide Version 6.1,* Mathworks Inc., 2002.

[61] Cohen, L., "Time-frequency distributions - A review," *Proceeding of The IEEE*, Vol. 77, No. 7, 1989, pp. 941-981.

[62] Qian, S. and Chen, D., "Joint time-frequency analysis," *IEEE Signal Processing Magazine*, Vol. 16, No. 2, 1999, pp. 52-67.

[63] Peng, Z. K. a. C. F. L., "Application of the wavelet transform in machine condition monitoring and fault diagnostics: a review with bibliography," *Mechanical Systems and Signal Processing,* Vol. 18, No. 2, 2004, pp. 199-221.

[64] Rioul, O. and Vetterli, M., "Wavelets and signal processing," *IEEE Signal Processing Magazine*, Vol. 8, No. 4, 1991, pp. 14-38.

[65] Baydar, N. and Ball, A., "Detection of gear failures via vibration and acoustic signals using wavelet transform," *Mechanical Systems and Signal Processing*, Vol. 17, No. 4, 2003, pp. 787-804.

[66] Li, C. J. and Ma, J., "Wavelet decomposition of vibrations for detection of bearing-localized defects," *NDT & E International*, Vol. 30, No. 3, 1997, pp. 143-149.

[67] Liu, B. and Ling, S. F., "On the selection of informative wavelets for machinery diagnosis," *Mechanical Systems and Signal Processing*, Vol. 13, No. 1, 1999, pp. 145-162.

[68] Hamstad, M. A., O'Gallagher, A., and Gary, J., "A wavelet transform applied to acoustic emission signals, Part 1: Source identification," *Journal of Acoustic Emission*, Vol. 20, 2002, pp. 39-61.

[69] Jeong, H. and Jang, Y.-S., "Wavelet analysis of plate wave propagation in composite laminates," *Composite Structures*, Vol. 49, No. 4, 2000, pp. 443-450.

[70] Bishop, C. M., *Neural Networks for Pattern Recognition,* Oxford University Press, Great Britain, 2000.

[71] Thodoridis, S. and Koutroumbas, K., *Pattern Recognition,* Academic Press, USA, 1999.

[72] Hyvärinen, A., Karhunen, J., and Oja, E., *Independent Component Analysis,* John Wiley & Sons, USA, 2001.

[73] Pontoppidan, N. H. and Larsen, J., "Unsupervised condition change detection in large diesel engines," *2003 IEEE Workshop on Neural Networks for Signal Processing*, 2003, pp. 565-574

[74] Li, W., GU, F., Ball, A. D., Leung, A. Y. T., and Phipps, C. E. "A study of the noise from diesel engines using the independent component analysis," *Mechanical Systems and Signal Processing*, Vol. 15, No. 6, 2001, pp. 1165-1184.

[75] Sharkey, A. J. C., Chandroth, G. O., and Sharkey, N. E., "A multi-net system for the fault diagnosis of a diesel engine," *Neural Computing & Applications*, Vol. 9, No. 2, 2000, pp. 152-160.

[76] Sharkey, A. J. C., Chandroth, G. O., and Sharkey, N. E., "Acoustic emission, cylinder pressure and vibration: A multisensor approach to robust fault diagnosis," *Proceedings of the IEEE-INNS-ENNS International Joint Conference on Neural Networks*, Vol. 6, 2000, pp. 223-228.

[77] Li, W., Parkin, R. M., Coy, J., and Gu, F., "Acoustic based condition monitoring of a diesel engine using self-organising map networks," *Applied Acoustics*, Vol. 63, No. 7, 2002, pp. 699-711.

[78] Autar, R. K., "An automated diagnostic expert system for diesel engines," *Transactions of ASME, Journal of Engineering for Gas Turbines and Power*, Vol. 118, No. 3, 1996, pp. 673-679.

[79] Parikh, C. R., Pont, M. J., and Jones, N. B., "Application of Dempster-Shafer theory in condition monitoring applications: A case study," *Pattern Recognition Letters*, Vol. 22, No. 6-7, 2001, pp. 777-785.

[80] Zhang, Y., Zhang, Z. P., and Zhou, Y. C., "Research on the fuzzy and dynamic monitoring of the diesel engine operating conditions," *Proceedings of the Institution of Mechanical Engineers, Part D: Journal of Automobile Engineering*, Vol. 212, No. 5, 1998, pp. 421-426.

[81] Maji, K. A., Satpathi, D., and Kratochvil, T., "Acoustic emission source location using Lamb wave modes," *Journal of Engineering Mechanics*, Vol. 123, No. 2, 1997, pp. 154-161.

[82] Surgeon, M. and Wevers, M., "One sensor linear location of acoustic emission events using plate wave theories," *Materials Science and Engineering A*, Vol. 265, No. 1-2, 1999, pp. 254-261.

[83] Ziola, S. M. and Gorman, M. R., "Source location in thin plates using cross-correlation," *Journal of the Acoustical Society of America*, Vol. 90, No. 5, 1991, pp. 2551-2556.

[84] Gaul, L. and Hurlebaus, S., "Identification of the impact location on a plate using wavelets," *Mechanical Systems and Signal Processing*, Vol. 12, No. 6, 1998, pp. 783-795.

[85] Holford, K. M. and Carter, D. C., "Acoustic emission source location," *Key Engineering Materials*, Vol. 167, 1999, pp. 162-171.

[86] Mba, D. and Hall, L. D., "The transmission of acoustic emission across large-scale turbine rotors," *NDT & E International*, Vol. 35, No. 8, 2002, pp. 529-539.

[87] Tobias, A., "Acoustic emission source location in two dimensions by an array of three sensors," *Non-Destructive Testing*, Vol. 9, No. 1, 1976, pp. 9-12.

[88] Wang, Q. and Chu, F., "Experimental determination of the rubbing location by means of acoustic emission and wavelet transform," *Journal of Sound and Vibration*, Vol. 248, No. 1, 2001, pp. 91-103.

[89] Engelbrecht, J., *Nonlinear Wave Dynamics: Complexity and Simplicity,* Kluwer Academic Publishers, Netherlands, 1997.

[90] Miller, R. K., Pollock, A. A., Watts, D. J., Carlyle, J. M., Tafuri, A. N., and YezziJr, J. J., "A reference standard for the development of acoustic emission pipeline leak detection techniques," *NDT & E International*, Vol. 32, No. 1, 1999, pp. 1-8.

[91] Wilkinson, P., Reuben, R. L., Jones, J. D. C., Barton, J. S., Hand, D. P., Carolan, T. A., and Kidd, S. R., "Tool wear prediction from acoustic emission and surface characteristics via an artificial neural network," *Mechanical Systems and Signal Processing*, Vol. 13, No. 6, 1999, pp. 955-966.

[92] Achenbach, J. D., *Wave Propagation in Elastic Solids,* Elsevier, Netherlands, 1975.

[93] Graff, F. K., *Wave motion in elastic solids,* Dover, New York, USA, 1991.

[94] Holroyd, T. J., *The acoustic emission and ultrasonic monitoring handbook:*

machine and systems condition monitoring series, Coxmoor, UK, 2000.

[95] Gorman, M. R., "Plate wave acoustic emission," *Journal of the Acoustical Society of America*, Vol. 90, No. 1, 1991, pp. 358-364.

[96] Halmshaw, R., *Non-Destructive Testing, 2nd Edition,* Edward Arnold 1991.

[97] Cremer, L. and Heckl, M., *Structure-borne sound: structural vibrations and sound radiation at audio frequencies, 2nd edition,* Springer-Verlag, Germany, 1988.

[98] Iowa State University, Mode Conversion, NDT Resource centre: Education Resource, http:// www.ndt-ed.org/EducationResources/ComunityCollege/Ultra-sonics/Physics/modeconversion.htm, 2004.

[99] Iowa State University, Material Properties Tables, Acoustic Properties, http://www.ndt-ed.org/GeneralResources/MaterialProperties/UT/ut_matlprop_ index.htm, 2004.

[100] The Institution of Metallurgists, *Ultrasonic Non-Destructive Testing, Monograph no. 9,* The Institution of Metallurgists, London, UK, 1980.

[101] Graham, L. J. and Alers, G. A., "Acoustic emission in the frequency domain," *Monitoring Integrity by Acoustic Emission, ASTM STP-571, American Society for Testing Materials*, 1975, pp. 11-39.

[102] Prosser, W. H., "Advanced AE techniques in composite material research," *Journal of Acoustic Emission*, Vol. 14, No. 3-4, 1996, pp. 1-11.

[103] Finlayson, R. D., Luzio, M. A., Miller, A., and Pollock, A. A., "Continuous health monitoring of graphite epoxy motorcases (GEM)," *CINDE Journal*, Vol. September/October, 2003, pp. 15-24.

[104] Ying, S. P., Hamlin, D. R., and Tanneberger, D., "A multichannel acoustic emission monitoring system with simultaneous multiple event data analyses.," *Journal of the Acoustical Society of America*, Vol. 55, No. 2, 1974, pp. 350-356.

[105] Ding, Y., Reuben, R. L., and Steel, J. A. "A new method for waveform analysis for estimating AE wave arrival times using wavelet decomposition," *NDT and E International*, Vol. 37, No. 4, 2004, pp. 279-290.

[106] White, P. H., "Cross correlation in structural systems: dispersion and nondispersion waves," *The Journal of Acoustical Society of America*, Vol. 45, No. 5, 1969, pp. 1118-1128.

[107] Holmes, P. J., "The experimental characterization of wave propagation systems: I. non-dispersive waves in lumped systems," *Journal of Sound and Vibration*, Vol. 35, No. 2, 1974, pp. 253-275.

[108] Holmes, P. J., "The experimental characterization of wave propagation systems: II. Continuous systems and the effects of dispersion," *Journal of Sound and Vibration*, Vol. 35, No. 2, 1974, pp. 277-297.

[109] Polesskaya, L. M. and Vangeli, M. S., "Reconstruction procedure for the original form of an acoustic emission signal propagating in a solid body," *Soviet Journal of Nondestructive Testing (English translation of Defektoskopiya)*, Vol. 17, No. 10, 1981, pp. 794-799.

[110] ASTM, "ASTM E976-99: Standard guild for determining the reproducibility of acoustic emission sensor response," *Annual Book of ASTM Standards*, Vol. 3.03, 1999, pp. 395-403.

[111] Higo, Y. and Inaba, H., "The general problems of AE sensors," *Acoustic Emission: Current Practice and Future Directions, ASTM STP 1077, Sachse, W., Roget, J. and Yamaguchi, K., Eds., American Society for Testing and Materials, Philadelphia, USA*, 1991, pp. 7-24.

[112] Perkins, *Workshop Manual, New 1000 series model AJ to AS and YG to YK, 4- and 6-cylinder diesel engines for industrial and agricultural application, TPD 1350E, Issue. 4,* Perkins company, UK, 2001.

[113] AE Watt project, *An EU-Project under the Competetive and Sustainable Growth Programme, Project NO: G3RD-CT-2002-00786, Marine Power Plant Management and Monitoring using Acoustic Emission.*

[114] Carlson, G. E., *Signal and Linear System Analysis,* Houghton Mifflin Company, Boston, USA, 1992.

[115] Dzenis, Y. A. and Qian, J., "Analysis of microdamage evolution histories in composites," *International Journal of Solids and Structures*, Vol. 38, No. 10-13, 2001, pp. 1831-1854.

[116] Hsu, N. N., Simmons, J. A., and Hardy, S. C., "An approach to acoustic emission signal analysis - Theory and experiment," *Material Evaluation*, Vol. 35, No. 10, 1977, pp. 100-106.

[117] Kline, R. A., "Acoustic emission signal characterization," *Acoustic emission:*

Non-destructive testing monograhps and tracts vol. 2, edited by J. R. Matthews, Gordon & Breach, USA, 1983, pp. 105-138.

[118] Mathworks, *MATLAB, Curve fitting Toolbox User's Guide Version 1,* Mathworks Inc., 2002.

[119] Shehadeh, M., El-Ghamry, M., Steel, J. A., and Reuben, R. L., "AE source location in long pipes using cross-correlation and wavelet transforms," *Proceeding of the 17th International Conference on Condition Monitoring and Diagnostic Engineering Management, COMADEM, Cambridge, UK,* 2004, pp.250-259.

[120] Stephens, R. W. B. and Pollock, A. A., "Waveforms and frequency spectra of acoustic emissions," *Journal of the Acoustical Society of America*, Vol. 50, No. 3 pt. 2, 1971, pp. 904-910.

[121] Shao, Y. and Mechefske, C. K., "Transmission of vibration signals through static mechanical interfaces - Part I: Single metal stacks," *Proceeding of the 17th International Conference on Condition Monitoring and Diagnostic Engineering Management, COMADEM, Cambridge, UK,* 2004, pp. 240-249.

[122] Newland, D. E., *An Introduction to Random Vibration Spectral and Wavelet Analysis,* Prentice Hall, Singapore, 1993.

[123] Heisler, H., *Advanced Engine Technology,* Butterworth-Heinemann, UK, 2003.

[124] Robertson, A. I. F., Douglas, R. M., Nivesrangsan, P., Brown, E. R., Steel, J. A., and Reuben, R. L., "Source identification using acoustic emission on large bore cylinder liners," *Proceeding of the 26th European Conference on Acoustic Emission Testing, EWGAE, Berlin, Germany,* 2004, pp. 637-643.

[125] Lim, T., Nivesrangsan, P., Corney, J. R., Steel, J. A., and Reuben, R. L., "Predicting AE attenuation within solids by Geometric Analysis," *International Conference on Shape Modeling and Applications SMI-05*, 2005 (Submitted).

Appendix A: Detailed drawings and dimensions of various cast iron and source-sensor positions

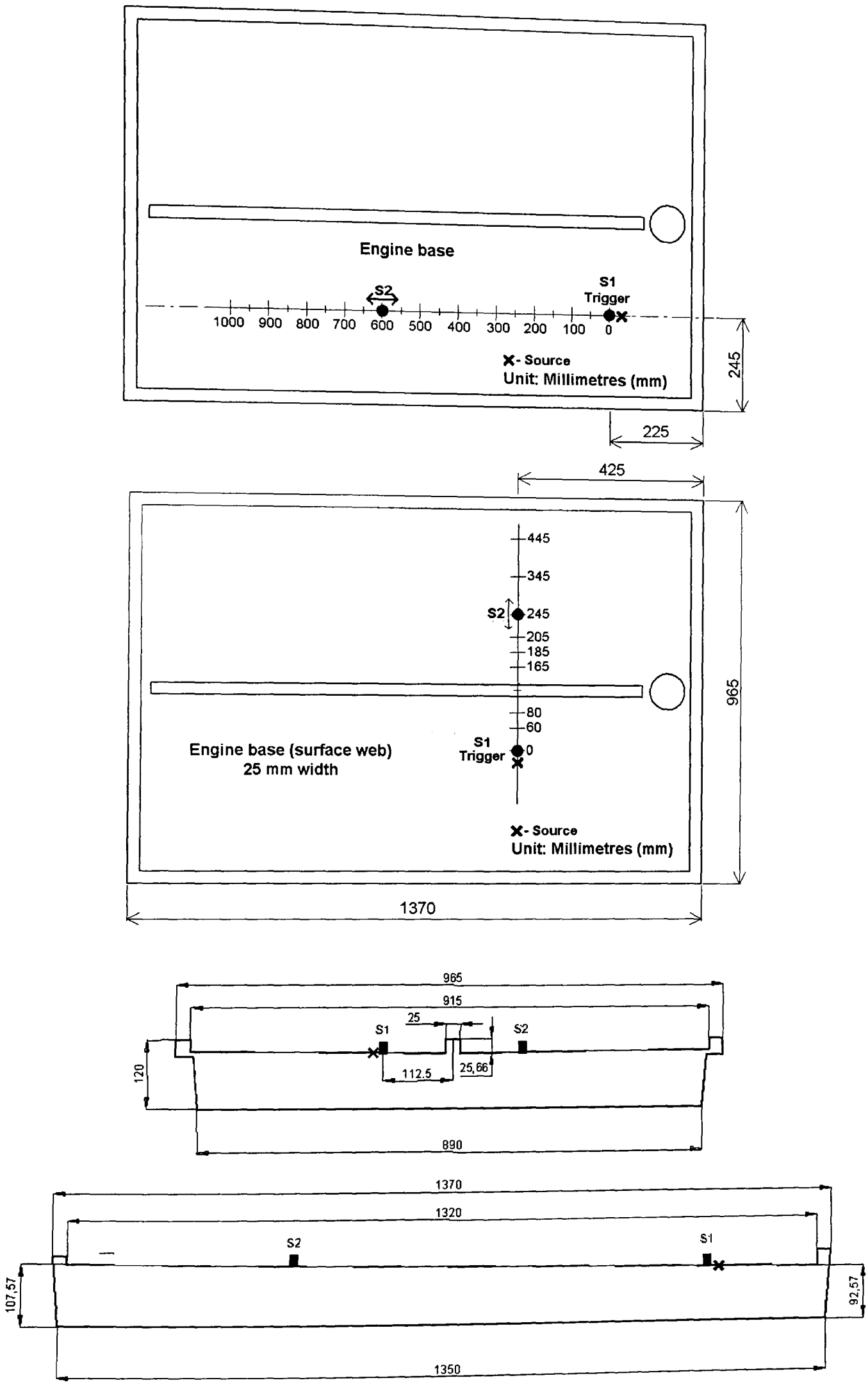

Figure A-1: Drawings and dimensions of the engine base and source-sensor positions

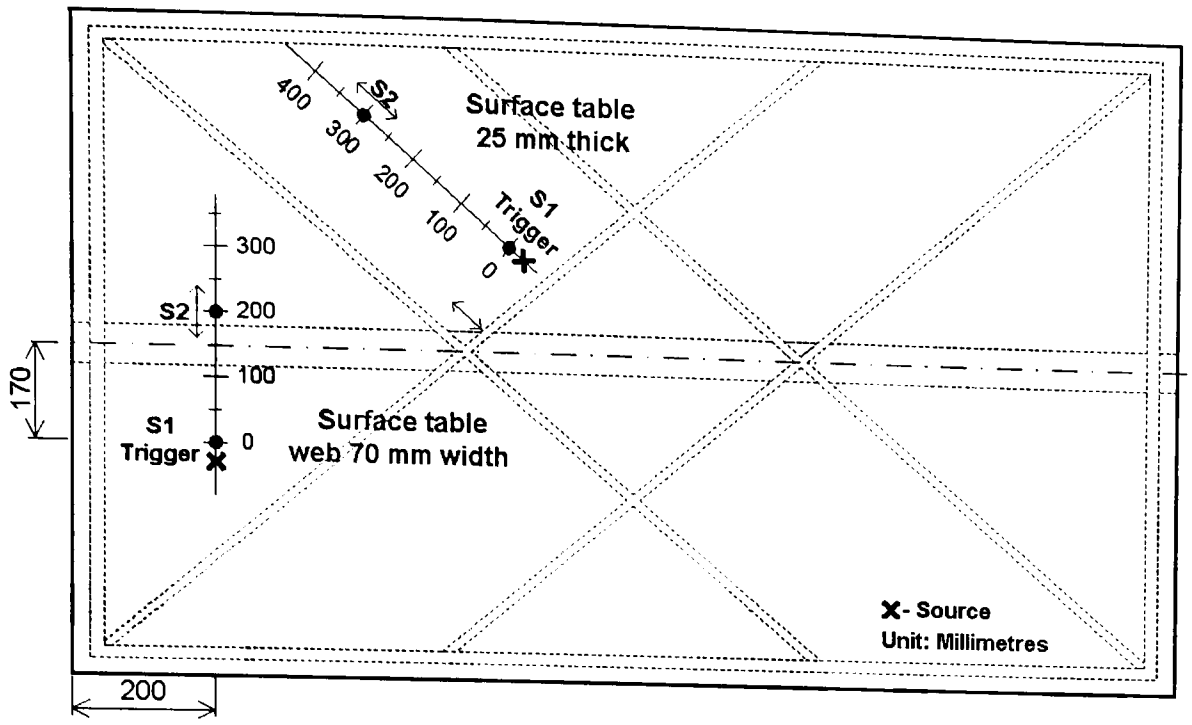

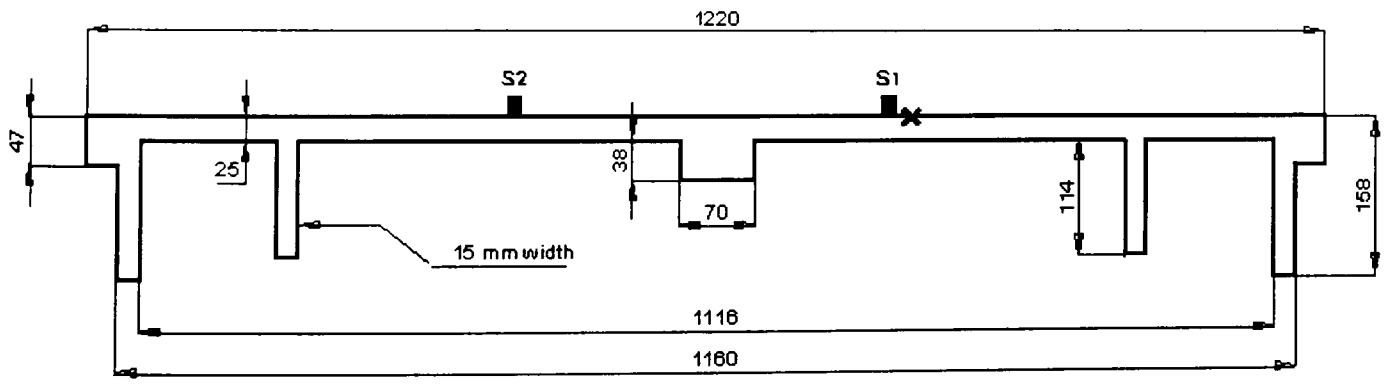

Figure A-2: Drawings and dimensions of the engine base and source-sensor positions

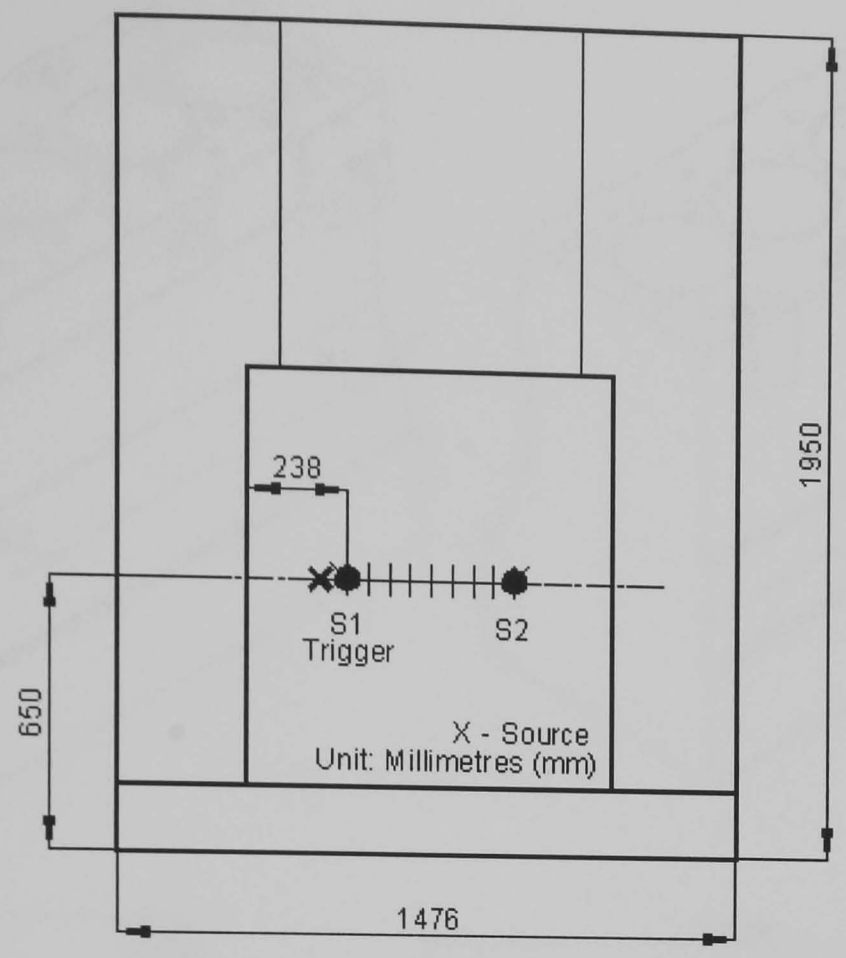

Figure A-3: Dimensions of the flat panel of a large marine diesel engine and source-sensor positions

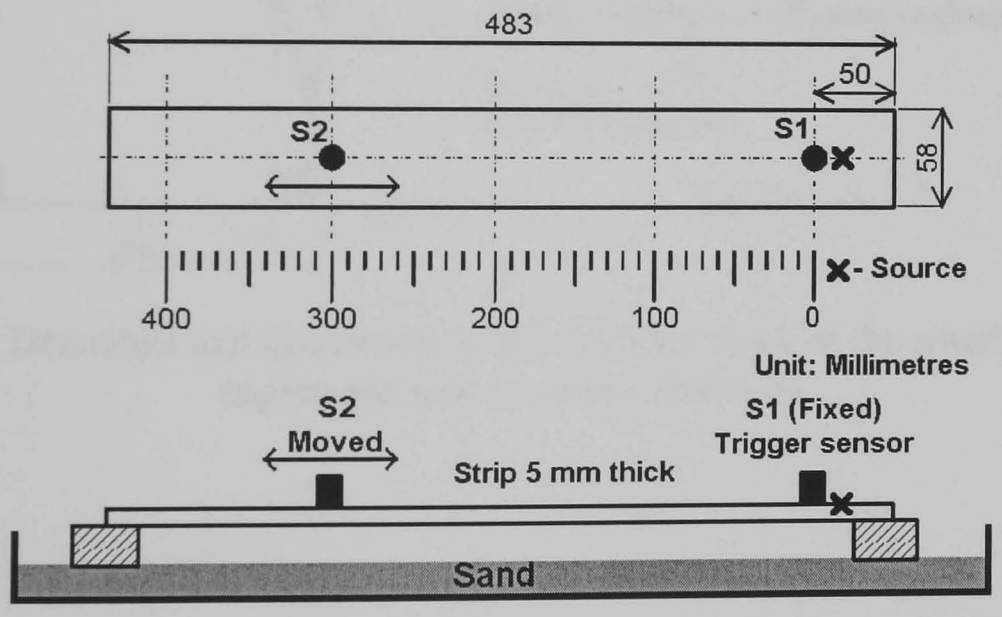

Figure A-4: Dimensions of the strip and source-sensor positions

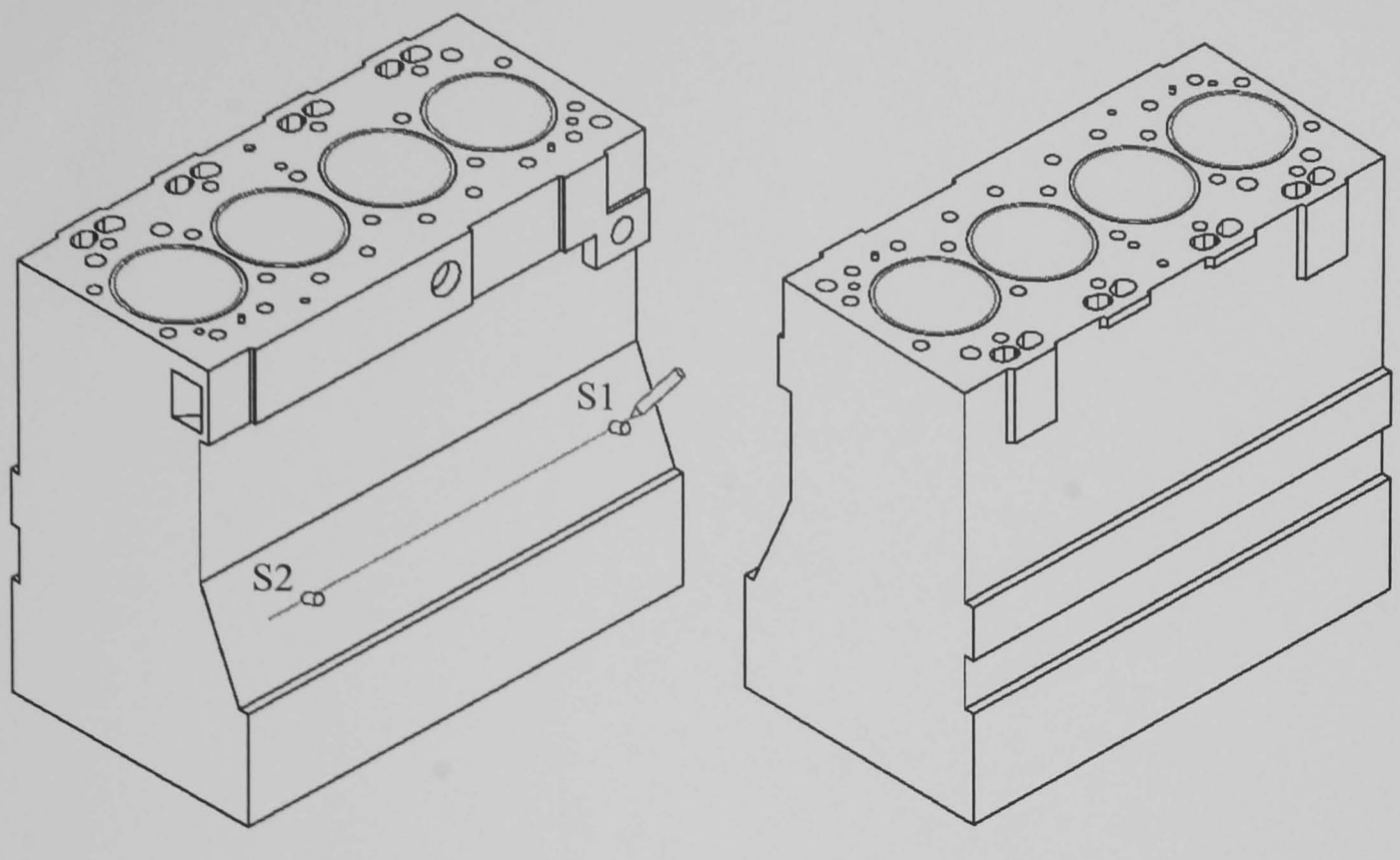

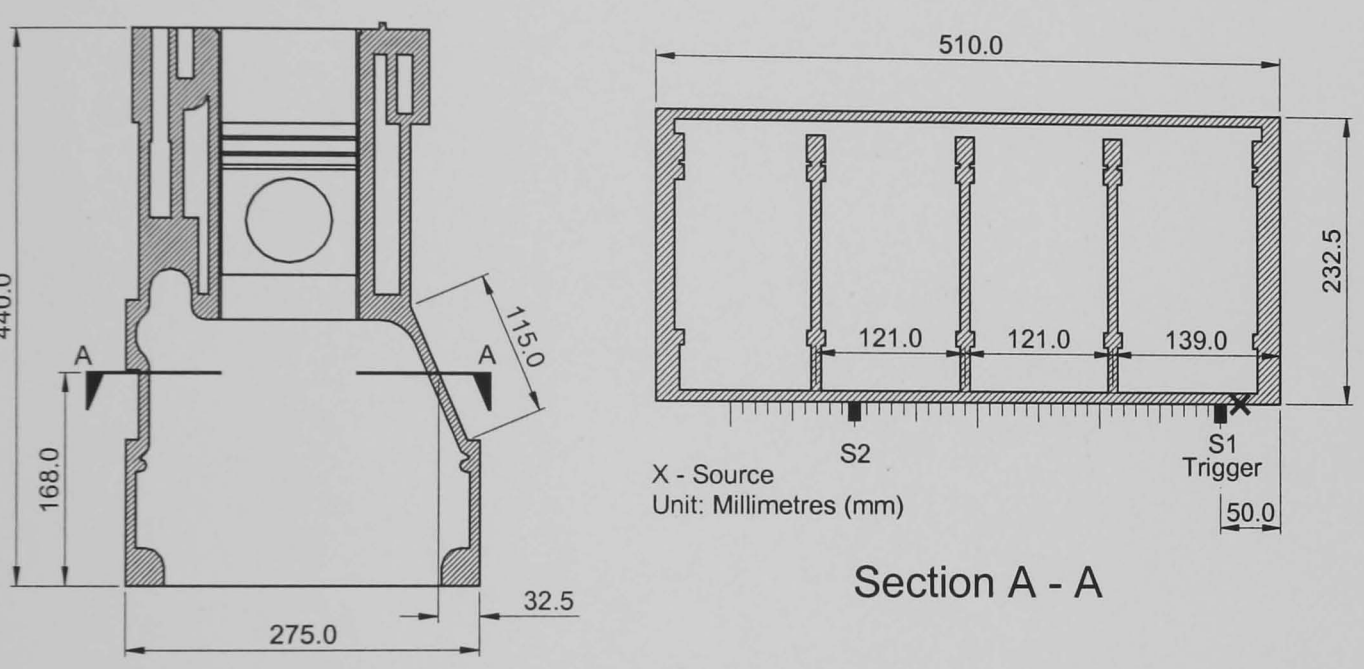

Figure A-5: Drawings and dimension of the cylinder block of the small HSDI diesel engine and source-sensor positions.